ABSTRACT

CHEN, QUNYI. Design and Control of a Fast Long Range Actuator for Single Point Diamond Turning. (Under the direction of Dr. Thomas A. Dow).

This dissertation focuses on the design and control of a fast long range actuator to machine non-rotationally symmetric (NRS) optical surfaces with millimeters of sag at high production rates. The goal is to retain the surface quality (form error of less than 200 nm PV and surface finish of less than 5 nm RMS) of existing diamond turning machines while moving the tool over a range of 4 mm at a frequency of 20 Hz.

The actuator in this dissertation features a light-weight slide supported by an air bearing, the tool feed motion is controlled by a linear motor, a linear encoder and real-time control platform. The first actuator prototype was built and tested in 2004-2005, but its performance was found to be unacceptable due to various deficiencies. This dissertation research has developed a methodology for the design and control of this type of actuator to optimize its performance. It essentially takes a three-step approach: investigate the characteristics of the tool motion control in the diamond turning in terms of tool motion trajectories, disturbances to the tool motion, and the required tool positioning precision; develop an actuator system to meet motion control requirement; integrate the actuator with a diamond turning machine and conduct precision machining and precision metrology for performance validation. In this research, the original actuator is modified and upgraded with new system components including a linear amplifier, two control platforms, two linear encoders and an add-on counterbalance drive. Effective feedback and feedforward control techniques for profile tracking and disturbance rejection are investigated and implemented. Critical implementation issues for motion planning are resolved to improve the quality of motion trajectory generation and the quality of motion synchronization while machining. Modification of the first prototype has pushed the limits of performance on both tool motion control (±30 nm for position holding error and ±70 nm for 2 mm 20 Hz sinusoidal tracking error) and machining results (plated copper flat with 7.4 nm RMS surface finish for, non-rotationally symmetric PMMA tilted flat with 50.8 mm diameter and 4 mm excursion with 0.9 μm PV flatness error

and 17 nm RMS surface finish). Further improvement performance depends on a total redesign of the actuator. The desirable system component characteristics to achieve required tool positioning quality, of the slide piston, the air bearing, the amplifier, the motor and counterbalance, are proposed and analyzed. Critical system configuration issues regarding the amount of moving mass, the size of the motor, the sampling rate of digital control system and the necessity of physical damping are also addressed.

Finally, by creating a biconic mirror with fiducial features for kinematic coupling, this dissertation has also proven the feasibility of fabricating real-world optics with this type of actuator.

Design and Control of a Fast Long Range Actuator for Single Point Diamond Turning

by
Qunyi Chen

A dissertation submitted to the Graduate Faculty of
North Carolina State University
In partial fulfillment of the
Requirements for the degree of
Doctor of Philosophy

Mechanical Engineering

Raleigh, North Carolina

2009

APPROVED BY:

_____	_____
Jeffrey W. Eischen	Paul I. Ro
_____	_____
Ronald O. Scattergood	Thomas A. Dow
	Chairman of Advisory Committee

BIOGRAPHY

Qunyi Chen obtained a Master of Science in Mechanical Engineering from Northeastern University in China in 1996. He entered North Carolina State University in 1997, received a Master of Science in Mechanical Engineering in 1998 and a Master of Science in Electrical Engineering in 1999. Then he went to work as a Mechanical Engineer with GE Healthcare in Waukesha, WI, designing and developing electro-mechanical positioning subsystems and their interfaces and integrations for medical diagnostic X-ray equipment. He returned to North Carolina State University in 2005 to pursue a PhD degree in Mechanical Engineering.

ACKNOWLEDGEMENTS

I would first express sincere appreciation to my advisor, Dr. Thomas A. Dow, for his support, guidance and insights that made this work successful. I am most impressed with his everlasting energy, passion and dedication to explore unknowns and new things, and his commitment to complete objectives and make good things happen.

Additionally, I would like to extend appreciations to three other committee members: Dr. Paul Ro originally brought me back to NC State University and provided valuable inputs on the control system analysis for this research work. Dr. Jeff Eischen helped me on the analysis of the air bearing and structural dynamics. Dr. Ron Scattergood taught me the knowledge of tool-workpiece interactions in the machining process.

My gratitude certainly goes to two research staffs at the Precision Engineering Center for their strong support on the experimental work: Ken Garrard helped me with the implementation of control system, motion planning and data processing. Alex Sohn helped me with the machining, metrology and troubleshooting of electronics malfunctions. The implementation of DSP-based real time control platform was also made possible with the support of PMDi president Mile Erlic, and the associates Derek Richardson and Glen Field.

Special thanks go to Dr. Kari Tammi from Finland, during his tenure at NC State University as a post-doctoral fellow, we worked together on the loop shaping technique and a technical paper, and he led me into the initial application of AFC.

I consulted with several professors including Dr. Feng Wu and Dr. Greg Buckner at NCSU, Dr. David Trumper at MIT and Dr. Tsu Chin Tsao at UCLA, their comments and suggestions are very valuable for the control of this actuator. I also want to recognize following people, Dave Youden, Karl Falter, Arun Veeramani, Erik Zdanowicz, Dave Brehl and Meirong Shi, for their contributions to my research work at PEC.

Finally, the understanding and support of my wife, my parents and my parents-in-law are indispensable for me to complete my doctoral study. They have taken care of my family in the past few years so that I could have dedicated to my study.

LIST OF CONTENTS

LIST OF TABLES

LIST OF FIGURES

1. Introduction

1.1 Machining of Freeform Optical Surfaces

Diamond turning (DT) has revolutionized the fabrication of optical surfaces for consumer, defense and science applications such as contact lenses, forward-looking infrared radar and infrared spectrometers. It has made this impact not only because it can accurately and rapidly fabricate diffractive, refractive and reflective optical surfaces, but also because it can create reference features tied to the optical surfaces to assist in the assembly process [13, 14]. An emerging trend in optical design is the use of non-rotationally symmetric (NRS) surfaces to reduce complexity, bulk and weight while improving optical performance [15-18]. However, there are also many challenges in the fabrication of freeform surfaces with diamond turning machine (DTM) due to the existence of NRS component. To create NRS surface components, the diamond tool moves as a function of spindle rotation and DTM slide translation. The different tool servos are set apart by the methods of creating tool motion: short stroke Fast Tool Servo or FTS, slow tool servo and long range fast tool servo. Figure 1-1 shows two typical T-base DTM configurations, with a tool post or a tool servo being mounted on the carriage of either the X-slide or Z-slide. The workpiece is mounted on the chuck of the spindle. The slide parallel with the spindle axis is defined as Z-axis (or Z-slide), X-axis (or X-slide) is orthogonal to the Z-axis. Multi-axis motions are synchronized by generating the tool motion command as a function of the spindle position and X-slide location.

Short Stroke Fast Tool Servo (FTS)

The FTS is typically piezoelectrically driven, and has a stroke of 10-400 μm with a bandwidth of 200-1000 Hz. The high stiffness and low moving mass of PZT actuators allow for high bandwidth in the tool motion control. The main limitation with piezoelectric servos is their lack of stroke. A stack of piezoelectric (PZT) disks produces a strain of 0.1% or 1 μm

per mm of length. Mechanical amplification of the piezo's motion can be used to extend the range of motion, but it significantly reduces the stiffness, and also introduces inaccuracies in the tool motion. One of the earliest FTSs was initially designed by Patterson and Magrab [19] at Lawrence Livermore National Lab to correct spindle errors on the DTM but was quickly expanded to produce biconic contact lenses for correcting astigmatism and zone plates for optical applications [20]. It has 2.5 μm stroke, 660 Hz bandwidth (-3dB), and 1.3 nm dynamic repeatability. [21] describes a system for asymmetric turning, by using a piezoelectric actuator to drive a tool through a lever assembly. The FTS had 50 μm stroke and 200 Hz bandwidth.

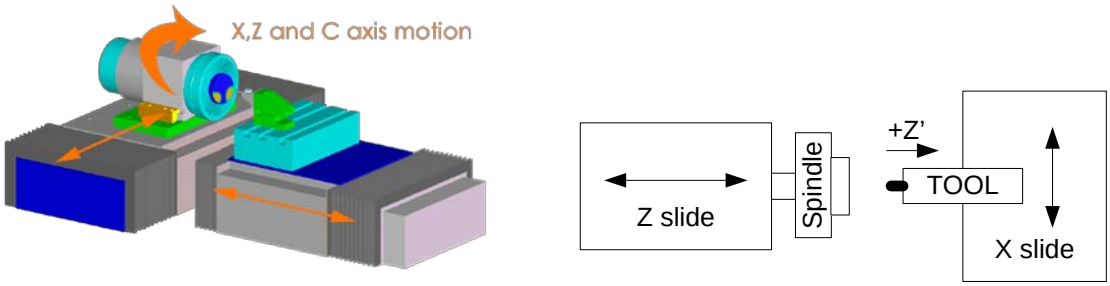

(a) Configuration one (Precitech) (b) Configuration two (Rank-Pneumo ASG2500)

Figure 1-1 Typical DTM system configurations with a tool post or a tool servo

Several different versions of FTS have been developed at the Precision Engineering Center at North Carolina State University. Falter designed a FTS capable of 20 μm total stroke, but only 5 μm stroke at 1 KHz [22]. Based on the similar concept, MAC 100 [23] was built with a 100 mm hollow PZT stack to achieve 100 μm of range. Falter and Youden designed a device that is commercially available on a machine for contact lens fabrication. This fast tool servo has 400 μm stroke at DC and 600 Hz bandwidth. It uses a T lever to achieve 14:1 mechanical motion amplification [24].

Kinetic Ceramics produced the Variform with 400 μm of stroke using a lever amplifier and a flexure-based tool holder. They also produced a longer range version (Varimax) with 600 μm stroke. These commercial units are marketed for the contact lens industry by

Sterling UltraPrecision in Tampa FL. Cuttino developed a FTS of 100 μm stroke and 100 Hz bandwidth [25], its PZT stack was 13 cm long and had an open-loop stiffness of around 70 N/μm.

In addition to the significant research activities on piezoelectrically driven FTSs, there are a few electromagnetically driven FTSs developed at the Precision Motion Control lab of MIT. Montesanti designed a rotary motor FTS capable of 50 μm stroke at 2 KHz, and a hybrid rotary/linear FTS with a stroke of 70 μm and 10 KHz bandwidth [9]. Lu created an ultra-fast linear tool servo with 50 μm stroke and 10 KHz bandwidth [5]. Wang designed a voice-coil-based actuator to achieve 0.4 mm stroke and 0.1 μm resolution [26]. A commercial FTS500 made by Precitech is capable of 0.5 mm stroke and 1000 Hz bandwidth, this drive system features very linear response curves within 100 Hz which contribute to their achieving high form accuracy.

Slow Tool Servo (STS)

The slow tool servo, also known as slow slide servo [27, 28], uses DTM Z-slide for the tool motion by adopting linear motor for DT machine slide drives to replace ball screws. This change allowed more flexibility in the motion of the slide without damage to the ball screw. It has advantages of fabricating parts with much larger deviation than would be possible with a short-stroke FTS. However, when NRS surfaces is machined by coordinating the motion of all of the axes (including the spindle), the spindle speed is reduced to the point where the heavy slides (a few hundred pounds) can follow the position commands. The tool motion is limited to about 1 Hz for a stroke of a few millimeters. As such, the slow tool servo is plagued by thermal drift during the extremely long fabrication time just like those traditional fabrication methods such as grinding and polishing, or flycutting [29].

Long Range Fast Tool Servos

The long range fast tool servo can be operated with millimeter level stroke at tens of Hertz, and is of most interest in this research. The development of long-range fast tool servo is driven by the need to create NRS surfaces with millimeters of stroke at high-speed while retaining the surface quality of existing DTMs. This class of actuator typically utilize Lorentz force for actuation, such as voice coil motor (VCM) or brushless linear and rotary motor, the maximum achievable acceleration is limited by the heat generated in the coil [30].

The use of a linear motor and air-bearing slide as the basis for a fast tool servo was first proposed by Douglas in Oak Ridge National Lab in 1983 [123]. The application was to machine off-axis sections of parabolic mirrors on axis. Greene and Shinstock developed a linear servo with 6 mm stroke and 100 Hz bandwidth [31]. The moving coil-tool assembly is supported by a simple flexural bearing, and the position is measured by a capacitance gage. The linear VCM (BEI LA13-12-000A) was powered by a PWM amplifier (Copley 201). The natural vibration mode of physical system at 15 Hz was found to be the performance limiter, so the authors proposed a new design with bigger motor and larger stiffness for the flexural bearing.

A rotary servo designed by Ludwick and Trumper [8, 32] eliminated the reaction force by a balanced rotary design, but it created the more difficulty in the trajectory generation. It was made for the machining of plastic spectacle lenses, and has a stroke of 3 cm and 200 Hz bandwidth.

Weck *et al* at Fraunhofer Institute for Production Technology have developed a hybrid long stroke fast tool servo, which integrated two mechanically coupled actuators [33]. The piezoelectric system has a stroke of 40 μm at 1 KHz bandwidth, and the linear motor has a stroke of 2 mm at 40 Hz. The piezoelectric translator had a maximum force of 2400 N, a stiffness of 50 N/ μm and a resonance frequency with the loaded mass close to 2 KHz. The peak thrust force was 900 N with a time constant of 5 ms. The power loss of the linear motor and the piezoelectric translator was dissipated by a water-cooling system. The moving mass is supported by parallel springs. The reaction force is reduced by allowing a counter

movement of the motor stator during the linear actuation. The overall design was not completely successful since 68 Hz resonance of the moving mass/spring cannot be attenuated from closed-loop servo control.

A second long stroke actuator was developed by Weck [34] with 16 mm of range and a bandwidth of 100 Hz. The slide of the actuator consists of CFK (carbon fiber reinforced plastic) frame and nickel coated aluminum skin. The moving mass is supported aerostatic bearing, driven by a linear motor consisting of two stationary coils and two moving magnets as shown in Figure 1-2. The motor is powered by a current controlled analog amplifier with a maximum current of +/-8 A. The position measurement by a combination of a LIP403 Heidenhain linear scale encoder and a Heidenhain IK410 encoder interpolator had a resolution of about 2 nm. The position feedback control is PC-based. The software of the control system includes the device driver for the PCI I/O board and a server system which facilitates the building of the control algorithm and the set point generator as well as elementary features like online representation of position data. To provide deterministic time response, FSMLabs Real Time Linux is used as the operating system. The employed servo sampling rate is in the range from 8 KHz to 25 KHz. A free form mirror with a maximum excursion of 1.1 mm was cut with this actuator at 200 rpm spindle speed, and 6 μm depth of cut and 1.8 mm/min cross feedrate [36]. The resulted surface finish was in the range of 15-25 nm Ra, the form error was within 0.8 μm. This actuator design did not consider the reaction force reduction. The counterbalance problem was fully resolved by a dual-drive design in another actuator with hydrostatic bearing support, but it was intended for the machining of steel [35].

Byl and Trumper developed a linear long-range fast tool servo shown in Figure 1-3 [4]. The servo consists of a 2”x2” porous air bearing stage driven by a unique three-phase oil cooled linear motor. The motor is powered by a linear amplifier, and the position is measured a linear encoder. The moving mass of 3 Kg has 25 mm total stroke and can accelerates at 100 m/s^2. The overall servo control performance is limited by the current loop bandwidth of 2 KHz, resonance mode of slide piston structure at 1600 Hz, and position measurement error.

In a sinusoidal tracking test of 2 mm amplitude and 20 Hz frequency, the tracking error is within ±1 μm. There were no machining results reported for this tool servo.

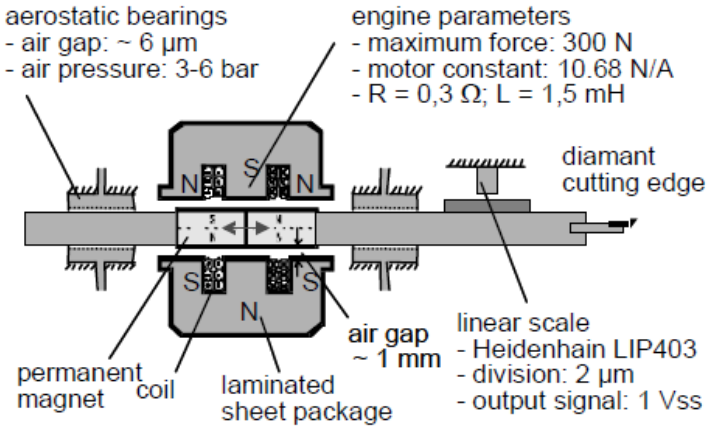

Figure 1-2 Schematic drawing of a fast tool servo [34]

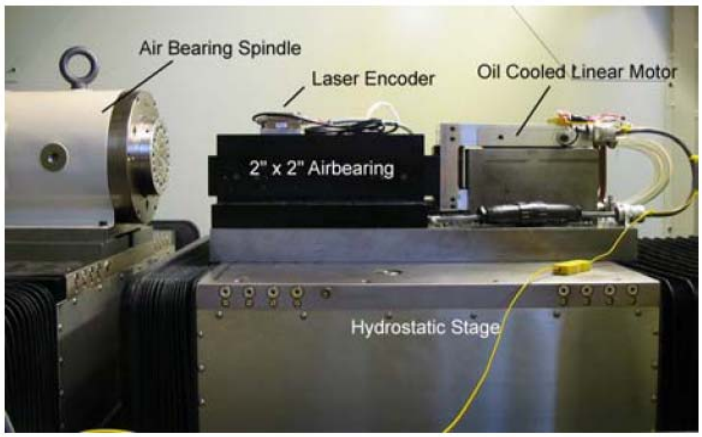

Figure 1-3 Photograph of the long-range fast tool servo mounted on a Moore DTM [4]

The long-range fast tool servo developed by Rakuff [3] utilizes a flexure driven by a VCM and a custom built linear amplifier. The position is measured by a laser interferometer. The complete servo system is shown in Figure 1-4. It has 2 mm stroke and 140 Hz bandwidth. To improve the servo control performance, both active electromotive damping and passive

viscoelastic damping were applied to increase the natural frequency of physical system and reduce the magnitude of resonance peak. A sinusoidal tracking test of 0.5 mm amplitude and 10 Hz frequency shows 0.2 % tracking error. A tilted flat with radius of 20 mm and tilt angle of 0.0005 radian was machined at a spindle speed of 2000 rpm. This corresponds to a sinusoidal tool motion of 10 μm and 67 Hz frequency, the measured flatness error is within 500 nm (peak-to-valley). Seven lobed 6061-T6 aluminum parts were also machined with 0.762 nose radius tool at a spindle speed of 840 rpm, 7 mm/min cross federate and 13 μm depth of cut. The measured surface finish by Mirau interferometer was in the range of 20 to 30 nm Ra for small amplitude parts (5 μm) and up to 40 nm Ra for large amplitude part (500 μm).

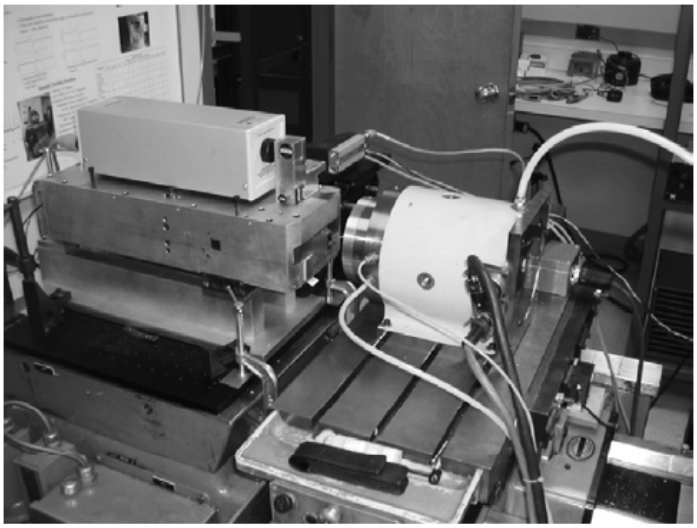

Figure 1-4 A picture of the long-stroke fast tool servo installed on a Moore DTM [3]

Moore Nanotechnology System, Inc. introduced a commercial NFTS-6000 in 2007 with a total stroke of 6 mm and capable of sinusoidal motion of 3 mm amplitude at 20 Hz. It consists of a voice coil motor with fully constrained porous air bearing design, integrated counter balance, a linear scale encoder and a linear amplifier. The control system is supported by an independent DSP controller. However, there is little technical information available on the performance of this device.

In the course of this literature review, a few long-range actuators for conventional non-circular machining were uncovered. The principles in the design and control of these actuators are transferable for diamond turning applications. Wu *et al* used a long stroke servo to machine an engine piston with elliptical cross section of 0.8 mm peak-to-peak amplitude at 1200 rpm spindle speed [37]. Figure 1-5 shows a schematic system setup of voice coil actuated direct drive developed by Babinski and Tsao for the turning of automotive camshaft [38, 39]. The actuator consists of a voice coil motor and a tool slide of 1.5 Kg supported by Rulon-LR bearing, and uses a laser position error with a resolution of 0.618 μm for position feedback. It achieves a 100 μm peak-to-peak position error following a cam trajectory with a tool travel of 6.5 mm, a peak acceleration of 9.8 m/s^2, and a maximum velocity of 0.6 m/s.

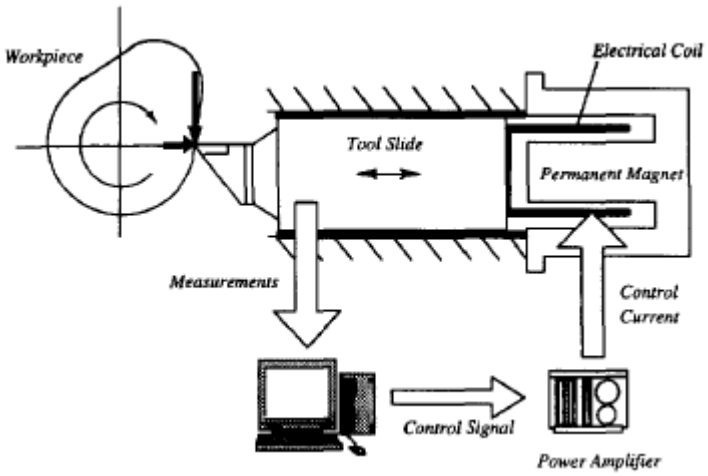

Figure 1-5 A schematic system setup of direct drive with VCM [38]

Kim and Tsao developed a novel dual-stage actuator system for the noncircular automotive camshaft turning process [40-42]. It consists of a first electrohydraulic actuator for 25-mm gross motion and a second piezoelectric actuator for 40 μm fine motion, the seoncd actuator is installed inside of the hollow piston of the first stage actuator as shown in Figure 1-6. The tracking error from the first stage electrohydraulic actuator is used as reference for the second stage piezoelectric actuator. In a tracking experiment of an

automotive cam profile at the rate of 600 rpm, the dual-stage servo system generated tracking error of 4 μm peak-to-peak and 0.80 μm root-meansquare (RMS) value.

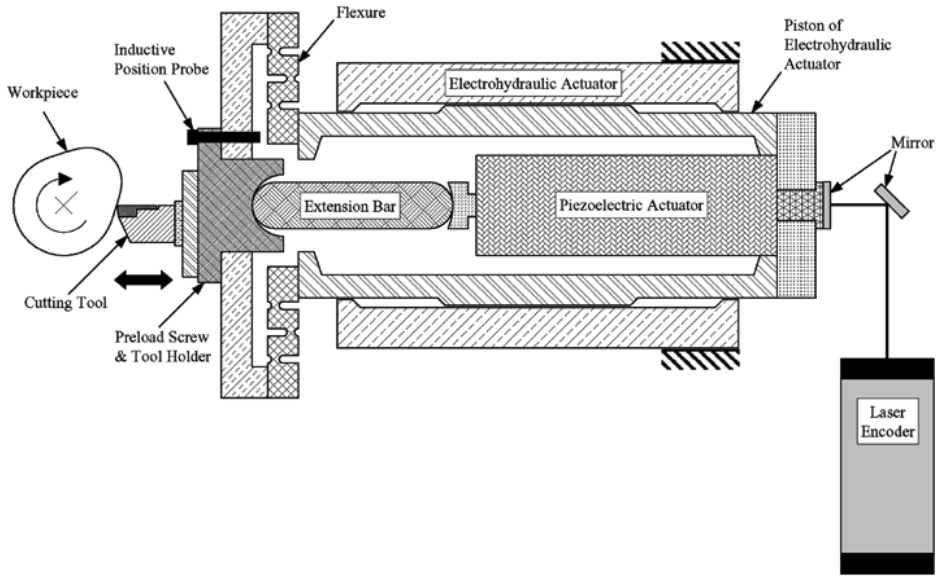

Figure 1-6 Cross-sectional view of a dual-stage actuator system [40]

1.2 Problem Statement

From the existing fabrication technologies for the freeform optical surfaces, it can be seen that, the FTS offers limited stroke and the slow slide servo is plagued by thermal drift during extremely long fabrication time. In addition, those long-range fast tool servos cannot effectively retain the surface quality of existing DTMs while creating NRS surfaces with millimeters of stroke at high-speed. The objective of this dissertation research is to develop such an actuator that can meet the simultaneous requirement of range, speed and precision of tool motion, so that it can be truly used to make high quality NRS optical surfaces, consequently, to reduce the fabrication time and cost for freeform optics. This dissertation research is built upon an initial prototype of Fast LOng Range Actuator (FLORA) developed by the Precision Engineering Center (NCSU) and Precitech under contract with NASA [1].

Figure 1-7 shows a photograph of actuator prototype mounted on a Rank-Pneumo ASG-2500 DTM. The FLORA consists of a light-weight, aluminum-honeycomb triangular piston, an orifice air bearing, an ironless three-phase linear motor mounted on the back of piston, a linear amplifier, a laser linear encoder mounted on the top of piston, the diamond tool attached to the front of piston. To achieve the ultimate goal of creating optical quality surfaces of less than 200 nm form error and less than 5 nm RMS surface finish, while moving the diamond tool over a range of ±2 mm at a frequency of 20 Hz with this type of actuator, there are three major tasks to be accomplished in this research.

(1) Identify the deficiencies in the first prototype, improve its performance by optimizing its components design, integration and controls.

(2) Determine the desirable characteristics for components selection, design and integration in a total redesign of a second prototype.

(3) Prove the feasibility of creating real-world optic with this actuator.

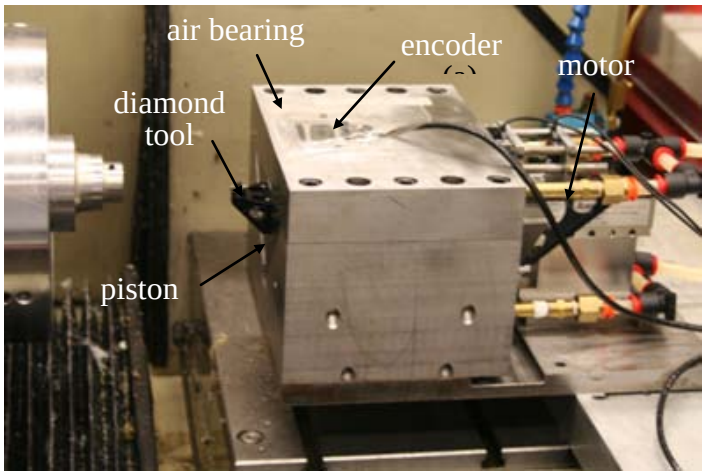

Figure 1-7 The FLORA system on a DTM

To accomplish these tasks, it is necessary to address the nature of this development effort in the context of diamond turning process. There are many factors that influence the surface quality in terms of form error and surface finish as shown in Figure 1-8.

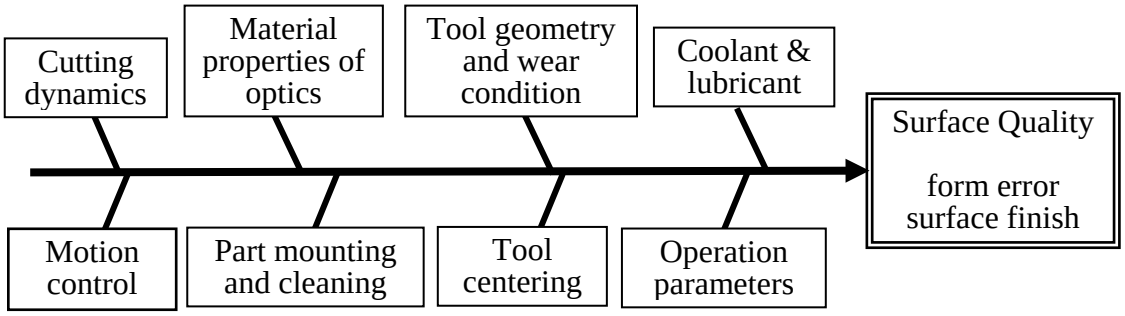

Figure 1-8 Diagram of major contribution factors for surface quality.

With the addition of this new actuator, the only difference in the machining process is the motion control, which is to control the relative position between the part and the tool tip. This is a chain process to determine this relative position, from tool to read head to X-slide, to the machine base, to the Z-slide, to the spindle chuck to workpiece. Among all the motion control factors that affect the surface quality as shown in Figure 1-9, the only new thing with FLORA is the way the tool is positioned. Compared with a tool post, the FLORA adds tool positioning error in the cutting process. On the ASG 2500 DTM, extensive amount of work has been done at the Precision Engineering Center in the past to study various contribution factors at the process level such as [10, 11] and motion control level such as [6, 44], and establish the baseline surface quality with a standard tool post or a PZT FTS. Any degradation from the baseline performance is due to the deficiencies of the tool motion control. Some critical issues to be addressed in this dissertation are the reaction force management, the structure and bearing stiffness, and the tool motion trajectory generation and tracking. The development of FLORA is full of interactions between physical design and controller design. The criteria of these tradeoff processes are always determined by the

features of the tool motion control in the machining process including the characteristics of motion trajectory and disturbances forces, and positioning requirement.

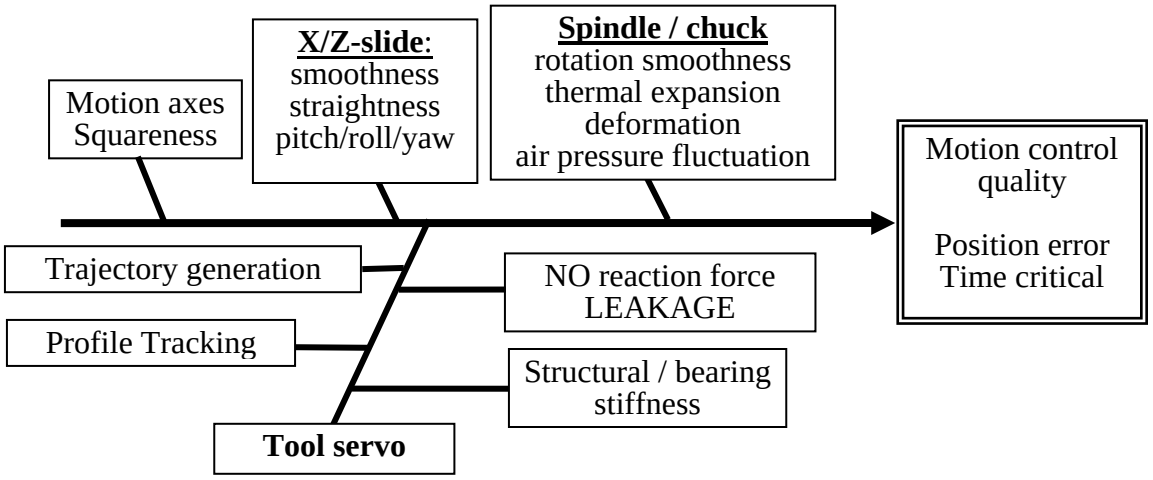

Figure 1-9 Diagram of major contribution factors for motion control quality

The organization of this dissertation is as follows: Section 2 discusses the design of actuator components and the concept for further improvement for a new design. Section 3 fully discusses the characteristics of tool motion control and the requirement for the servo control. Section 4 explores the effective control approaches for this application to push the servo performance to the limit of physical system. Section 5 first verifies the effect of tool motion control on the surface quality by cutting flat and tilted flat surfaces, then demonstrates the feasibility of creating deployable optic by creating a biconic mirror with fiducial features for kinematics coupling.

2. Fast Long Range Actuator Concept and Design

This chapter discusses the features, the concepts, and the designs of the fast long range actuator for diamond turning. The actuator has a travel range of 25 mm, which is mainly limited by the air bearing and the sliding piston design. The maximum acceleration of 122 m/s^2 is determined by the moving mass of 665 g and the peak motor actuation force of 81 N. Although the basic operational principles of FLORA is very straightforward, the capability of main system components, including the linear motor, linear amplifier, linear encoder, linear air bearing and sliding piston, and control platform, could be explored to a cost-limit to achieve the ultraprecision motion control performance. The original prototype shown in Figure 2-1 has been modified with a new amplifier, glass scale linear encoders and faster control platform. New concepts are proposed and the desirable characteristics are identified for a total redesign of the prototype in [2].

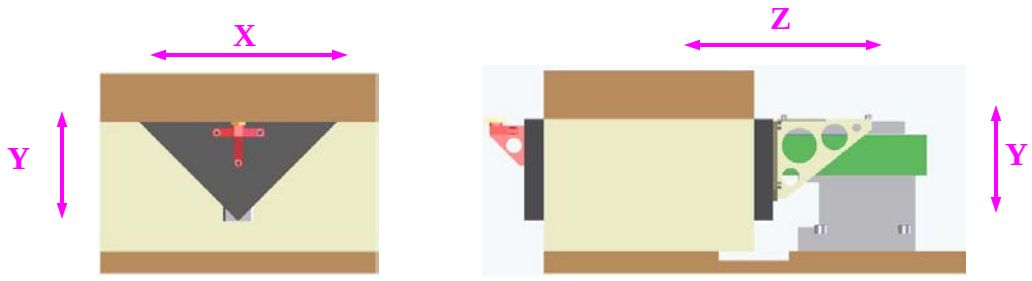

Figure 2-1 Front and side view drawings of the FLORA [1]

2.1 Linear Air Bearing and Piston

The linear air bearing and sliding piston are the most critical mechanical components for the FLORA. The aluminum honeycomb, triangular piston used for the first prototype with its air bearing were retained for this work. This piston was fabricated using sheets of aluminum honeycomb for each face and the first natural frequency was above 3500 Hz. The triangular cross-section is 140 mm wide and 70 mm high with a mass of 517 grams.

The piston is supported by a 90º v-block base assembly and a flat top as shown in Figure . The air bearing was designed by Precitech and incorporates innovations in both design and fabrication. The bearings in the base assembly were optimized for stiffness and damping in frequency range of the first dominant vibration mode. Static stiffness measurements were made by loading the piston in the vertical direction (300 N/μm) and at one edge (0.2 Nm/μ rad).

Some deficiencies with current linear air bearing and piston design have been identified:

(1) There is significant amount of acoustic noise when the air bearing is on, which indicates the air flow inside of air bearing is not well designed.

(2) The air gap of the orifice-type of air bearing is about 15 μm. Furthermore, the pressure distribution across the loading surface is not uniform due to limited number of orifices. The oscillations of the tool tip in X (±200 nm) and Y (±100 nm) direction were measured with a capacitance gage (Lion C2-B) when the piston was actively held in position by the motor and the results are shown in Figure 2-2. These non-desirable oscillations deteriorate the surface finish as analyzed in Section 3.1.

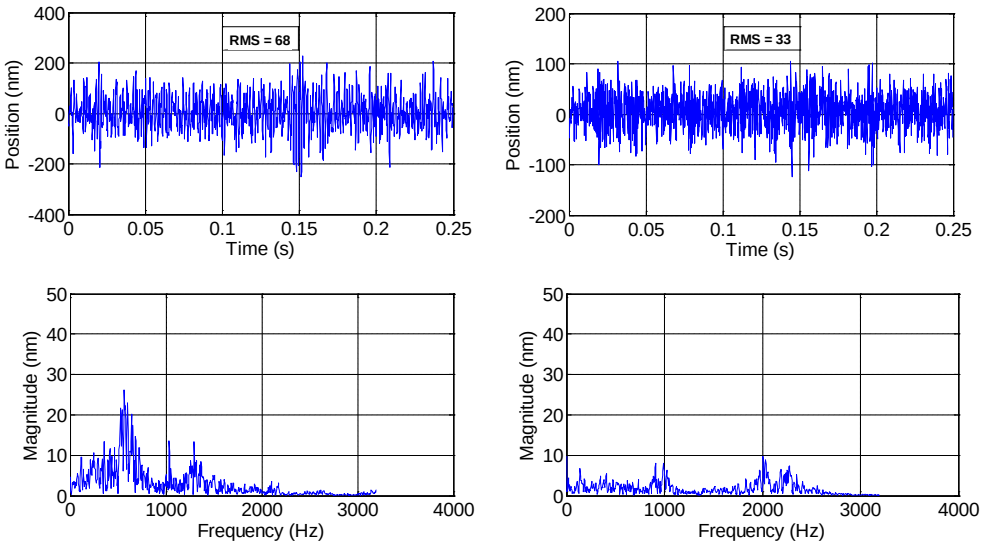

(a) Horizontal direction X (b) Vertical direction Y

Figure 2-2 Measured oscillation at the tool tip

2.2 Linear Motor

The initial prototype of the actuator was intended to eliminate the Z-slide motion of a diamond turning machine. A brushless three-phase linear motor is used because it provides long actuation stroke. The Airex P12-1 motor is retained from the initial prototype for its fast response and smooth motion characteristics [66]. Its lower coil mass (100 g) and low inductance make it possible to have high acceleration and deceleration, its aircore forcer design eliminates cogging and magnetic attraction. However, with sinusoidal commutation (Appendix C), the force delivered by the motor is not perfectly smooth due to variations in the magnets, mismatch between coil pitch and non-uniformity in the air gap along the range of travel.

Table 2.1 lists the electrical characteristics for the motor. The effective motor constant (ratio between the controller current command and the motor force output) for the motor/linear amplifier in Wye connection is 12.6 N/Amp and the peak current limit is 5.81 Amp.

Table 2.1 Airex P12-1 linear motor specifications

	Resistance R (Ohms)	Inductance L (mH)	Force constant K_f (N/Amp)	Back EMF constant K_e (V/m/s)	Peak current Ip (Amp)
Per coil	8.7	1.9	8.4	8.4	10.06

Figure 2-3 shows the construction of this linear motor. The forcer is made of wound coils and held together with epoxy. The winding assembly is attached to an aluminum base plate. The plate is used for the load support and also for heat removal. The generated force is first exerted on the whole forcer assembly with I-shape cross-section. It is tested to have an elastic modulus of 1.88×10^6 psi [1]. However, for the total structural assembly of moving mass, the effect of the bending mode of the over-extended motor forcer coupled on the piston through a mounting bracket is discussed in Section 3.2.2. Section 2.9 also discusses the heat management issue for the motor coil, which is the main limiting factor when the usage of motor approaches performance extremes.

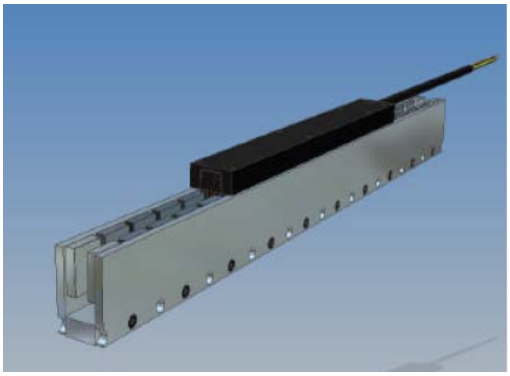

(a) 3-D model

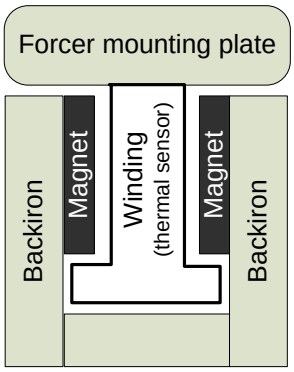

(b) Sectional view

Figure 2-3 Aircore linear motor construction

2.3 Linear Amplifier

The Pulsed Width Modulated (PWM) amplifier from the original prototype was replaced with a linear amplifier (Aerotech BL10-80A) to drive the linear motor. The rational was to reduce the high-frequency noise associated with a PWM and its influence on the control system. Together with the controller, the linear amplifier provides software based sinusoidal motor commutation in a dual-phase command configuration (Appendix C), which is limited to the servo loop sampling rate [67-72]. The dual-phase inputs (i.e. Phase A and B) are sinusoidal and are 120º out of phase from each other; the third phase (i.e. Phase C) is internally generated by the amplifier. By setting the amplifier's trans-conductance DC gain to 1, 1 volt input signal for a phase would produce a 1 amp output in that phase.

The dual-phase input configuration is an industrial standard for linear amplifiers, but it has some deficiencies. Table 2.2 shows the actual and expected voltage on each phase of the motor with a static test using a 0.5 amp command. The motor has a WYE connection in the measurement. Notice that the actual voltages do not sum to zero as expected and that there is noise on each phase. In the control system the output of Phase A and B can be biased to remove these offset values. However only two analog outputs are used and therefore the output bias in Phase C cannot be removed directly. Frequency analysis of the noise is shown in Figure 2-4. Each phase shows 60 Hz noise along with all of the odd harmonics. The noise

in Phase C not only has higher peak-peak value than the summation of Phase A and B, but also has peaks around 6 KHz and 8600 Hz. The deficiencies of dual-phase control can be addressed by a three-phase command configuration in which each phase current is controlled by an independent single-phase amplifier.

Table 2.2 Amplifier phase output voltage and errors for 0.5 amp command

	Theoretical value (DC volt)	Measured value	
		Mean (volt)	Noise (PP volt)
Phase A	0	-0.0015	0.1086
Phase B	3.8105	3.8090	0.3320
Phase C	-3.8105	-3.6641	0.6955
Sum	0.0	0.1434	

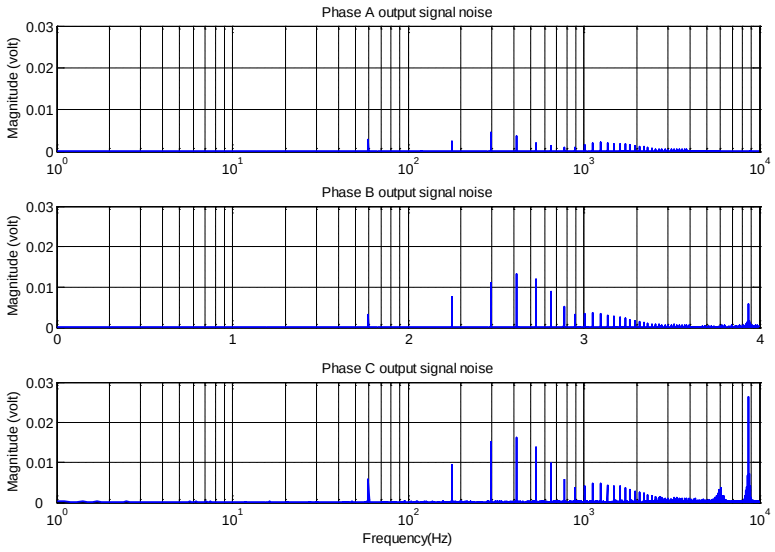

Figure 2-4 Frequency analysis of noise in amplifier output voltage

The amplifier has a built-in analog PI controller (gain set by numerous resistors and capacitors) to regulate the current loop. The block diagram in Figure 2-5 shows the basic current control process for Phase A and Phase B only. Equation (2.1) is the transfer function (G_I) supplied by Aerotech between the commanding current to the resulting current on a per phase basis. L refers to the line-to-neutral inductance, 1.9 mH; R refers to the line-to-neutral

resistance, 8.7 Ohms; *m* refers the moving mass, 0.665 Kg; *B* refers to the damping; and K_f refers to the motor force constant in WYE connection.

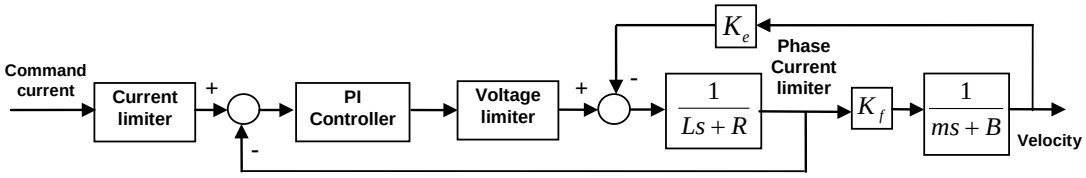

Figure 2-5 Block diagram of the phase current control loop in Aerotech amplifier, Irex motor, air bearing and piston.

$$G_I(s) = \left[\frac{6.622}{L}\right] * \frac{s + 15151.52}{s^2 + s\left[\frac{0.0033\times10^{-6} * R + 2.193\times10^{-8}}{0.0033\times10^{-6} * L}\right] + \frac{100666.67}{L}} \qquad (2.1)$$

Figure 2-6 is the bode plot of Equation (2.1). Due to the current loop PI controller gain settings, the magnitude starts to rise above 0 dB at 100 Hz, peaks around 800 Hz, and drops to -3 dB at 1543 Hz. The current loop introduces a maximum of 102º phase lag at 3000 Hz where the output is 20% of input.

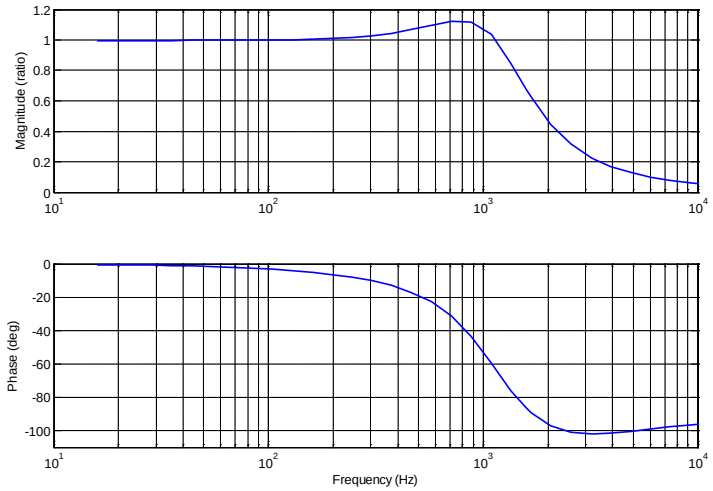

Figure 2-6 Frequency response for the transfer function of phase current loop control

2.4 Linear Encoder

To measure the tool position, a linear encoder offers a much better solution than a laser interferometer for several reasons:

(1) It enables a modular design of the actuator, and makes it possible to have “plug and play” in the actual usage, since the installation and alignment of the encoder only needs to be done once in the initial actuator assembly process.

(2) It has more reliable robust performance under various environmental factors. The measurement has less drift over time than the laser interferometer.

(3) It can be placed close to the tool to minimize the Abbe error in the measurement.

A linear encoder only measures the relative position between its read head and the scale. As shown in the Figure 2-7, the read head is mounted on the bearing housing, and the scale is attached to the moving piston. To achieve the measurement requirement of high accuracy and maximum velocity up to 251 mm/sec, three different linear encoders have been implemented in this actuator.

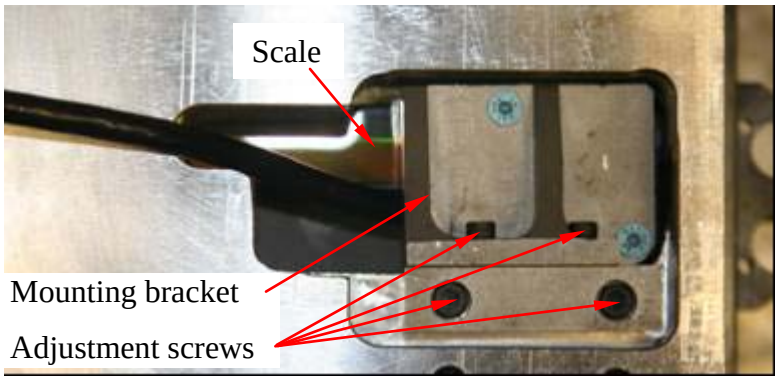

Figure 2-7 Sony BH25 encoder mounted on the bearing housing

Renishaw Encoder

When the actuator was initially built in 2004, a Renishaw RGH24B linear encoder was integrated with DELTA TAU UMAC controller to give a theoretical resolution of 5 nm [1].

The 20 μm period of the Renishaw steel tape is relatively long and, coupled with noise on the sine waves, reduces the resolution to approximately 50 nm.

Heidenhain Encoder

A glass scale Heidenhain encoder (LIP 401R) then replaced the Renishaw metal scale encoder from the original prototype. This Heidenhain encoder has 2 μm signal period. With ×100 signal interpolation it also provides 5 nm measurement resolution, but its noise level remains within 5 nm at the static condition. Because of the low frequency limit of the interpolator (EXE 660), the acceptable maximum speed is only 20 mm/sec. The calibration chart provided by Heidenhain indicated the LIP 401R has measurement error due to the glass scale grating error. This uncertainty can be taken as an accumulated measurement error in a slope of 6 nm per 1 mm measurement length with respect to the encoder index point. In addition to the encoder resolution quantization error and the scale grating error, there is periodic interpolation error occurring within one signal period of the encoder's output signals. This interpolation error is caused by encoder signal quality and is typically 1% to 2% of the signal pitch. Figure 2-8 shows the XY representation of two sinusoidal encoder signals with 90º phase shift on an oscilloscope. Ideal output signals appear as a circle. The size of the circle, which corresponds to the amplitude of output signals, can vary within certain limits without influencing the measuring accuracy. However, any deviations in the circular form caused by position error within one signal period will go directly into the result of the measurement. Non-perfect mounting alignment between the encoder scanning head and the glass scale, and insufficient signals conditioning can lead to the signals deviating from the ideal sinusoidal shape as shown in Figure 2-8. To this end, the laserscale is first aligned to the piston feed-direction by a cross-hair generator and fixed on the top piston using 3M Scotch super glue, then the read head is aligned to the read head by adjusting four mounting screws and monitoring the XY plot of two sinusoidal signals in the oscilloscope.

A comparison of position measurement by the encoder and a capacitance gage (LION, C2-B) in Figure 2-9 clearly shows the existence of this periodic spatial error in the encoder

measurement. The vertical axis in Figure 2-9 is the difference between the encoder and the cap gage measurement. The dots are the original measurement difference; the thick line is the trend line. The amplitude of the error is about 20 nm with a period of 1 μm.

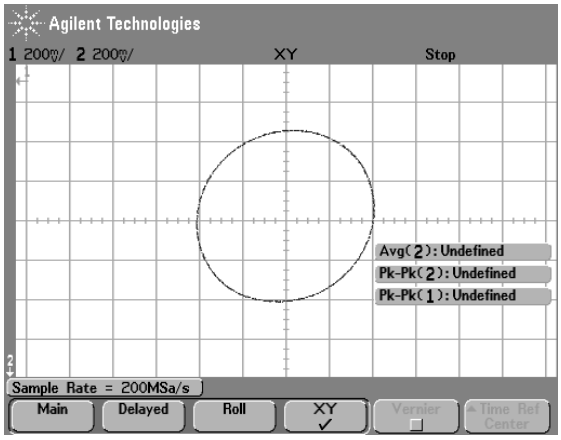

Figure 2-8 Oscilloscope XY representation of two encoder sinusoidal signals

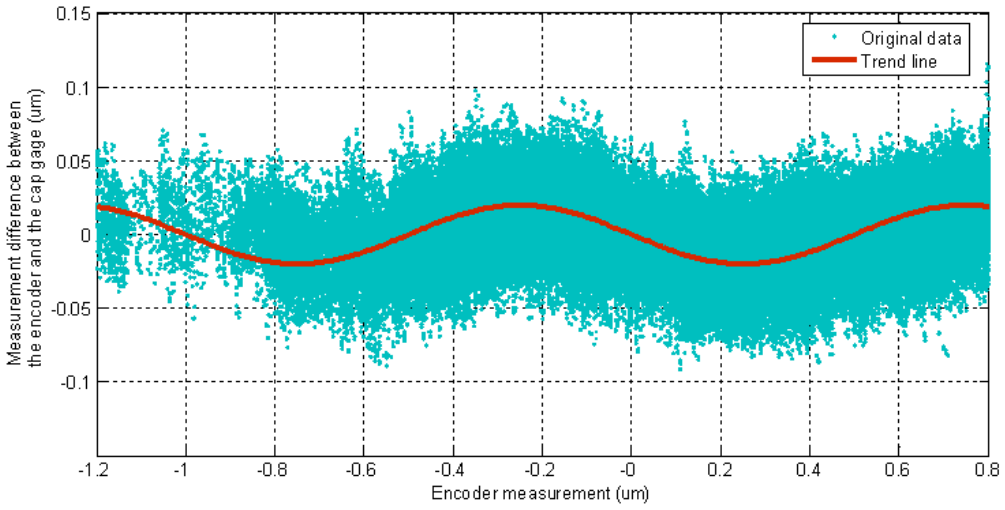

Figure 2-9 Encoder periodic spatial errors in the position measurement

Sony Encoder

The desirable position measurement quality is achieved with a Sony BH25 linear encoder. Its laserscale has 1 μm grating pitch, but the generated signal pitch is 250 nm. Figure 2-10(a) shows a picture of the scale and read with connector, Figure 2-10(b)shows two sinusoidal encoder signals with magnitudes of 0.871 V(PP) and 0.824 V(PP) and phase error of 2-3°.

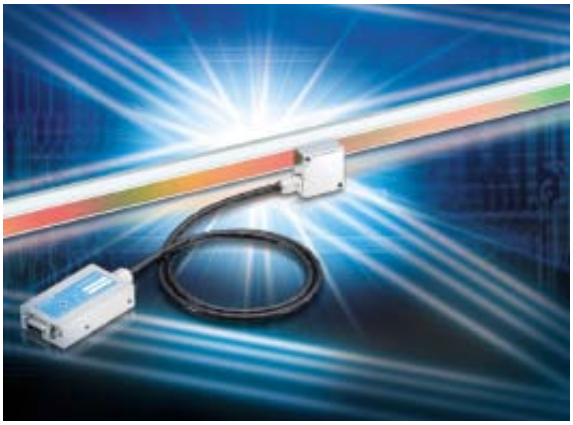

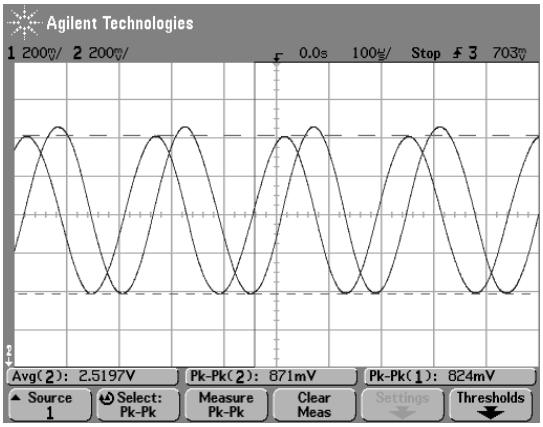

(a) Picture of the encoder (b) sin/cos signals measured by an oscilloscope

Figure 2-10 Sony BH25 reflective linear laserscale encoder

2.5 Real Time Control System Platforms

A digital control system is required to integrate all the components of FLORA. There are two main factors for a selection of control system platform:

(1) The capability of interfacing to components such as analog sensors, switches, quadrature encoders, sin/cos encoder and amplifier drives: critical performance indicators are noise level, resolution and rate in the analog and digital I/Os.

(2) The computational power (speed): minimum requirement for a sequence of real time control actions from acquiring signals to updating outputs, which determined by a mixture of hardware and software capability; the capability to implement tool motion trajectory generation and control algorithms required in the machining process.

The most important impact of implementing a digital control system is the delay associated with the sample-hold. The zero-order hold (ZOH) maintains the same output voltage throughout the sampling period until the next value is available, so the sampling rate shall be increased as high as possible. Nevertheless, the selection of the best sampling rate for a digital control system needs to compromise among many factors. The cost and availability associated with high-speed control electronics are the basic motivation for lowering the sampling rate. Furthermore, a decrease in sampling rate also means more time available for data processing and control calculations. There is always some amount time delay to sample the signals from (analog and digital) input channels, complete computations, and output new signals through output channels, the total time delay determines the achievable sampling rate. It has been observed that when the time delay exceeds 90% sample period, the real time performance degrades. Common practices to select a lower limit on the acceptable sampling rate are [5, 73]:

(1) Tracking effectiveness: the sampling rate needs to be 20 times (or higher) of the cross-over frequency of the closed-loop system loop gain.

(2) Disturbance rejection: the sampling rate needs to be 20 times (or higher) of the maximum frequency of the disturbance to be rejected.

Three different control platforms have been implemented for the FLORA.

DeltaTau UMAC Controller

The first implementation [1] of the FLORA with the Nanoform 600 DTM used a multi-axis DeltaTau Turbo UMAC controller as shown in Figure 2-11. The UMAC provides all the hardware and software needed for the control of the FLORA. This controller was neither flexible nor fast (2300 Hz servo sampling rate).

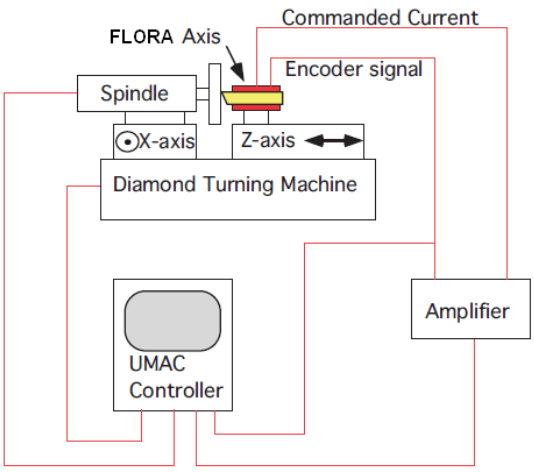

Figure 2-11 Control system structure with DeltaTau UMAC on Nanoform 600 DTM [1]

MATLAB xPC Target

The initial deployment of independent real-time system for FLORA was implemented using the MATLAB xPC Target development environment and its compatible National Instrument electronic components including PCI-6052E Multifunction I/O, Connector Block (BNC-2120), Cable (SH68-68-EP Cable - 2m), PCI-6601 Counter Timer (32 channels Digital I/O), Connector Block (CB-68LP) and Cable (R6868 Cable -1m).

In this environment, a desktop PC is used as the host running MATLAB, Simulink, Stateflow and Real Time Workshop to create and simulate a control algorithm via Simulink block diagrams. Once the simulation is complete and the results are acceptable, executable code is created and downloaded to a second "target" PC running the xPC Target real-time kernel. After the downloading, the target application can be run in a stand-alone, real-time mode. The xPC Target control development and rapid prototyping system integrate the entire development cycle into a single environment so that the individual development stages between simulations and tests can be run and rerun without frequent readjustment. However, this flexibility has its cost – overhead time. Measurements of the cycle time for a simple test with one analog input and one analog output, revealed a 20 µs overhead task execution time. This time stayed constant as more complicated computational tasks were added. This control

configuration was only used for bench-test of the FLORA, and replaced by an independent DSP controller to further increase the sampling rate.

PMDi System

The real time control system was switched to products made by Precision MicroDynamics, Inc (PMDi). In this implementation, the tool motion is slaved to the spindle motion and cross-feed motion of x-slide. Figure 2-12 shows a basic control system configuration, more detailed electrical schematics of the FLORA and its interconnection to the ASG-2500 DTM is provided in Appendix A. The control system hardware consists of a servo motion board (DMC100), and four field modules for analog input (MW70) and analog output (MW71), and quadrature encoder board (MW51) and sin/cos encoder board (MW53) connected to the controller through MotionWire communication line:

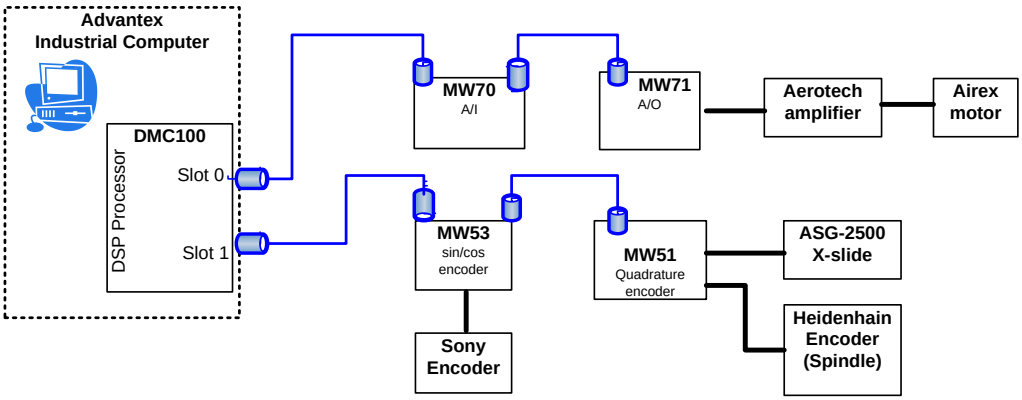

Figure 2-12 Simplified interconnection schematic with PMDi control plotform

DMC100: It is a PC-based motion controller and data acquisition card with an on-board DSP (40 MHz Analog Devices SHARC processor ADSP-21061L). It has four communication ports that constitute a link between the main controller and the modules attached to the ports, and manages the communication between the system, modules, and PC while running DSP control programs.

MW70: It is analog input module with four 16-bit analog-to-digital inputs (ADC) with adjustable settings, ±10 V is used in this application. The ADC inputs are differential converters operating at a maximum sampling rate of 250 KHz.

MW71: It is analog output module with four 16-bit digital-to-analog outputs (DAC) with adjustable settings, ±10 V is used in this application.

MW53: It is an interpolator module reading analog encoder inputs on two channels and converts them to digital positional data. Each channel accepts two 90° phase-shifted sinusoidal signals with peak-peak magnitude in the range of 0.6 and 1.3 V.

MW50: It is a two-axis decoder module used for monitoring incremental quadrature encoders. It has two 32-bit counters taking the maximum input frequency of 10 MHz.

The DMC100 is installed in a PCI slot of an Advantex industrial computer, it uses the PCI bus to communicate with a PC host. MotionWire is PMDi's high-speed (120Mbps per port), synchronous and deterministic motion control network, these features are essential for high speed ultraprecision tool servo control. MotionWire uses RJ45 connectors and CAT5e cabling in a star and daisy-chain topology for the communication link between the servo controller and modules. The quadrature encoder board of the FLORA takes the spindle encoder signal and the x-slide interferometer signal for the tool motion command generation. The ground lines from the computer to the two separate 5 VDC power supplies are essential to guarantee the proper communication of all MotionWire devices. A safety box was also built to disable the amplifier under some fault condition as described in Section 2.8. Figure 2-13 shows a photograph of FLORA control cabinet and close-up view for the MotionWire module enclosure.

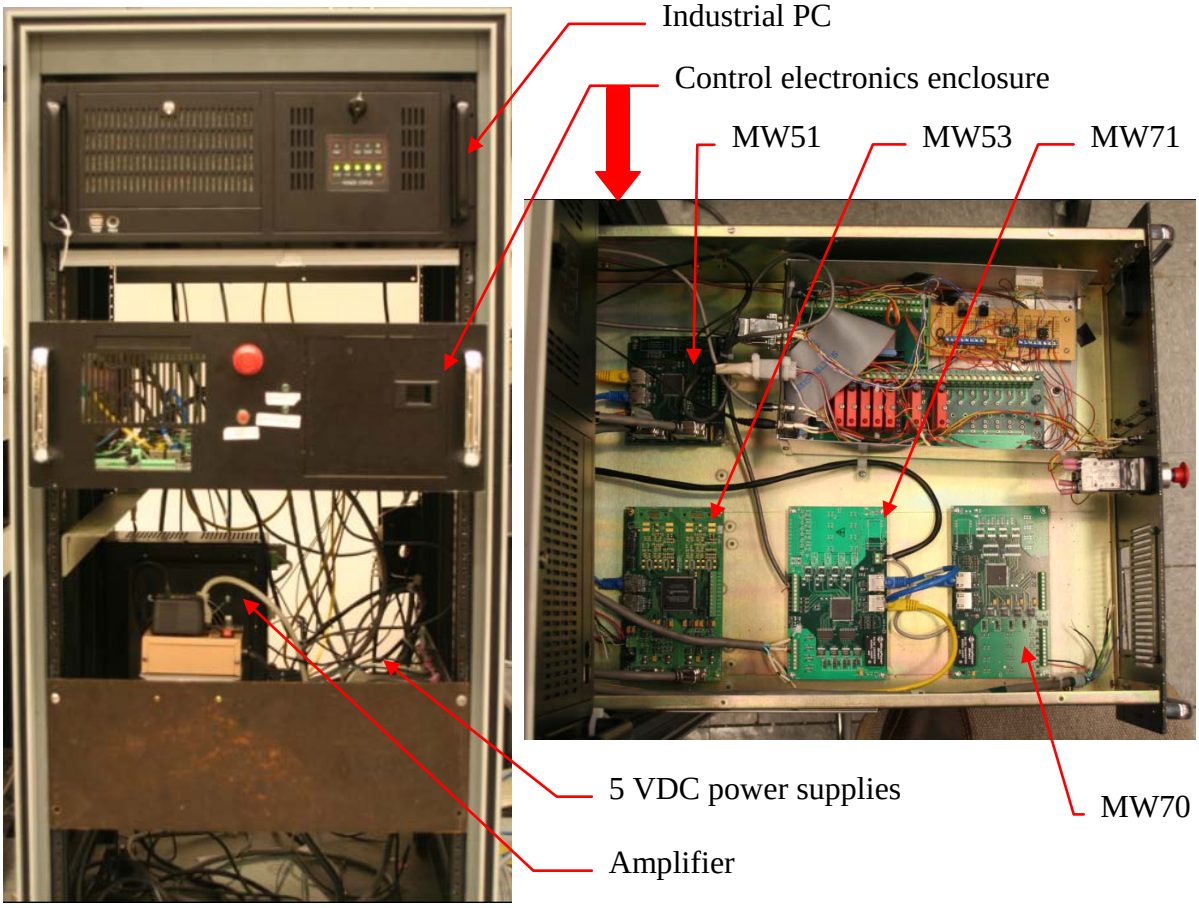

Figure 2-13 Photographs of FLORA control cabinet and field module enclosure

The customized control software is developed from a basic framework provided by PMDi, Figure 2-14 shows the basic functionality of the FLORA control software, the complete program listing and flow diagrams are included in Appendix F. The real time codes for IO access, all computations and data acquisition are built and compiled in Visual DSP++ environment, the executable file is loaded into DSP processor and executed on a interrupt timer as a background task. The less time critical foreground control tasks are implemented with Visual C# and runs on the host PC in Windows operating system. These two parts of the control software exchange the data through the shared memory space in the DSP processor.

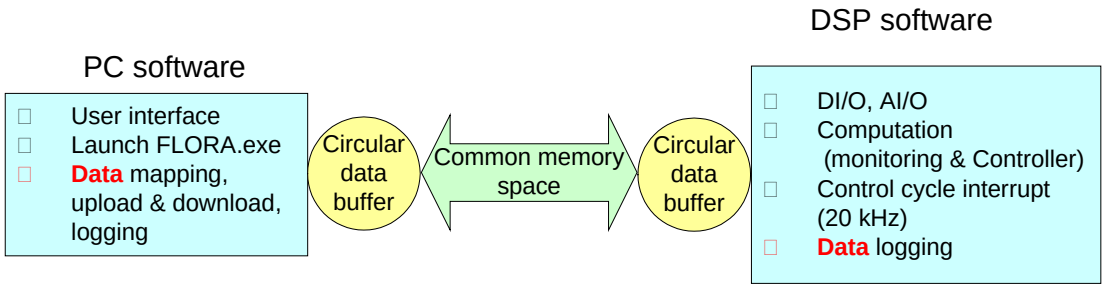

Figure 2-14 FLORA control software functions

A graphic user interface is created in Figure 2-15 for three main functions:

Figure 2-15 Graphic user interface for the operation of FLORA

(1) Display the positions of all four motion axes on the DTM for monitoring. The "Relative" position of each motion axis is obtained by offsetting the "Absolute" position. The offset values become effective once the momentary "Reset" buttons are selected and the font color of the button turns into black.

(2) Acquire and log the data for real time control variables for the purpose of analysis. By clicking the momentary button "Snapshot Data", 66536 data points are logged into the hard drive. On the other hand, the pushbutton "Stream Data" provides longer time duration data logging capability up to 4,000,000.

(3) Set the tool motion control operation mode: enable/disable the amplifier and motion control from the GUI, determine the tool motion control path either as jogging, point-to-point movement, a tilted flat cutting, or a free form optical surface cutting. Particularly, the ability to load data file (defining the surface geometry in polar mesh grid discussed in details in Section 3.3) into the DSP memory for interpolation purpose provides the flexibility to generate tool motion profile and machine free form optical surfaces.

The main motivation of developing customized control software is to simplify the complicated operation logics typically required in standard commercial software, so that the servo sampling rate can be increased as much as possible with PMDi system. To this end, the GUI only provides minimum amount interface needed in the operation of FLORA, the real time DSP code executed on each interrupt cycle is also simplified as much as possible as shown in Figure 2-16 (a more detailed flow diagram is provided in Appendix F, Figure F.2). The trade-off is that there is minor reprogramming effort to generate tool motion trajectory for workpieces of different size and geometry.

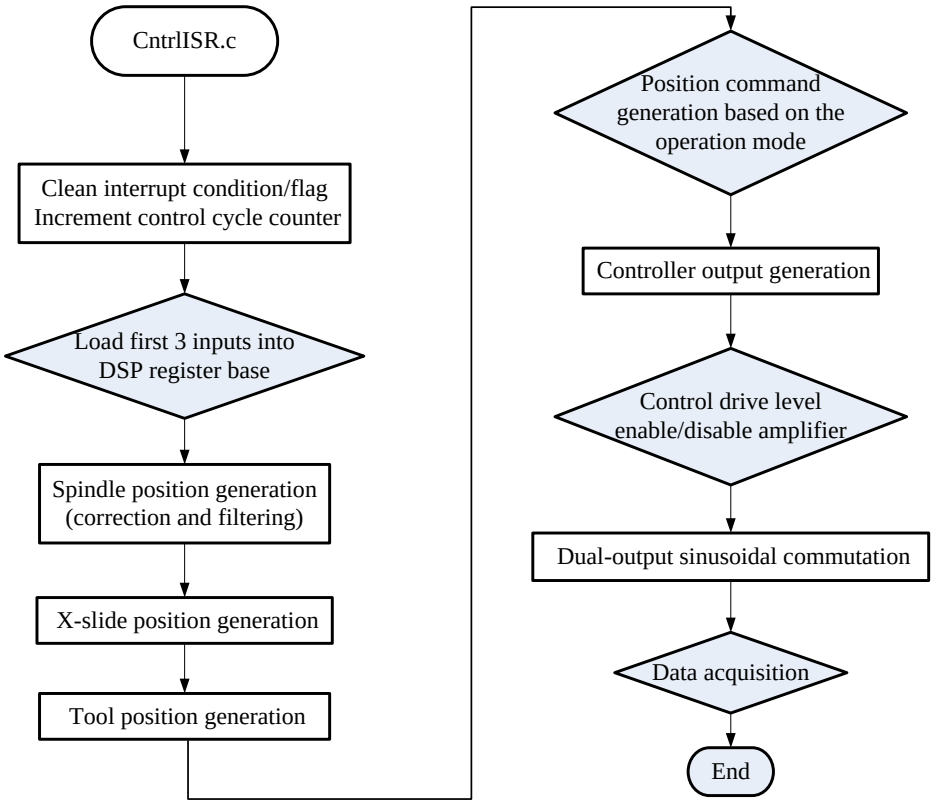

Figure 2-16 Simplified flow diagram of the control task on each sampling cycle

2.6 Reaction Force Management

The reaction force created in the actuation the FLORA piston (0.665 Kg mass) results in a significant disturbance to the DTM. The necessity of having a counter balance solution for reaction force reduction in the linear actuation topology is due to the fact that the reaction force induces non-desirable movements in the DTM motion axes during the cutting process, thus deteriorate the surface quality. Figure 2-17 shows the significant amount of induced DTM slides oscillations from 2 mm amplitude sinusoidal piston motion at the frequencies of 10 Hz and 20 Hz corresponding to maximum actuation force of 5.25 N and 21 N. These non-desirable DTM slide oscillations have a deleterious effect on the surface quality in the machining process. For lower frequency at 5 Hz sine wave piston motion, the maximum force was 1.3 N and the piston actuation had negligible effect on the DTM slides.

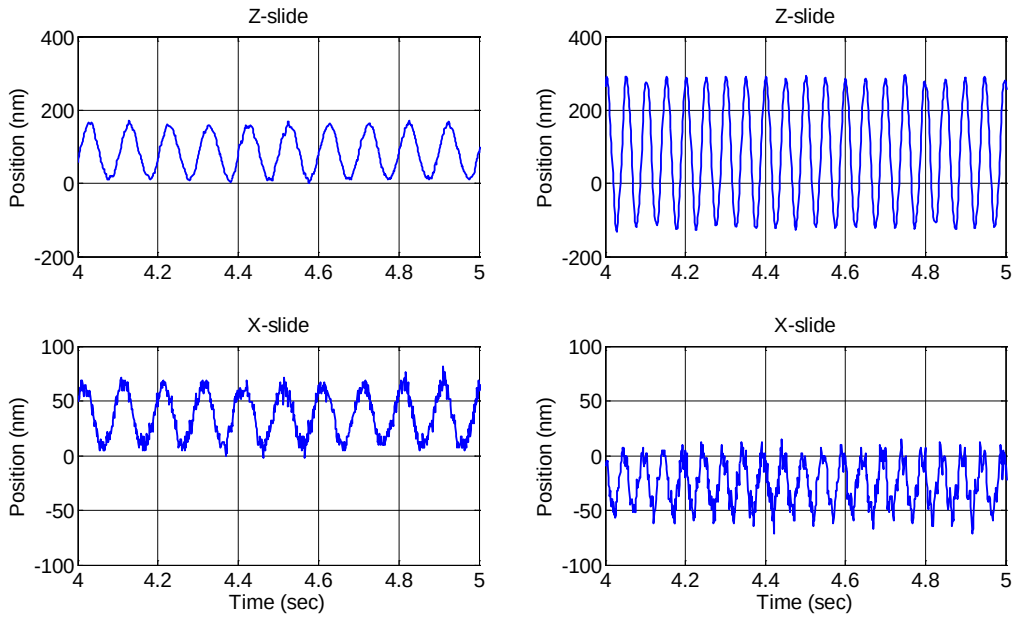

(a) At 10 Hz (b) At 20 Hz

Figure 2-17 Induced DTM slide motion due to sinusoidal piston actuation

A PZT FTS with a moving mass of tens of grams operating in the range of a few hundred Hertz also produces significant amount of reaction force at these frequencies. However, since the typical bandwidth of the interconnected structure is below 100 Hz, the high frequency reaction force above 100 Hz is damped out by the interconnected structure and produces little impact on the DTM. But for the FLORA operating below 100 Hz, the reaction force then must be contained within the actuator itself. Ideally, no reaction force should be transmitted through the DTM stages to the workpiece. Figure 2-18 shows a schematic drawing with two identical drives (motor/amplifier/controller/sensor) acting back-to-back in opposite direction with one for machining and the other for counterbalance. In theory, stationary parts of the two motor (permanent magnets) exerts the same amount of force in-line on the motor bracket, so there is no net force or moments on the base plate of the assembly. The disadvantage of this configuration is that the dual drives increase the cost of the actuator. Since the reaction does not need to be completely attenuated, a compromise can be made to use open loop control for the counterbalance drive, so that it does not need any position sensor, and the design can also be much simplified.

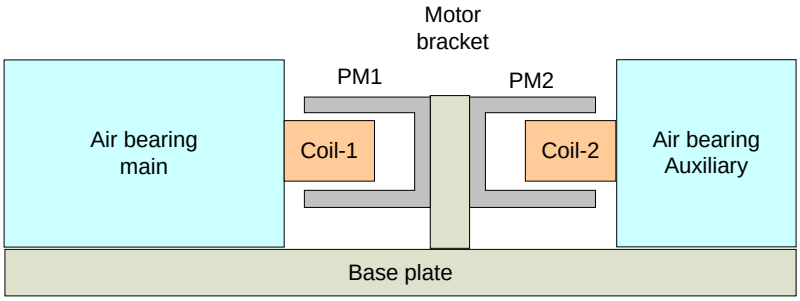

Figure 2-18 Schematic of ideal reaction force attenuation with symmetric actuation

To prove the feasibility of this concept, an active reaction force attenuation approach using a commercial shaker[1] supported by a linear ball bearing slide placed on the base of the FLORA is shown in Figure 2-19.

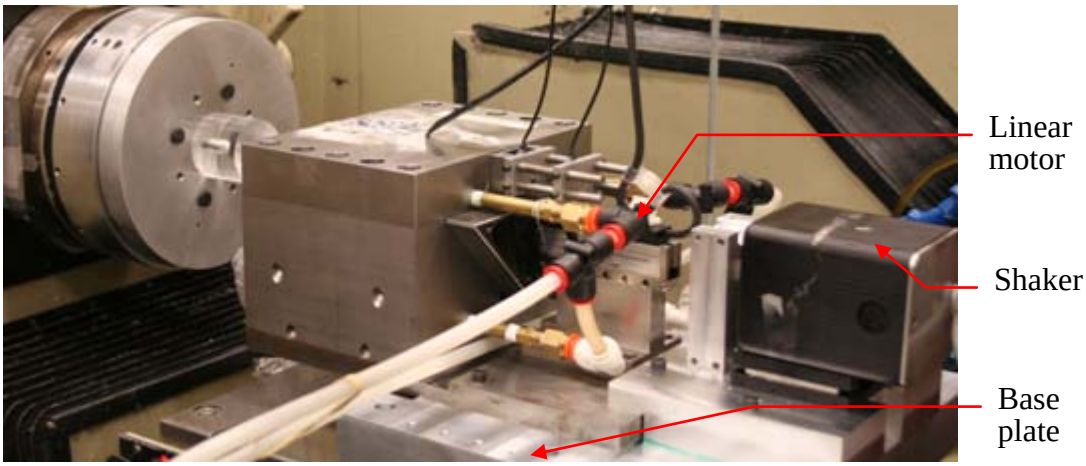

Figure 2-19 Photograph of the FLORA system mounted on the ASG-2500 DTM.

[1] Labworks shaker ET 132-2, driven by Kepco amplifier BOP 15-20M

Calibration process: To properly tune the control signal to the shaker, an accelerometer[2] was used to measure the structure vibration level either at the actuators base plate or encoder read head. The steps to find the proper signal to the counterbalance mass were:

(1) Actuate the shaker alone, take the phase lag (*PH1*) of control signal to the Kepco amplifier and accelerometer signal in position output mode, and the peak-peak amplitude (*VA1*) of accelerometer output signal in voltage,

(2) Actuate the piston alone, take the phase lag (*PH2*) of control signal to the Kepco amplifier and accelerometer voltage output, and the peak-peak amplitude (*VA2*) of accelerometer output signal in voltage,

(3) The final phase correction for the voltage command to the amplifier is *PH1-180-PH2*

(4) The final magnitude correction ratio for the voltage command to the amplifier: *VA2/VA1*.

Table 2.3 shows the performance of the reaction force reduction when the piston is commanded to move in a constant state of 2 mm, 20 Hz sine wave motion. In these tests, the accelerometer was attached to the side surface of encoder read head in-line with the piston actuation direction. The reaction force for a 2 mm, 20 Hz sinusoidal piston motion is 21 N. The shaker can effectively attenuate most of the reaction force from the linear motor. The measured vibration level is reduced by 37 times. However, it can also be seen from that, there is some amount of increase for the magnitude of 40 Hz and 80 Hz motion components, which indicates the shaker introduced non-desirable force components in the actuation process. In a test of motion profile for the cutting of a tilted flat, the reaction force could be attenuated by less than 50%. The degradation of reaction force reduction shows the deficiency in this add-on counterbalance solution. The linear motor and the shaker have different dynamic characteristics. In addition, they exert reaction forces on two brackets

[2] Charge accelerometer Bruel & Kjar 4393 with charge amplifier 2635

supported by two different plates. For this reason, this setup was not used for subsequent machining experiments. On the other hand, for operation at a lower frequency (2 mm 5 Hz) sinusoidal piston motion, the maximum reaction force is about 1.3 N and there is little change of accelerometer measurement signals under three scenarios: no piston motion, piston activated, both the piston and the shaker activated. This measurement result shows that reaction force around 1 N or less exerts little impact on the rest of the DTM system. It is taken as the target for an effective counterbalance design.

Table 2.3 Reaction force reduction with a shaker

Shaker actuation state	Accelerometer output signal (volt)				
	Peak-peak value in time domain	Change of harmonics magnitude in frequency domain when the shaker is activated			
		20 Hz	40 Hz	60 Hz	80 Hz
Not activated	0.630	-35 dB	15 dB	0dB	10dB
Activated	0.017				

2.7 Tool Height Adjustment

Tool height needs to be adjusted for the tool centering process before any machining work can be done. To allow for tool height adjustment, a notched flexure plate to which the air bearing housing and magnetic track are attached is cantilevered on the base plate as shown in Figure 2-20. A simple bolt assembly in Figure 2-20 is placed under the front base of the flexure plate. The T nut of the assembly is fitted into the T slot on the X-slide platform, the height of the bolt can be easily changed in the T nut and locked in position by the lock nut. The flexure plate always bends upward by the bolt in the height adjustment to preload this flexural bending mechanism. However, it was found that, one bolt assembly supporting mid of the base plate is not sufficient, the torsional vibration of the FLORA possibly degraded the achievable surface finish as indicated in Section 5.1. As a result, a pair of bolt assemblies was later used to support the both side of the flexure plate. This change stabilizes the support but make the tool height adjustment more difficulty since it is hard to synchronize the turning

of two bolts in the highly confined space. Furthermore, the bending of FLORA on the flexure plate could also make the motion of the piston not in-line with the DTM Z-slide motion (or not normal to the spindle chuck surface). It would be ideally to support the entire assembly by a micro-height adjuster.

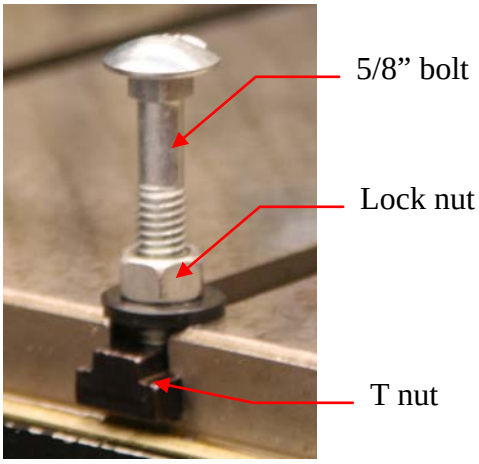

Figure 2-20 A photograph of the bolt assembly for the vertical tool adjustment

2.8 Operation Reliability

EStop Loop

To ensure the operation reliability of the actuator either in the standalone motion control test or in the machining experiment, it is critical to develop a safety system for the actuator. A safety box as shown in Figure 2-21 is built to remove power to the motor by disabling the amplifier. The electrical schematic diagram of the safety system in Figure 2-24 shows that the power disabling process is a hard-wired serial connected loop. It occurs under a number of conditions, including hitting the limits of travel in both direction, loss of air pressure, motor overheating or amplifier fault. “Control Enable” software user interface is coupled into this sequential electrical logic loop by an optical solid relay. Furthermore, a momentary pushbutton “Estop Reset” needs to be activated before energizing the motor, “Estop” is used for any emergence condition to cut-off the power to the motor.

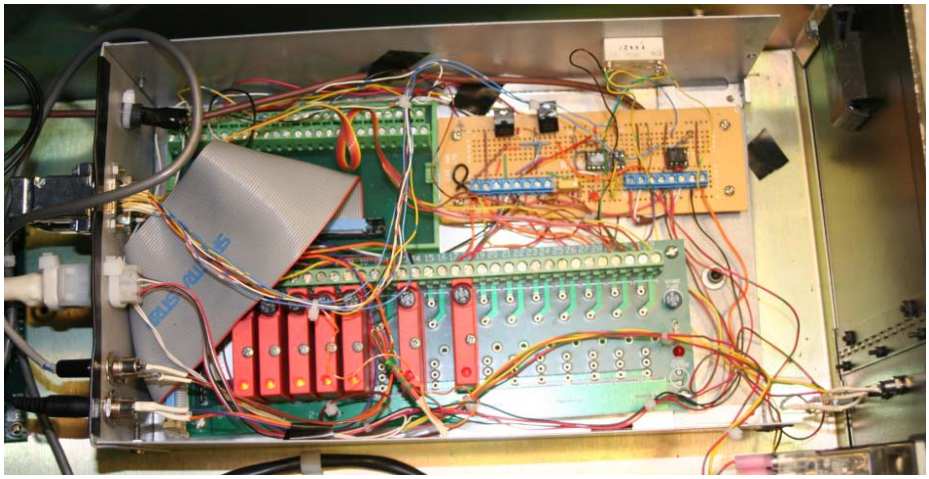

Figure 2-21 A photograph of safety box

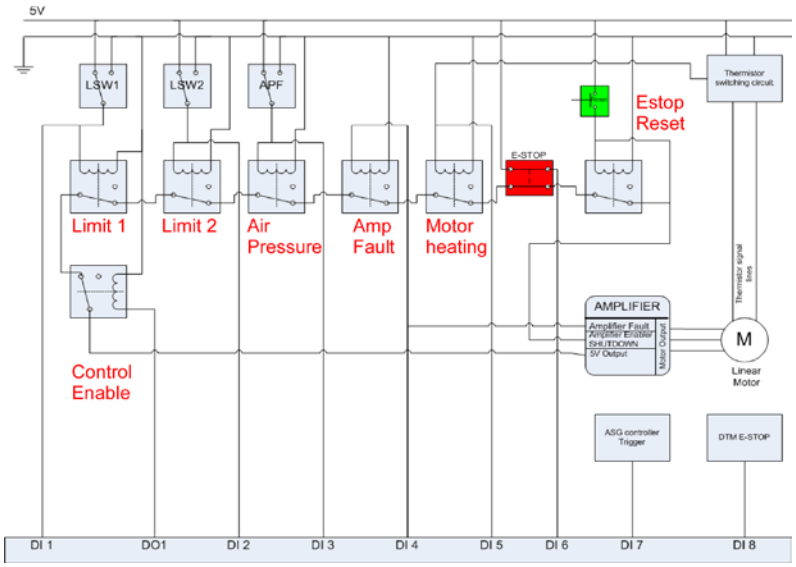

Figure 2-22 Safety system for LRS control

Contamination Prevention for Critical Components

In addition to put the safety system into place before activating the motor, it is also important take proper measurement to protect contamination of actuator components in the machining. The encoder, limit switches and piston surface are easily got damaged by the

cutting fluid or chips. If the fluid or the chip gets into the gap of air bearing, it will also produce viscous damping in the sliding piston mode. With current FLORA prototype, only a temporary solution with plastic wrap was used during the cutting. A more protective cover for the actuator is suggested for a new prototype.

2.9 Motor Heat Management

Heat dissipation is the principle limiting factor when the application of the aircore linear motor approaches performance extremes for high speed machining [66]. All motor coils contain resistance, as current is driven through the resistance, heat is produced. The power loss *P* due to the heat is

$$P = \frac{3}{2} I^2 R \tag{2.2}$$

Where *I* is the current drive level and R is the motor coil resistance as shown in Table 2.1. For example, to move the tool in a 2 mm amplitude and 20 Hz frequency sine wave motion, the current level is 1.67 A, and the heat generation is 36 W. When the frequency of motion reduces to 10 Hz, the heat generation reduces to 2.25 W.

The heat must be removed fast enough to maintain a temperature below the maximum rating to avoid any coil damage in the actuation process. Since the motor forcer coil is made of wound coils and held together with epoxy, the heat must leave the coils by conduction into the aluminum plate and out to the attached mass, and to a lesser degree by convection and radiation into the surrounding environment. Both of these paths have high thermal resistance and thus make thermal management of the motor difficult. Furthermore, as the coil resistance increases with the increase of coil temperature, it not only increases the heat generation, but also changes the critical dynamic characteristics of the motor for servo control. When the sliding piston acts as a heat sink to conduct heat away form the motor, the heat also introduces structural deformation affecting the tool positioning accuracy.

A thermistor (GE9.7A) is used to monitor the coil temperature, and the safety system will disable the amplifier if the temperature becomes greater than 35°C. The rising edge of the curve in shows that, when the generation is around 2 W, the equilibrium temperature is around 22.25°C after 400 sec of sinusoidal tool motion at 2 mm amplitude and 10 Hz frequency. However, when the motion frequency is doubled, the heat generation increases 16 times, the coil quickly increases to the limit at 35°C in 50 sec as shown in Figure 2-24.

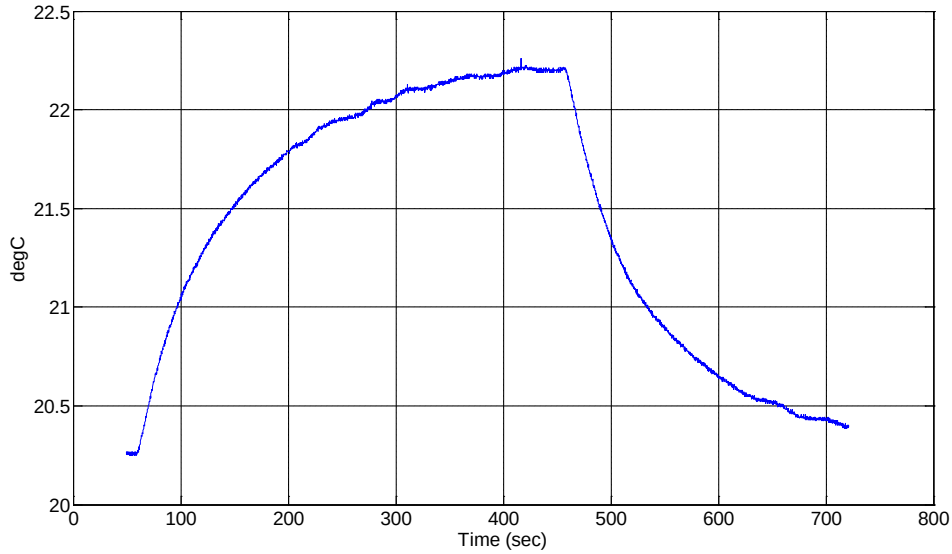

Figure 2-23 Coil temperature during and after 2 mm 10 Hz sine wave motion

Disabling the amplifier if the temperature exceeds some value is not a good solution. Without power, the piston/tool assembly will hit the workpiece, potentially damaging one or both. A better solution is to improve cooling by forced air convection. A test blowing the air into the forcer in the magnet track showed a decrease in temperature. A more detailed cooling concept was developed in Appendix B, but it was not implemented on the FLORA.

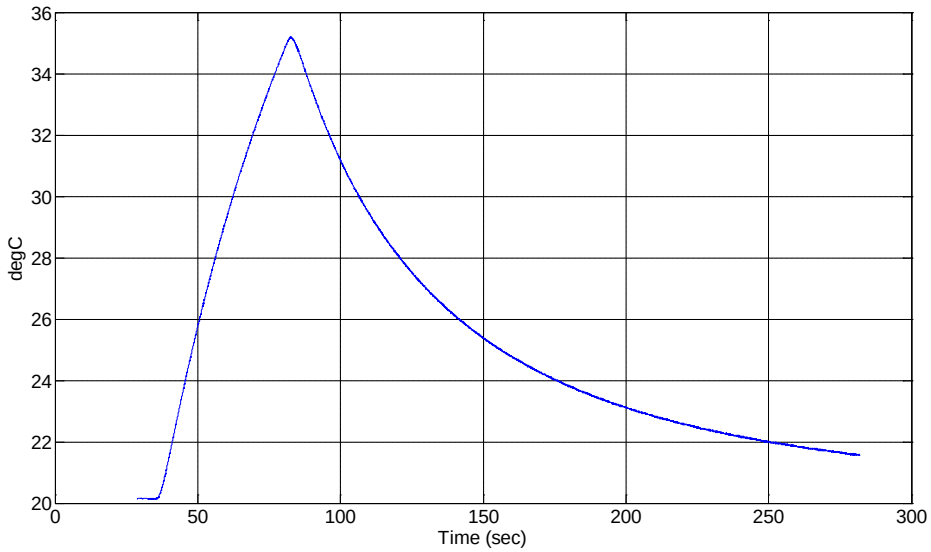

Figure 2-24 Coil temperature during and after 2 mm 20 Hz sine wave motion

3. Tool Motion Control

Tool motion control is one of those critical factors that determine the relative position between the tool and the work piece. Based on the physical process of surface formation, the tool motion control requirement to achieve desirable surface quality is first analyzed. Then, this section integrates all the factors in a motion control system from a control perspective, and discuss the essential elements to meet the goal of motion control. While Section 2 shows the physical design of FLORA to make it more controllable in the first place, the controller design comes into play to minimize the influence of error, noise and disturbance on the system performance according to the features of diamond turning process. With increased sensitivity of the low-mass direct-drive to internal/external disturbances and the dependence of stiffness on the servo controller, understanding the physical dynamics and natures of these error sources in the system has a great effect on the tool positioning quality.

3.1 Tool Positioning Requirement

If there is no motion error between the tool and the workpiece, the workpiece surface profile is formed by the repetition of the tool profile at intervals of cross-feed per spindle revolution. Under this ideal condition as shown in Figure 3-1, the surface profile cusp left by a round nose tool in the radial direction can be approximated by parabolic functions of the cross-feed rate (f_x) and the tool radius (R_t)

$$PV = \frac{f_x^2}{8R_t}; \quad RMS = \frac{f_x^2}{26.6R_t} \tag{3.1}$$

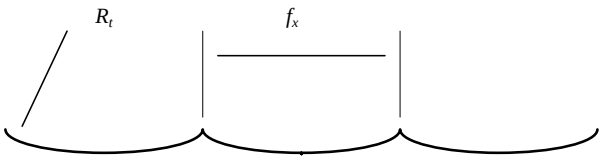

Figure 3-1 Illustration of ideal surface profile along the radial direction

However, the real surface quality is much worse than the ideal condition due to many other factors as discussed in Section 1.3. Besides the material property and the tool edge condition, the motion error between the tool and the workpiece is the next largest factor in determining the surface quality. Even with a conventional stationary tool post, there is unwanted motion errors between the tool and the work piece originated from various physical sources such as the spindle runout and the DTM motion axes vibrations, these errors lead to a modification of the surface profile. A number of researchers integrated the basic cutting edge profile with machine vibration in feed (Z) direction to investigate the effect of cutting parameters on the surface quality [84-91]. The frequency spectrum analysis of spiral groove trace at the work piece center by [91] shows the existence of these error motion modes. The synchronous error motions at low frequencies mainly increase the figure error, because the amount of change from these modes in each radial profile stays the same from one revolution to the next. But for the asynchronous error motions, due to the phase shift in each revolution, the resulted surface roughness profile appears to be irregular cusps with different depth and width in the radial direction, it has significant effect on the surface finish. It was found that [85, 87, 91], as a low cross-feed rate, the surface finish on a machined part can be better than the vibration level in the Z direction. The reason is the averaging effect from the round-nose tool: at low cross-feed rate where some of cutting passes are absent in the surface formation process, only those passes with the peak motion into the work piece will leave the final cusps on the surface. [91] further expanded the surface roughness model by adding the error motion in the cross-feed (X) direction, a negative effect on the surface finish was also found since the profile cusps no longer have uniform heights and widths.

These basic conclusions can be applied to the turning process with the FLORA. The FLORA adds significant capability to the diamond turning, but at the same time, adds unwanted positioning errors to the tool in XYZ direction. Take the simplest face turning of a flat as an example, since the FLORA is oriented normal to the Z axis, the additional tool positioning error in Z direction can be written as:

$$Z_t = A_z \sin(\omega_z t) \tag{3.2}$$

where A_z is the error magnitude at the frequency of ω_z. At the cross-feed rate of f_x and the spindle rotation frequency of Ω, the radial position of the tool is

$$X_t = \Omega f_x t \tag{3.3}$$

The change of the effective depth of cut around the periphery of the part is derived by removing the time variable in the Equations (3.2) and (3.3).

$$Z_t = A_z \sin\left(\frac{\omega_z X_t}{\Omega f_x}\right) \tag{3.4}$$

Let ε be the decimal fractional part of the ratio between the frequencies of spindle rotation and error motion in Z direction, the phase shift in error motion per revolution of spindle is

$$\Delta\phi = 2\pi\varepsilon \tag{3.5}$$

This phase shift produces a modulation effect on the basic surface profile defined by Equation (3.1), the modulation has a periodic wavelength of f_x /ε in the radial direction. It can be seen that the synchronous error motion in the Z direction increases the form error in Figure 3-2(a), but the asynchronous error motion increases the surface roughness in Figure 3-2(b).

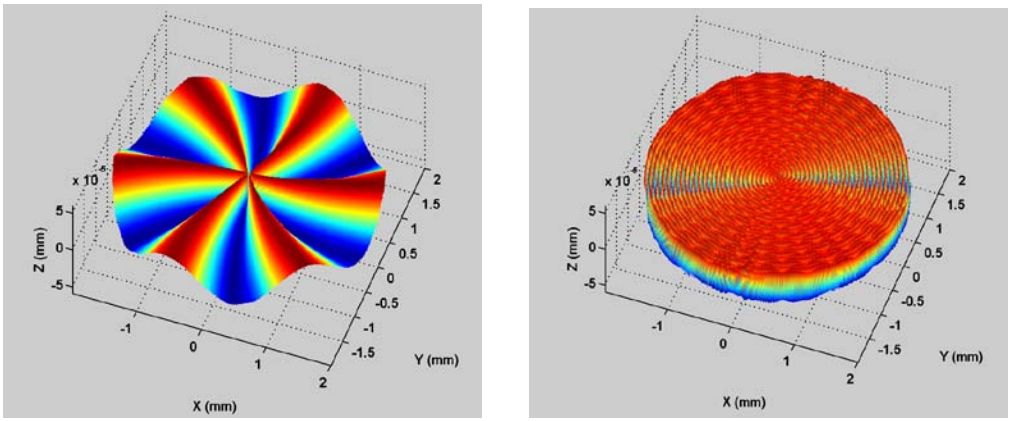

(a) Synchronous motion (b) Asynchronous motion

Figure 3-2 Simulation of the impact of Z motion error on the surface formation

The additional tool positioning errors in the radial direction (X and Y) are caused by side motion of the piston in the air bearing, flexibility of the tool holder and deflection of the support structures (piston and height adjuster) under the influence of the disturbance force in the machining process. These positioning errors in created surface plane do not change the depth of cut, but make the surface profile deviate from uniform cusps, thus increase roughness. It can also be noticed that, the surface profile Figure 3-1 is greatly exaggerated for clarity. The residual cusp typically has very small aspect ratio. For example, with a 0.5 mm nose radius tool and 5 μm/rev cross feed rate in finish pass, the aspect ratio is 100:1. As a result, the surface roughness is much less sensitive to the tool positioning error in X and Y direction. To demonstrate this simple concept, a simulation of surface profile is taken in Figure 3-3, for the uniform cusps, the peak-to-valley roughness is 6.25 nm. With 10 nm vertical position error, the PV roughness in Figure 3-3(b) increases to 12.25 nm. It takes 2 μm radial position error to increase the PV roughness to 12.25 nm.

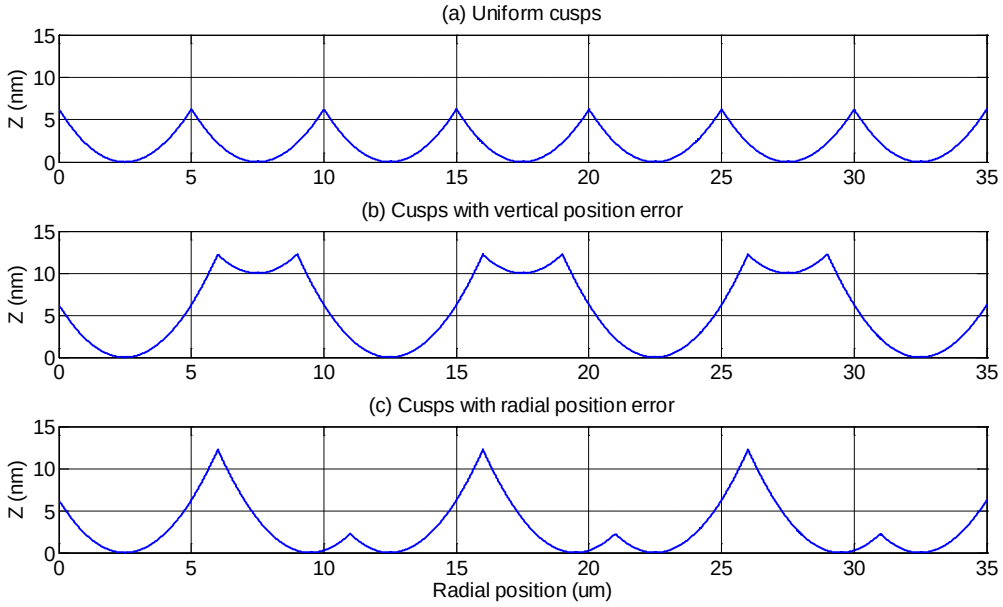

Figure 3-3 Concept of surface profile change with position errors

This analysis for flat surface can be extended to more general situation. Since the optical surface typically has slopes in both radial and circumferential direction, the positioning error in X, Y and Z direction can be converted into the error components in the radial, tangential and surface normal directions. Similar to the flat surface, the error in normal direction affects both form and surface finish and the error in other two directions mainly affect surface finish. By considering maximum surface slope of 45° in both radial and circumferential direction, the tool positioning errors in XYZ direction are equally important. If 150 nm PV figure error and 2-3 nm RMS surface finish is typical surface quality from a stationary tool post, to achieve form error of 200 nm PV and surface finish of 5 nm RMS with the FLORA, it is desirable to have ±20 nm (~5 nm RMS) tool positioning error in all XYZ directions. Positioning the tool in X and Y directions within the required tolerance relies on the stiffness of air bearing and support structure, but there are much more contribution factors for the tool servo control in the Z direction.

The FLORA also adds unwanted positioning errors in rotational directions. The pitching error is insignificant to the machining process. The effect of rolling error was observed in the machining of flat surfaces with single bolt support for tool height adjustment as discussed in Section 5.1, but there is a quick fix to resolve this issue.

3.2 The Dynamics of Tool Servo Open Loop System

3.2.1 Open Loop Dynamics Identification

In the open loop tool servo control, the position of the piston is controlled by directly applying current command in the software. Appendix C describes the sinusoidal commutation and detailed test procedures to identify the open loop dynamics. A test of open loop system dynamics in commutated operation would include all the system components at shown in Figure 3-4.

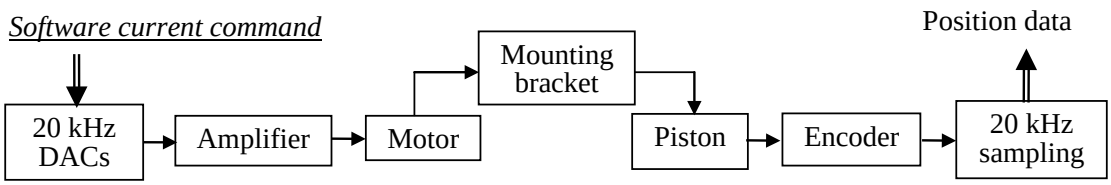

Figure 3-4 Schematic system flow diagram for open loop operation

Detailed procedures for the open loop frequency response tests are listed in Appendix C. Figure 3-5(a) shows the measured open loop system transfer function from current input in amp to position output in mm up to 3 KHz since the contribution of system dynamics above 3 KHz to the servo control is insignificant. Figure 3-5(b) shows the result when the command is modified based on Equation (3.6). In this case the transfer function is from the equivalent position command to the measured position, both in mm. Where K_f is the motor force constant in WYE connection, I is the amplitude of applied current command. This change removes in the -40 dB/decade slope in Figure 3-5(a) so that the high frequency features stand out in the magnitude plot.

$$A_P = \frac{K_f I}{m\omega^2} \tag{3.6}$$

Figure 3-6 further compares the converted open loop response in Figure 3-5(b) with the current loop dynamics. The difference between two lines is due to effect of flexible structure supported by the elastic air bearing, the analyses and test results in Section 3.2.2 provide some explanations to the sources of additional high-frequency dynamics in the open loop system.

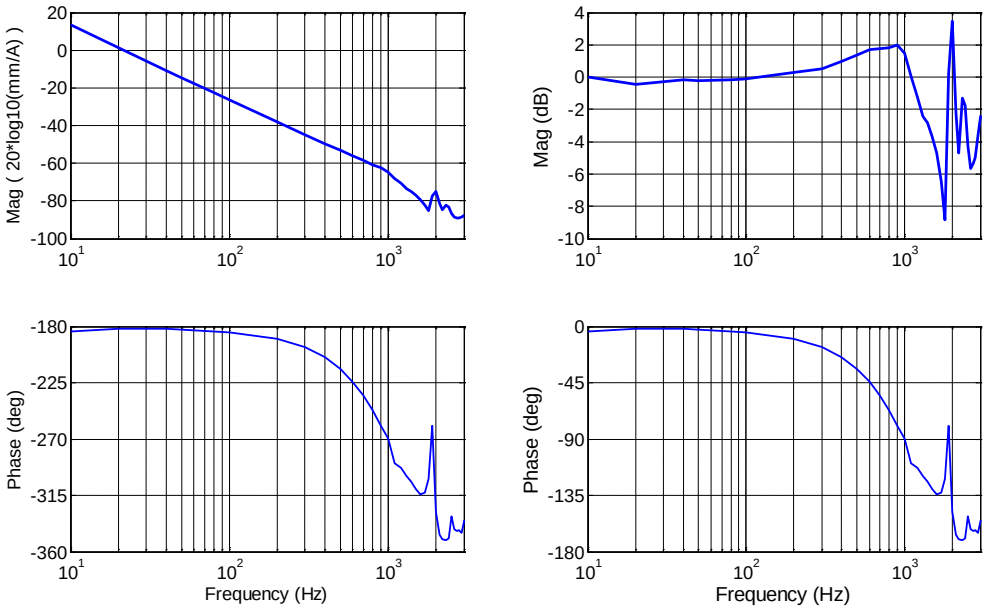

(a) From current command I (b) From position command A_P

Figure 3-5 Commutated open loop system transfer function frequency responses

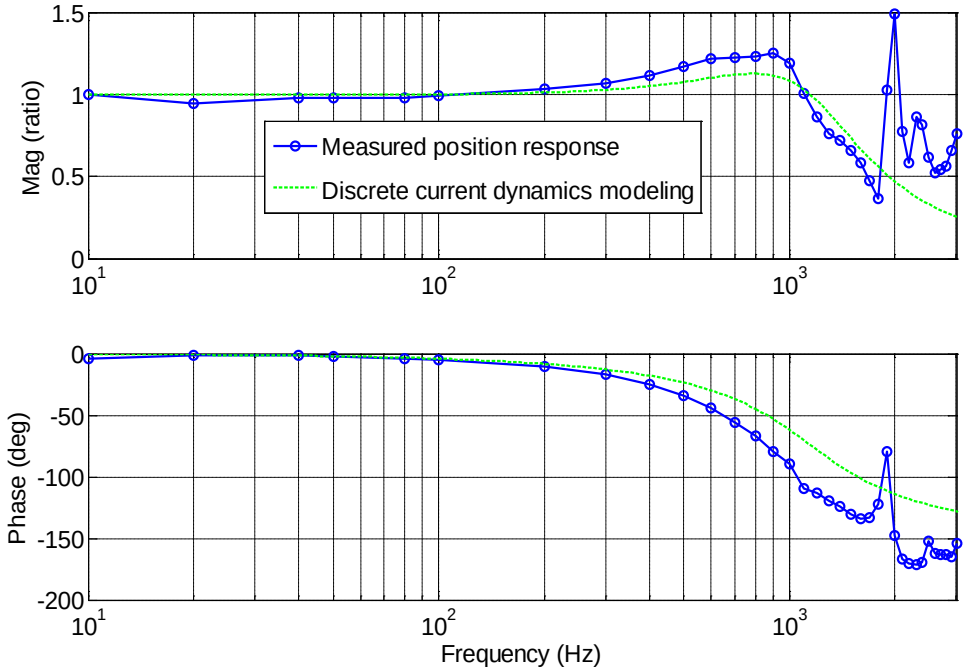

Figure 3-6 A comparison of converted open loop response and current dynamics

Based on the frequency response in Figure 3-5(a), a MATLAB function *invfreqz* is used to identified the open loop transfer function below 1500 Hz with one zero and four poles. The identified discrete function is then converted into continuous form in Equation (3.7). This is the nominal system dynamics equation to be used for controller synthesis.

$$G_{n1}(s) = \frac{51806782\,(s + 13448)}{s^2 \cdot (s^2 + 5717s + 37424559)} \tag{3.7}$$

Figure 3-7 shows a comparison of open-loop frequency response between the measured and the identified discrete model. The difference between the true dynamics of the system $G(s)$ and the nominal model $G_{n1}(s)$ is referred as model uncertainty. Typical sources of uncertainty in FLORA system include unmodeled (high-frequency) dynamics, the motor parameter perturbations due to the change of temperature. It is useful to consider the true system to be a nominal model with a multiplicitive perturbation Δ_3.

$$G(s) = G_{n1}(s)(1 + \Delta_3(s)) \tag{3.8}$$

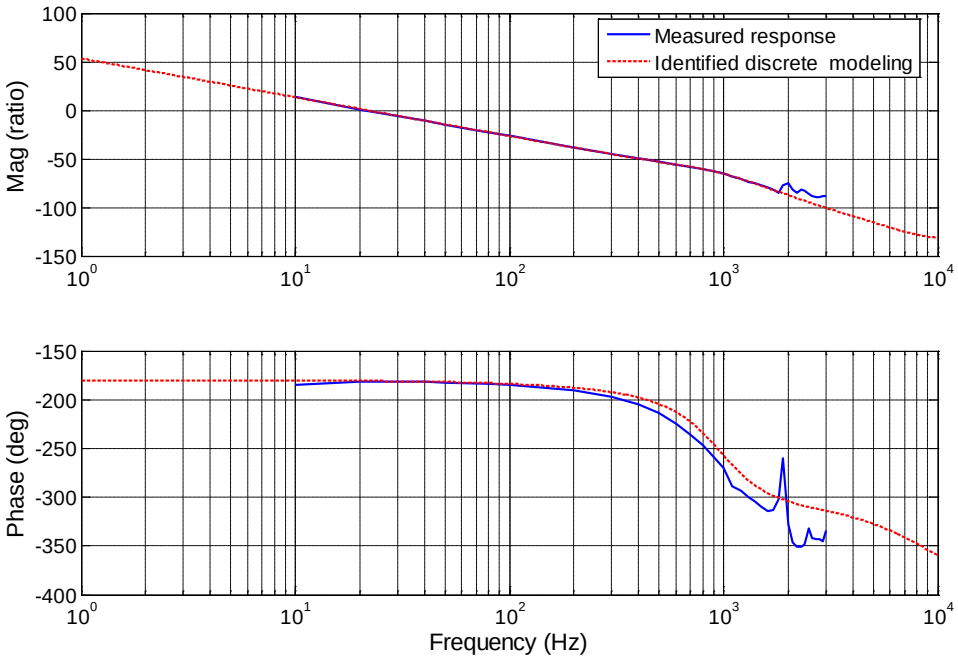

Figure 3-7 A comparison of open-loop control system frequency response for FLORA

For example, to take the major peak around 2 KHz into account

$$\Delta_3(s) = \frac{725s - 18437174}{s^2 + 650s + 151219253} \tag{3.9}$$

The order of Δ_3 denominator increases by 2 for every additional mode to be considered in the Δ_3. This multiplicative modeling error defines an upper bound in the loop shaping controller design approach in Section 4.1. As a result, when the controller is designed based on the nominal model, there shall be sufficient amount of gain and phase margins to obtain stability robustness.

3.2.2 The Dynamics of Flexible Structure on Elastic Bearing Support

Because the encoder scale is mounted on the top of slide piston, the pitching motion of the piston creates linear scale motion in the tool feed direction. The position measurement is a combination of rigid body modes and flexible modes existed in the air bearing and the moving mass structure as shown in Figure 3-8.

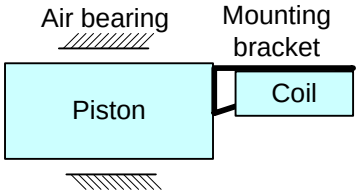

Figure 3-8 Schematic of the moving mass supported by an orifice air bearing

The discussion in this section assumes the high frequency dynamics seen in Figure 3-6 comes from the pitching mode of the air bearing and bending mode of the structure. Figure 3-9(a) shows the condition with the piston alone sliding in the air bearing. Figure 3-9(b) shows the 2-DOF vibration system when the coil and the mounting bracket attached to the piston. The model temporarily ignores the rigid body mode in the tool feed direction so that it is easier to observe the effect of high frequency modes from two different physical sources. The non-uniform pressure distribution of orifice air bearing and the tool/workpiece

interaction forces introduces an oscillatory pitching moment to the piston (M_1). In addition, the actuation force may not be perfectly aligned with the gravity center of moving mass (either higher or lower in the vertical direction), thus introduce pitching moment (M_2) to the coil/bracket other than their gravity.

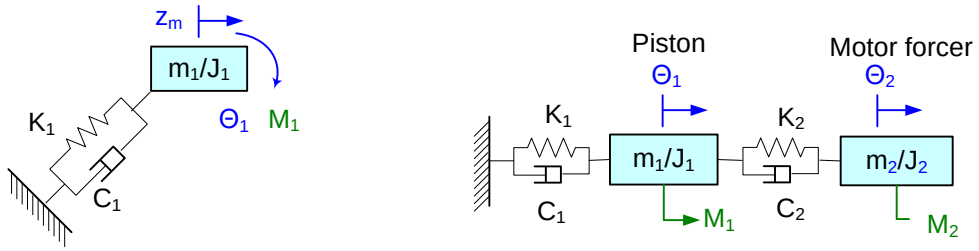

(a) 1-DOF vibration system

(b) 2-DOF vibration system

Θ_1: parasite motion for piston
m_1/J_1: the piston mass/inertia
M_1: excitation moment from air bearing
K_1: bearing pitching stiffness
C_1: bearing pitching damping

Θ_2: pitching motion for motor coil
m_2/J_2: the forcer mass/inertia
M_2: excitation moment at the forcer
K_2: structural coupling stiffness
C_2: structural coupling damping

Figure 3-9 Equivalent flexible model due to pitching modes

For 1-DOF system in Figure 3-9(a), suppose the distance between the scale and the pivot center is l_1 in the vertical direction, the equation of measured motion (z_m) by the encoder due to the pitching motion of the piston is

$$\begin{cases} z_m = l_1 \sin\theta_1 \approx l_1\theta_1 \\ J\ddot{\theta}_1 + C_1\dot{\theta}_1 + K_1\theta_1 = M_1 \end{cases} \tag{3.10}$$

The corresponding transfer function is

$$Z_m(s) = \frac{l_1}{Js^2 + C_1 s + K_1} M_1(s) \tag{3.11}$$

For 2-DOF system in Figure 3-9(b), the following equation of motion is obtained

$$\begin{cases} J_1\ddot{\theta}_1 = M_1 - K_1\theta_1 - K_2(\theta_1 - \theta_2) - C_1\dot{\theta}_1 - C_2(\dot{\theta}_1 - \dot{\theta}_2) \\ J_2\ddot{\theta}_2 = M_2 + K_2(\theta_1 - \theta_2) + C_2(\dot{\theta}_1 - \dot{\theta}_2) \end{cases} \tag{3.12}$$

To further simplify the discussion, the damping terms in Equation (3.12) are ignored. Laplace transformation is then applied to derive

$$\begin{Bmatrix} \theta_1(s) \\ \theta_2(s) \end{Bmatrix} = \frac{1}{\Delta_1} \begin{pmatrix} J_2 s^2 + K_2 & K_2 \\ K_2 & J_1 s^2 + K_1 + K_2 \end{pmatrix} \begin{Bmatrix} M_1(s) \\ M_2(s) \end{Bmatrix} \tag{3.13}$$

where $\Delta_1 = J_1 J_2 s^4 + \left[(J_1 K_2 + J_2(K_1 + K_2)\right] s^2 + K_1 K_2$

$$\begin{cases} \theta_1(s) = \dfrac{J_2 s^2 + K_2}{\Delta_1} M_1(s) + \dfrac{K_2}{\Delta_1} M_2(s) \\ \theta_2(s) = \dfrac{K_2}{\Delta_1} M_1(s) + \dfrac{J_1 s^2 + K_1 + K_2}{\Delta_1} M_2(s) \end{cases} \tag{3.14}$$

Let $r = \dfrac{J_2}{J_1}$; $\omega_1 = \sqrt{\dfrac{K_1}{J_1}}$; $\omega_2 = \sqrt{\dfrac{K_2}{J_2}}$, then

$$\begin{cases} \theta_1(s) = \dfrac{s^2 + \omega_2^2}{J_1 \Delta_2} M_1(s) + \dfrac{\omega_2^2}{J_1 \Delta_2} M_2(s) \\ \theta_2(s) = \dfrac{\omega_2^2}{J_1 \Delta_2} M_1(s) + \dfrac{s^2 + \omega_1^2 + r\omega_2^2}{J_2 \Delta_2} M_2(s) \end{cases} \tag{3.15}$$

where $\Delta_2 = s^4 + \left(\omega_1^2 + (1+r)\omega_2^2\right) s^2 + \omega_1^2 \omega_2^2$

Because the inertia ratio *r* has a non-zero value, the resulted modes for 2-DOF system are shifted from the individual modes of ω_1 and ω_2. It can be seen that, $\theta_1(s)/M_1(s)$ (or $\theta_2(s)/M_2(s)$) is a collocated transfer function since the excitation force and the position sensing are on the same mass. This function has two zeros in the numerator term of $s^2 + \omega_2^2$ (or $s^2 + \omega_1^2 + r\omega_2^2$) that add phase lead for at the frequency of ω_2 (or $\sqrt{\omega_1^2 + r\omega_2^2}$). $\theta_1(s)$ $/M_2(s)$ (or $\theta_2(s)/M_1(s)$) is a non-collocated transfer function since the force and the sensing

are on two different masses, it has no zeros. This is the way how the modes from two different physical sources are distinguished.

The existence of these modes was verified by measuring piston oscillation at the encoder in the tool feed direction. Figure 3-10(a) shows the scenario of Figure 3-9(a) when the motor coil and mounting bracket were detached from the slide piston, the frequency spectrum of the oscillation indicates the peak around 900 Hz and 1700 Hz due to the air bearing pitching modes. Figure 3-10(b) shows the scenario of Figure 3-9(b), it has additional higher peaks around 2000 Hz and 2300 Hz due to the flexible modes of attached structure, the modes originated from the air bearing decreases to 650 Hz and 900 Hz. In addition, the peak around 900 Hz becomes the highest. Overlapping of this resonance peak frequency with the mode in the current loop dynamics around 900 Hz has been proven to have a dominant negative impact on the tool servo control and the surface finish of machined surfaces.

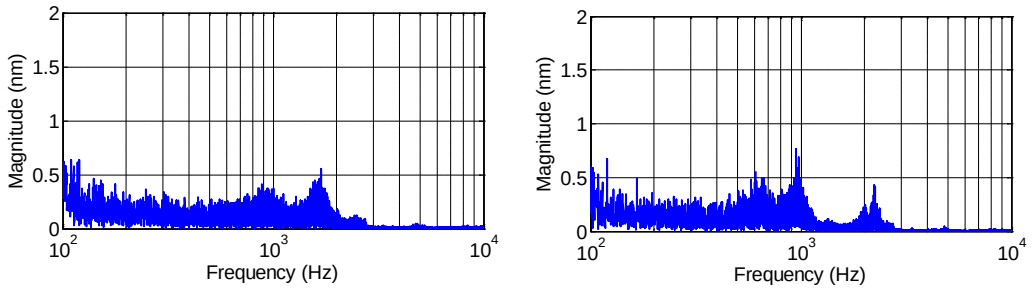

(a) Without motor coil (b) With motor coil

Figure 3-10 Frequency spectrum of measured piston oscillation by encoder

These high frequency modes limit the achievable performance of closed loop tool servo control as discussed in Section 4.1. The solution is to push these modes up to a higher level by a new design, i.e. above 3 KHz, and also reduce their peak levels. It can be accomplished by

(1) Increasing stiffness of the piston structure and the mount coupling the piston and the motor forcer.

(2) Using a porous-type air bearing to guide the moving mass because it has much more uniform pressure distribution across the bearing surface and smaller air gap, thus,

increasing the pitching stiffness and reducing the amount of unbalanced excitation moment and pitching motion.

3.3 Tool Motion Planning

To create freeform surface, the diamond tool cuts along a cross-sectional spiral path. In this machining process, the position of the tool is synchronized to the position of the DTM axes by generating its motion command (Z_C) as a function of the spindle angular position (θ), z-slide position (Zs) and cross-feed slide position (Xs).

$$Z_c = f(X_s, Z_s, \theta) \tag{3.16}$$

The tool motion trajectory in the machining of free form surface has wide frequency spectrum with a few dominant frequencies, and time varying amplitude and phase, so the servo control system is continuously in transient state, never reaches a steady state used for initial controller gain tuning. The quality of motion synchronization depends not only on the profile tracking performance of the actuator but also on the real-time generation of tool motion commands. The quality of tool motion trajectory generation, on the other hand, depends on both position measurement in DTM motion axes and the numerical method to represent the surface geometry. Laser interferometers (Zygo ZMI 501A) installed on the RankNemo ASG-2500 have measurement resolution below 2 nm for z-slide and x-slide position, and the environmental effect on the laser interferometer is less of a concern than the other error contribution factors in the motion trajectory generation discussed in the rest of this section.

3.3.1 Spindle Angular Position Measurement

The spindle rotation on the ASG-2500 is controlled by a DC brush motor, a PWM amplifier, a dSPACE controller and a tachometer. In the machining process, the spindle is typically driven at a constant speed command. However, there may some amount of

fluctuation in the spindle speed due to the measurement error in the sensor and disturbance from the motor, amplifier and air bearing. A 20,000 count/rev encoder (Heidenhain ERO1324) is used for the spindle angular position measurement. However, this encoder has manufacturing defects and does not have sufficient resolution for this application, this section presents methods to resolve these issues so that the physical spindle angular position can be better estimated from the encoder counts.

Spindle encoder runout error correction

The encoder alignment was found to contribute to the errors in the tool motion trajectory. The runout in the encoder disk will appear as a non-uniform pitch of the angular steps when read by the stationary read head as shown in Figure 3-11. Because the rotary error repeats once per revolution and the spindle speed is assumed to be constant over that short interval, this measurement error can be calibrated and compensated at the servo sampling rate.

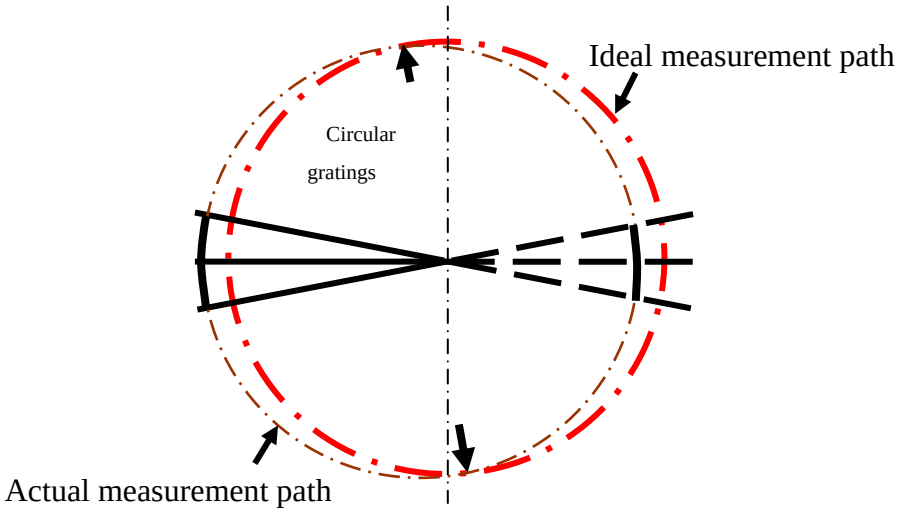

Figure 3-11 Non-uniform pitch caused by rotary encoder disk runout

Figure 3-12 shows how this error can be calibrated and compensated. Figure 3-12(a) and (b) show the encoder counts readings at the start and the end for one full revolution of encoder sampling at 20 KHz for the spindle speed of 630 rpm, the first and the last points are

extrapolated from the measured data. Under the assumption of constant spindle speed, the difference between the actual reading and ideal reading (the linear line fitting between the first and last data point) produces the error in counts shown in Figure 3-12(c). Removing the sinusoidal component of error in counts due to the encoder disk runout in Equation (3.17), the residual error in Figure 3-12(d) is within one encoder count. This result is repeatable for the measurement at other spindle speed of 300 rpm, 600 rpm and 1200 rpm. The effectiveness of this technique was experimentally verified using a tilted flat as illustrated in Section 5.3.

$$\tilde{\theta} = 5.045\cos\left(\Omega t + 84.754^{\circ}\right) \tag{3.17}$$

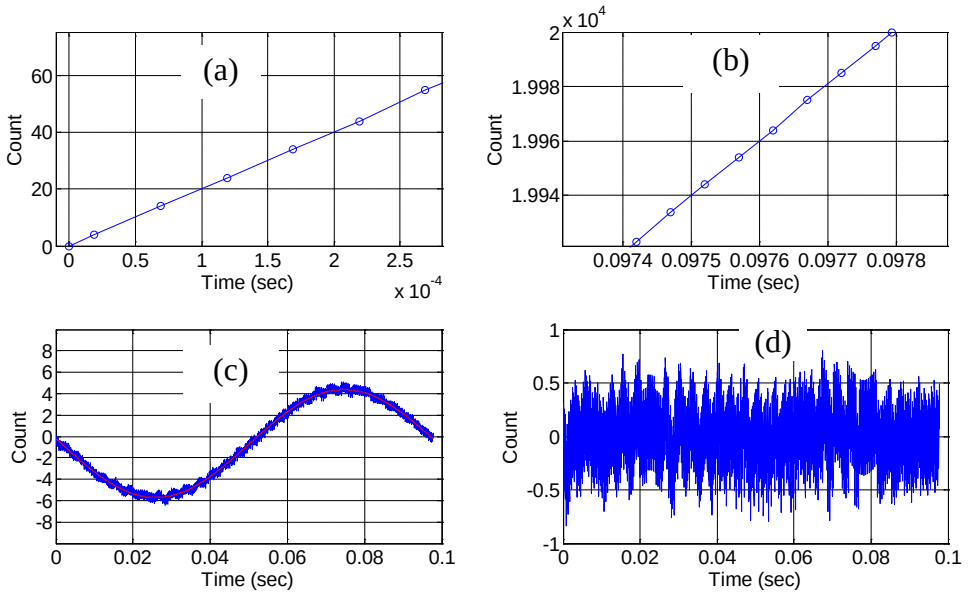

Figure 3-12 Calibration and compensation of spindle encoder readling (a) Start of encoder reading for one revolution of encoder, (b) End of encoder reading for one revolution of encoder, (c) The encoder reading error due to disk runout, (d) The residual error after the compensation of disk runout error.

Spindle encoder feedback smoothing technique

The output of the spindle encoder is a quadrature signal producing 20,000 counts/rev. The controller reads this input at the clock rate of 20 KHz so the number of counts is related to the spindle speed. These two processes are not synchronized with each other. For example, at a spindle speed of 630 rpm, the counter will see a change of 10 or 11 counts per sampling cycle. When this integer difference changes by one full count, it will generate a quantization step in the motion command. For 2 mm motion amplitude, this quantization step has a maximum value of 628 nm in the motion command. To reduce the quantization magnitude due to the limited resolution issue, a smoothing algorithm has been designed and implemented on the PMDi digital signal processor in addition to the correction of encoder runout error to generate spindle angular position feedback. The code is listed in Appendix F.1.

The algorithm uses the fact that while the instantaneous spindle speed derived over one sampling period has larger fluctuation than the physical spindle speed, the mean spindle speed derived by taking the average of the instantaneous spindle speed over larger number of sampling periods (ARMA) removes the high frequency in the speed estimation. Therefore, using the average change in counts at the actual spindle speed will smooth steps and provide a higher resolution estimation of the angular position of the spindle. The change in counts per controller sampling cycle and the average of some time interval can be written as:

$$\begin{aligned} \Delta_{count} &= counter(t) - counter(t-1) \\ count_{avg} &= \Sigma counts / number\ of\ cycles \end{aligned} \tag{3.18}$$

Based on the average count, the angular position in counts can be estimated as

$$position(t) = position(t-1) + count_{avg} \tag{3.19}$$

The error (e) from this estimation of position can be determined and driven to zero by a adding or subtracting a fixed correction (0.01 count for example) depending on the sign of the error.

$$e(t) = \Delta_{count} - count_{avg} + e(t-1) \tag{3.20}$$

For e > 0

$$\begin{aligned} position(t) &= position(t) + correction \\ e(t) &= e(t) - correction \end{aligned} \tag{3.21}$$

For e < 0

$$\begin{aligned} position(t) &= position(t) - correction \\ e(t) &= e(t) + correction \end{aligned} \tag{3.22}$$

An example of the application of this smoothing algorithm to the spindle speed of 630 rpm is shown in Figure 3-13. This graph shows that the digitized number counts change per sampling cycle is either 10 or 11, the fluctuation of counter change is either 0 or 1. When the algorithm discussed above is applied with the average spindle speed derived over 1000 sampling cycles, the fluctuation of counter change is reduced to within the range of (0-0.03). As a result, this filtering technique reduces the maximum quantization step size to 20 nm for 2 mm tool motion command. Furthermore, it increases the effective resolution of the encoder without introducing any additional phase distortion since the estimation error always stays within one encoder count.

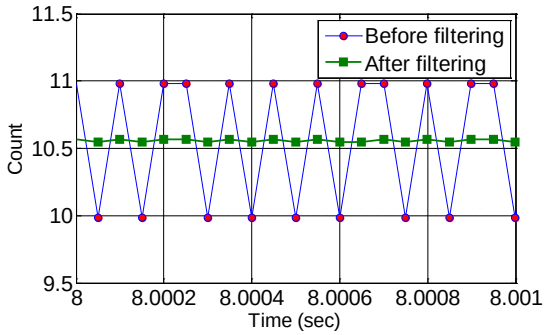

Figure 3-13 Spindle encoder quantization and reduction in step size by filtering

The effect of spindle rotation and position measurement on motion synchronization

Since the tool motion trajectory is generated as a trigonometric function of the spindle angular position, both non-constant spindle speed and residual position measurement error

influence the quality of the motion trajectory. While these two error sources are not distinguishable in the generated trajectory, it is desirable to follow the fluctuation of spindle rotation speed in the tool servo control for the purpose of motion synchronization, but not desirable to follow the measurement error. Even with the above explicit methods to improve the estimation of spindle position, the difference is still significant when the tool servo control switching from single frequency motion trajectory tracking to motion synchronization to spindle rotation. As shown in the Figure 3-14Figure 3-14, the first trajectory is $2sin(40\pi t)$ mm, in which the time variable t is determined by the servo sampling clock cycle; the second trajectory is $2sin(\theta)$ mm, in which the spindle angular position θ is measured under constant spindle speed command of 1200 rpm or 20 Hz. Both trajectories have a peak at 20 Hz, but the magnitude at non-peak frequency locations for the second case is 200 times higher than that of the first case. Correspondingly, with a combination of PID and acceleration feedforward controller for servo tracking test, the tracking error for the latter case is ±30 nm higher. The aliasing effect in the trajectory due to the encoder measurement error can be further improved by more accurate estimation of spindle speed as suggested by [5, 92], in which the momentary spindle speed was determined by measuring time span in processor time clock cycle between every two consecutive encoder counts.

3.3.2 Bilinear Interpolation for Trajectory Generation

Except for a few special cases such as tilted flat surface, there is no closed-form analytical equation to describe the free form surface geometry as a function of the DTM motion axes position, especially after the compensation for the local radius of the tool. Only a grid of sparsely spaced data points in polar coordinates (θ and Xs) can be used to represent the surface to be machined. This interpolation table is created off-line, but the tool motion command is generated on-the-fly by interpolating over these point cloud data set. There are two implementation decisions for the interpolation process.

(1) Selection of interpolation algorithm: bilinear interpolation is used for computational efficiency, higher order interpolator such as cubic function can produce more

accurate estimation but require much more computational time and larger interpolation table [93].

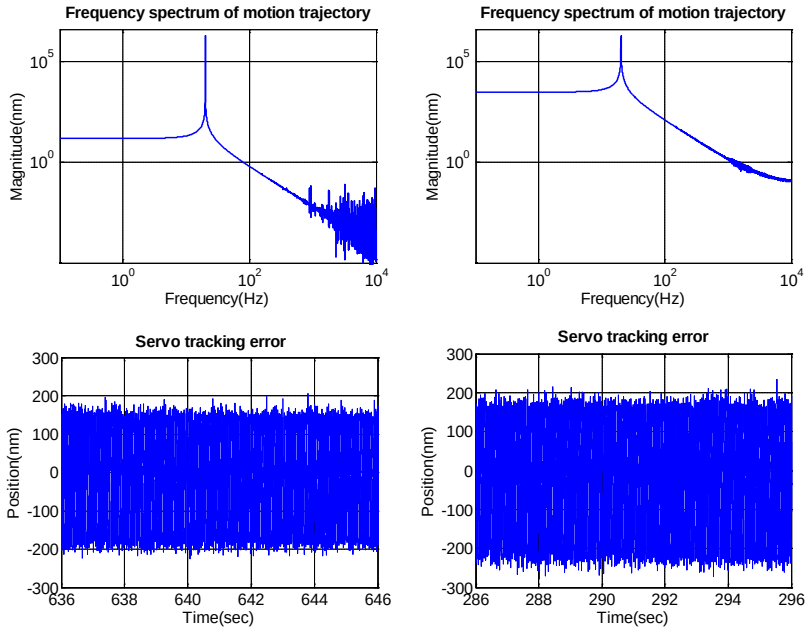

(a) 2sin(40πt) mm (b) 2sin(θ) mm

Figure 3-14 The effect of spindle rotation and position measurement on servo tracking

(2) Density of polar mesh grid: For the two-dimensional interpolation table, the grid size must be as large as possible to reduce residual errors due to the linear interpolation, but the feasible grid size is limited by the DSP processor memory space size, i.e. only 50,000 data points in double precision can be implemented in this study. To this end, the freeform surface should be decomposed into a simple surface that can be represented by a simple algebraic equation and the residual non-rotationally symmetric shape, so the excursion of NRS surface component represented by interpolation table is minimized. For examples, the biconic mirror surface is decomposed into a best fit sphere and a NRS component with tool radius compensation, the fiducial feature for kinematic coupling is decomposed into a sinusoidal surface and a tool radius compensation component.

Appendix F.2 presents the detailed data structure for the interpolation table and code for the implementation of bilinear interpolation over equal-spaced polar mesh grid to generate position and acceleration command. From the GUI, the data file for interpolation purpose is loaded from the PC hard drive into the DSP memory, it provides the flexibility to generate tool motion trajectory for the machining of free form optical surfaces. The effect of interpolation error on motion synchronization to spindle rotation can be demonstrated by tool servo control tests. In these tests, motion synchronization of $2sin(\theta)$ is implemented with an analytical motion trajectory and an interpolated motion trajectory under a constant speed command of 630 rpm, a combination of PID and acceleration feedforward controller was also used. For the latter case, the data table is a grid of 3600 (θ) and 2 (Xs). From Figure 3-15, the tracking error for the case of interpolated trajectory has larger peak-to-peak and RMS value, its frequency spectrum also shows larger magnitude at first 5 harmonics.

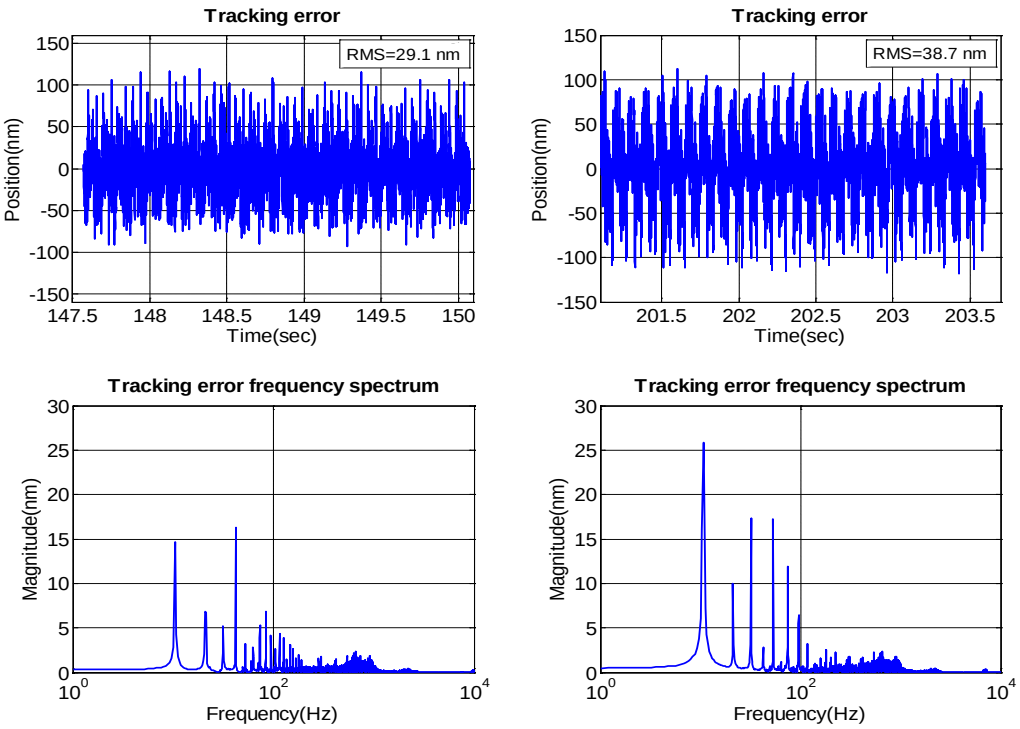

(a) From analytical equation (b) From interpolation

Figure 3-15 Motion synchronization tests of $2sin(\theta)$ with two trajectory generation

3.3.3 The Characteristics of Tool Motion Trajectory

The motion trajectory is generated in spiral cutting path when the tool moves across the work piece surface. With the 25 mm total stroke, the FLORA can meet tool motion requirement for both RS surface component (slow speed but long travel range) and NRS surface component (high speed and small travel range) for free form surface. shows a good example of this implementation for the machining of a biconic mirror. On the other hand, the motion trajectory for NRS surface is directly related to the frequency of spindle rotation. In spite of the large variations of optical design, the tool motion trajectory typically has dominant magnitudes in the first few harmonics of the fundamental spindle frequency, magnitudes at other frequency locations are insignificant.

Trajectories for continuous surfaces typically feature simple arithmetic relationships between their dominant frequency contents and the fundamental spindle frequency. The trajectory in Figure 3-16 is created for the NRS surface component of an off-axis sphere with 600 mm spherical radius, 14 mm radial offset, ∅168 mm aperture size. The tool completes one cycle of motion per revolution of workpiece, the motion amplitude reduces and neutral position of the motion cycle shifts when the tool moves from the outer edge of the workpiece to the rotational center. A tilted flat surface completes one cycle of the tool motion per revolution of the workpiece in Section 5.3. A toric surface features two tool motion cycles per revolution. These three cases have time varying amplitude but constant dominant frequencies. The motion path for fiducial surface in Figure 5-18 has time varying dominant frequency but close-to-constant amplitude. Of course, the changes of frequency and amplitude are slow in the finish cutting pass.

For discontinuous surfaces, such as lenslet arrays featuring repetitive shapes nested together across the surface [94], maximum spindle speed is often limited by the following error created when the tool is instructed to make a radical change in its path as it crosses a discontinuity in the surface. The settling time of the tool servo should be considered whenever there are abrupt changes in the slope of the surface or steps in the height of the surface. It is a common practice to add a transition area or edge zone between discontinuous

surfaces. Surface quality in the edge zone is normally allowed to exceed those in the optical surface, or the tool does not engaging into cutting in the edge zone. Figure 3-17 provided by [94] shows this basic idea, the circumferential speed of the workpiece as it passes by the tool is 150 mm/sec. The residual error is equal to the allowable form error in the optical surface region. The cutting speed is adjusted so that the residual error on exiting the transition area is less than the allowable form error, the size of recovery zone is determined by the settling time of the tool servo. In another example of (complete) off-axis concave sphere machining on a flat surface, [12] smoothed out the sharp corner of the surface design so that the trajectory meets the velocity and acceleration limits.

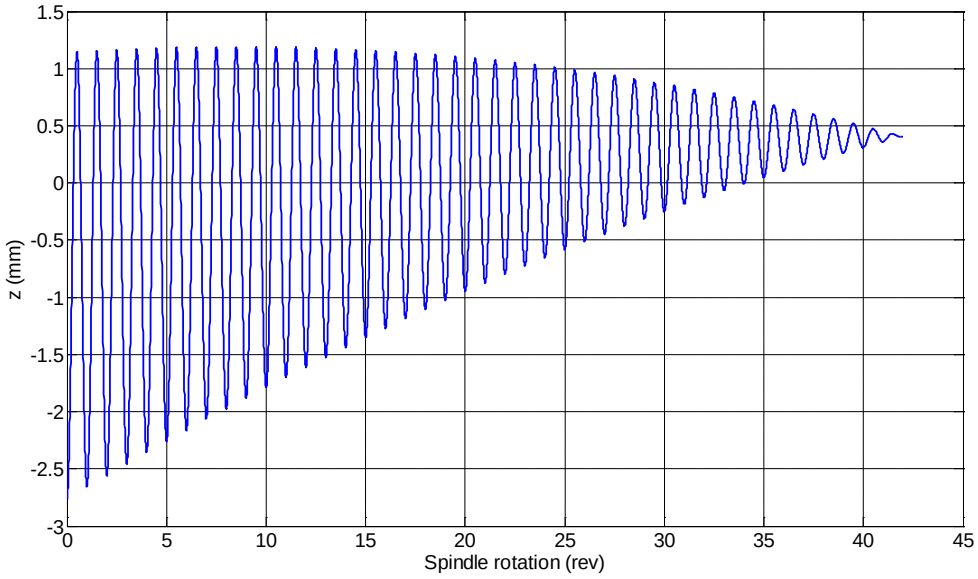

Figure 3-16 Tool motion trajectory for an off-axis sphere

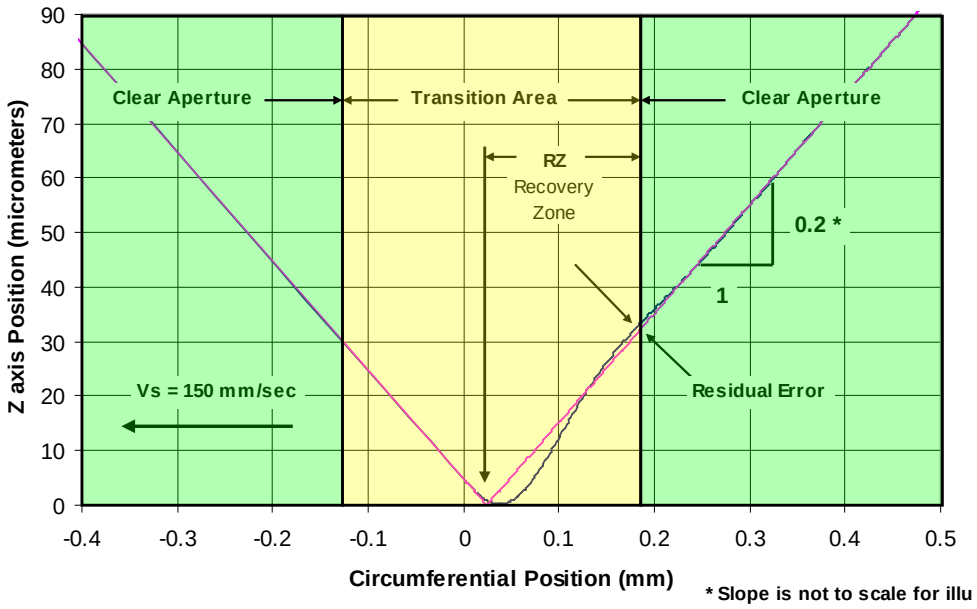

Figure 3-17 Traversing a -0.2 to +0.2 slope change at 150 mm/sec [94]

3.4 Disturbance to the Tool Motion

The characteristics of disturbance to the tool motion determine the achievable motion control performance. All the disturbances in the control of tool motion can be put into three categories: non-desirable actuation forces, internal mechanical disturbance forces, and the tool - work piece interaction forces.

Non-desirable actuation force

The error components in the generation of actuation force other than what is desired in the controller computational output are from various sources:

(1) The noise and quantization errors in the digital-to-analog converters and the uncompensated random noise and biases in the amplifier output stage (Section 2.3) produce disturbance with non-significant magnitude but wide frequency contents.

(2) The 60 Hz harmonics noise in the amplifier output stage produces their own harmonics in the non-linear electro-magnetic force generation process.

(3) The fundamental frequency in the motion profile also produce harmonic error forces in the non-linear electro-magnetic force generation process.
(4) The ripple in force generation with sinusoidal commutation due to the non-perfect physical construction of the linear motor (Section 2.2).
(5) Since the geometry of the moving mass is not symmetric in the Y direction, very small amount misalignment between the motor actuation force and the gravity center of the moving mass will produce a pitching moment to the sliding piston motion.

Internal mechanical disturbances

(1) The non-uniform air distribution of the orifice-type of air bearing in the FLORA presents a major disturbance to the tool motion in the X, Y and pitching directions (Section 2.1 and 3.2.2).

(2) The motor coil cable has minor impact on the tool motion once the cable is made of super flexible material, and there is sufficient space to be properly routed in a loop.

(3) Reaction force out of the linear actuation process affects the tool motion as a format of output disturbance because the induced vibration affects the tool positioning directly and most noticeably in the X and Z direction (Section 2.6).

The tool - work piece interaction forces

The interaction forces between the tool and work piece in the machining process are affected by many factors such as cutting operation parameters, tool geometry and condition, work piece material properties, machine error etc. This is a well-studied subject area in the field of machining [76-82], and there has been significant amount of accomplishment made at the Precision Engineering Center of North Carolina State University [10, 11]. The schematic in Figure 3-18 shows the orthogonal cutting geometry for 0° rake angle tool and the tool force components considered in this simplified discussion.

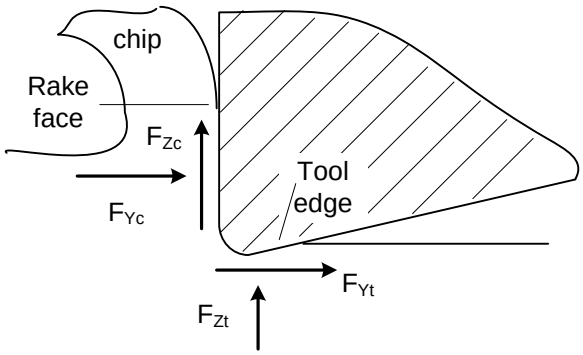

Figure 3-18 Orthogonal tool forces model

In this model, the chip thickness is uniform and equal to the tool in-feed depth. But in the actual round nose tool cutting geometry, the chip thickness varies from zero near the bottom of the cut to a maximum over the contact angle of the tool. Nevertheless, the physical origination of force and force composition under these two scenarios can be taken as the same. In this view there are two pairs of force components. One pair acts on the tool rake face and the other at the tool edge. Each pair consists of normal and tangential forces. F_{Yc} is generated due to the chip formation process as a function of flow stress, which is dependent on material hardness and work hardening effect in the cutting process. F_{Zt} is generated due to the contact on the tool edge behind the rake face and determined by the material hardness, elastic deformation and the contact area. The width of contact is determined by a function of edge condition (rounding, clearance face wear, chipping, etc.) and elastic spring back of the workpiece material. F_{Zt} is negligible for a newly sharpened tool, but it increases as tool wear increases. The other two tangential force components are generated due to the normal forces on the contact surface and the friction. The final tool cutting force F_Y and thrust force F_Z are

$$F_Y = F_{Yc} + F_{Yt}; \qquad F_Z = F_{Zc} + F_{Zt} \tag{3.23}$$

In the rough pass of machining process, there is intermittent cutting that introduces large fluctuation of interaction forces up to a few Newton, which in turns causes the large oscillation of the tool positioning. But the resulted surface quality in rough passes is not an issue as long as the tool servo remains stable under these conditions. The final surface quality

is determined by the finish pass. In the finish pass, there is small depth of cut (<5 μm) and small cross-feed rate (<5 μm/rev), the cutting is continuous (not for brittle materials such Si and Ge), so the fluctuation of interaction forces are much smaller, about 0.2 N reported in [11, 83], this variation of interaction forces is the main concern in the tool positioning. For metals, due to microstructure effect (such as inclusions, grain size/boundary/orientation), the increase of cutting force increase the frequency range of tool forces. In [77], the author noted significant frequency content in the experimental tool force signal at wavelengths equal to the average grain size of the material being cut. Based on the machining of aluminum, [81] showed that, the maximum frequency range of the thrusting force was much less in the sample with the larger grains than it is in the samples with smaller grains. The cutting force did not exhibit the same trend and remained fairly constant. Since the aluminum cutting is in the ductile regime, the chip produced is continuous and therefore the cutting force shows very little frequency content. When cutting brittle material, due to non-continuous chip formation, the cutting force did not stay constant. In the acrylic (PMMA) both forces had little variations. Besides the factor of material property, the variation of disturbance forces and the tool positioning error have regenerative relationship since the change of relative position between the tool and work piece, particularly depth of cut, changes the magnitude of interaction forces.

Because of the surface slope, the thrust force can be further decomposed into the disturbance forces in X and Z direction. The disturbance forces in X and Y (cutting) direction due to the tool – work piece interaction produce translational error motions in the XY plane and pitching error motion at the tool tip, they are one of the main considerations in the design of tool holder structure and air bearing. Furthermore, the oscillatory disturbance force in Z direction become the main constraint for the tool servo control when the moving mass reduces from 250 lb in the Z slide to 665 grams in the FLORA. Since the FLORA has no passive stiffness, it relies on the servo controller to provide dynamic stiffness.

Figure 3-19 shows the frequency spectra of position holding error in the machining of plated copper flat. In these tests, the tool was actively held at a fixed position with a PID controller, the spindle ran at 500 rpm, and a tool radius of 0.5 mm was used. (a) was obtained

right before the cutting, (b) was for finish cutting pass with 2 um depth of cut and 4 μm/rev cross-feed rate, and (c) was for rough cutting pass with a larger depth of cut (4 um) and a larger cross-feed rate (20 um/rev). Comparing with the non-cutting condition, the magnitude increase within 1 KHz in the spectrum is minor for the finish pass, but significant for the rough pass because of larger disturbance forces (mainly thrust force). Even for the finish pass, when the servo control system has less stiffness (i.e. lower bandwidth), the increase of magnitude was more significant as shown in Figure 4-10. In these tests, the closed-loop system with PID controller in Figure 3-11 can only reject disturbance below 430 Hz, but amplify the effect of the disturbances above 430 Hz on positioning error. It can be taken that disturbance forces in the machining process have noticeable influence on the tool servo control in the low frequency range up to 500 Hz.

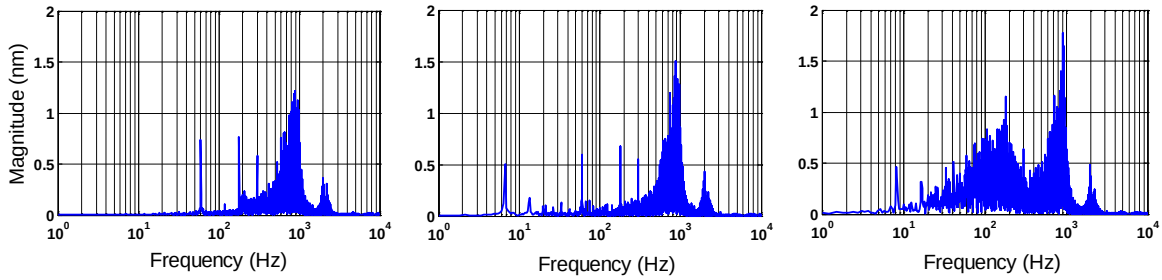

(a) No cutting (b) Finish pass (c) Rough pass

Figure 3-19 Frequency spectrum of position holding error

3.5 Piston Position Feedback Error

By integrating the Sony BH25 linear encoder with PMDi interpolator (MW53), the position measurement shows 3 nm of noise when the air bearing is turned off and the piston maintains static position. However, there was frequency limit for the sin/cos encoder signals entering the interpolator in the standard interpolation process. Below this limit, the interpolation of 0.25 μm encoder signal pitch can be programmed up to a factor of 8096 (31 pm resolution). Beyond this limit, the resolution degrades to 125 nm. Figure 3-20 and Figure 3-21 shows the positioning error in a test of sinusoidal profile tracking at 2 mm amplitude

and 20 Hz. The error for both cases is about ±200 nm PP. The frequency limit of the encoder measurement has significant impact on the motion control performance. With 100 KHz limit, the high frequency position error glitches due to 125 nm measurement resolution exists in almost 100% of motion cycle; with 325 KHz limit, about 21 % of motion cycle is free of this error glitch. The frequency spectrum in both figures only shows the section of magnitude from 0 to 4 nm to compare these two cases. It can be seen that, the magnitudes for frequencies above 1 KHz in Figure 3-21 is only half of those in Figure 3-20.

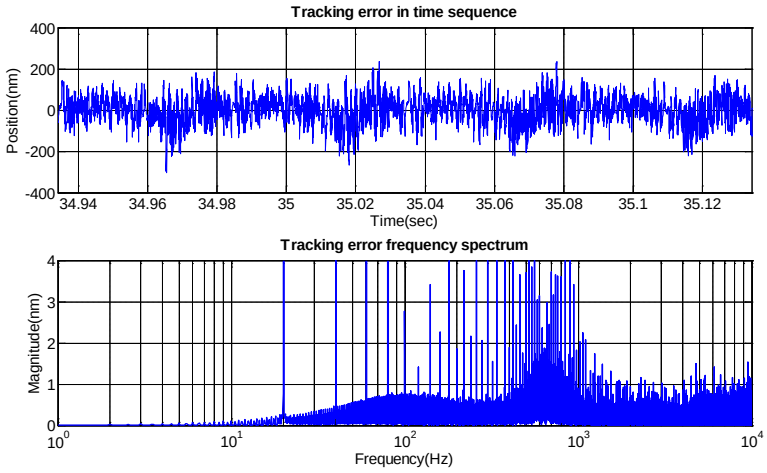

Figure 3-20 2 mm 20 Hz sinusoidal tracking with 100 KHz encoder limit

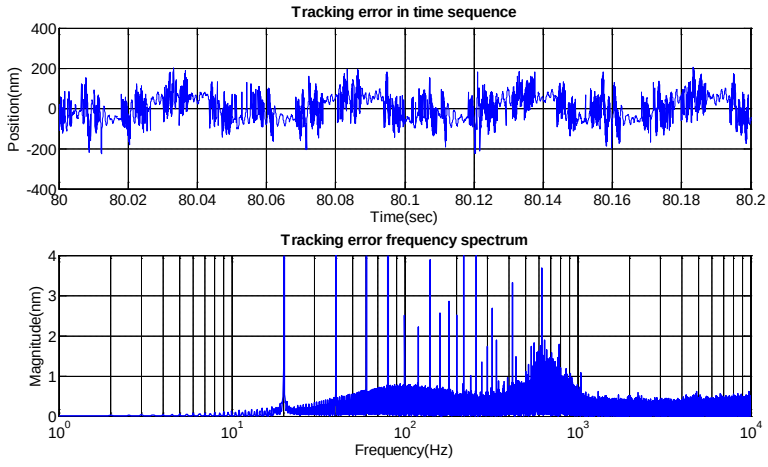

Figure 3-21 2 mm 20 Hz sinusoidal tracking with 325 KHz encoder limit

To addresses this issue, collaborative efforts with PMDi were taken to increase the frequency limit of interpolation process above 1 MHz. This is the sine wave frequency for the peak speed of the ± 2 mm, 20 Hz sine wave or 250 mm/sec.

The existence of this frequency limit is due to the working principle of the encoder signal interpolation process as shown in Figure 3-22. The interpolator takes in two differential sinusoidal signals with 90° out of phase from the encoder, records zero crossing of these signals and sub-resolves each wave quadrant. The problem is the subdivision process has a frequency limit for the sinusoidal signal. The actual analog sinusoidal signals are never perfect, the data acquisition system always needs some amount of time to remove the noise, make correction for phase, amplitude, DC offset errors, and then do the interpolation.

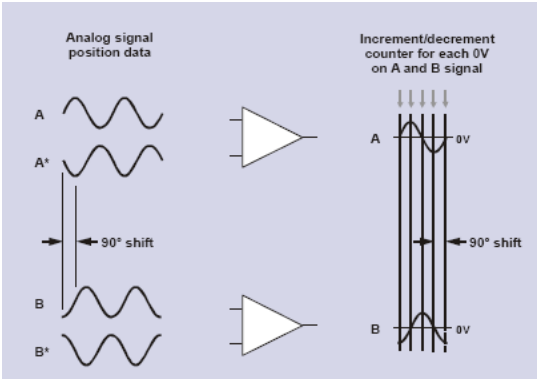

(a) Sin/cos signals out of the encoder

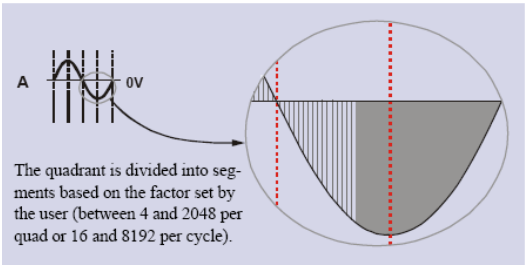

(b) Subdivision of a wave quadrant

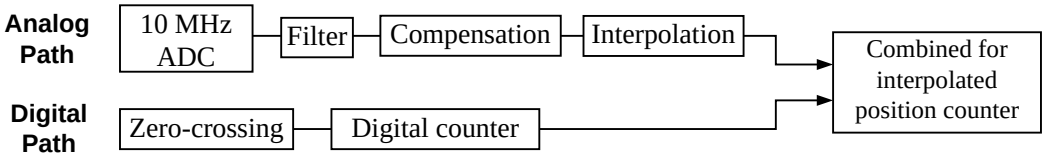

(c) The process of generation of interpolated encoder counts

Figure 3-22 Encoder signal interpolation process (PMDi manual)

The solution is first to remove the filtering and compensation in the analog path, which increases the frequency limit from 100 KHz to 325 KHz. To push the frequency limit above

1 MHz, another critical step taken to synchronize the analog path and digital path by adding a delay time in the digital path since there is 575 ns time latency in the analog path. The Figure 3-23 shows the variations of position reading change for two continuous samples at 20 KHz sampling rate when the interpolator takes in encoder signals. The single-ended signals are first generated by a dual channel function generator (HP 8904A), and then converted into differential signals by a conditional electronics. These signals are close to ideal condition with 1 v peak-to-peak, negligible phase error, and 2.5 v DC offset value. If the interpolation process is perfect, the variation shall be at the position resolution level of ±1 nm. However, Figure 3-23(a) shows, at every 240 samples interval, there is higher spike within ±3 nm. Figure 3-23(b) shows that, when the frequency of signals increase to 500 KHz. The magnitude of spikes increases to 12.5 nm. These intermittent spikes are caused by the SYNC jitter in the MotionWire communication between the DSP processor (DMC100) and the interpolator (MW53). Most of time, it takes one clock cycle (25 ns for 40 MHz DSP processor) for the interpolator to receive the SYNC signal, but every 60 samples, it takes two clock cycles. The root-cause of jittering remains unknown, but the consequence is that the sampling of the 10 MHz ADC in the analog path is short of 100 ns when the jittering occurs and over counts 100 ns in the next sample. For 100 KHz, the timing difference causes 2.5 nm fluctuation, but 12.5 nm for 500 KHz. The magnitude of spikes is reduced by taking ×4 interpolation of 10 MHz ADC data at the 40 MHz DSP clock cycle. For 500 KHz signals, the fluctuation stays within ±5 nm with interpolation as shown in Figure 3-23(c).

By removing the signals filtering and compensation to lift up the interpolation frequency limit, the interpolation process may become more sensitive to the encoder signal quality. To check the robustness of this solution, the same tests were conducted for 1 MHz signals with 2-4° phase error. These signals are generated by two single-channel function generators (HP 3312A). When the peak-to-peak level of signals is at 1 v, the fluctuation in Figure 3-24(a) is within ±10 nm. The fluctuation level is more than doubled in Figure 3-24(b) once the peak-to-peak magnitude of the signals drops to 0.64v.

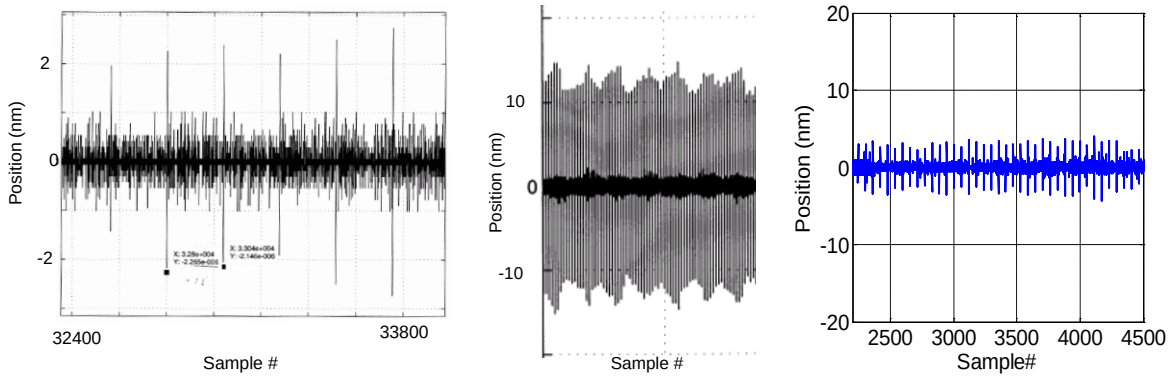

(a) (b) (c)

Figure 3-23 The variations of position reading change for two continuous samples (a) 100 KHz signals without interpolation (b) 500 KHz signals without interpolation, (c) 500 KHz signals with interpolation

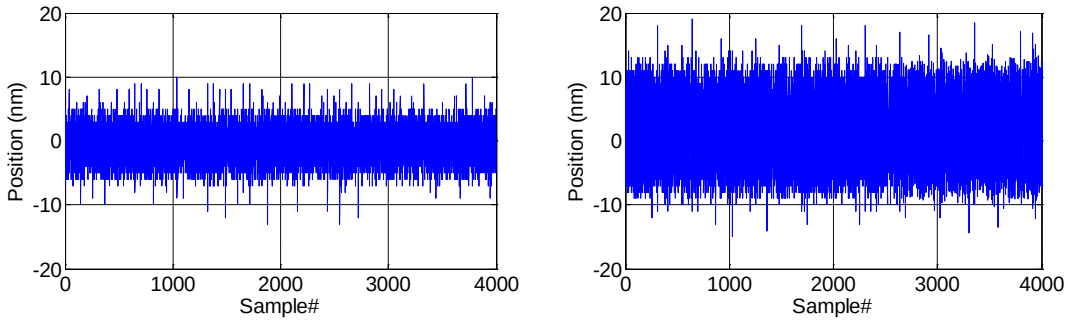

(a) Signal with 1 v peak-to-peak level (b) Signal with 0.64 v peak-to-peak level

Figure 3-24 The variations of position reading change for 1 MHz signals

As a result, it is desirable to have the signal magnitude as large as possible if the phase error can not be eliminated. With the signal levels of 0.871 V (PP) and 0.824 V (PP) and phase error about 2-3 ° as shown in Figure 2-10, the predicted measurement error at 250 mm/sec is about ±12 nm. A further reduction of this error would be feasible with the interpolation by a faster DSP processor, i.e. at 500 MHz clock cycle, the error can be reduced down to a few nanometers. Figure 3-25 shows the tracking error in a test of sinusoidal profile tracking at 2 mm amplitude and 20 Hz. The error is about ±170 nm PP and free of high frequency glitches due to 125 nm measurement resolution as shown in Figure 3-20 and

Figure 3-21. The frequency spectrum only shows the section of magnitude from 0 to 4 nm for the purpose of comparison with Figure 3-20 and Figure 3-21. The magnitude for frequencies above 1 KHz in Figure 3-25 is much lower but still exists for future improvement.

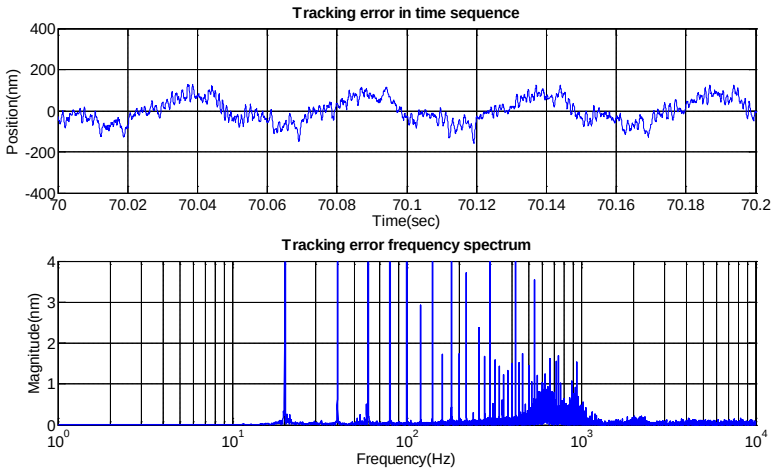

Figure 3-25 2 mm 20 Hz sinusoidal tracking with above 1 MHz encoder limit

In addition to all the above discussions, high-resolution, interferometric encoders are sensitive to external disturbances. As a result, the 5 VDC power supply source for the sensor and the interpolation electronics must be clean and stable. Shielding and grounding practice recommended in the specification and manual must be followed and the encoder housing, the cables, the interpolation cards/box and control card must have the same ground potential.

3.6 Closed-Loop Tool Servo Control

It shall be noted that actuation force from the motor, the position measurement by the linear encoder and the tool tip to be positioned are at different physical locations in the assembly of FLORA. The tool positioning in the feed (Z) direction depends on the too servo control and the dynamics between the tool tip and the encoder scale. The active tool servo only controls the relative position between the encoder read and scale. The tool servo control in Z direction is a single DOF system shown in Figure 3-26, it consists of an undamped mass

m, a force disturbance $F_d(t)$, and the displacement of the sliding piston $Z_t(t)$. The piston position is controlled by manipulating the signal voltage to the amplifier/motor, providing the actuation force $F_a(t)$, in response to a position error between the commanded position $Z_c(t)$ and the measured position $Z_m(t)$.

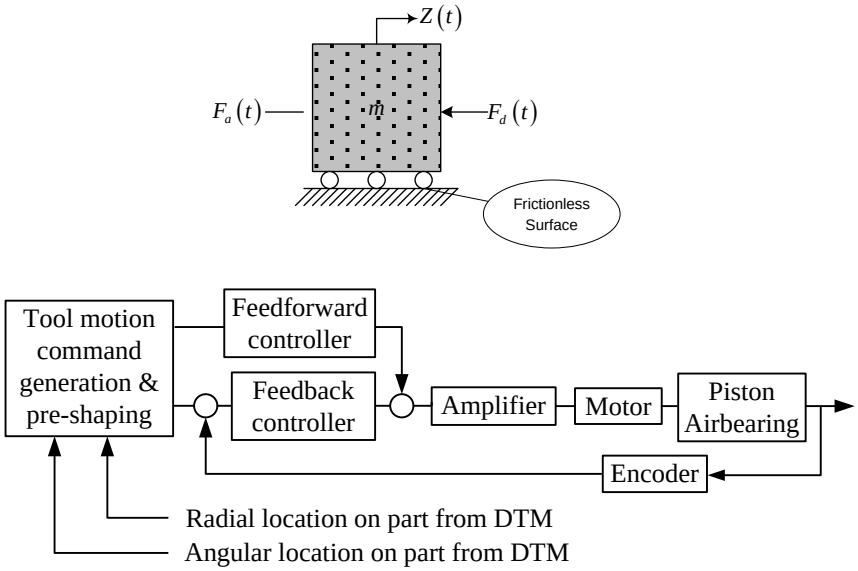

Figure 3-26 Tool servo control structure for FLORA

Figure 3-27 shows the block diagram representation of the servo control structure in Figure 3-26, where K is the general term of controller, G_I(s) is the current loop dynamics, K_f is the motor force constant, and P(s) contains the dynamics of the tool holder. N(s) is the encoder position feedback error or noise, R(s) is the position command for the tool motion, D(s) is the disturbance, and Z(s) is the resulted tool position.

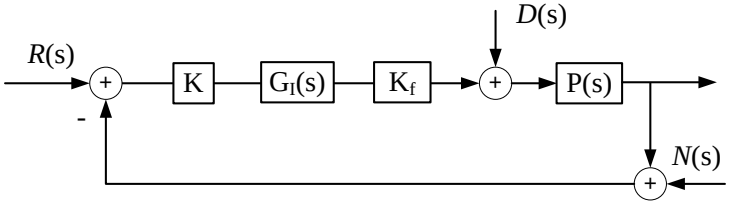

Figure 3-27 Closed-loop control diagram for FLORA

The true tool positioning error $E(s)$ is the difference of $R(s)$ and $Z(s)$, and can be expressed as a function of all closed loop system inputs and dynamics

$$\begin{aligned} E(s) &= ER(s)+ED(s)+EN(s) \\ &= \frac{1}{1+KG_I(s)K_f P(s)}\cdot R(s)-\frac{P(s)}{1+KG_I(s)K_f P(s)}D(s)+\frac{KG_I(s)K_f P(s)}{1+KG_I(s)K_f P(s)}\cdot N(s) \end{aligned} \tag{3.24}$$

Profile tracking

$$ER(s) = \frac{1}{1+KG_I(s)K_f P(s)}\cdot R(s)= G_R \cdot R(s) \tag{3.25}$$

The tool motion profile has wide frequency spectrum but dominant magnitude at the harmonics of spindle frequency. The existence of tracking error $ER(s)$ is first caused by errors in $R(s)$ from spindle encoder measurement error and numerical error in the interpolation for trajectory generation. Second, even if $R(s)$ is perfect, the transfer function G_R is not zero. To avoid system instability due to the amplifier saturation limit under large profile command input to the controller, both the magnitude of position error and the rate of position error change shall be limited.

Disturbance rejection

$$ED(s) = -\frac{P(s)}{1+KG_I(s)K_f P(s)}\cdot D(s)= G_D \cdot D(s) \tag{3.26}$$

In the diamond turning, there are random disturbances mainly in the low-frequency range as well as periodic disturbances synchronized with the spindle rotation. Disturbance rejection is an important characteristic of a motion control system. Section 3.4 fully discusses the physical nature of these disturbances. Disturbances induced position error $ED(s)$ is caused by the existence of disturbance $D(s)$, the transfer function G_D can only reduce but not totally eliminate its effect on $ED(s)$.

Position feedback noise reduction

$$EN(s) = \frac{KG_I(s)K_f P(s)}{1 + KG_I(s)K_f P(s)} \cdot N(s) = G_N \cdot N(s) \tag{3.27}$$

The transfer functions for the tracking profile $R(s)$ and the encoder noise $N(s)$ are inversely related, i.e. $G_R + G_N = 1$. The high controller gains that reduce the profile tracking error *ER*, increase the encoder noise induced position error *EN*. This is a classical challenge in the motion control system. The best solution is to reduce the feedback error as much as possible. The measurement of piston position has been improved over three versions of linear encoder and data acquisition system as discussed in Section 2.4, the residual error can be taken as white noise input to the dynamic system.

In summary, the functional requirement for the servo control is to track a commanded trajectory while confronted by disturbances, measurement noise, plant uncertainty, actuator saturation and bandwidth limitations. The simultaneous tool positioning requirement on range, speed, and accuracy makes the servo control of FLORA a challenging task in terms of trajectory generation, controller design, and position measurement. For this low-mass, direct-drive motion control system, there are significant challenges:

(1) Positioning Error - The ultra-positioning accuracy requirement for high speed dynamic operation condition and known motion path (i.e. multi-frequency sinusoidal trajectory tracking with time varying motion amplitude and phase). To create a surface finish of 5 nm RMS while moving with 2 mm amplitude at 20 Hz, the servo control error must be within ±20 nm, on the order of 0.001% of the motion command.

(2) Disturbance Rejection - The low-mass (0.665 kg) direct-drive system is sensitive to internal and external disturbances.

A systematic approach can be taken to tackle these challenges in the servo control by following the conceptual process of error generation:

(1) Design a physical system that is easy to control: Optimize the system components selection/design and integration to minimize error, noise, disturbance and nonlinearities such as friction, backlash and hysteresis, i.e. in the terms $R(s)$, $D(s)$ and

N(s); and increase their dynamic resonance frequencies in the terms G_I(s) and P(s) as far as possible from the FLORA operation frequency.

(2) Develop an effective control approach K to minimize the influence of error, noise and disturbance on tool positioning error E(s).

By combining the physical design and controller design to create a new FLORA, it provides the power to optimize the performance better than either single approach would provide. This interaction of design and control in the development process of the FLORA are most critical in evaluating the influence of major design variables on the servo control performance.

(1) The moving mass is reduced to increase the bandwidth of the servo system, thus improving the profile tracking, but lower mass motion system become more sensitive to the disturbance. Further reduction of moving mass from 0.665 Kg depends on not only the characteristics of disturbance in feasible physical implementation of the FLORA, and the characteristics of the thrust force in the cutting process, but also the effectiveness of control approaches to reject disturbances.

(2) The sampling rate of the digital control system shall be as high as possible since the motion profile to be tracked and the disturbance to be rejected has wide frequency contents up to a few hundred Hertz. The 20 KHz sampling rate is selected based on a compromise between the computation requirement in the machining tasks (both trajectory generation and controller) and minimum requirement on the sampling rate selection as discussed in Section 2.6. Once the minimum requirement of sampling rate is met, the performance gain from further increase of sampling rate is not significant.

(3) The actuation force available from the small motor is sufficient to move the piston at the desired rate, and additional actuation force from a bigger motor does not improve disturbance rejection, and only has marginal improvement on the profile tracking, i.e. smaller overshoot peak and shorter settling time in the transient state response.

(4) Physical damping is not needed for the FLORA servo control in Z direction. At high frequencies the amplitudes and thus the forces are too small to make any appreciable

difference. At low frequency and high amplitude, the damping forces are high but are not needed and only lead to higher motor force. The physical damping is needed for the passive control of tool position in X and Y direction, but determined by the air bearing design.

Once errors in the tool motion trajectory and the tool position measurement are explicitly minimized, the controller design for the closed-loop servo control system mainly needs to consider profile tracking and disturbance rejection. Figure 3-28 shows a block diagram of the proposed composite controller structure to achieve control task. A position feedback controller (K_{POS}) is designed based on the dominant linear model to establish the basic closed-loop control system. A feedforward controller (K_{FF}) is applied to compensate the phase lag in profile tracking. A disturbance observer (*DOB*) improves the disturbance rejection in the low frequency range. An adaptive feedforward controller (K_{AFC}) is designed to further improve trajectory tracking and reject disturbances at selected frequencies. The detailed design process of these controllers is presented in Section 4.

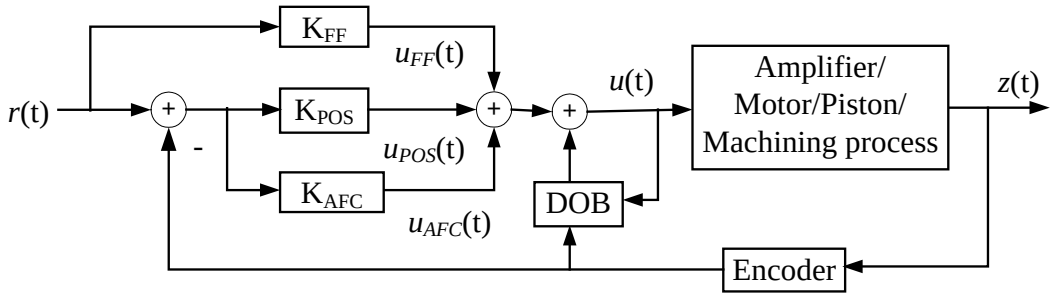

Figure 3-28 Schematic diagram of the proposed controller structure

4. Controller Development for Tool Servo

This section presents the detailed analysis, design and test of the controllers used for the fast long range actuator. Based on the identified open loop system dynamics and the characteristics of the motion trajectory and disturbances in the diamond turning of free form surfaces, the control algorithms were first analyzed and simulated in both time and frequency domain. A Matlab SIMULINK model of servo control is shown in Appendix D. Then, these different control components were either implemented separately or integrated as the structure in Figure 3-28.

4.1 Classical Loop Shaping Design for Position Feedback Controller

Feedback control not only improves the command following and disturbance rejection and disturbance rejection in the servo control, but also increase robustness of control to uncertainty in the system. The closed-loop block diagram with feedback control in Figure 4-1 is reconstructed from Figure 3-27, where *C* contains the dynamics of actuator and feedback controller together, and *P* contains the dynamics of the sliding mass. *N*(s) is the encoder position feedback error or noise, *R*(s) is the position command for the tool motion, *D*(s) is the disturbance, and *Z*(s) is the resulted tool position.

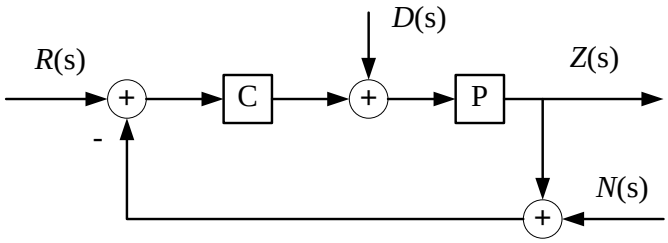

Figure 4-1 FLORA control system diagram

The true tool position *Z*(s) is derived as

$$Z(s) = \frac{C \cdot P}{1 + C \cdot P} \cdot R(s) + \frac{P}{1 + C \cdot P} D(s) - \frac{C \cdot P}{1 + C \cdot P} \cdot N(s) \tag{4.1}$$

The true tool positioning error E(s) is again defined as the difference between R(s) and Z(s), and can be expressed as a function of all closed loop system inputs and dynamics

$$E(s) = \frac{1}{1 + C \cdot P} \cdot R(s) - \frac{P}{1 + C \cdot P} D(s) + \frac{C \cdot P}{1 + C \cdot P} \cdot N(s) \tag{4.2}$$

Three common terms in C·P/(1+ C·P), 1/(1+ C·P) and P/(1+ C·P) in Equation (4.1) and (4.2) are called system transfer function *T*, error transfer function *S* and disturbance transfer function *M* respectively.

$$T = \frac{C \cdot P}{1 + C \cdot P}; \qquad S = \frac{1}{1 + C \cdot P}; \qquad M = \frac{P}{1 + C \cdot P} \tag{4.3}$$

The process of designing feedback controllers is to make proper compromises among different factors based on these three functions.

If a classical position feedback controller was used for this ultra-precision positioning application, it would require a high controller gain that destabilizes the system due to the actuator saturation and high frequency dynamics. The inadequacy of classical feedback controller can be illustrated by a simple case of profile tracking with no disturbance or position feedback error ($D(s) = 0$, and $N(s) = 0$). To meet profile tracking accuracy, the magnitude of sensitivity function $S(s)$ must remain within certain boundaries defined by the dynamic system. For example, to track 2 mm amplitude, 20 Hz frequency sine wave with less than 100 nm position error, the magnitude of error function must be less than 50×10^{-6}. This requires the feedback controller gain to be larger than 1.67×10^{4} A/mm. The closed-loop system for this controller gain is unstable.

$$\left|S(i\omega)\right| = \left|\frac{1}{1 + C(i\omega)P(i\omega)}\right| \le \frac{E(i\omega)}{R(i\omega)} = \frac{100\,nm}{2\,mm} = 50 \times 10^{-6} \tag{4.4}$$

As a general guideline of classical loop shaping controller design [73], a controller manipulates the loop function $C \cdot P$ to obtain a desirable shape, so that system performance,

stability and robustness requirements can be achieved. To this end, design specifications are translated into following frequency response characteristics:

- High loop-gain ($|C \cdot P|$) in the low frequency range for desirable performance on tracking and disturbance rejection.
- Adequate loop-gain ($|C \cdot P|$) crossover frequency for high speed-of-response (rise time and settling time).
- A slope of -20 dB/decade for the loop-gain ($|C \cdot P|$) at the crossover frequency, and a minimum of 30° phase margin for stability.
- Low loop-gain ($|C \cdot P|$) in the high frequency range to have sufficient gain margin for modeling uncertainty, reduce the effect of the noise (or error) in the position command and measurement, and avoid actuation saturation.

A high-gain controller (at low frequencies) is very important to achieve good performance on tracking and disturbance rejection. It can be done by pushing the loop-gain crossover frequency to a higher value, and by increasing the slope of loop-gain. However, the crossover frequency is normally limited by high frequency modes in the amplifier and mechanical resonances. When a set of components are driven faster than their natural mode frequencies, the system will saturate. The frequency response behaviors of closed-loop transfer functions for stable linear system must satisfy the frequency domain integral constraint or Bode Integral Constraint in Equation (4.5) [65, 74]. It means, the area of sensitivity below 1 must be equal to the area of sensitivity above 1. It has also been known as the waterbed effect. Because of this integral constant, if the amplitude of the frequency response is reduced in one part of the spectrum, it must get larger in the other part. The actual trade-off process all depends on the characteristics of the open system dynamics, motion trajectory and disturbances, as illustrated by three designs of controllers.

$$\int_0^\infty \ln\left|S(j\omega)\right| d\omega = 0 \tag{4.5}$$

A graphic representation of these design requirements and constraints is given in Figure 4-2.

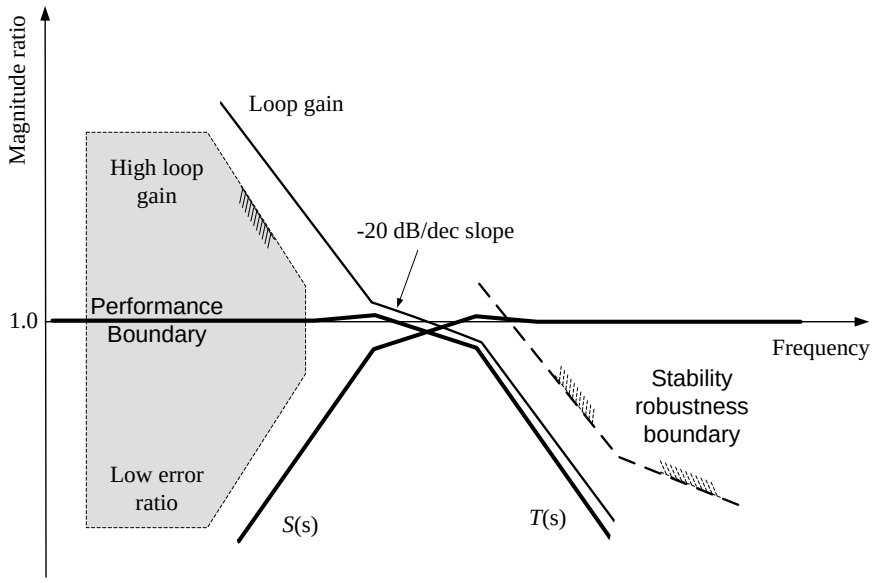

Figure 4-2 Loop shaping design criteria

4.1.1 PID Controller

PID controller represents an industrial standard for manufacturing servo control due to its intuitive nature. Equation (4.3) shows continuous form of the controller in three different formats.

$$K_{PID}(s) = K_P + \frac{K_I}{s} + K_D s = \frac{K_D(s+z_1)(s+z_2)}{s} = K_D \frac{s^2 + 2\xi\omega_{PID1} + \omega_{PID1}{}^2}{s} \qquad (4.6)$$

where $K_P = K_D(z_1 + z_2)$, $K_I = K_D z_1 z_2$. There is an explicit tuning process based on time-domain response for step or sinusoidal input when the system model is not available. For the model-based tuning process, it can be analyzed according to the loop shaping process.

- The loop-gain crossover frequency is predominantly determined by the term of K_D.
- The loop gain (magnitude and slope) in the low frequency range is predominantly determined by the two PID controller's zeros (z_1 and z_2). It is desirable to increase

their values as much as possible within acceptable phase margin limit, so the ratios of K_I and K_P to K_D shall be large for this purpose.

Equation (4.7) is a discrete form of the controller with *Ts* as the sampling period resulted from bilinear transformation [73].

$$K_{PID}(z) = \frac{\left(K_P + \frac{K_I T_s}{2} + \frac{K_D}{T_s}\right) z^2 - \left(K_P + \frac{K_I T_s}{2} + \frac{2K_D}{T_s}\right) z + \frac{K_D}{T_s}}{z^2 - z} \tag{4.7}$$

Since the high-frequency dynamics such as mechanical resonances have an impact on the stability of a system, the basic form of PID controller can be augmented to keep the high-frequency loop gain low. Equation (4.8) adds an extra pole at $-\omega_{PID2}$ to alleviate the high-frequency amplification.

$$K_{PID-M}(s) = K_D \cdot \frac{s^2 + 2\xi\omega_{PID1} + \omega_{PID1}^{\ 2}}{s(s + \omega_{PID2})} \tag{4.8}$$

4.1.2 Lag-lead Controller

The lag-lead controller uses frequency design approach to obtain desired frequency response. In general, a lead compensator is designed for fast response and a lag compensator for high gains.

Lead compensation

Lead compensation adds phase lead. To alleviate the high-frequency amplification of the numerator term, a pole is added in the denominator at a frequency higher than the breakpoint of the numerator term. Thus, the phase increase still occurs, but the amplification at high frequencies is limited [73].

$$K_{lead}(s) = \frac{\alpha\tau_{lead}\, s + 1}{\tau_{lead}\, s + 1} \tag{4.9}$$

where $\tau_{lead} = \frac{1}{\omega_c \sqrt{\alpha}}$, $\alpha\tau_{lead} = \frac{\sqrt{\alpha}}{\omega_c}$, ω_c is the desired the loop-gain crossover frequency.

Lag compensation

Lag compensation adds a pole at zero for high gain in low-frequency range. The frequency (ω_{lag}) of its zero is typically selected as 0.1-0.2 of the loop-gain crossover frequency, so that the pole-zero pair does not significantly interfere with the dynamic response of the overall system as determined by the lead compensation. This is accomplished at the cost of a phase decrease below the break point frequency.

$$K_{lag}(s) = \frac{\tau_{lag} s + 1}{\tau_{lag} s} \tag{4.10}$$

where $\tau_{lag} = 1/\omega_{lag}$.

The individual terms of lead and lag compensation can be converted into discrete form by bilinear transformation. A double lead compensation is implemented to obtain a phase margin larger than 30°. Finally, the overall controller gain K_c is selected to make the loop gain equal to one at the crossover frequency ω_c.

$$\left| K_c \cdot K_{lead}^2(z) K_{lag}(z) P(z) \right| = 1 \tag{4.11}$$

4.1.3 Comparison of Controller Designs

The transfer functions for controllers are defined between the position error input (mm) and current command output to the amplifier (amp). Based on the measured open loop system frequency response characteristic, three different position feedback controllers were designed with different loop gain crossover frequencies of 100 Hz, 600 Hz, and 1000 Hz, the controller parameters defined in Equation (4.4) and (4.7) are selected as:

PID controller: (600 Hz) K_P =120; K_I = 42560; K_D = 0.160;

Lag-lead compensator: (100 Hz) α=6; $\omega_c = 2\pi \cdot 100$; $\omega_{lead} = 2\pi \cdot 100$; $\omega_{lag} = 2\pi \cdot 20$

Lag-lead compensator: (1 KHz) α=15; $\omega_c = 2\pi \cdot 1000$; $\omega_{lead} = 2\pi \cdot 1000$; $\omega_{lag} = 2\pi \cdot 100$

The corresponding algorithms in discrete time *Z*-domain in the same order are:

$$K_{PID}(z) = \frac{3321z^2 - 6519z + 3200}{z^2 - z} \tag{4.12}$$

$$K_{LL1}(z) = \frac{233z^3 - 692z^2 + 685z - 226}{2z^3 - 5.7037z^2 + 5.4184z - 1.7147} \tag{4.13}$$

$$K_{LL2}(z) = \frac{20407z^3 - 57411z^2 + 53822z - 16815}{2z^3 - 3.1848z^2 + 1.3602z - 0.1755} \tag{4.14}$$

As shown in Figure 4-3, these three controllers behave similarly in the frequency domain; that is, they increase loop gains at low frequency, add phase lead to obtain phase margin at the crossover frequency and lower the gain at high frequency.

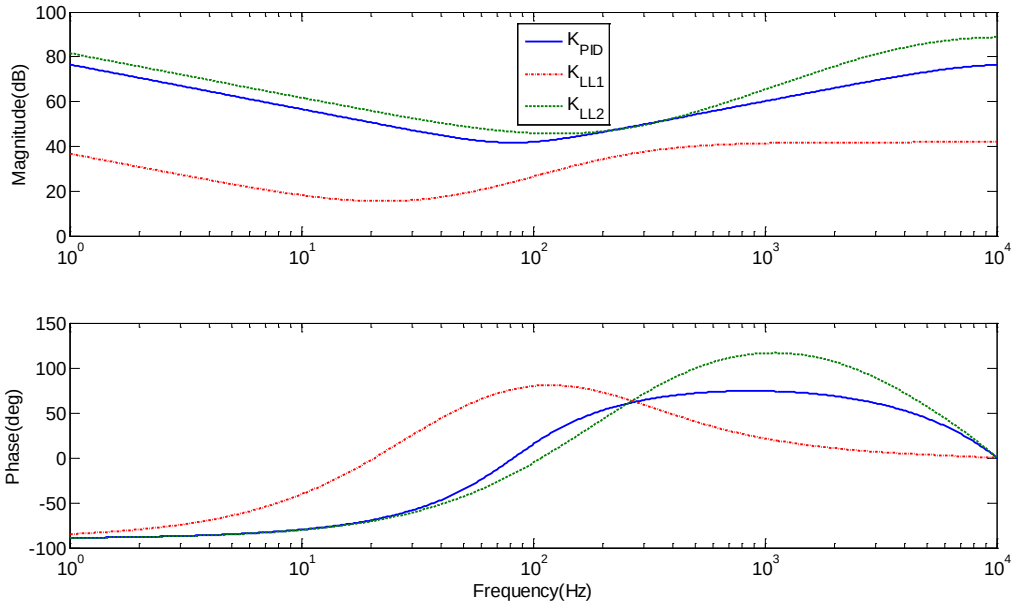

Figure 4-3 Simulations of controller frequency responses

Figure 4-4 compares the frequency responses of loop function ($C \cdot P$) without controller and with three different controllers based on the nominal system dynamics in Equation (3.7). K_{LL1} has the most conservative controller gains, it has the largest stability margin with 76.1° PM and 15.6 dB GM. K_{PID} obtains 41.6° PM and 4.76 dB GM, K_{LL2} obtains 39.2° PM and 6.8 dB GM.

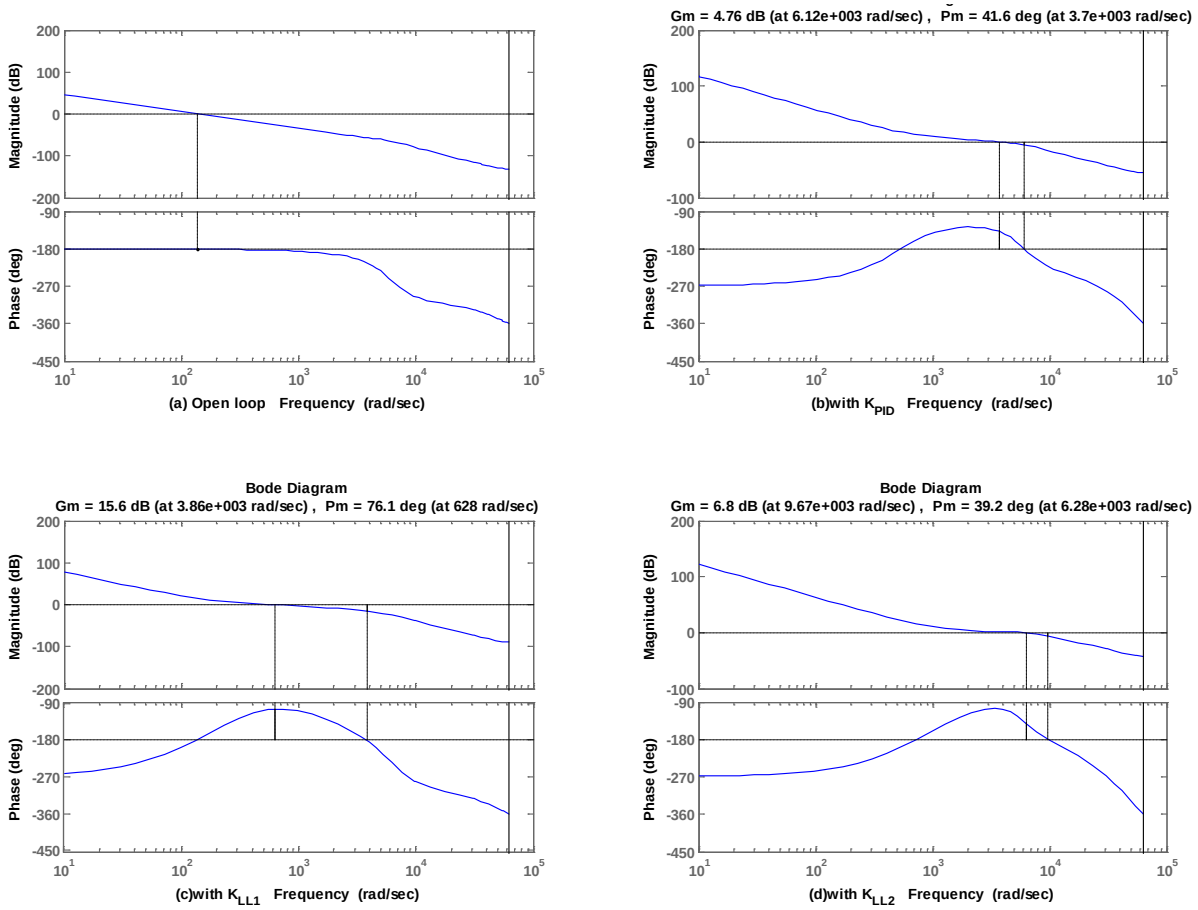

Figure 4-4 Simulations of loop function ($C \cdot P$) frequency responses

The resulted closed-loop system frequency response is shown in Figure 4-5. By placing the loop-gain crossover frequency much lower than the first mode in the open loop system around 900 Hz (combined contributions from current dynamics and mechanical resonance), K_{LL1} makes obvious difference from the other two controllers. It has the lowest peak magnitude and the highest stability margin, but it also has the lowest speed of response and

stiffness for the servo control. K_{PID} and K_{LL2} place their loop-gain crossover frequencies close to the first mode, so they both produce much larger peak magnitudes around the mode frequency as verified by experimental results in Figure 4-8, Figure 4-9 and Figure 4-10. However, there are still some differences between these two controllers.

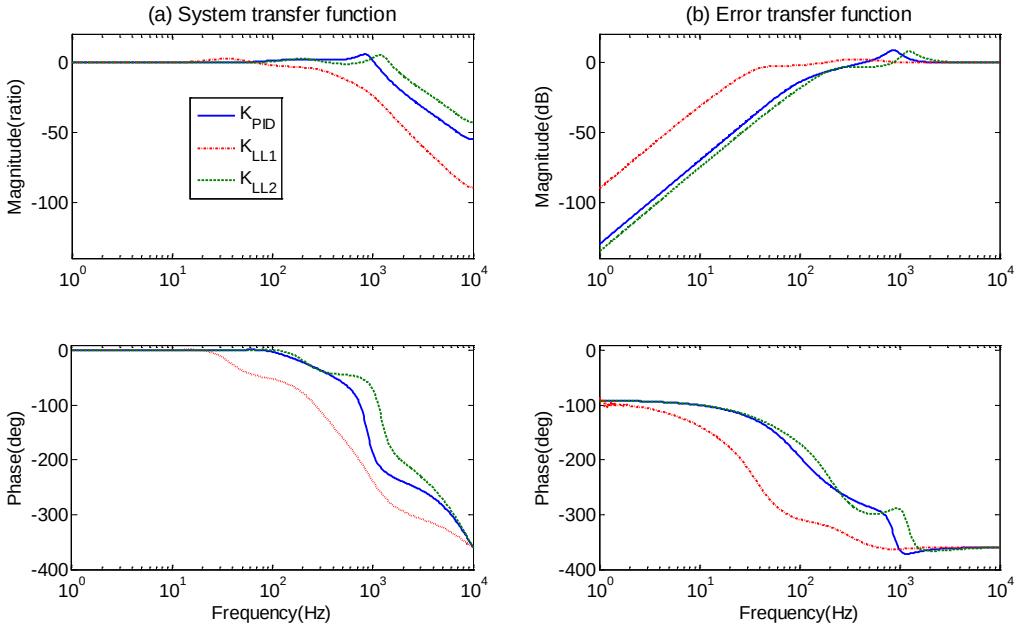

Figure 4-5 Closed loop simulations controllers with different crossover frequencies

(1) The complementary sensitivity function in Figure 4-5(a) shows the closed-loop system has a bandwidth (at -3 dB point) of 1122 Hz with K_{PID} and 1594 Hz with K_{LL2}. As a result, the response of closed-loop system with K_{LL2} will be faster, but with slightly larger magnitude peak level. These peaks were proven to be a main contributor to the surface roughness in Section 5.1.

(2) The sensitivity function in Figure 4-5(b) is a measure of the ability of the system to track commands and reject disturbances. In fact, when the closed-loop system sensitivity magnitude frequency response exceeds 0 dB, the system totally relies on the mass to reject disturbances, and the controller actually amplifies the disturbances at frequencies higher than 0 dB crossover frequency (430 Hz for the K_{PID}, 830 Hz for K_{LL2}). Below 100 Hz, the sensitivity magnitude from K_{LL2} is about half that of K_{PID}.

On the other hand, by pushing up the crossover frequency to have lower sensitivity magnitude below 1000 Hz, the system with K_{LL2} also has much higher amplification of disturbances and high-order system dynamics above 1000 Hz. In addition, since K_{LL2} has its loop-gain crossover frequency above the mode in the current dynamics around 900 Hz, it causes saturation problem in profile tracking.

(3) Since two controllers are designed based on the nominal dynamics, it is useful to check if closed-loop systems remain stable with the multiplicative error in Equation (3.8) and (3.9). The inverse of the magnitude frequency response of this error determines an upper bound on the magnitude of complementary sensitivity function T(s) in Equation (4.15) [73]. Figure 4-6 shows the magnitudes of system transfer functions stay below the uncertainty bound, but K_{LL2} pushs its magnitude close to the limit. As a common practice, the frequency response of loop function shall have adequate gain margin (GM) and phase margin (PM) for robust stability.

$$|T(s)| < \frac{1}{|\Delta_3(s)|} \tag{4.15}$$

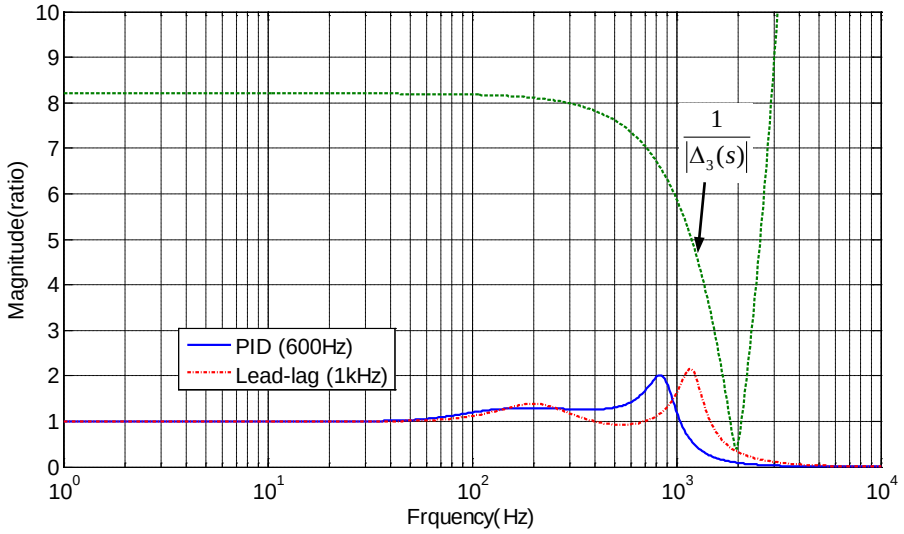

Figure 4-6 Stability robustness measure

When the mechanical resonance characteristics are know exactly and are well beyond the desired crossover frequency, they can be reduced significantly by notch filters. A discrete format for a notch filter in Equation (4.16) is suggested by [75].

$$H_{notch}(z) = b_0 \cdot \frac{1 - 2\cos\omega_m z^{-1} + z^{-2}}{1 - 2a\cos\omega_m z^{-1} + a^2 z^{-2}} \tag{4.16}$$

For example, for the resonance frequency of 2 KHz, at 20 KHz sampling rate, the parameters in the equation are selected as:

$$b_0 = 0.926180; \quad a = 0.9; \quad \omega_m = 2\pi \frac{2kHz}{20kHz} = 0.628319$$

Since the open loop system characteristics fundamentally limits the servo performance, it is desirable to improve the actuator design by using an amplifier with faster supply of current and increasing the mechanical resonance modes to a higher level. To illustrate this idea, it is supposed that there is a new amplifier with its bandwidth 2.5 times of the existing one, and no peak in the magnitude frequency response. The frequency response of system transfer function in Figure 4-7 simulates the improvement from such a change for the closed-loop system with the PID controller. This change allows higher gain without saturation, and servo stiffness and loop-gain crossover frequency can be placed at a higher level without high magnitude peak.

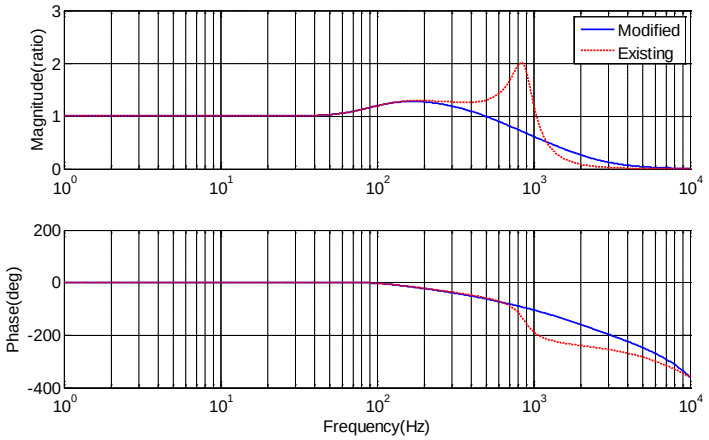

Figure 4-7 Simulation of system transfer functions with modified open loop dynamics

4.1.4 Servo Control Tests

Experiments were conducted to evaluate the servo control performance with the basic position feedback controllers.

Position holding test without cutting

In a position holding test without cutting, the dominant error source is from the disturbance due to electronic noise. Figure 4-8 shows the best results when the FLORA was mounted on a steel bench and held position at the 24.8 mm. Positioning error for the Lead-lag controller (K_{LL1}) is ±40 nm PP (10.3 nm RMS), ±40 nm PP (10.8 nm RMS) for the PID controller (K_{PID}), and ±30 nm PP (8.0 nm RMS) for the Lead-lag controller (K_{LL2}). It is clear from Figure 4-8 that the magnitudes are the smallest for frequencies less than 1 KHz in the case of K_{LL2}, but that controller has the highest magnitudes for frequencies higher than 900 Hz. The system with 100 Hz crossover frequency (K_{LL1}) has the lowest stiffness in the lower frequency range so the magnitudes below 500 Hz are the highest.

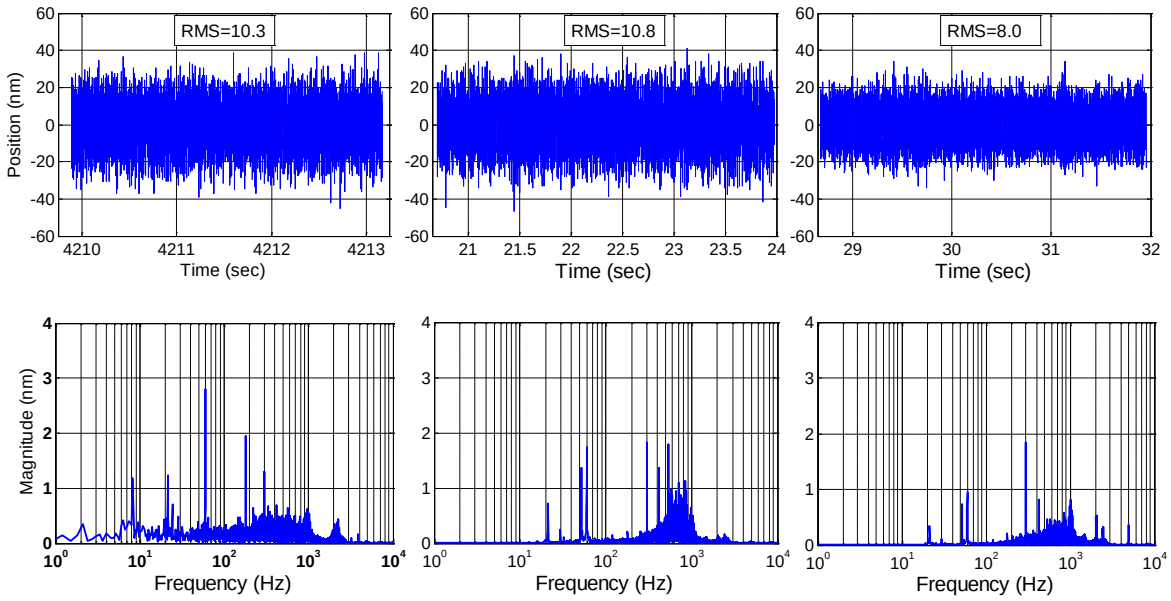

(a) K_{LL1} (b) K_{PID} (c) K_{LL2}

Figure 4-8 Position holding at 24.8 mm without cutting

Figure 4-9 shows the increased positioning error when the FLORA was mounted on the ASG-2500 x-slide stage, and all control electronics were re-packaged in the computer enclosure. Right before the flat cutting, the position is held at 17.1 mm where the piston is at the mid travel range of the air bearing. Comparing with the results in Figure 4-8, the positioning error increase 5.2 nm for K_{PID} and 5.5 nm for K_{LL2}.

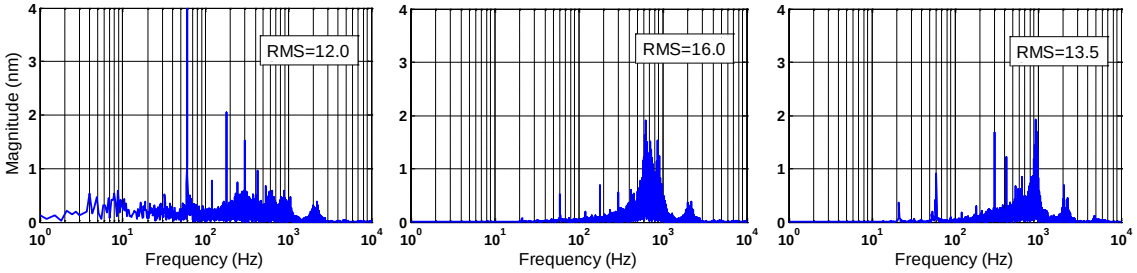

(a) K_{LL1} (b) K_{PID} (c) K_{LL2}

Figure 4-9 Frequency spectrum of position holding error without cutting

Position holding test in the flat cutting

Position data were captured when plated copper flats were machined with 0.53 mm radius tool, at a 2 μm depth of cut, 2 mm/min cross-feed rate, and 500 rpm spindle speed. In addition, the tool is held at the position of 17.1 mm. The frequency spectra and corresponding RMS positioning errors are shown in Figure 4-10.

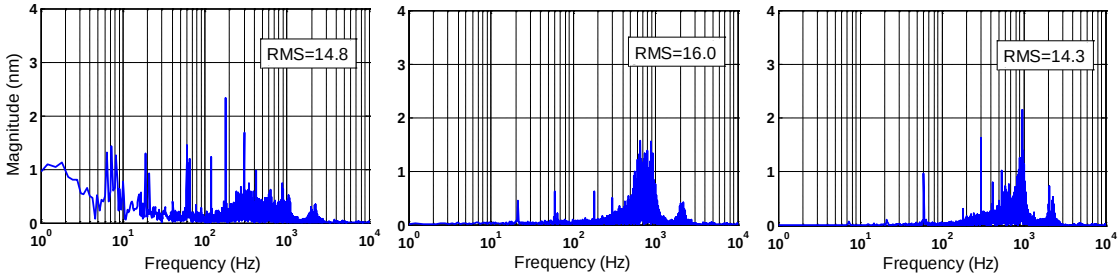

(a) K_{LL1} (b) K_{PID} (c) K_{LL2}

Figure 4-10 Frequency spectrum of position holding error in the flat cutting

A comparison of spectra with Figure 4-9 indicates that the tool-material interaction forces (cutting force and thrust force) in the finish cutting process of plated copper flat have minor impact on the tool position holding for the K_{PID} and K_{LL2}. But for the K_{LL1}, there is significant amount of amplitude increase in the low frequency range due to its low stiffness, as a result, the RMS error increases by 2.8 nm. Nevertheless, Section 5.1 shows that the controller K_{LL1} achieved best surface finish among three controllers. It can be concluded, it is essential to reduce the magnitude level above 500 Hz in the tool positioning error for good surface finish. To this end, the approach is not to lower the crossover frequency of servo system by manipulating controller design but to remove (or lower) the modes peak around 900 Hz in the open-loop physical system. It can only be done by a new design of air bearing and piston, and a new selection of linear amplifier.

Step command response

A 12.566 μm step command input is introduced into the servo system. The closed-loop system with K_{PID} in Figure 4-11(a) has a settling time of 10 ms and a overshoot of 20%. The system with K_{LL2} has larger speed of response and higher stiffness, as a result, it has smaller settling time of 6 ms and smaller overshoot of 13% in Figure 4-11(b).

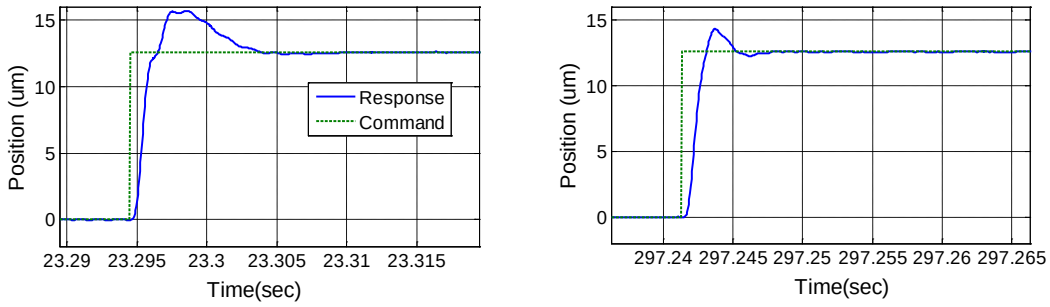

(a) K_{PID} (b) K_{LL2}

Figure 4-11 Step command response with two controllers

Step disturbance force response

0.294 N input disturbance force is introduced by attaching a 30 gram weight with a nylon string at the piston tool holder and hanging the string over a pulley. The weight is first added and then dropped. The response is only captured for the weight dropping process since it generates more consistent result, although it is not a perfect step input. Figure 4-12 shows the experimental response settles within 10 ms for the servo system with K_{PID}, which is consistent with the simulated results.

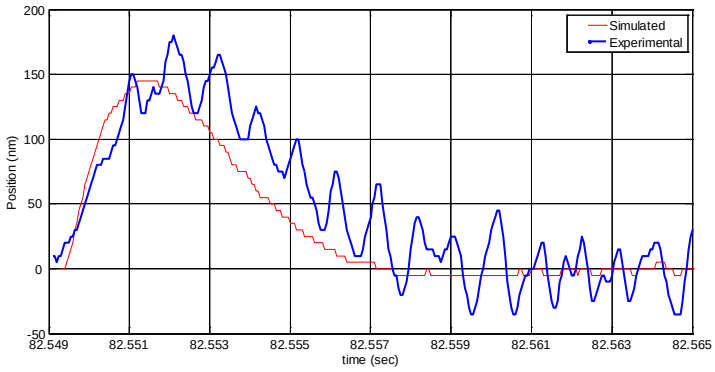

Figure 4-12 A comparison of step disturbance force response.

Sinusoidal disturbance force response

A low frequency disturbance force was introduced at the piston front end to verify the disturbance rejection capability of controllers. The measured displacement magnitude at the tested frequency 60.73 Hz are listed in Table 4.1. The sensitivity magnitude from K_{LL2} is about half that of K_{PID}, this result is consistent with the theoretical prediction.

Table 4.1 Sinusoidal disturbance force rejection for two controllers

Measurement at 60.73 Hz		No control action	K_{PID}	K_{LL2}
Magnitude (nm)	No disturbance	4	1.68	0.88
	With disturbance	164	6.89	3.6
Sensitivity gain by active control (dB)		/	-27.53	-33.17

Notch filter performance

Figure 4-13 shows the improvement on position holding from a notch filter. The frequency spectra of position data is only displayed in the range from 1500 Hz to 3000 Hz, Figure 4-13(a) is for the case that the piston is held in place by a rubber band without any control action, Figure 4-13(b) is for the case that the piston is actively held in place with the PID controller, Figure 4-13(c) is for the case that the piston is actively held in place with a combination of the PID controller and the notch filter. It can be seen that, the closed-loop system with the PID controller amplifies the peak around 2000 Hz and 2300 Hz. But a notch filter significantly reduces the controller gain around the notch frequency, so that the corresponding peak level is not increased due to the active control. The performance gain achieved by implementing a notch filter in this system is not significant, but it will be more important when the bandwidth of current dynamics increases to a level much higher than 2000 Hz.

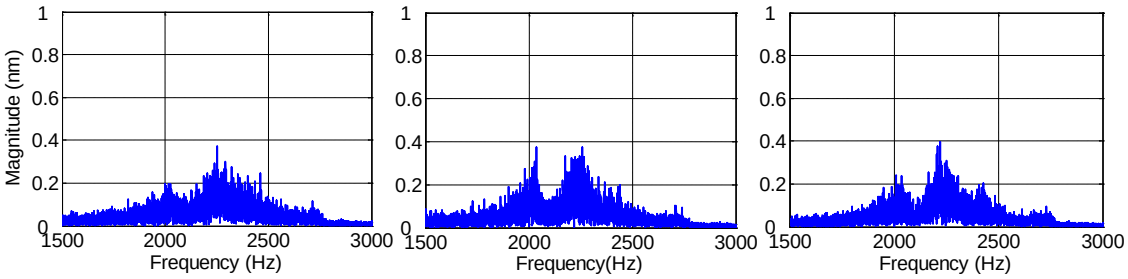

(a) A rubber band (b) PID controller (c) PID controller and notch filter

Figure 4-13 Frequency spectrum of position data when holding position

In summary, the classical position feedback controller (PID or lead-lad) improves the robustness, profile tracking and disturbance rejection of the servo control system, and provides a firm ground for other control components to be added. However, due to the inherent limitation of wide-band position feedback control approach, it is impossible to obtain ideal response across all frequency range while maintaining the stability of the closed-loop system. The capability of profile tracking and disturbance rejection is further enhanced by controllers in following sections.

4.2 Feedforward Controller

In tracking control, feedforward controller can achieve faster response because it does not act based on the measured positioning error. A feedforward controller uses various inverse dynamics techniques to design input and improve tracking performance. The main issues with these inversion techniques are nonminimum phase (system with zeros outside of the unit circle) and noncausality (the dependence of the output on the future inputs) [45]. For machining process, the causality is not a problem as the desired trajectory is known in advance. Nonminimum phase is common in digital motion control system with flexible structure. Tomizuka developed a zero-phase error tracking controller (ZPETC) for tracking control of nonminimum phase system [46-50]. It is an algorithm that cancels the poles and stable zeros while removing the phase shifts caused by uncancellable zeros. A similar concept is created in digital signal processing by decomposing the nonminimum system into a minimum-phase system and an all-pass system [75]. The basic ZPETC algorithm was modified for performance enhancement by other researchers [60-63]. An optimal solution in [61] can be used to track time-varying command profile, the adaptive ZPETC in [62] identifies the controller parameters in real time to assure performance with plant modeling error and plant parameter variations. Despite the acclaimed superior performance of these higher-order controllers, a basic form of acceleration feedforward controller (FFA) was proven to be effective in this application with mathematical simplicity.

By processing initial command input by a feedforward controller which acts as an inverse of the open/closed loop system as shown in Figure 4-14, the effective bandwidth of the overall system can be improved compared with feedback control alone. G is the actual open loop system, G_n is the nominal open loop system (by measurement), G_{cn} is the nominal system transfer function resulted from G_n and K_{pos}. The implementation format in Figure 4-14(b) is typically called as command shaping since the reference is pre-shaped by the feedforward controller before it is used as the command for the feedback control loop [45-54]. The design of this controller depends on the feedback controller, so it is less flexible than the format in Figure 4-14(a) [57-59].

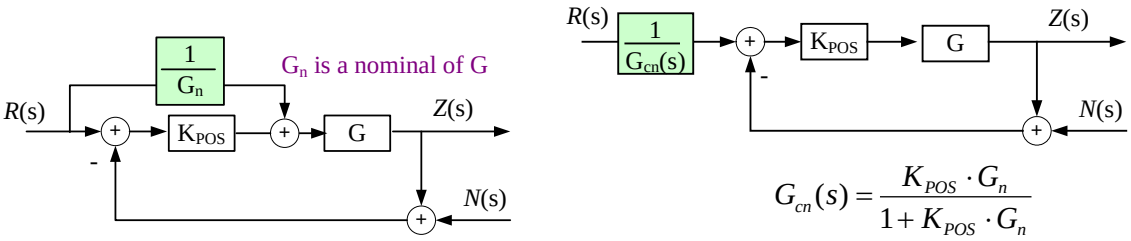

(a) from open loop system dynamics (b) from the closed-loop system dynamics

Figure 4-14 Implementation structure of the feedforward controller

Functionally, two schemes in Figure 4-14 are equivalent and have the same error transfer function S_{r1} for the profile tracking.

$$S_{R1} = \frac{1 - K_{FF} G}{1 + K_{POS} G} \tag{4.17}$$

Considering the initial definition of error transfer function for profile tracking without feedforward controller

$$S = \frac{1}{1 + K_{POS} G} \tag{4.18}$$

Take the feedforward controller K_{FF} in the form of

$$K_{FF} = \frac{1}{G_n} \tag{4.19}$$

Two error transfer function for profile tracking has a simple relationship

$$S_{R1} = S \cdot (1 - K_{FF} G); \tag{4.20}$$

The simplest design of feedforward control law is an acceleration feedforward controller, $K_{FFA}(s)$. It is done by ignoring all high-frequency dynamics (current and mechanical) to obtain the simplest open loop transfer function from the command current input to the position output in continuous time domain (Laplace domain)

$$G_{n2}(s) = \frac{\hat{K}_f}{\hat{m}s^2} \tag{4.21}$$

where $\hat{K}_f$ is the estimated motor force constant, $\hat{m}$ is the estimated moving mass. The acceleration feedforward controller is taken as the inverse of $G_{n2}(s)$.

$$K_{FFA}(s) = \frac{1}{G_{n2}(s)} = \frac{\hat{m}}{\hat{K}_f} s^2 \tag{4.22}$$

The function of Equation (4.22) can be explained as follows. By only considering the moving mass dynamics, the equation of motion for the FLORA in Laplace form is

$$\hat{m}s^2 Z(s) = \hat{K}_f \cdot U(s) + D(s) \tag{4.23}$$

where $Z(s)$ is the position, $U(s)$ is the control effort, and $D(s)$ is the disturbance. For the tracking error $E(s)$ defined as the difference between the position command $R(s)$ and the actual position $Z(s)$.

$$E(s) = -\frac{\hat{K}_f}{\hat{m}s^2} \cdot U(s) + \frac{1}{m} \cdot D(s) + R(s) \tag{4.24}$$

As a part of the total control effort $U(s)$, the output from the acceleration feedforward controller $U_{FFA}(s)$ generates the control effort required for the desired acceleration.

$$U_{FFA}(s) = K_{FFA}(s) \cdot R(s) \tag{4.25}$$

As a result, the command trajectory term $R(s)$ in Equation (4.24) is cancelled out, the tracking control becomes a regulation task in Equation (4.26). It means that, with perfect feedforward controller, the servo system only needs to consider the disturbance rejection.

$$E(s) = -\frac{\hat{K}_f}{\hat{m}s^2} \cdot U(s) + \frac{1}{\hat{m}} \cdot D(s) \tag{4.26}$$

The term s^2 in Equation (4.22) is to take double-derivative of the desired position motion path $R(s)$. For arbitrarily shaped reference trajectories, there is no analytical expression. Implementation of acceleration controller needs to take a discrete format.

$$K_{FFA}(z) = \frac{\hat{m}}{\hat{K}_f}\left(\frac{1}{T_s^2}\frac{z^2 - 2z + 1}{z}\right) \tag{4.27}$$

Equation (4.27) does not introduce any phase distortion in the calculation of acceleration command from the position command. Because the high sampling rate (i.e. 20 KHz) amplifies the errors in the position command when deriving acceleration command from the position command, the desired acceleration profile is normally generated off-line to avoid the measurement noise issue in the position trajectory in real time. Furthermore, it is also critical to use small position step (or mesh grid) to minimize the quantization errors in the acceleration profile.

A simulation of error transfer functions in Figure 4-15 shows the enhancement for trajectory tracking with the K_{FFA}. The dashed-line in Figure 4-15 has much lower error magnitude in low frequency range, about 33 dB (44.7 times) for frequencies below 100 Hz in the simulation. The zero-crossing frequency also increases from 430 Hz to 610 Hz.

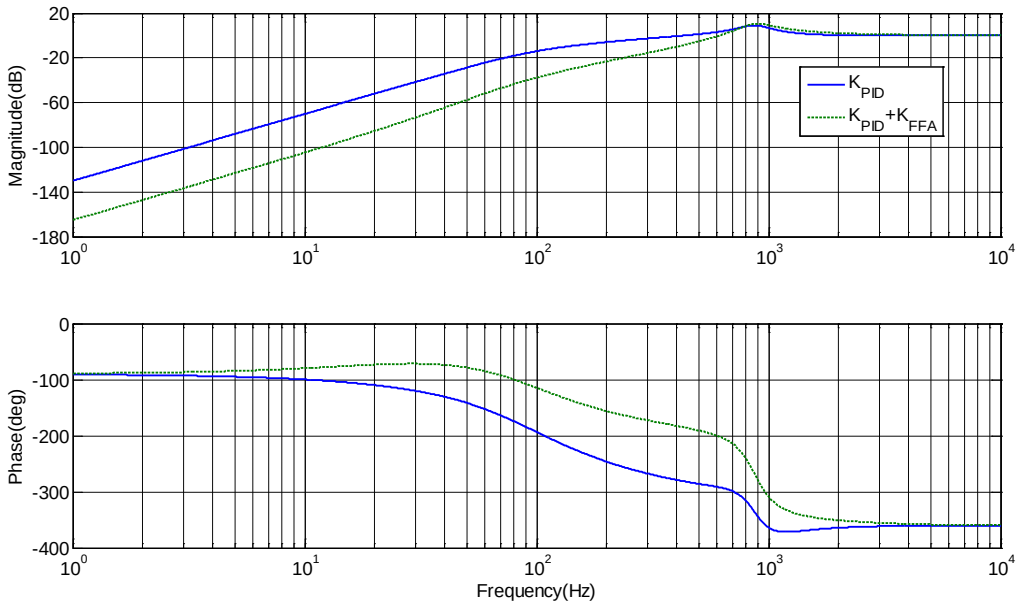

Figure 4-15 Simulation of the error transfer function for motion system

Figure 4-16 shows the positioning error in a test of sinusoidal profile tracking at the amplitude of 2 mm and the frequency of 20 Hz. In this test, the maximum velocity is 251 mm/s, and the maximum acceleration is about 31 m/s^2. A combination of PID and acceleration feedforward controller is used. The tracking error in Figure 4-16(a) is within ±160 nm. The frequency spectrum in Figure 4-16(b) shows the tracking error has significant magnitudes at the harmonics of fundamental frequency (20 Hz). For example, the magnitude at 20 Hz is about 100 nm. With PID control only, the error magnitude at 20 Hz is 5 μm for the same tracking test, so the acceleration feedforward control gives 50 times reduction on the fundamental frequency tracking performance

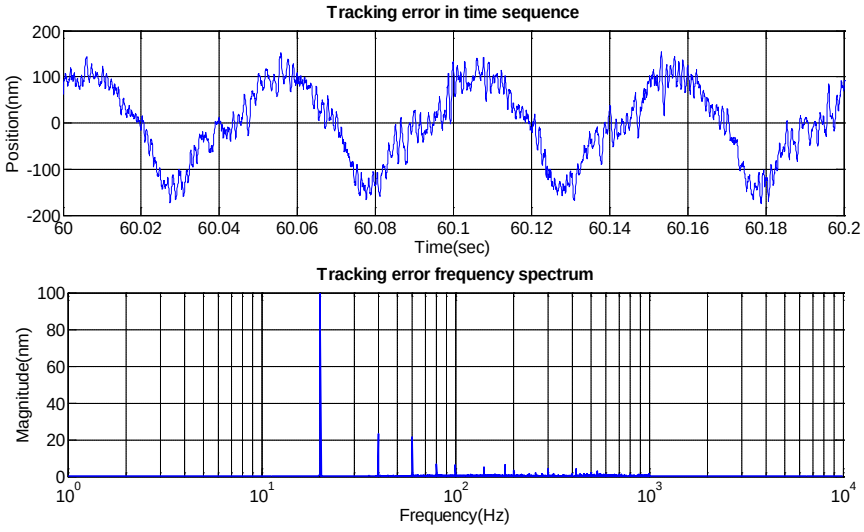

Figure 4-16 2mm 20 Hz sinusoidal tracking test with FFA and PID controller

Theoretically, a further improvement of tracking performance over acceleration feedforward control is possible by implementing the inverse of higher order model for the open loop dynamics at the cost of more computational time. In the extreme case, the entire measurement points of system frequency response can be kept to build an inverse dynamics filter instead of using reduced-order modeling, this is only feasible with off-line deconvolution technique [12].

As an example, take the fourth-order model $G_{n1}(s)$ in Equation (3.7), and apply zero-order hold (ZOH) digital-to-analog conversation process to obtain the discrete transformation.

$$G_{n1}(z) = \frac{0.0000011728 \cdot z^{-1}(1+4.038z^{-1})(1-0.5105z^{-1})(1+0.2996z^{-1})}{(1-z^{-1})^2(1-1.671z^{-1}+0.7514z^{-2})} \tag{4.28}$$

In Equation (4.28), there is a zero at -4.038 outside of unit circle, a new feedforward controller in Equation is derived using ZPETC method.

$$K_{FF}(z) = \frac{z(1-z^{-1})^2(1-1.671z^{-1}+0.7514z^{-2})}{0.0000011728(1-0.5105z^{-1})(1+0.2996z^{-1})}\frac{(1+4.038z)}{(1+4.038)^2} \tag{4.29}$$

However, it provides little improvement over the acceleration feedforward controller in the 2 mm 20 Hz sine wave tracking test. This indicates the second-order model for feedforward controller already obtains the achievable performance for this type of controller. The effectiveness of the simplest feedforward controller attributes to the winning features in the device design such as no major hysteresis, no passive stiffness and no physical damping. As a result, in the development cycle of design/control interactions, the physical design is always fundamental to achieve desirable performance for the servo control of tool motion.

Despite the enhancement of profile tracking by a feedforward controller, it is never a replacement of feedback controller [64]. Even with the deconvolution technique in [12], there are still modeling errors (and uncertainties) in the identification process, so it is impossible to completely cancel out the commanding trajectory term $R(s)$ in Equation (4.22). In addition, this type of feedforward control approach does not provide any control stiffness in the presence of disturbances.

4.3 Adaptive Feedforward Controller

4.3.1 The Principle of Adaptive Feedforward Controller

In many precision motion control applications, it is common to see periodic signals in trajectories or disturbances, repetitive control can be applied to further improve control performance on profile tracking and disturbance rejection. This category of control approach is developed based on the internal model principle [73, 96, 104], which augments the open loop dynamics with signal models for trajectories or disturbance as if they are part of open loop system. The underlying property is that, a linear feedback control system has perfect tracking and disturbance rejection at a certain frequency when the controller has infinite gains at that frequency. For a sinusoidal signal, it requires the controller have poles at the corresponding frequency.

For the tool servo control in the diamond turning, both motion trajectory and disturbance have significant magnitudes at first few harmonics of spindle rotational frequency. A special type of repetitive control, Adaptive Feedforward Controller (AFC) [95-109] is used for this purpose. Each element (resonator) of the AFC only acts on a single frequency, driven by the estimated spindle speed. Figure 4-17 shows the block diagram of AFC. The sinusoids are generated outside of the basic feedback control loop, the coefficients of cosine and sine are estimated adaptively based on the error signal, and the weighted sinusoids are then combined to produce a control signal with required amplitude and phase to remove the error at selected frequencies.

The variables g_n and ϕ_n are the controller parameters to be tuned. It has been proven that the transfer function from the error to the output in Figure 4-17(b) has a linear-time-invariant (LTI) equivalence in Equation (4.30) [4, 95, 96]. The complete AFC in Figure 4-17(a) contains multiple basic elements connected in parallel, the total control effort is a summation of individual output. The AFC algorithm is also called Harmonic Control in [106, 107] and Higher Harmonic Control in [108, 109], where it is used to compensate multiple rotation harmonics in a rotor system.

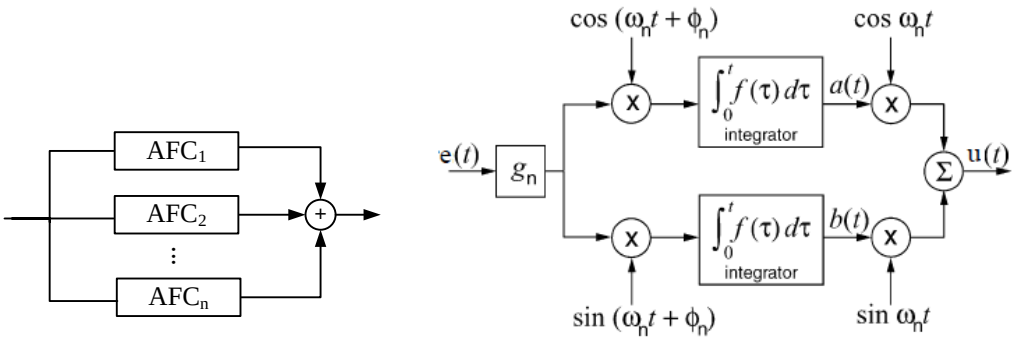

(a) Complete structure (b) Basic AFC element [4]

Figure 4-17 Block diagram of adaptive feedforward controller

$$K_{AFCn} = g_n \frac{s\cos\phi_n + \omega_n \sin\phi_n}{s^2 + \omega_n^2} \tag{4.30}$$

Since the AFC has large equivalent gain at the selected frequency but very small gain elsewhere, it is typically combined with other controllers in Section 4.1 and 4.2 for implementation due to the broad-band frequency components in actual system. When the AFC (K_{AFC}) is integrated with the wide-band position feedback controller (K_{POS}), there are three implementation schemes as shown in Figure 4-18. The selection of controller parameters in the parallel implementation shown in Figure 4-18(a) was done by trial and error [7, 100]. In Figure 4-18(b), adding a parallel feedthrough term with the AFC in the serial implementation increases the convergence rate and robustness, ϕ_n is also chosen as the phase of open loop system transfer function at the specific frequency to further enhance stability robustness and convergence rate [96, 97]. Lu elaborates the selection of controller parameters in the serial implementation by integrating the design of AFC with a lead-lag controller [5]. The outer loop structure in Figure 4-18(c) is implemented using Nyquist technique to determine the control gain and the phase advancement for single and multiple AFC elements [4, 8, 95] at the selected frequencies, but it has the problem of very low controller gain at frequencies other than those selected discrete frequencies. The parallel implementation structure is selected in this research for its conceptual simplicity by adding

additional controller gains at the selected frequencies. The control approach is analyzed and explicit guideline is provided for the selection of controller parameters.

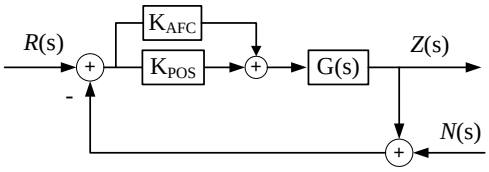

(a) Parallel implementation

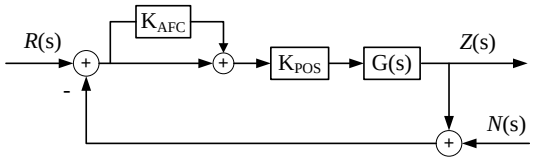

(b) Serial implementation

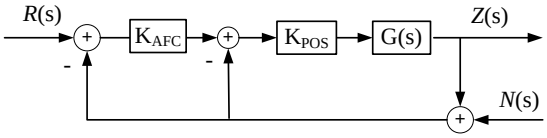

(c) Outer loop implementation

Figure 4-18 Integration of AFC with wide-band position feedback controller

4.3.2 Analysis of AFC at Single Frequency

In this study, the AFC uses an integrative adaptation law to estimate the coefficients of cosine and sine based on the error signal [7].

$$U_F^{\omega}(n+1) = U_F^{\omega}(n) + \alpha A_F^{\omega} E_F^{\omega}(n+1) \tag{4.31}$$

where n is the time index, U_F^{ω}, E_F^{ω}, and A_F^{ω} are the control signal, the modulated error signal, system inverse, respectively at a selected frequency ω. Hence, E_F^{ω} is to be minimized by adapting U_F^{ω}. The parameter α is a convergence coefficient which is tuned to maximize the convergence rate while guaranteeing stability. The modulated error signal is calculated using the following complex reference signal

$$E_F^{\omega}(n) = e(t)e^{-i\omega t} \tag{4.32}$$

where $e(t)$ is the measured position error in the time domain, taken as the difference between position command r(t) and measured position z_m(t). The final control output $u_{AFC}(t)$ in the time domain is obtained as

$$u_{AFC}(t) = 2\,\mathrm{Re}\left(U_F(n)e^{\mathrm{i}\omega t}\right) \tag{4.33}$$

The function Re(·) is the real part operator. The block diagram for the proposed feedback control with a parallel implementation of AFC and K_{POS} is in Figure 4-19.

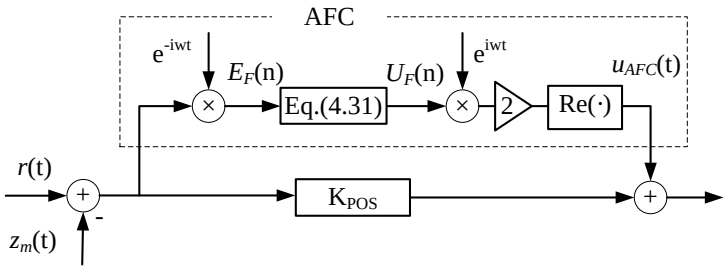

Figure 4-19 Feedback controller with a combination of AFC and K_{POS}

To provide guideline in the determination of convergence coefficient α, a transformation of the original block diagram is taken in Figure 4-20.

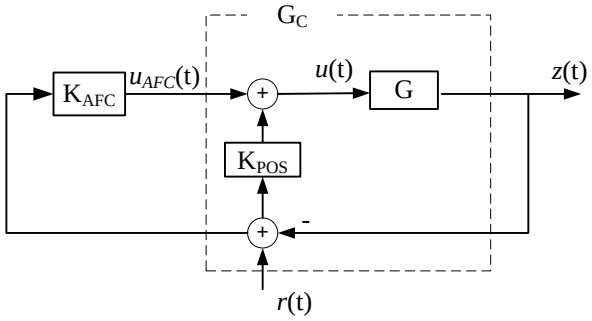

Figure 4-20 Transformed diagram for feedback system

In the perspective of Figure 4-20, the additional control effort $u_{AFC}(t)$ from AFC is output to the inner closed-loop system with a K_{POS} only. *Gc* is the actual transfer function from u_{AFC} (t) to $z(t)$ for the inner loop.

$$G_C(s) = \frac{G(s)}{1 + K_{POS} G(s)} \tag{4.34}$$

The sensitivity function for the profile tracking is

$$S_{R2}(s) = \frac{1}{1 + K_{AFC}(s) G(s)} \cdot \frac{1}{1 + K_{POS}(s) G_C(s)} \tag{4.35}$$

The design of harmonic controller is dependent on the inner closed-loop. Let G_{cn} be a nominal term of *Gc*, then, at the selected frequency ω

$$G_{cn}(i\omega) = A_C e^{i\phi} \tag{4.36}$$

where *AC* and ϕ are nominal magnitude and phase derived from the frequency response. The following equation is derived based on Equation (4.31)

$$U_F(n+1) = U_F(n) + \alpha G_{cn}^{-1}(i\omega)\left(R(n+1) - U_F(n) G_C(i\omega)\right) \tag{4.37}$$

Apply Z-transformation to Equation (4.37),

$$U_F(z) = \frac{z G_{cn}^{-1}(i\omega)}{z - 1 + \alpha G_{cn}^{-1}(i\omega) G_C(i\omega)} R(z) \tag{4.38}$$

To have a bounded control effort (or stable system), the pole of the Equation (4.38) must remain in the unit circle

$$|z| = \left|1 - \alpha G_{cn}^{-1}(i\omega) G_C(i\omega)\right| < 1 \tag{4.39}$$

If

$$G_{cn}^{-1}(i\omega) G_C(i\omega) \approx 1 \tag{4.40}$$

Then

$$0 < \alpha < 2 \tag{4.41}$$

Practical selection of α is usually more stringent than derived above. If there is a small amount of uncertainty of the nominal transfer function at the selected frequency, then

$$G_{cn}^{-1}(i\omega)G_C(i\omega) = a + bi \tag{4.42}$$

where *a* is close to 1 and $|b|<<1$. Figure 4-21 shows the vector of the pole in the *z*-plane. It is desirable to have the pole on the positive real axis in the range of (0, 1) for fast convergence performance: the closer to zero, the higher the convergence rate. Correspondingly, the α shall be in the range of (0, 1): the closer to one, the higher the convergence rate. However, when α approaches the value of one, the vector approaches the unit circle, and the stability margin reduces. The harmonic control then becomes sensitive to the phase error between the actual phase and nominal phase for the inner closed-loop system. On the other hand, having the pole on the positive real axis also means the exact cancellation of phase error at the selected frequency, which provides the maximum phase margin of 90°.

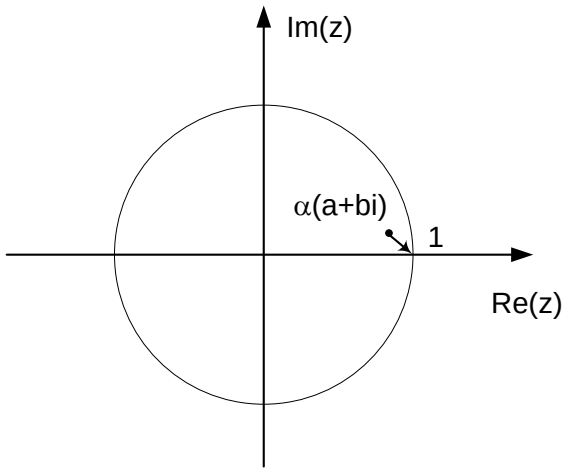

Figure 4-21 The pole in the z-plane

To derive the discrete time LTI equivalent of this algorithm, Equation (4.33) is re-written as a summation of a conjugate pair with T_S as the sampling interval in second

$$u_{AFC}(n) = 2\,\mathbf{Re}\left(U_F(n)e^{\mathrm{i}\omega nT_S}\right) = U_F(n)e^{\mathrm{i}\omega nT_s} + \overline{U}_F(n)e^{-\mathrm{i}\omega nT_S} \tag{4.43}$$

And u_{AFC}(n) is also a summation of two variables u_1(n) and u_2(n) with

$$u_1(n) = U_F(n)e^{\mathrm{i}\omega nT_S}; \qquad u_2(n) = \overline{U}_F(n)e^{-\mathrm{i}\omega nT_S} \tag{4.44}$$

Based on the update law in Equation (4.31),

$$\begin{aligned} u_1(n+1) &= e^{\mathrm{i}\omega(n+1)T_S}U_F(n+1) \\ &= e^{\mathrm{i}\omega(n+1)T_S}\left(U_F(n) + \alpha A_F E_F(n+1)\right) \\ &= e^{\mathrm{i}\omega(n+1)T_S}\left(u_1(n)e^{-\mathrm{i}\omega nT_S} + \alpha A_F e(n+1)e^{-\mathrm{i}\omega(n+1)T_S}\right) \\ &= e^{\mathrm{i}\omega T_S}u_1(n) + \alpha A_F e(n+1) \end{aligned} \tag{4.45}$$

$$\begin{aligned} u_2(n+1) &= e^{-\mathrm{i}\omega(n+1)T_S}\overline{U}_F(n+1) \\ &= e^{-\mathrm{i}\omega T_S}u_1(n) + \alpha\overline{A}_F e(n+1) \end{aligned} \tag{4.46}$$

Apply Z-transformation to Equation (4.45) and (4.46),

$$U_1(z) = \frac{\alpha A_F z}{z - e^{\mathrm{i}\omega T_S}}E(z); \qquad U_2(z) = \frac{\alpha\overline{A}_F z}{z - e^{-\mathrm{i}\omega T_S}}E(z) \tag{4.47}$$

As a result,

$$\begin{aligned} U(z) = U_1(z) + U_2(z) &= \left(\frac{\alpha A_F z}{z - e^{\mathrm{i}\omega T_S}} + \frac{\alpha\overline{A}_F z}{z - e^{-\mathrm{i}\omega T_S}}\right)E(z) \\ &= \frac{2\alpha}{A_C}\frac{z^2\cos(\phi) - z\cos(\omega T_s - \phi)}{z^2 - 2z\cos(\omega T_s) + 1}E(z) \end{aligned} \tag{4.48}$$

The transfer function form of AFC is

$$K_{AFC} = \frac{2\alpha}{A_C}\frac{z^2\cos(\phi) - z\cos(\omega T_s - \phi)}{z^2 - 2z\cos(\omega T_s) + 1} \tag{4.49}$$

.

4.3.3 Design and Test of AFC

The equivalence of the AFC and the internal model transfer function allows linear system techniques such as loop shaping to be used to analyze the performance of control system with AFC. While the bound of coefficient α is determined to be within (0, 1) in Section 4.3.2, the final selection of α value needs to maximize the convergence rate without sacrificing the loop gain cross-over frequency and stability robustness (gain margin and phase margin) resulted from the closed-loop system with K_{POS} only. To understand this tuning process, the frequency response of feedback controller (PID, AFC and a combination) is given in Figure 4-22 and Figure 4-23. The operation frequency of the AFC is at 20 Hz. α is chosen to be 0.001 in Figure 4-22 and α is 0.1 in Figure 4-23. It can be seen that, with a good selection of α value, the AFC has little influence on feedback controller frequency response other than in the vicinity of the selected frequency. As a result, adding the AFC does not change the loop gain cross-over frequency and stability margin of the closed-loop system with K_{PID} only. However, when α increases to a large value, 0.1, the closed loop system is no longer stable.

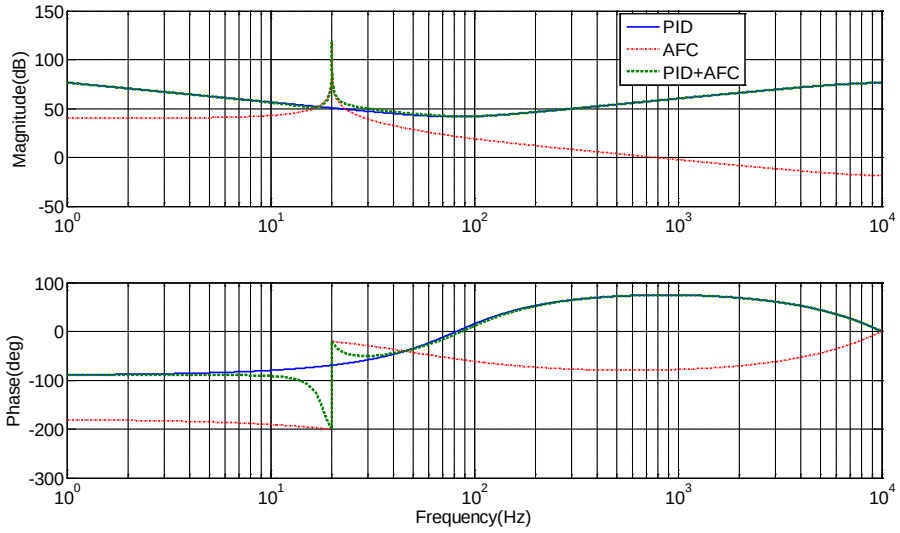

Figure 4-22 Frequency response of feedback controller (AFC: α=0.001)

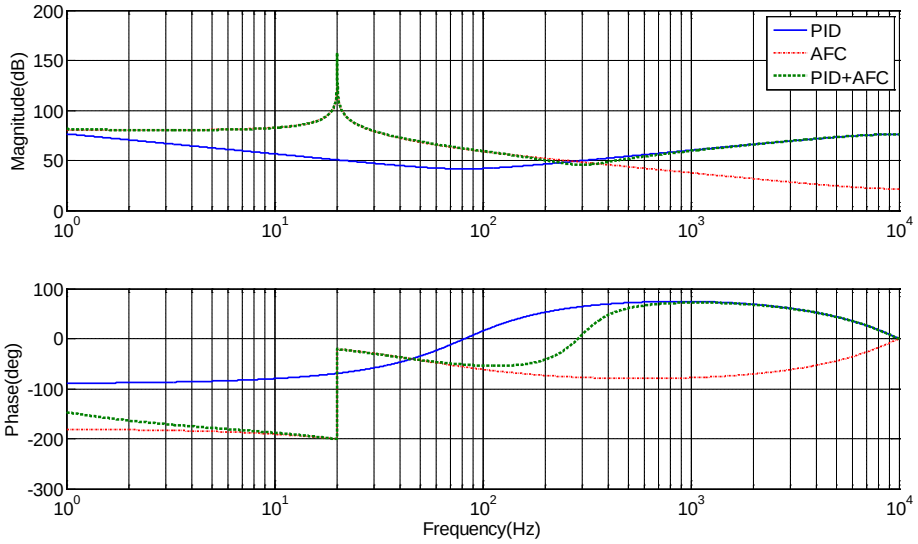

Figure 4-23 Frequency response of feedback controller (AFC: α=0.1)

Figure 4-24 shows a simulation of the frequency response for the error transfer functions of the closed-loop system with PID, FFA and AFC. The notch at 20 Hz for the magnitude frequency response means the positioning error at 20 Hz either due to the disturbance force and tracking profile can be further reduced. More specifically, comparing with the close-loop system with PID controller only, the change from dotted line (PID) to dashed line (AFCPID) shows the improvement for disturbance rejection with the addition of AFC. The change from the dotted line (PID) to the solid line (AFCFFAPID) shows the improvement of profile tracking with the addition of FFA and AFC.

Figure 4-25(a) shows the tracking profile of biased cosine wave with 2 mm amplitude and 20 Hz frequency is introduced at the time instant of 2 second, it takes less than 0.01 second for the tracking error reduces to the range of ±100 nm in Figure 4-25(b). The steady state tracking error within the range of ±70 nm in Figure 4-25(c) is only 0.0035% of the position command, when the error magnitude at 20 Hz is removed as shown in Figure 4-25(d). Note that, without AFC, the error magnitude is about 100 nm in Figure 4-16.

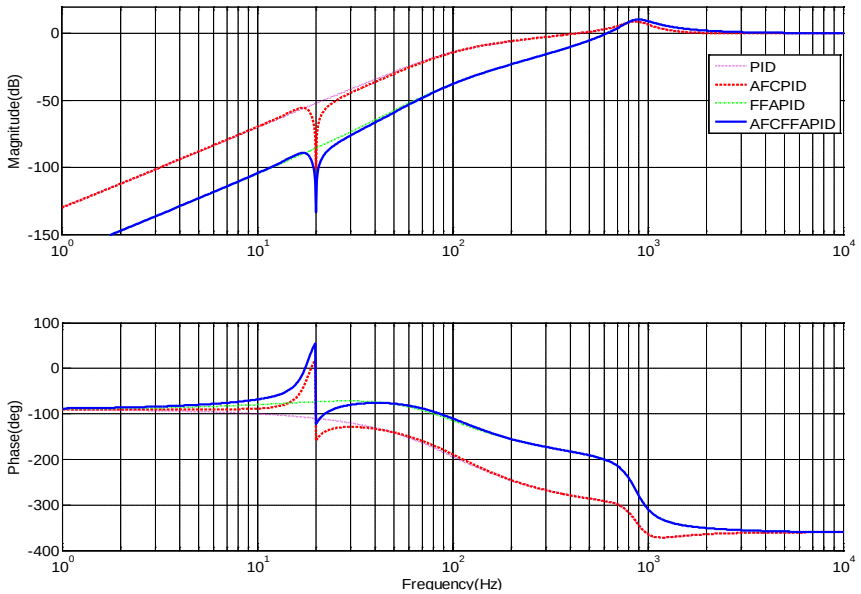

Figure 4-24 Simulation of the error transfer function for motion system

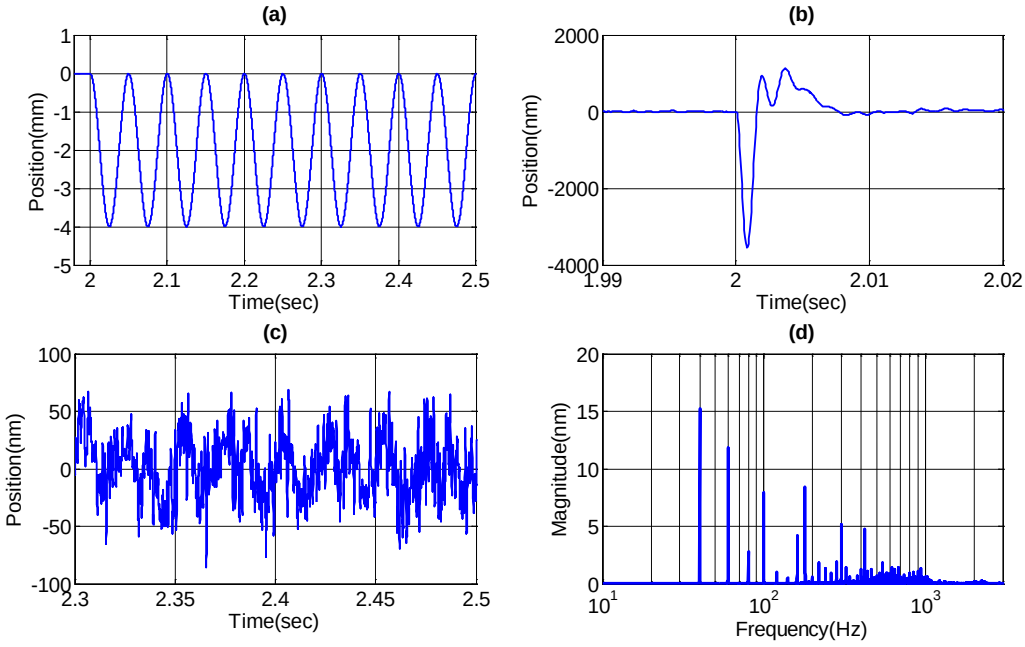

Figure 4-25 2 mm 20 Hz sinusoidal tracking test with PID, FFA and AFC (a) Tracking profile (b) Tracking error in transient steady state (c) The steady state tracking error (d) The frequency spectrum of tracking error

The criterion of tuning the convergence coefficient α can be extended to the AFC with multiple elements. Figure 4-26 shows the cases of two (20 & 40 Hz) and three elements (20, 40 & 60 Hz), α is 0.001 for both cases. The 2 mm 20 Hz sinusoidal tracking tests were carried out at different time after the control electronics was repackaged, so the baseline noise levels are different. The tracking errors with different AFC are shown in Figure 4-27. With three AFC elements, the RMS tracking error reduces to 27.7 nm. This is in comparison to the 16.0 nm RMS position error in the regulation control when holding position at 17.1 mm in Figure 4-9. A further reduction of tracking error by removing error magnitude at higher harmonics is theoretical possible but very computationally costive.

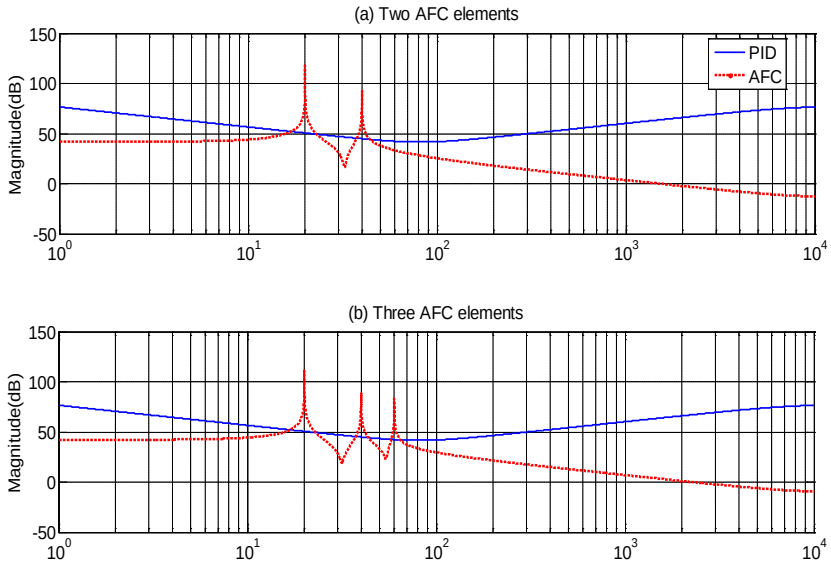

Figure 4-26 Frequency response of multiple-element AFC

Although the AFC and the internal model method are functional equivalent, and the transfer function in Equation (4.49) takes much less computational effort, the explicit AFC is claimed to be a better implementation. Equation (4.49) places poles in the vicinity of unity circle in the z-plane, it is very sensitive to the numerical errors in implementation. Most of all, on the DTM, the spindle speed does not stay at a constant value, and there is larger error in the estimation of the speed than that of the position, the internal model method is less

robust to the perturbations in the actual frequencies, while the calculation of soinsoids for the AFC can be easily synchronized with the angular position. DSP code of the AFC with the basic position feedback controller and acceleration feedforward controller is listed in Appendix F.3. In conclusion, the AFC is the best for a motion system with a few pronounced harmonics in the error signal.

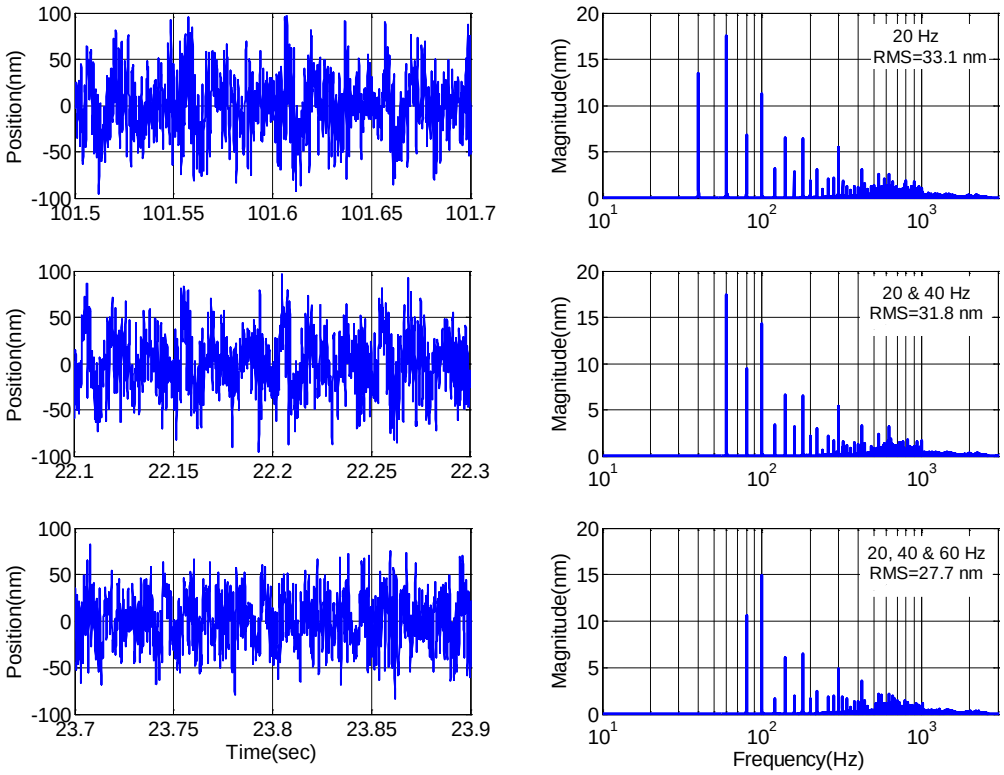

(a) Tracking error (b) Frequency spectrum of tracking error

Figure 4-27 2 mm 20 Hz sinusoidal tracking test with multiple AFC elements

4.4 Disturbance Estimation

For the tool motion in the machining process, the disturbance forces to the moving mass have periodic component synchronized with the spindle rotation and non periodic component concentrated in the low-frequency range. Since there is no passive stiffness and damping for the FLORA, the dynamic stiffness of the servo system comes from the controller and the mass. For a closed-loop feedback control system as shown in Figure 4-1, the transfer function from the disturbance force D(s) to the tool position output Z(s) is

$$M = \frac{P}{1 + C \cdot P} \tag{4.50}$$

The numerator term in Equation (4.50) is the dynamics of moving mass. Without physical stiffness and damping, it is

$$P(s) = \frac{1}{ms^2} \tag{4.51}$$

The sensitivity of disturbance rejection is an inverse function of the mass. When the moving mass of tool holder is reduced to increase the bandwidth of the servo system and reduce the reaction force, i.e. 250 lb for DTM z-slide vs. 665 grams for the FLORA, the motion system becomes much more sensitive to the disturbance. Figure 4-5(b) shows that, when the magnitude of sensitivity function frequency response for the closed-loop system exceeds 0 dB, the motion system totally relies on the mass to reject disturbances, and the controller actually amplifies the disturbances at frequencies higher than 0 dB crossover frequency. A further reduction of the mass (down to 200-300 grams) and physical size (down to ¼) is feasible only if the following requirement can be satisfied

(1) Maintain or even increase the stiffness of sliding piston and air bearing with a new design (Section 2.1).

(2) Reduce the error in the force generation with a new type of linear motor such as VCM and a power amplifier with less electronic noise (Section 2.2 and 2.3).

(3) Apply a more effective control approach to compensate the loss of disturbance rejection capability in the low frequency range due to the reduction of mass.

For the machining application, it is easy to implement a feedforward controller for trajectory tracking since the motion profile is known ahead of time. However, this approach is not possible for disturbance rejection since most of disturbances from various physical sources cannot be predicted, and they are technically or economically not measurable. Nevertheless, the actual disturbances can be estimated from a disturbance observer, and the estimate can then be utilized as a cancellation signal. Figure 4-28 shows the Disturbance Observer (DOB) in the dashed square box proposed by a number of researchers [46, 49, 54-56, 58, 60, 112-118]. The basic principle is to take the difference between the commanded force and the estimated force to the motion system, and adjust current force command by this difference.

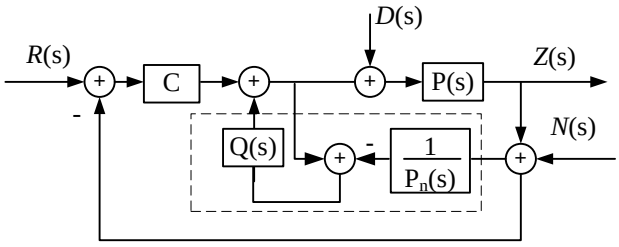

Figure 4-28 FLORA feedback control system diagram with DOB

The force to the motion system is estimated by filtering the measured position with the inverse of P_n(s). P_n(s) is the estimated model of actual tool holder dynamics P(s).

$$P_n(s) = \frac{1}{\hat{m}s^2} \tag{4.52}$$

Q(s) is a low-pass filter to make DOB practically realizable. The DOB adds an inner control loop to the closed-loop system with position feedback controller (K_{POS}). The effectiveness of this approach depends on several factors. First, the sampling rate needs to much higher than the disturbance frequency of interest. For example, the difference in a disturbance at a

frequency less than 400 Hz sampled at 20 KHz is negligible for 2 continuous samples. Therefore, the estimated disturbance force from the last sampling can be used in control output adjustment in the current sampling interval. Second, the estimated model P_n(s) needs to be as close to the actual system P(s) as possible. Third, the design of Q(s) shall ensure the rejection of disturbance at low frequencies while attenuating the sensor noise at high frequencies and obtaining the stability of inner loop.

The new transfer function from the disturbance force D(s) to the tool position output Z(s) with the addition of disturbance estimation is

$$\frac{Z(s)}{D(s)} = \frac{P(s)P_n(s)(1-Q(s))}{P_n(s)+Q(s)(P(s)-P_n(s))+C\cdot P(s)P_n(s)} \tag{4.53}$$

If P_n(s) ≅ P(s)

$$\frac{Z(s)}{D(s)} \approx (1-Q(s))\frac{P(s)}{1+C\cdot P(s)} = \begin{cases} = 0 & for\ \ Q=1 \\ = \dfrac{P(s)}{1+C\cdot P(s)} & for\ \ Q=0 \end{cases} \tag{4.54}$$

Equation (4.54) indicates that when the P_n(s) is very close to the P(s), within the bandwidth of Q(s), the disturbance induced position error is very close to the zero. However, there is definitely some time delay in the estimation process based on the position feedback signal. To further improve the disturbance rejection, a different type sensor such as a force dynamometer or an accelerometer for feedback can provide faster and more direct information about the disturbances so the control system can react faster to cancel the disturbance [38, 51, 55, 120-122]. In fact, a stiff servo controller makes a motion system to be an acceleration (force) control system.

A design of DOB is taken with Q(s) selected as follows

$$Q(s) = \frac{1}{\hat{K}_f}\cdot\frac{\omega_n^2}{s^2+2\xi\omega_n s+\omega_n^2} \tag{4.55}$$

where $\hat{K}_f$ is the estimated motor force constant. Figure 4-29 shows a simulation of disturbance transfer function frequency response with the mass only (no control action), with PID controller, and with a combination of PID controller and DOB. When the Q(s) has a damping ratio ξ of 0.7 and natural frequency ω_n of 200 Hz, the disturbance rejection sensitivity magnitude at 20 Hz moves from -72.5 dB (PID) to -89.4 dB (PID+DOB), this is about 7 times improvement for disturbance rejection at 20 Hz.

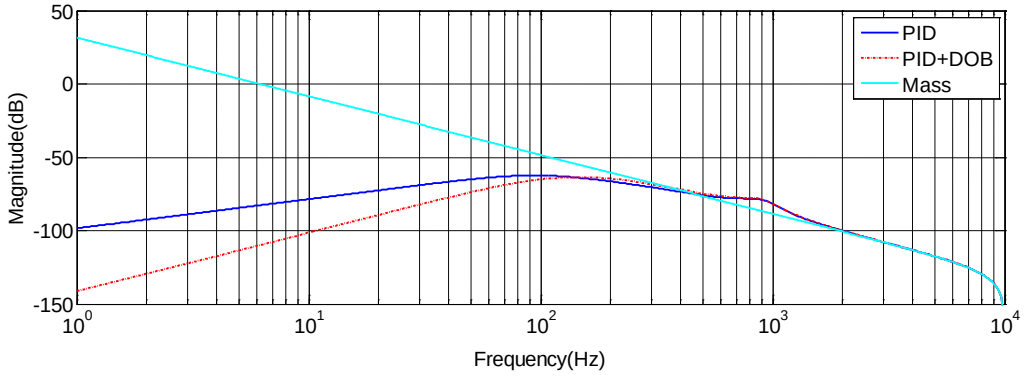

Figure 4-29 Comparison of disturbance rejection transfer function frequency response

The simulation result is verified by tests of sinusoidal disturbance force rejection at 1 N amplitude and 20 Hz frequency. By adding the DOB, the peak-to peak value of position oscillation under the disturbance in Figure 4-30 reduces by 3 times, and the error magnitude at 20 Hz reduces by 7 times.

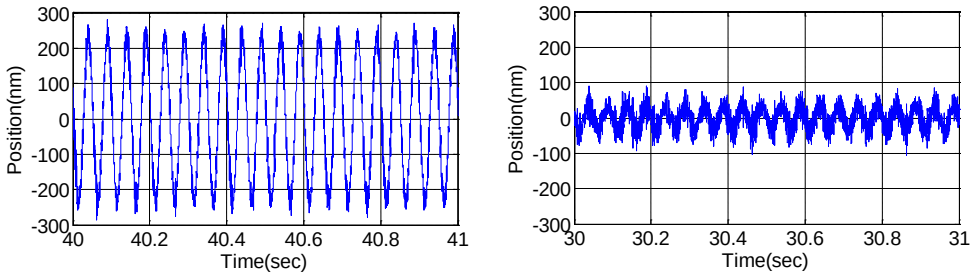

(a) With PID controller (b) With PID controller and DOB

Figure 4-30 Position oscillation under 1 N 20 Hz sine wave disturbance force

Another set of test for position holding also shows the DOB reduces the error magnitude around 20 Hz (caused by the disturbance from the motor cable) and at 60 Hz (caused by the disturbance from the electronic noise), but the DOB also increase the magnitudes in 600-700 Hz. The implementation of DOB with PID controller is listed in Appendix F.4.

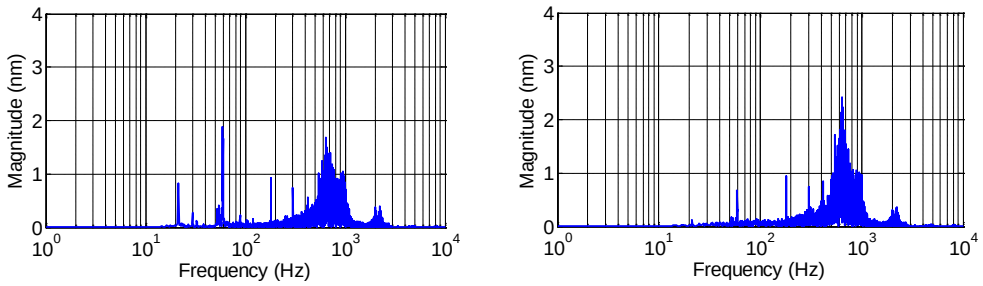

(a) With PID controller (b) With PID controller and DOB

Figure 4-31 The effect of DOB on position holding

5. Diamond Turning Experiments

Machining tests were conducted on a Rank Pneumo ASG-2500 DTM to evaluate the performance of the actuator in optical fabrication. Initial experiments involved machining flats, spheres and tilted flat. Once the baseline capability of the actuator was fully tested, a real-world example of a free-form optic, the biconic mirror (M4) form the NASA-IRMOS spectrometer with fiducial features for kinematic coupling, was created. There are serveral common tasks when integrating the FLORA with the DTM for machining experiment:

(1) Align the piston motion in the direction of the DTM Z-slide within 2 μm for 20 mm of travel. Align the workpiece and the diamond tool with respect to the spindle rotational center within 1 μm in both X and Y direction.

(2) Cover the FLORA top-front with a plastic sheet to avoid contamination of the air bearing and the encoder by cutting fluid and chips.

(3) Remove the chips generated in the cutting process by horizontally flushing the tool tip with the continuous stream of lubricant.

For the created surfaces, the surface finish is measured by a Zygo NewView white light interferometer, the form error is measured either by a Zygo GPI laser interferometer or by a LVDT.

5.1 Flat Surface Machining

Flat surfaces were machined to test the ability of the FLORA piston to hold position while being excited by the machining forces. Tests with different materials such as PMMA, aluminum (6061), brass, copper and plated copper under the same cutting condition produced different surface quality, but only plated copper was systematically tested under different tool holding conditions. The electroplated copper was selected for thorough study because of its high microhardness, small grain structure (~10 nm), lack of ductility and lack of second-phase particulates. Surface profiles produced in this material have sharp cusp corners and

smooth up-feed grooves, making it easier to observe the effect of tool positioning quality on the surface finish.

Two tables in this section compare the RMS of flat surface finish when the tool is locked or positioned by the servo control system. For the locked case, the air bearing was locked down by removing the air from the lower sides of the triangular piston while keeping it on the top surface. Comparing to the case of the locked tool, the three controllers added surface roughness. This is due to the tool positioning error in X, Y and Z direction. The flats in Table 5.1 were machined with a 0.53 mm radius diamond tool at 500 rpm with a 2 mm/min feedrate (4 μm/rev) and 2 μm depth of cut on the finish pass. The theoretical surface finish is 1.1 nm RMS, but the surface finish achieved with the piston locked is 3.7 nm RMS.

(1) The achievable surface finish is much lower than the corresponding motion error. This is consistent with the analysis of surface formation process for low cross-feed rate when some cutting passes do not leave any cusps on the surface.

(2) From the frequency spectrum of position holding error in the tool feed direction in Figure 4-10, it can been that, the case of K_{PID} has the highest error magnitude in the frequency range between 500-1000 Hz, so the corresponding surface finish is the highest, 11.4 nm RMS. The cases of K_{LL1} and K_{LL2} have the nearly the same piston motion error, but the case of K_{LL1} has lower motion error magnitude in the high frequency range, so its corresponding surface is the lowest, 7.4 nm RMS.

Table 5.1 Comparison of RMS error with a locked and actively held tool holder

Unit (nm)	Tool holding method (Two-bolt height adjuster)			
	Piston Locked	Actively held		
		K_{LL1}*	K_{PID}	K_{LL2}*
RMS Piston motion error	1	14.4	16.0	14.3
RMS Surface finish	3.7	7.4	11.4	10.5

* Controller only used for flat surface cutting

As discussed in Section 2.8, the tool height adjustment on FLORA is accomplished by bending the base plate with a single or pair of bolts under the front of the base. The surface finish results in Table 5.1 were obtained when the tool height adjustment was done by two

bolts (one for each side of the FLORA base). The flat machining test was done with a 0.5 mm radius diamond tool when the FLORA was supported by a single bolt in the middle of the front and the results are shown in Table 5.2 . Comparing the results in Table 5.1,

(1) The surface finish error in Table 5.2 is much closer to the motion error. This relative increase of surface roughness may be caused by additional torsional vibration from the single support.

(2) The motion errors in Table 5.2 are smaller. These tests were implemented when all the control electronics was installed in separated aluminum enclosures. Repackaging of electronics in the computer enclosure box somehow increases the electronic noise in the system resulting in larger motion errors in Table 5.1.

Table 5.2 Comparison of RMS error with a locked and actively held tool holder

Unit (nm)	Tool holding method (Two-bolt height adjuster)			
	Piston Locked	Actively held		
		K_{LL1}*	K_{PID}	K_{LL2}*
RMS Piston motion error	1	12.7	13.1	8.0
RMS Surface finish	6.7	9.8	12.3	9.0

* Controller only used for flat surface cutting

The Zygo NewView measurement in Figure 5-1 shows a 144×108 μm patch on this surface that represents approximately 72 tool passes. It has an average surface finish of 9.0 nm (RMS) for the case of K_{LL2} in Table 5.2.

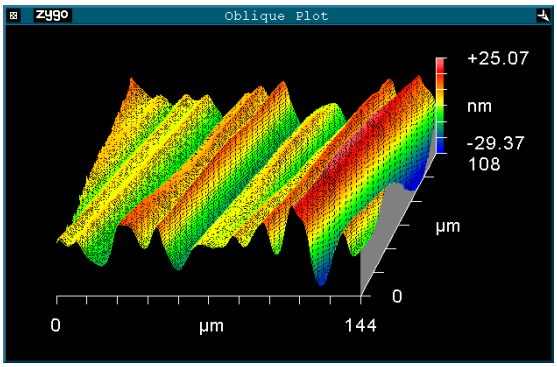

Figure 5-1 ZYGO image of surface finish (RMS=9.0 nm) of a plated copper flat (0.53 mm tool nose radius, 500 rpm spindle speed, 4 μm/rev cross feedrate, and 2 μm DOC)

5.2 Spherical Surface Machining

To create a spherical surface, the FLORA piston is commanded to move as a function of the tool radial position. In addition to the circular path generated by equation, the motion path typically needs to be compensated for residual error due to the tool nose geometry waviness. The residual tool error can be determined by the cross-section profile of the machined surface from GPI measurement, a polynominal equation was used to capture most of error magnitude. This cutting effort was to create a proper rotationally symmetric surface before the NRS components were added to the surface geometry. (a) shows a test of tool motion at the spindle speed of 500 rpm and cross-feed rate of 200 mm/min when the radial position changes from zero mm to 50 mm, the tool servo (with PID and acceleration feedforward controller) tracking error in (b) is within the ±75 nm.

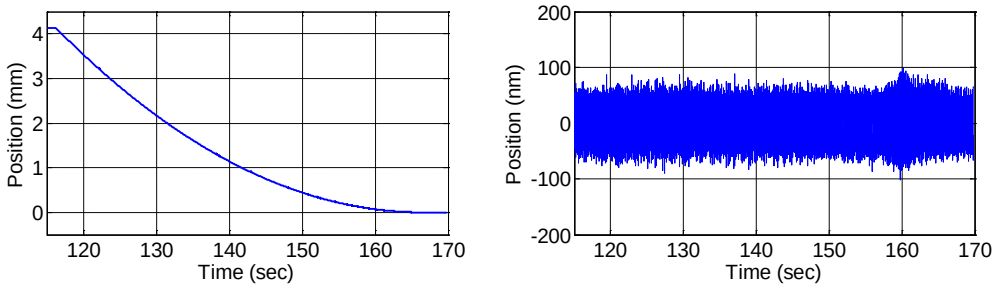

(a) Relative toolpath from the neutral position of 17.1 mm (b) Tracking error

Figure 5-2 Motion test for spherical surface

Figure 5-3 shows the spherical error of 225 nm PV for an aluminum (6061-T651) part of 98 mm diameter machined at 500 rpm with a 0.9977 mm radius diamond tool. The measured surface finish is 22 nm RMS for a 10 mm/min cross-feed rate and 5 μm depth of cut on the finish pass.

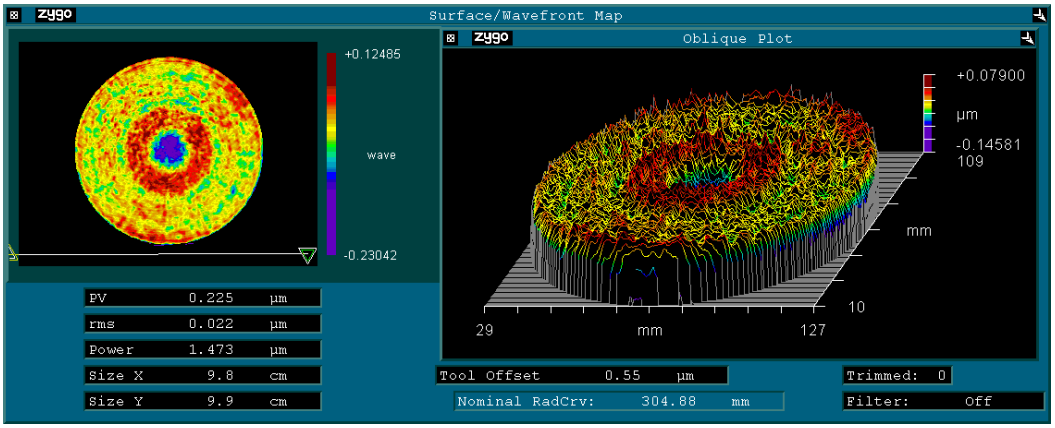

Figure 5-3 Measured 225 nm (PV) spherical error of the 98 mm diameter aluminum sphere (1 mm tool nose radius, 500 rpm spindle speed, 20 µm/rev cross feedrate, and 5 µm DOC)

5.3 Tilted Flat Surface Machining

Tilted flats were machined to evaluate the ability of the servo to create non-rotationally symmetric optical surfaces. The tilted flat requires a sine wave motion of the tool with the amplitude changing linearly with the radius. This shape is a good test of the performance of the actuator as the amplitude changes but the frequency remains constant. The machined surface should be a flat and thus easy to measure in a laser interferometer.

Figure 5-4 shows a top-down view for the setup of the experiment. The tool is mounted on the X-axis which moves in the horizontal (radial) direction starting at the outside diameter of the part where the amplitude is highest. The Z-axis supporting the spindle remains stationary during the cut. The commanded motion to the tool is in Equation (5.1), where A is the slope of the tilted flat, r is the radial position of the tool contact point and ω is the angular speed of the spindle.

$$Z = A \cdot r \cdot \sin(\theta) \tag{5.1}$$

Correction to the tool path is required in the tilted flat machining to compensate for the tool radius (R_t). Notice from Figure 5-4 that the tool will touch the part on the left of its centerline at its longest extension and a half-cycle later to the right of its centerline at its shortest extension. Half way in between, it will touch at the tool centerline. This change in

contact position (or contact angle α) results in a small change in part radius (depending on the radius of the tool) and therefore height at the location where the cutting occurs. The solution is to modify the tool commanded position to account for the tool radius. The command modification (ΔZ) is approximately a small sine wave which is twice the frequency of the spindle rotation.

$$\Delta Z = \left| R_t \left(1 - \frac{1}{\cos\alpha} \right) \right|; \quad \alpha = \tan^{-1}\left(A\cos\theta \right) \tag{5.2}$$

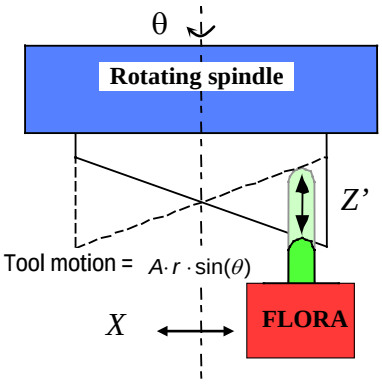

Figure 5-4 Schematic configuration of tilted flat machining

A combination of acceleration feedforward and PID controller was first used to position the tool for the tilted flat experiments. Tilted flats machined in PMMA with 50.8 mm diameter and 4 mm sag were created at three different spindle speed, 300 rpm, 600 rpm and 1200 rpm with a 0.53 mm radius diamond tool, a 5 µm/rev cross-feed rate and 5 µm depth of cut on the finish pass. The measurement of flatness by the Zygo GPI laser interferometer for the tilting surface showed a consistent pattern as shown in Figure 5-5. The plots show the 3.6 µm PP surface residual error with the best-fit tilted flat removed. Note that the surface has astigmatism and the high spot of this astigmatism has about 80° lead to the high spot of the tilted flat.

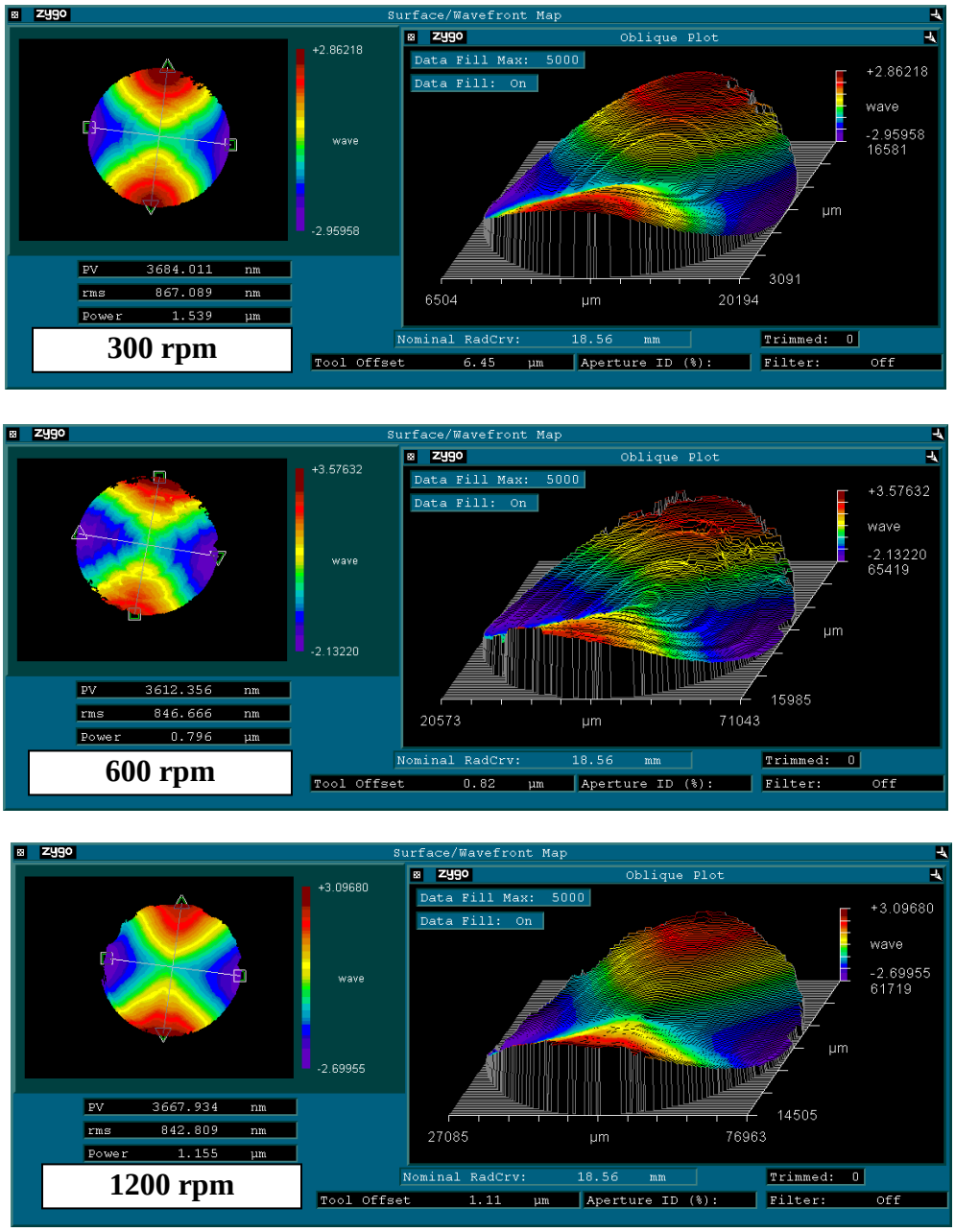

Figure 5-5 Measured flatness error of tilted flats with spindle encoder runout error (0.53 mm tool nose radius, 5 µm/rev cross feedrate, and 5 µm DOC)

The 3.6 µm flatness error was caused by the spindle rotary encoder feedback error due to the rotor runout as discussed in Section 3.3.1, which introduces once-per-spindle-revolution angular position feedback error in Equation (3.17). The flatness error generation can be

intuitively explained by a schematic in Figure 5-6 and the motion trajectory defined by Equation (5.1). When the spindle rotates counter-clock-wise, the tool cuts on the surface clock-wise. From 0 to 90° to 180°, the tool cuts the down-slope of the tilted flat; from 180° to 270° to 0°, the tool cuts the up-slope. At 80°, the angular feedback is less than the actual position, so the tool cuts at a higher position above the surface than ideal condition and the position error magnitude reaches the maximum value. At 260°, the angular feedback is more than the actual position, so the tool also cuts at a higher position above the surface than ideal condition and the position error magnitude reaches the maximum value. As a result, this once-per-spindle-revolution angular feedback error introduces twice-per-spindle-revolution error in tool motion trajectory. The maximum tool motion error increases in amplitude when the tool cutting depth increases, thus produces a consistent flatness error pattern in Figure 5-5.

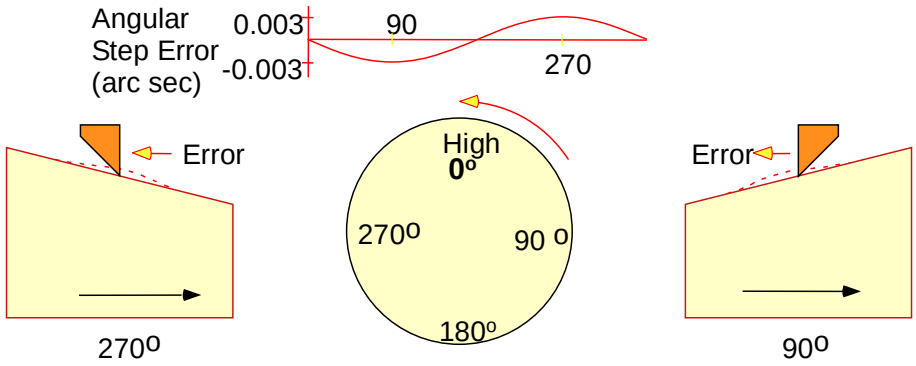

Figure 5-6 A schematic of flatness error generation process in the machining tilted flats due to spindle encoder runout error

Since this error is repeatable, it was measured and removed in the motion trajectory. The effectiveness of this solution is validated in machining tests at 630 rpm, in which the flatness is reduced to less than 1 μm in Figure 5-7. Figure 5-7 shows the flatness of the tilted flats created using two different cutting conditions at the spindle speed of 630 rpm after the spindle encoder feedback error was removed. The flatness error patterns appear to be different, but the error magnitudes have no significant difference.

(1) Cutting case one: This experiment was done with a single bolt supported height adjuster, the tool servo was controlled by a combination of acceleration feedforward and PID controller.

(2) Cutting case two: This experiment was done with the two-bolt supported height adjuster, the tool servo was controlled by a combination of acceleration feedforward, PID and first harmonic adaptive feedforward controller.

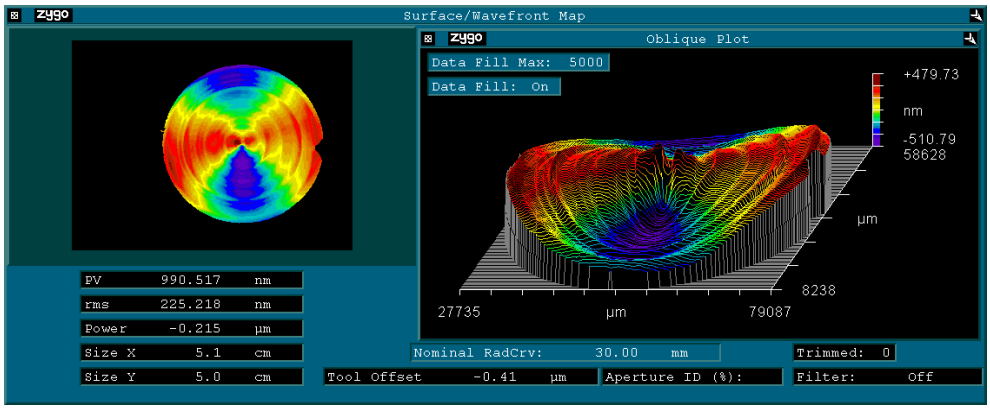

(a) Cutting case one: 990 nm PV flatness error

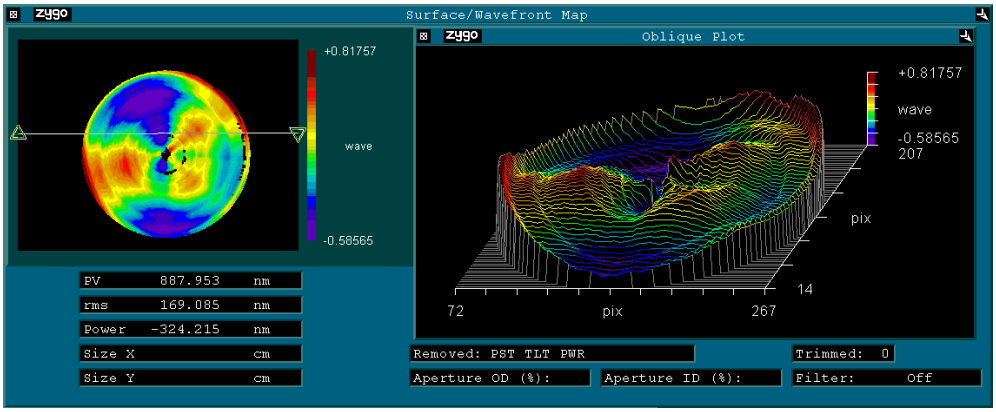

(b) Cutting case two: 888 nm PV flatness error

Figure 5-7 Measured flatness error of tilted flats with corrected encoder reading (0.53 mm tool nose radius, 630 rpm spindle speed, 5 µm/rev cross feedrate, and 5 µm DOC)

Figure 5-8 and Figure 5-9 show the tests of tool motion for machining case one and two at the spindle speed of 630 rpm and cross-feed rate of 50mm/min when the radial position changes from 26 mm to zero, the tool tracking error in both cases increases when the motion amplitude increases, but stay within ±100 nm. The frequency spectra of tracking error in Figure 5-8(a) and Figure 5-9(a) show the adaptive feedforward controller removes the motion error at the fundamental spindle frequency, so the tracking error reduces from 21.6 nm RMS in Figure 5-8(a) to 18.9 nm RMS in Figure 5-9(a). However, this improvement of motion control quality only affects the slope of the tilted flat, which is not measured in this study. Figure 5-8(b) and Figure 5-9(b) give the close-up views of the tool motion and tracking error for two revolution of spindle.

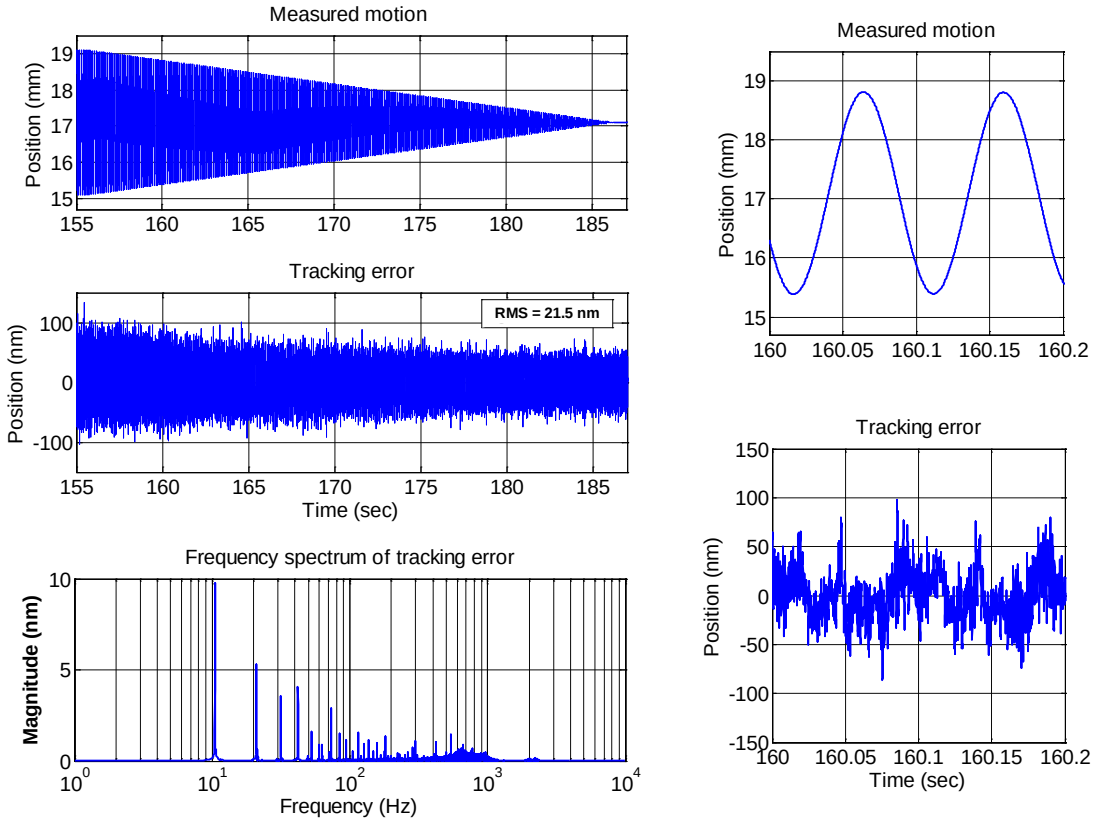

(a) Full motion profile (b) Close up view for two cycles

Figure 5-8 Motion test for the toolpath of 4 mm sag tilted flat (cutting case one)

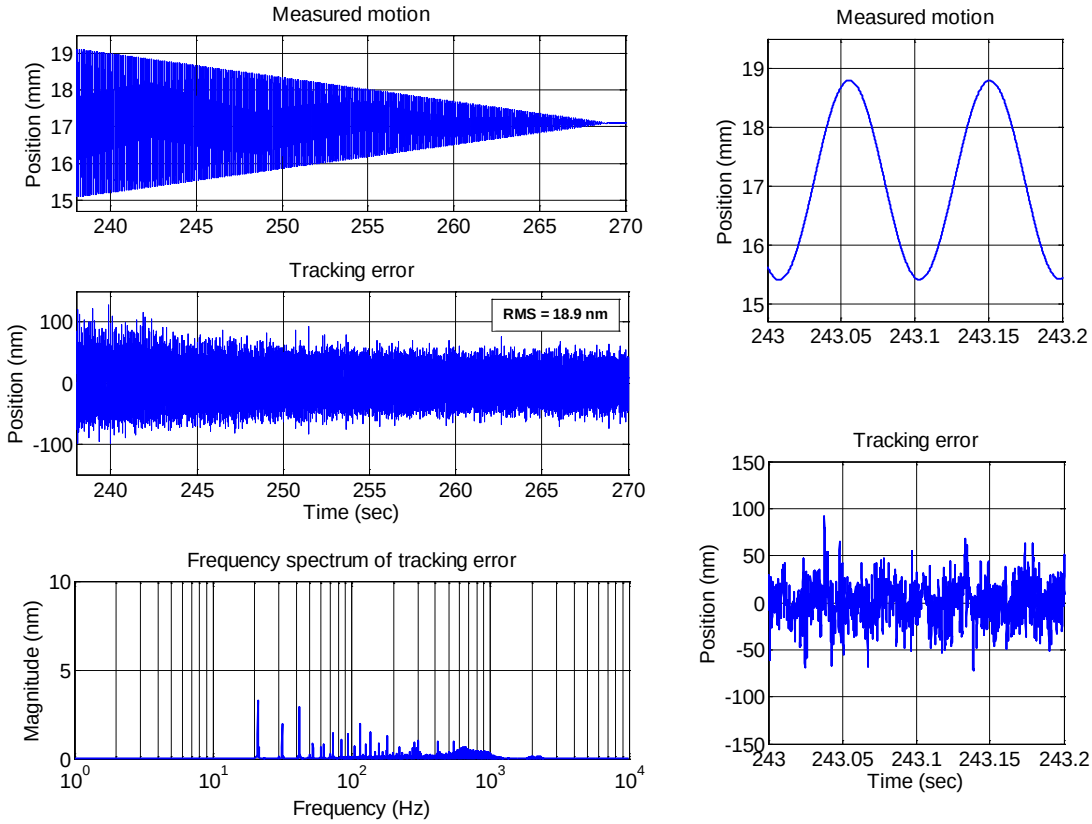

(a) Full motion profile (b) Close up view for two cycles

Figure 5-9 Motion test for the toolpath of 4 mm sag tilted flat (cutting case two)

Table 5.3 shows the measured surface finish on the tilted flat at 9 locations for these two cutting tests. In the tests, the high spot of the tilted flat is aligned with the zero angular spindle position. Because of the surface slope on the tilted flat: 0º and 180º angular positions have the maximum surface slope in radial direction; 90º and 270º angular positions have the maximum surface slope in circumferential direction. The tool positioning error in X and Y produces positioning error in the surface normal direction, as a result, the stiffness of tool height adjuster in the tilted flat cutting has bigger impact on the surface finish than the flat cutting, i.e. average 22 nm RMS for case one, average 17 nm RMS for case two. There are additional observations can be taken from Table 5.3:

Table 5.3 Measured surface finish of the tilted flat with 4 mm sag

Case one: average RMS = 22 nm						
Angular position	Radial position					
	central		Mid		Outer edge	
	PV (nm)	RMS(nm)	PV (nm)	RMS(nm)	PV (nm)	RMS(nm)
0º	264	24	112	18	181	13
90º			149	21	144	21
180º			150	25	172	26
270º			150	23	223	25

Case two: average RMS = 17 nm						
Angular position	Radial position					
	central		Mid		Outer edge	
	PV (nm)	RMS(nm)	PV (nm)	RMS(nm)	PV (nm)	RMS(nm)
0º	140	19	73	13	60	10
90º			127	24	143	24
180º			82	15	85	15
270º			100	16	113	22

(1) The surface finish at the mid and outer radial positions is similar indicating the increase of motion amplitude has little influence on the surface finish.

(2) When the FLORA is supported by the 2-bolt height adjuster (case two), the surface roughness at the angular positions of 0º and 180º is consistently much lower than that of 90º and 270º angular positions. This is due to the fact that the tool has close to zero velocity at 0º and 180º, but reaches the maximum velocity at 90º and 270º. For the case of 1-bolt height adjuster (case one), the difference of surface roughness at different angular positions are less significant, which is potentially caused by the additional torsional vibration from the single point support as observed in the machining of flat surfaces (Section 5.1).

For comparison, a PMMA flat with 50.8 mm diameter was also cut at 630 rpm when the piston was actively held in position by PID controller, and the height adjuster was supported by two bolts. The resulted flatness error is 0.202 μm (PV) as shown in Figure 5-10. When the machining moves from flat to non-rotationally symmetric tilted flat, the flatness error increases by about 0.7 μm (PV), which can potentially be attributed to four sources: the

motion trajectory error, the tool servo tracking error, waviness on the tool nose edge and the lack of counter-balance for linear actuation in the machining process. The average RMS surface finish for the flat is 11.5 nm, about 2 nm less than the average RMS error for tilted flat surface at 0º and 180º (case two in Table 5.3) where the tool velocity is close to zero. The larger error value for the latter is possibly caused by the surface slope of the tilted flat. When cutting at 0º and 180º angular position, the surface slope reaches the maximum value of 4/50 in the radial direction, the tool positioning error in Y direction produces significant amount of tool motion error normal to the surface, which in turns increases the surface roughness at these two angular location.

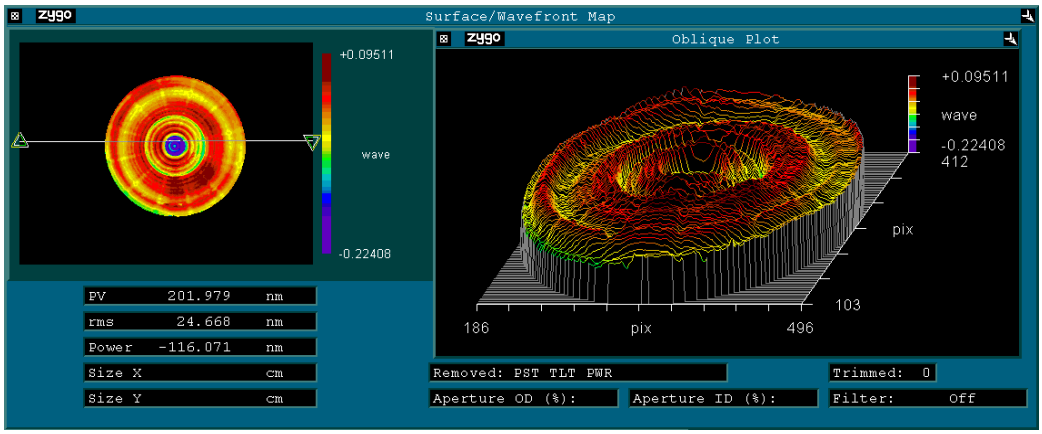

Figure 5-10 Measured 202 nm PV flatness error for a 50 mm diameter PMMA flat (0.53 mm tool nose radius, 630 rpm spindle speed, 5 μm/rev cross feedrate, and 5 μm DOC)

5.4 Biconic Mirror with Fiducial Features for Kelvin Coupling

5.4.1 The Optical Feature and the Fiducial Feature

The Infrared Multi-Object Spectrograph (IRMOS) mirror M4 is an off-axis biconic toroidal surface [93] designed by NASA for a space-based spectrometer. The surface is a blending of two oblate ellipses with different curvature and eccentricity in the XZ and YZ planes. As such it has no axis of rotational symmetry. Figure 5-11(a) shows a section of the

biconic surface as a wire frame and the aperture of the mirror blank as a solid. A general biconic optical surface can be defined in rectangular coordinates as

$$M4(x,y) = \frac{c_{XZ}\cdot(x-x_0)^2 + c_{YZ}\cdot(y-y_0)^2}{1+\sqrt{1-(1+k_{XZ})\cdot(x-x_0)^2\cdot c_{XZ}^2 - (1+k_{YZ})\cdot(y-y_0)^2\cdot c_{YZ}^2}} \tag{5.3}$$

With the origin at $(x_0, y_0, 0)$, the parameters that specify the shape of M4 are:

c_{XZ} = 0.002650 is the surface curvature in the XZ plane
c_{YZ} = 0.002458 is the surface curvature in the YZ plane
k_{XZ} = 0.0778 is an oblate ellipse in the XZ plane,
k_{YZ} = 0.1265 is an oblate ellipse in the YZ plane

The aperture of the mirror is 94 mm by 76 mm and its center is located at x_0 = -2.01 mm and y_0 =227.41 mm. The mirror surface is tilted 35.3° with respect to the optical axis so that the average normal from the front surface is parallel to the back surface. M4 has 7.549 mm of sag with respect to a plane parallel to its back surface. If a best-fit, rotationally symmetric asphere is also subtracted from M4, the sag of the resulting surface is 4.582 mm.

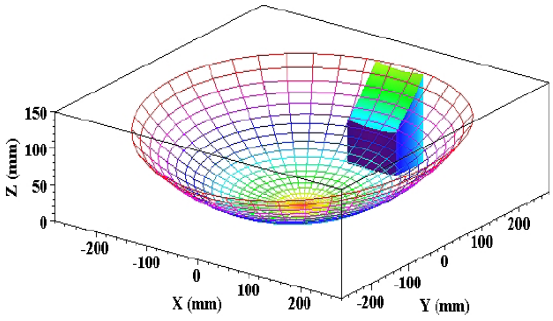

(a) Off-axis M4 surface

(b) Off-axis machining of M4

Figure 5-11 Off-axis biconic optic M4

This optic was machined in 2002 at the Precision Engineering Center of NCSU using a piezoelectric actuator with 400 µm range in Figure 5-11(b). The limited range of this actuator required the optical blank to be machine off-axis and tilted 35.3° with respect to the

fabricating axis. The actuator was also tilted with respect to the spindle axis. These two changes allowed the surface to be machined with this actuator.

With the extended range of the FLORA, it is feasible to machine M4 surface on axis. Figure 5-12(a) shows the on-axis M4 surface with aperture size of ∅98 mm, the surface is translated in Y direction by -227.41 mm and rotated at an angle of -35.3° around X axis. The total excursion of the on-axis surface is 4.054 mm, but after removing the best sphere of ∅304.881 mm, the required excursion of NRS component is 0.545 mm. After considering the tool radius compensation for 0.9977 mm tool radius, the best fit sphere has a diameter of 303.919 mm, but the excursion of NRS component has no change, Matlab code for surface analysis is listed in Appendix G.1.

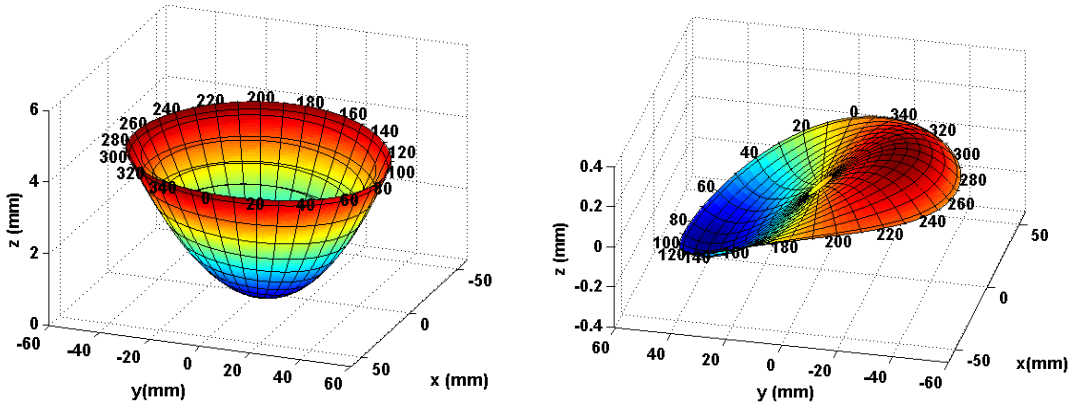

(a) On-axis M4 surface (b) NRS component

Figure 5-12 On-axis biconic optic M4

The ability to machine large-amplitude (> 1 mm) features also makes it possible to create fiducial locating features for assembly purpose in the same setup as the functional optical surface so that the geometric relationship of optical and fiducial features can be preserved within the tolerance of the DTM. The picture in Figure 5-13 shows a concept of kinematic coupling to provide deterministic location in all six degrees of freedom of two components (the mirror blank and the housing) in relation to each other without over-constraint. Over-

constraint is to be avoided since it causes stress in the structures of components that results in distortion and non-repeatable location.

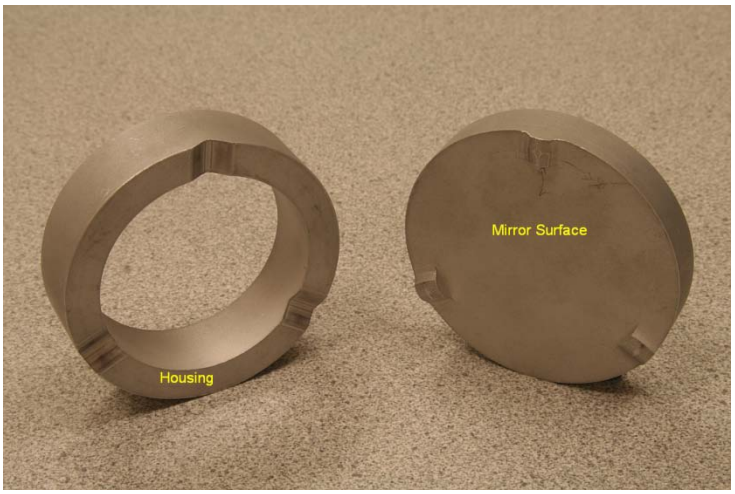

Figure 5-13 The concept of kinematic coupling on the mirror blank (right) and the housing

To design the fiducial feature for kinematic coupling on the mirror side, there are two main concerns:

(1) The stress at the contact should not exceed the yield stress of the material.

(2) The slope of contact surfaces should be sufficient to overcome friction at the interface so that the surfaces will move into contact at 6 points.

Figure 5-14 shows detailed shape of this fiducial feature. It has constant width is 4 mm in radial direction and the full sinusoidal wave in the circumferential direction has a constant wave arc-length of 8 mm. The mid-point of width in the radial direction is at 61.5 mm. At this radial position, the sinusoidal wave has the maximum amplitude of 0.6 mm, but the amplitude (A_F) changes as a parabolic function of radial position (r).

$$A_F = 0.6 - \frac{(r - 61.5)^2}{100} \tag{5.4}$$

The two designated contact points for each of the 3 features are shown in the Figure 5-14 at the radial position 61.5 mm and 60° away from the peak point (or 0.3 mm lower in height)

so that the two contact points are 8/3 mm arc-length apart in circumferential direction. The slope at the contact point is 22°, but the maximum slope reaches 25.22° on the feature, so a customized diamond tool with large clearance angle of 27° is used. Note that the friction coefficient for a pair of mating aluminum surfaces is 0.16, the minimum required slope is arctan(0.16), i.e. 9°. Matlab code for surface data generation is listed in Appendix G.2.

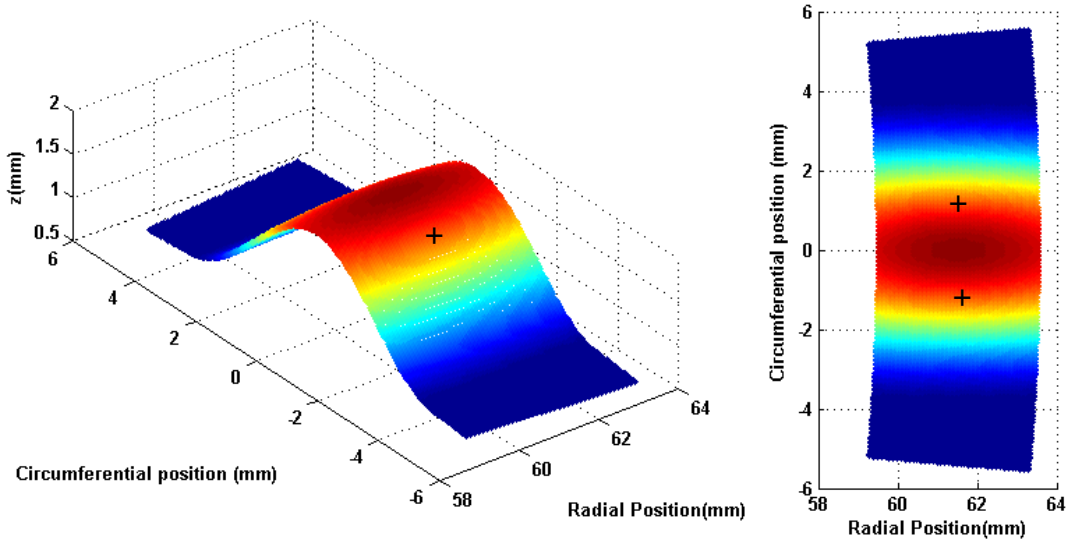

Figure 5-14 Details of the fiducial feature (The theoretical contact points with the v-groove is indicated by the crosses)

Figure 5-15(a) shows the solid modeling of the M4 mirror with the fiducial features placed at the outer edge. The whole part has a diameter of 127 mm, and a thickness of 63.5 mm is selected to minimize the distortion of surface when mounted to back plate. Figure 5-15(b) shows three fiducial features for the kinematic coupling distributed 120° intervals on the OD of the part. The rotational reference (zero degree) was at the mid point of one of the fiducial features, and this same rotational reference was used to define the biconic M4 surface in Equation (5.3). A flat surface was machined between the optical and fiducial features to create an axial reference surface. The height relationship between the optical feature and the fiducial feature is established from this surface. The spindle rotational center point on the M4 surface has 4.139 mm of sag when measured from the flat reference surface

in the axial direction, while the peak point of fiducial surface is 1.9 mm from the reference flat. As a result, the geometric relationship between the optical feature and fiducial features is established.

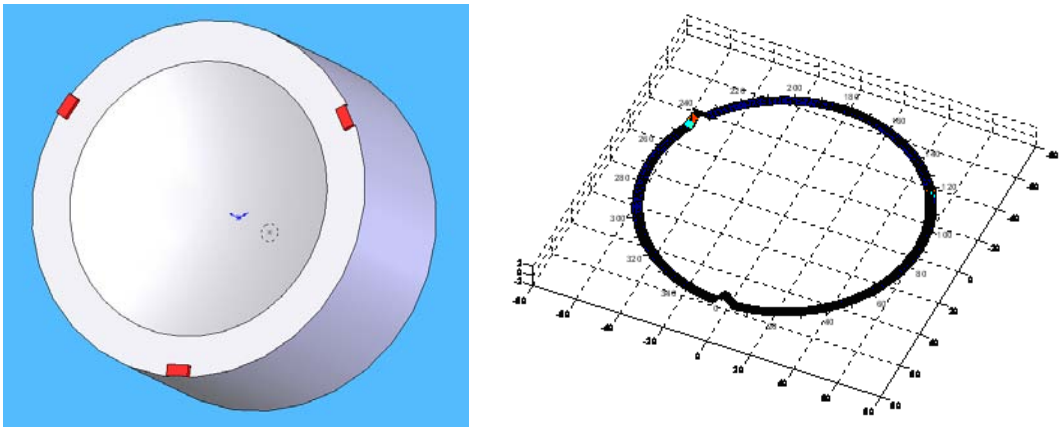

(a) 3D model of the part (b) Location of three fiducial features

Figure 5-15 Geometric relationship of optic surface and fiducial features

5.4.2 Toolpath Generation and Test

The surface of the optical feature and the fiducial feature can only be represented by a point cloud after the compensation for tool nose radius. For the M4 surface shown in Figure 5-12, the uniform polar mesh grid of 50×361 (1 mm radial grid step × 1° angular grid step) is created for the NRS component (Appendix G.1) and the bilinear interpolation algorithm is applied in real-time to generate NRS position command and acceleration command. The final position command for M4 mirror machining consists of three elements: circular path from the equation, NRS position command and residual error correction. (a) shows a test of tool motion at the spindle speed of 500 rpm and cross-feed rate of 200 mm/min when the radial position changes from 0 mm to 49 mm. With PID and acceleration feedforward controller, the tool servo on the FLORA has the tracking error within the ±100 nm in (c). (b) and (d) provides close-up view of the tool motion and error magnitude for four revolution of spindle.

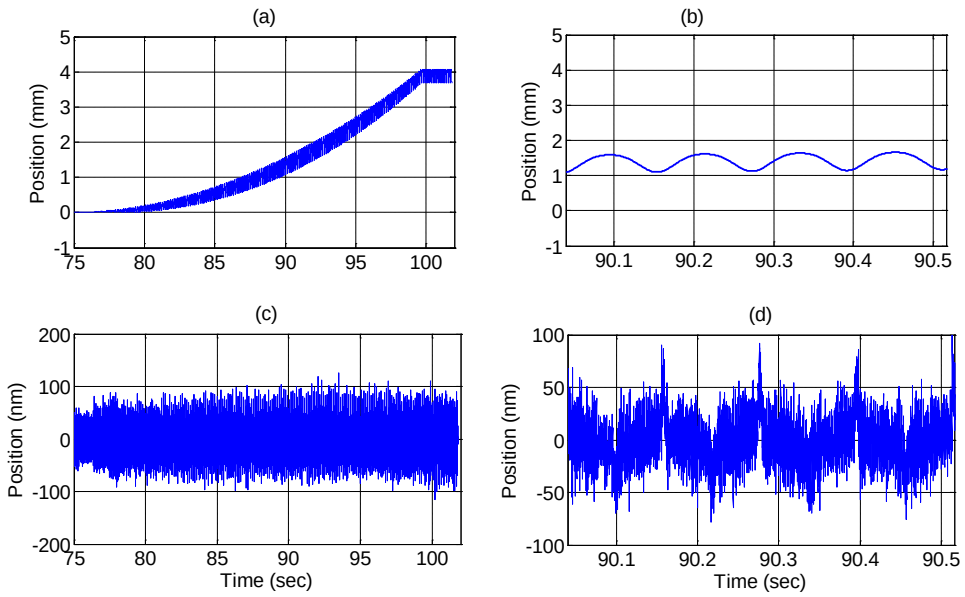

Figure 5-16 Motion test for the toolpath of M4 surface (a) The relative toolpath from the neutral position of 17.1 mm (b) Close-up view for toolpath around 90 sec for four revolutions of spindle (c) The tool servo tracking error in full toolpath (d) Close-up view for tracking error around 90 sec for four revolutions of spindle

For the case of the fiducial feature, the dominant position command (Equation (5.5)) and acceleration command can be easily generated from sinusoidal function. The polar mesh grid is only created for the tool radius compensation part of surface profile as shown in . Since the fiducial feature only has 8 mm wavelength in the circumferential direction and repeats itself every 120°, the grid covers an area a little larger than the size of the feature, i.e. radial range from 58.5 mm to 64.5 mm with grid spacing of 0.1 mm, the angle range within ±5° with grid spacing of 0.05°. The final position command is a combination of two elements including sinusoidal position command and additional position correction from tool radius compensation (Appendix G.2). In addition, there are two more considerations for the tool path generation:

$$Z_{F1} = A\left(1+\cos\left(\frac{\theta r}{8}\right)\right) \tag{5.5}$$

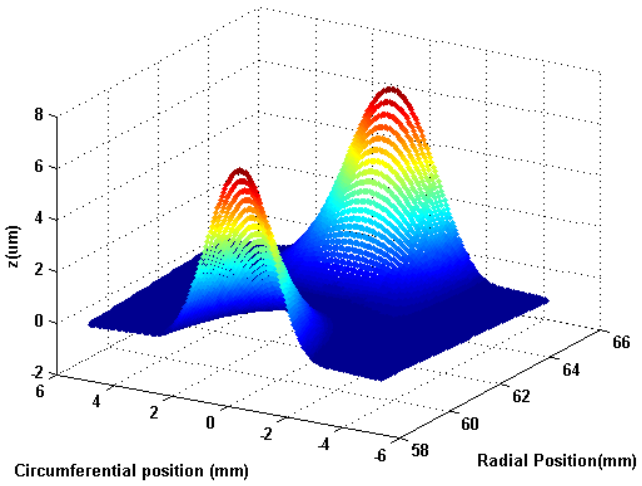

Figure 5-17 Tool radius compensation position profile for the fiducial feature

(1) Since the dominant motion frequency of tool used to create the fiducial surface is 46-50 times of spindle rotational frequency, the spindle speed was reduced to 21 rpm (a comparison to 500 rpm for mirror surface) to minimize the difference of dominant frequency level in the toolpath for both optical feature and fiducial feature. Changes in frequency of operation can introduce phase lag and the orientation of the fiducial surface with the optical surface.

(2) As shown in Figure 5-18, at the start and end of sinusoidal tracking, there are much bigger position errors. To reduce this error, three continuous cosine waves are used in the toolpath, but only the middle wave machines the surface. With PID and acceleration feedforward controller, the servo tracking error is less than ±500 nm.

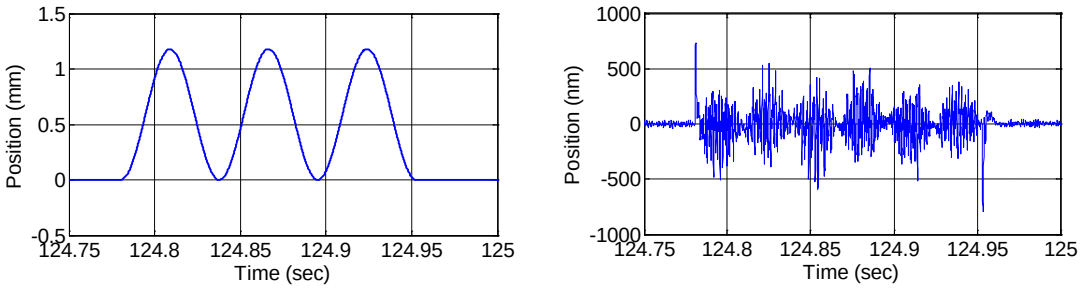

(a) Relative toolpath from the neutral position of 17.1 mm (b) Tracking error

Figure 5-18 Motion test for fiducial feature

5.4.3 Machining and Metrology of Surfaces

Initial machining of biconoic mirror was done on PMMA material, but the measurement of the surface shape by a computer-generated holographic (CGH) was not successful due to the low reflectivity of PMMA surface, aluminum material 6061-T651 was then selected. Due to the requirement of using one setup to create three surfaces, there are large amount of materials need to be removed by one tool, tool wear may be significant over long cutting distance for the diamond tool with a clearance angle of 27°. As a result, the depth of cut and cross-feed rate in the rough pass (See Appendix E for detailed parameter selection) were increased to reduce the amount of cutting distance. There are three major procedures to cut this free form optic as presented in details in Appendix E: rough machining, preparation machining of RS surfaces, and final machining. Figure 5-19(a) shows a photograph of machining setup on the ASG 2500 DTM for this M4 mirror with fiducial features, Figure 5-19(b) shows a close-up photograph of the finished optic surface with fiducial features.

(a) DTM setup for machining

(b) Close-up photograph for the mirror showing 3 fiducial features

Figure 5-19 Photographs of the machined M4 mirror

The optical surfaces and fiducials were measured using an air-bearing LVDT as no other technique could measure both the optical and fiducial surfaces and their relationship to each

other. The Lion LVDT has a range of 1 mm, a resolution of ±500 μm / 10 ±V. The setup is shown in Figure 5-18. During the measurement:

(1) The tip of LVDT (∅1.1811 mm) was aligned with respect to the spindle rotational center by a spherical reference mounted on the spindle chuck.

(2) To minimize the damage on the aluminum surface without sacrificing the signal quality, the LVDT probing force was set to 1.5 mN by a flexure of known stiffness

(3) The bandwidth of amplifier interfacing to the LVDT was set to be 100 Hz.

(4) A slow spindle speed of approximately 2 rpm was used to avoid LVDT tip jumping off from the measured surface.

(5) The flat surface was taken as the reference for the measurement of biconic surface and fiducial features.

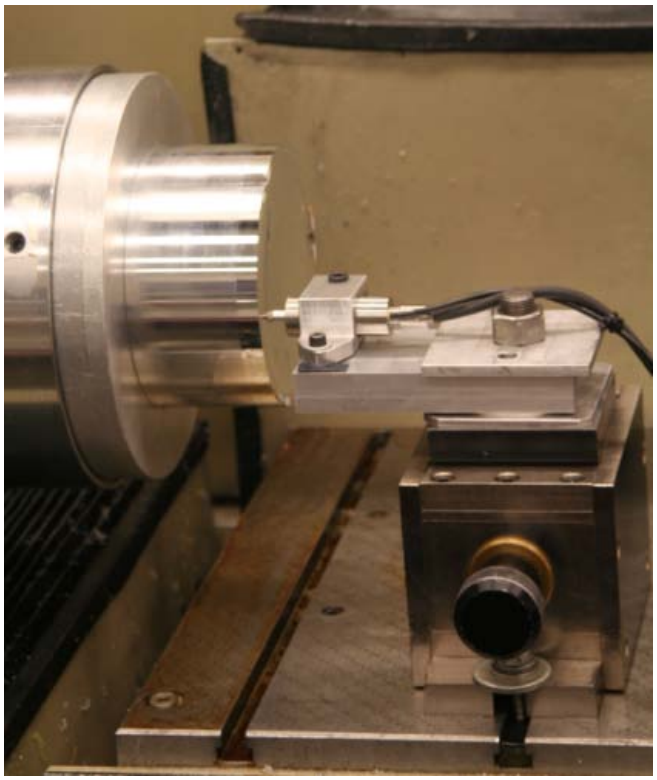

Figure 5-20 Measurement setup on DTM with LVDT

Figure 5-21(a) shows the measured fiducial surface profiles at its centerline or a radial position of 61.5 mm. Due to the limited range of the LVDT, only 0.8 mm are effectively measured within the ±2.5 mm arc length. Figure 5-21 (b), (c) and (d) show the deviation of measured profiles from the ideal surface profiles for fiducial features at three locations. It can be seen that:

(1) The peak points of the fiducial features are at the designated angular location. The difference of their height is within 100 nm, but they are all about 5.5 μm higher than expected value of 1.9 mm.

(2) The waviness error of 2 μm on the features may be caused by the tool servo tracking error (high frequency oscillation component) as shown in Figure 5-18.

(3) The tilting of 2 μm over 4 mm arc length is possibly caused by distortion of the part since the part was taken out for display before the measurement was done.

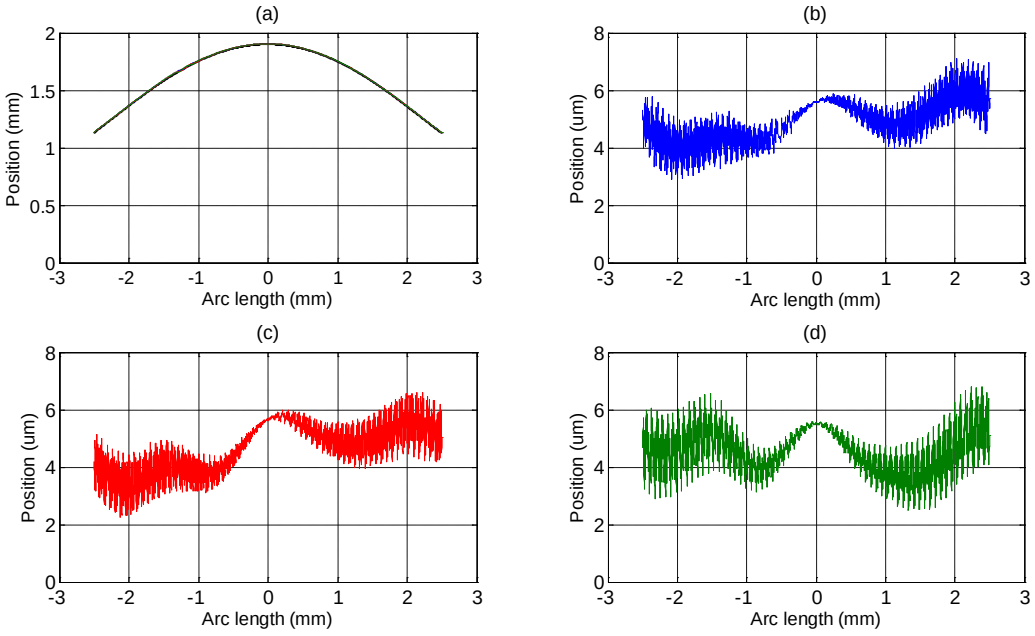

Figure 5-21 Measurement of fiducial features at peak radial position (a) Measured surface profiles (b) Deviation of the measured profile from ideal profile at 0° feature (c) Deviation of the measured profile from ideal profile at 120° feature (d) Deviation of the measured profile from ideal profile at 240° feature

In the measurement of the biconic surface, the DTM Z-slide was first placed at a location to obtain zero LVDT reading when the LVDT is contacted at the reference flat surfacce. Furthermore, since the biconic surface has 4.139 mm sag with respect to the reference flat surface, the DTM Z-slide needs to move into the surface when the measurement is started at the outer edge and moved toward the center, so that the measurement can be done even though the LVDT has the limited range of 1 mm. The required travel for the Z-slide is a function of the radial position

$$Z_{Slide} = 304 - \sqrt{304^2 - \left(X - 47.5\right)^2} \tag{5.6}$$

The amount of measured motion in the Z-slide (Z_{slide}) at a specific radial position is added to the LVDT measurement value to establish the total surface profile with respect to the reference flat surface. Figure 5-22(a) shows the measured biconic surface profiles at six different radial positions for one full spindle revolution. Figure 5-22(b) shows the difference between the ideal surface profiles and the measured profiles. All the errors stay within 4 μm, and error profiles have similar twice-per-spindle-revolution pattern with two high spots at the angular position close to 180° and 360°. The error may be possibly caused by the shifting of the workpiece on the chuck in the last cutting pass, which introduces non-continuous peak spots on the surface. The measured average surface roughness is 16 nm RMS for a 5 mm/min cross-feed rate and 1.5 μm depth of cut on the finish pass.

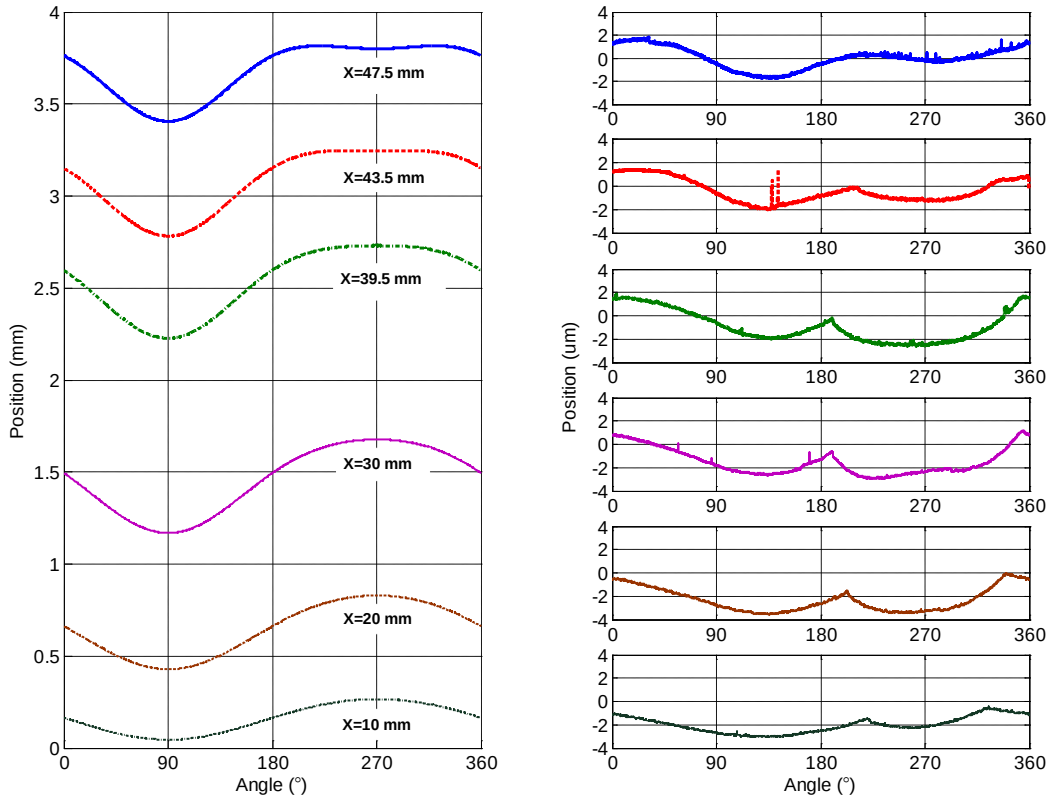

(a) Measured surface profiles (b) Error of surface profiles

Figure 5-22 Measurement of biconic surface with a LVDT

5.4.3 Diamond Tool Wear

Tool wear can be significant over long cutting distance on Aluminum 6061-T651 due to the requirement of create all surfaces in one setup. This custom-designed diamond tool has a nose radius of 0.9977mm and 27° clearance angle. The detailed specifications are in Appendix E. The wear of the tool is measured by a JEOL 6400 field emission scanning electron microscope (SEM). The electron beam induced deposition (EBID) method utilizes the effect of focusing a low voltage electron beam in the SEM chamber to grow hydrocarbon contamination lines on the surface of diamond tool [10]. These lines can be used to create contour profile on the tool edge so that the edge wear condition can be accurately determined.

The SEM images of the diamond tool in Figure 5-23 and Figure 5-24 were obtained with 2 kV accelerating voltage. Figure 5-23 shows the full tool edge at a low magnification of 45X. But a large magnification of 30,000X is used to capture the worn tool edge in Figure 5-24. In Figure 5-24, the tool rake face is pitched 60° upwards and yawed 45° backwards, the contamination line in Figure 5-24 is located about 10.5 μm away from the tool tip.

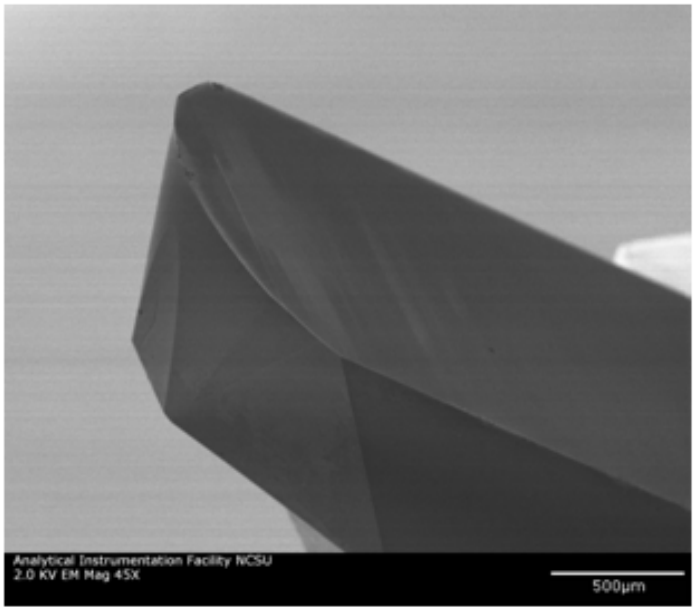

Figure 5-23 SEM images of full surface diamond tool with 45X magnification

A Matlab program was developed to measure the distance between two bending points of the contamination line, the thickness of wear land is 1.61 μm as marked in the dashed line in Figure 5-24(a). In addition, the wear area is 0.887 μm^2. Assume an uniform wear condition across 18° sweep angle for 0.9977 mm tool nose radius, the total wear volume is 278 μm^3 after about 6 km of cutting at various depth of cut and cross-feed rate from a brand-new tool. The wear volume of this round nose tool is within reasonable range of the projected tool wear from orthogonal cutting with flat nose tool [124], in which the wear volume is about 320 μm^3 over 6 km cutting distance with 2 μm depth of cut on Al6061.

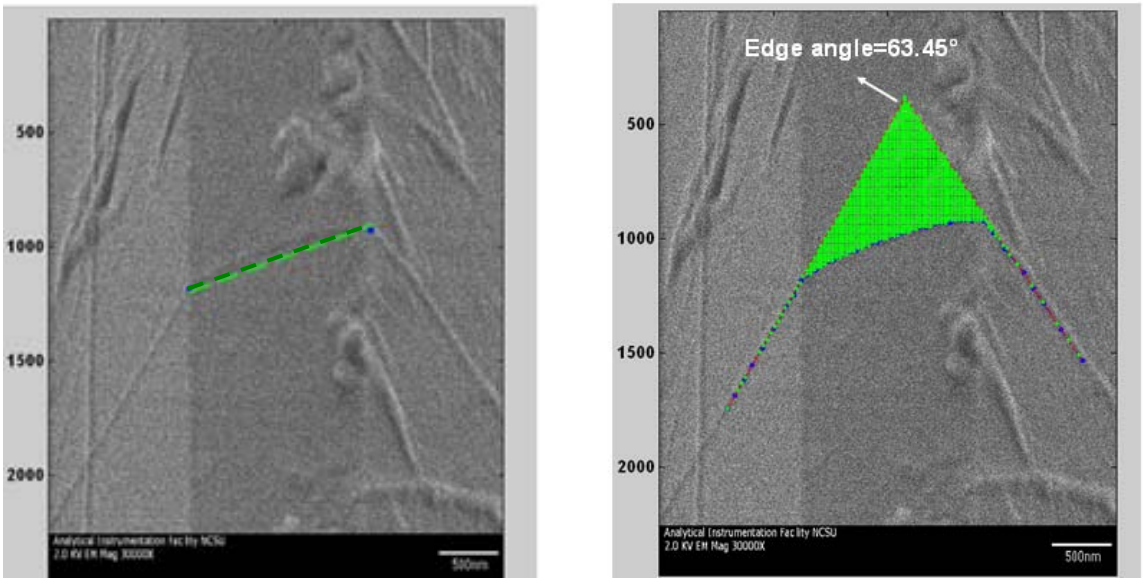

(a) Wear land width (b) Wear area

Figure 5-24 SEM images of diamond tool edge with 30,000X magnification

In summary, the machining of the biconic mirror with 3 fiducial features for kinematic coupling proves the feasibility of basic concept to create both functional and fiducial surfaces in one tool setup with the FLORA. The measurement of created surfaces with a LVDT also indicates surface profile has a reasonable error within 4 μm. On the other hand, the significant amount of tool wear (1.61 μm thickness of wear land) in this cutting process may present an ultimate performance limiter to further reduce the profile error.

6. Conclusions and Future Work

This dissertation has focused on the design and control of a Fast Long Range Actuator that consists of a light-weight slide, an air bearing, a linear motor, and a linear encoder using real-time control. It has been used to machine non-rotationally symmetric optical surfaces with millimeters of sag at high production rates with fiducial surfaces for alignment. To retain the surface quality of existing diamond turning machines, i.e. form error of less than 200 nm PV and surface finish of less than 5 nm RMS, the tool motion control quality needs to be within ±20 nm of desired position in all XYZ directions. This positioning objective is to be accomplished while tracking non-periodic motion profiles (with wide frequency contents within a few hundred Hertz) under the influence of disturbance force up to a few Newtons from various physical sources (with wide frequency contents within a few hundred Hertz). It has been proven to be a challenging motion control task due to the simultaneous requirement on the motion range, speed, acceleration and precision.

A systematic approach has been taken for the design and control of this type of actuator:

(1) Design a physical system that is easy to control: Optimize the system components selection/design and integration to minimize error, noise, disturbance and nonlinearities. To this end, a few actions have been taken, including the installation of a Sony encoder with 250 nm signal pitch and the removal of frequency limit for the encoder signal interpolation to minimize the position measurement error at high speed up to 250 mm/sec, a replacement of PWM amplifier with a linear amplifier to reduce electronic noise, the application of data processing techniques on the spindle encoder signal and careful selection of surface geometry representation and data interpolation to minimize the error in the motion trajectory, the development of a DSP-based real-time control platform with the sufficient sampling rate (20 KHz) and the flexibility for the machining tasks, an addition of a counterbalance drive with a VCM driven shaker to the back end of the actuator to reduce the reaction force in the linear actuation configuration.

(2) Develop an effective control approach to minimize the influence of error, noise and disturbance on tool positioning error: The PID and lead-lag controllers first establish the basic position feedback control system, the controller gains are proven to insufficient for the tool servo control due to the limitation of high frequency modes of the open loop system from the amplifier, air bearing and moving mass structure and the stability requirement for the closed-loop system, a feedforward controller and a disturbance observer are then designed to improve the profile tracking and disturbance rejection in the low frequency range up to a few hundred Hertz. A special type of controller (adaptive feedforward controller) with very high gains localized at the selected frequencies to deal with the high magnitudes in the non-periodic motion profiles and disturbances at those frequencies. The localization of the high gains at the discrete frequencies of interest enables stable closed-loop operation and achieve lower error magnitudes at these frequency components than would have been the case if the high gains were distributed evenly over the wide frequency range.

By combining the physical design and controller design to create a new FLORA, it was possible to improve the actuator performance better than either single approach would provide:

(1) The tool motion control performance: ±200 nm PV or 68 nm RMS or position error in X direction, ±100 nm PV or 33 nm RMS position error in Y direction, the tool servo in Z direction ±30 nm PV or 9 nm RMS for position holding error, ±70 nm PV for 2 mm 20 Hz sinusoidal tracking error.

(2) The machining test performance: 7.4 nm RMS surface finish for plated copper with 3.7 nm as baseline DTM performance, 11.5 nm RMS surface finish and 200 nm PV flat error for ∅50 mm acrylic flat, 17 nm RMS surface finish and 900 nm PV flatness error for ∅50 mm acrylic tilted flat with 4 mm excursion.

(3) The fabrication of deployable optic: a biconic mirror (∅98 mm aperture size) with fiducical features for kinematics coupling were created in one tool setup to preserve their geometric relationship within the tolerance of diamond turning process. This

optic is the first one of its kind and it is only feasible with this fast long range actuator.

A further improvement of actuator performance depends on addressing the major design deficiencies in the current prototype. The desired components characteristics are summarized as follows:

(1) Used a porous air bearing with smaller air gap to remove the non-desirable motions other than the feed direction and increase the pitching mode at least three times.

(2) Stiffened the coupling between the slide piston and the motor to increase the structural modes at least three times.

(3) Used a voice coil motor instead of a three-phase linear motor to reduce the error in the electromagnetic force generation.

(4) Used a linear amplifier with higher bandwidth around 5 KHz.

(5) Applied a counterbalance balance drive with the same characteristics as the main drive and back-to-back mechanical setup as the best solution for reaction force reduction.

(6) Increase the speed of digital signal processor (currently 40 MHz) for real-time computation by a factor 10 to further reduce error in the position measurement by the encoder and provide more computational power for trajectory generation and control algorithms.

(7) Increase the resolution of spindle encoder (currently 20000 counts/rev) by a factor of 10 to remove the quantization error in the motion trajectory.

The implementation of changes items (1)-(5) in a total redesign has enabled the second prototype to obtain even superior performance in the flat cutting [2]. On the other hand, while the design change in items (1)-(4) make it possible to implement a feedback control with 1 KHz loop-gain cross-over frequency (which is essential to deal with motion profile and disturbance with frequency contents up to a few hundred Hertz), the current design for the basic position feedback controller with PID and lead-lag approaches is still a trial and

error process, modern design tools such as H∞ and optimal control can be used to optimized the selection of controller parameters in “one shot”. Furthermore, when the tool servo tracks the motion profiles with peak magnitude at more than 10 harmonics of spindle rotation frequency, the adaptive feedforward controller with multiple elements becomes very computationally costive, a more computationally effective repetitive controller shall be explored for these situations.

REFERENCES

1. Nathan Buescher, Live Axis Turning, MS Thesis, Department of Mechanical and Aerospace Engineering, North Carolina State Univ., Raleigh, NC, 2005.

2. Erik Zdanowicz, Design of a Fast Long Range Actuator, MS Thesis, Department of Mechanical and Aerospace Engineering, North Carolina State Univ., Raleigh, NC, 2009.

3. S. Rakuff, Development of a Precision Long-Range Fast Tool Servo System for Diamond Turning. PhD Dissertation. Department of Mechanical Engineering, Univ. of North Carolina at Charlotte, Charlotte, NC, 2005.

4. Marten F. Byl. Design and Control of a Long Stroke Fast Tool Servo. PhD dissertation, M.I.T., Department of Mechanical Engineering, 2005.

5. Xiaodong Lu. Electromagnetically-Driven Ultra-Fast Tool Servos. PhD dissertation, M.I.T., Department of Mechanical Engineering, 2005.

6. Donald Lucas Lamonds, Surface Finish and Form Fidelity in Diamond Turning, MS Thesis, Department of Mechanical and Aerospace Engineering, North Carolina State Univ., Raleigh, NC, 2008.

7. Kari Tammi, Active control of radial rotor vibrations – Identification, feedback, feedforward, and repetitive control methods, Doctoral Dissertation, VTT Publications 634. Otamedia. Espoo. Finland, 2007.

8. Stephen J. Lucwick, A rotary fast tool servo for diamond turning of asymmetric optics. PhD Dissertation, MIT, Department of Mechanical Engineering, 1999.

9. Richard Montesanti, High Bandwidth Rotary Fast Tool Servos and a Hybrid Rotary / Linear Electromagnetic Actuator. PhD dissertation, M.I.T., Department of Mechanical Engineering, 2005.

10. J.D. Drescher, Tool Force, Tool Edge, and Surface Finish Relationships in Diamond Turning. PhD Dissertation, Department of Mechanical and Aerospace Engineering,, North Carolina State University, 1991.

11. C. Arcona, Tool Force, Chip Formation, and Surface Finish in Diamond Turning. PhD Dissertation, Department of Mechanical and Aerospace Engineering, North Carolina State University, 1996.

12. Witoon Panusittikorn, Error compensation using inverse actuator dynamics, PhD Dissertation, Department of Mechanical and Aerospace Engineering, North Carolina State Univ., Raleigh, NC, 2004.

13. K.B. Doyle, V.L. Genberg and G.J. Michels. "Integrated Optomechanical Analysis". SPIE Press, 2002.

14. R.E. Parks and W.P. Kuhn. "Optical alignment with the point source microscope". Proceedings of the SPIE, 5877, 2005.

15. J.M. Rodgers and K.P. Thompson. "Benefits of freeform mirror surfaces in optical design". Proc. of ASPE Winter Topical Meeting on Freeform Optics, 31, pp 73-78, 2004.

16. R.S. Winsor, R.G. Ohl, J.A. Connelly and J.W. McKenty. "Optical design of an infrared multi-object spectrometer utilizing a free-form optical surface". Proceedings of the ASPE Winter Topical Meeting on Freeform Optics, 31, pp 79-83, 2004.

17. J.J. Mader, D.M. Combs, N.E. Claytor and O.M. Lechuga. "Fabrication examples of non-rotationally symmetric optical elements". Proceedings of the ASPE Winter Topical Meeting on Freeform Optics, 31, pp 84-87, 2004.

18. R.G. Ohl, A. Sohn, T.A. Dow and K.P. Garrard. Highlights of the ASPE 2004 Winter Topical Meeting on free-form optics: design, fabrication, metrology, assembly. Proceedings of the SPIE, 5494, 2004.

19. S.R. Patterson and E. B. Magrab, "Design and Testing of a Fast Tool Servo for Diamond Turning", Precision Engineering, 1985, Vol 8, pg 123-128.

20. S.R. Patterson and T.T. Saito, "Diamond Turning Wavefront Correctors: opening new optical design flexibilities", Proc SPIE, Vol 676, pg 10-16, 1986.

21. J. D. Rasmussen. "Dynamic variable depth of cut machining using piezoelectric actuators". International Journal of Machine Tools and Manufacture,34(3):379-392, 1994.

22. T. A. Dow, M. H. Miller, and P.J. Falter. “Applicationof a fast tool servo for diamond turning of nonrotationally symmetric surfaces”. Precision Engineering, 13(4), 1991.

23. United States Patent 5,467,675. Apparatus and method for forming a workpiece surface into a non-rotationally symmetric shape. T.A. Dow, K.P. Garrard, G.M. Moorefield, II and L.W. Taylor, 1995.

24. K. J. Falter and David H. Youden. “The characterization and testing of a long stroke fast tool servo”. International Progress in Precision Engineering: Proceedings of 8th International Precision Engineering Seminar, 1995.

25. J. F. Cutttino. “Performance optimization of a fast tool servo for single-point diamond”. IEEE/ASME Trans. on Mechatronics, 4(2), June 1999.

26. X. Wang. “Experimental research on the linear motor micro-feed devices with high frequency response, long travel and high accuracy”. Annals of the CIRP, 40(1):379-382, 1991.

27. Y.E. Tohme and J.A. Lowe. “Machining of freeform optical surfaces by slow slide servo method”. Proceedings of the Eighteenth Annual Meeting of the ASPE, 30, 111-114, 2003.

28. R.S. Winsor, R.G. Ohl, J.A. Connelly and J.W. McKenty. “Optical design of an infrared multi-object spectrometer utilizing a free-form optical surface”. Proceedings of the ASPE Winter Topical Meeting on Freeform Optics, 31, pp 79-83, 2004.

29. E. Brinksmeier, D. Grimme and W. Preuss. “Generation of freeform surfaces by diamond machining”. Proc. of the 17th Annual Meeting of the ASPE, 27, 542-545, 2002.

30. D. Trumper and X.D. Lu, “Fast Tool Servos: Advances in Precision, Acceleration, and Bandwidth”, Towards Synthesis of Micro-/Nano-systems, The 11th International Conference on Precision Engineering (ICPE) August 16–18, 2006, Tokyo, Japan, p11-19.

31. W. Greene and D. Shinstock, “Design of a linear voice coil actuator for fast tool servo applications”. Proc. Of ASPE Annual Conference, 1997 p187-190.

32. S. Ludwick and D. L. Trumper, “Design of a rotary fast tool servo for ophthalmic lens fabrication”, Precision Engineering, 23(4):253-259, 1999.

33. M. H. Weck, H. Oezmeral, K. Mehlkopp, T. Terwei, “A new hybrid concept for a long stroke fast tool servo system”. Proc. of ASPE 1995 annual meeting, 1995, p211-214.

34. M. Weck, “New Structured Air Bearings without Nozzles”, Proceedings 1st euspen conference, Bremen, Germany, 1999.

35. M. Weck, J. Hennig, O. Wetter, “Long Stroke Fast Tool Servo with Dynamic Mass Compensation and Hydrostatic Bearings”, Proc. of euspen conference, Aachen, 2003.

36. C. Brecher, M.Weck, M. Winterschladen and O. Wetter, “Manufacturing of Free-Form Surfaces Using a Fast Tool Servo (FTS) and an Online Trajectory Generator”, ASPE Proceeding, Topical meeting on Control of Precision Systems, April 2004.

37. D. Wu, X. Wang, T. Zhao and W. Lv, “Application of active disturbance rejection to tracking control of a fast tool servo system”, Proceedings of the 2005 IEEE Conference on Control Applications, Toronto, Canada, August 28-31, 2005, p547-552.

38. A. Babinski and T-C. Tsao, "Acceleration Feedback Design for Voice Coil Actuated Direct Drive," Proc. American Control Conference, 3713-3717, San Diego, CA, June 1999.

39. R. G. Reddya, R. E. DeVor, S. G. Kapoora and Z. Sun, “A mechanistic model-based force-feedback scheme for voice-coil actuated radial contour turning “, International Journal of Machine Tools and Manufacture, Volume 41, Issue 8, June 2001, P1131-1147

40. Kim, B. S., Li, J. and Tsao, T-C., "Control of a Dual Stage Actuator System for Noncircular Cam Turning Process," Proc. American Control Conference, 2549-2554, Arlington, VA, June 2001.

41. B. S. Kim, J. W. Li, T. C. Tsao, “Two-parameter robust repetitive control with application to a novel dual-stage actuator for noncircular machining”, IEEE/ASME Transactions on Mechatronics, 9(4): 644-652, 2004.

42. B. S. Kim, T. C. Tsao, “A performance enhancement scheme for robust repetitive control system”, Journal of Dynamic Systems, Measurement and Control, 126(3): 224-229, 2004.

43. K. Srinivasan and T-C. Tsao, "Machine Tool Feed Drives and Their Control - A Survey of the State of the Art", ASME Journal of Manufacturing Science and Engineering, 119, 1997, p743-748.

44. M.H. Miller, K.P. Garrard, T.A. Dow and L.W. Taylor, “A controller architecture for integrating a fast tool servo into a diamond turning machine”, Precision Engineering, January 1994, vol 16, NO 1, pp42-48.

45. Reynold and Meckl, “The application of command shaping to the tracking problem”, ASME Journal of Dynamic Systems, Measurement and Control, May 2008, Vol. 130, 031007 (p1-12).

46. Ho Seong Lee, and Tomizuka, M., “Robust motion controller design for high-accuracy positioning systems”, IEEE Transactions on Industrial Electronics, v 43, n 1, Feb. 1996, p 48-55

47. M. Tomizuka, “Zero phase error tracking algorithm for digital control”, ASME Journal of Dynamic Systems, Measurement and Control, 1987, Vol 109, p65-68.

48. M. Tomizuka, “On the design of digital tracking controllers”, ASME Journal of Dynamic Systems, Measurement and Control, 1993,Vol 115, 412-418.

49. S. Endo, H. Kobayashi, C. J. Kempf, S. Kobayashi, M. Tomizuka and Y. Hori, “Robust digital tracking controller design for high-speed positioning systems”, Control Engineering Practice, Vol. 4, Issue 4, April 1996, p527-536.

50. M. Tomizuka, M.S. Chen, S. Renn and T.C. Tsao, “Tool positioning for noncircular cutting with lathe”, Journal of Dynamic Systems, Measurement and Control, Transactions ASME, v 109, n 2, Jun, 1987, p 176-179.

51. H. Shim, M. Kochem, and M. Tomizuka., “Use of accelerometer for precision motion control of linear motor driven positioning system”, IECON '98. Proceedings of the 24th Annual Conference of the IEEE Industrial Electronics Society (Cat. No.98CH36200), 1998, vol.4, pt. 4, p 2409-2414.

52. E.D Tung, M. Tomizuka and Y. Urushisaki, “High-speed end milling using a feedforward control architecture”, Transactions of the ASME. Journal of Manufacturing Science and Engineering, v 118, n 2, May 1996, p178-87

53. M. Tomizuka, “Robust digital motion controllers for mechanical systems”, Robotics and Autonomous Systems, 1996, vol. 19, p143-149.

54. A. T. Elfizy, G. M. Bone and M. A. Elbestawi, “Model-based controller design for machine tool direct feed drives”, International Journal of Machine Tools and Manufacture, Volume 44, Issue 5, April 2004, Pages 465-477

55. D. Renton and M.A. Elbestawi, “Motion control for linear motor feed drives in advanced machine tools”, International Journal of Machine Tools and Manufacture, Volume 41, Issue 4, March 2001, Pages 479-507

56. D. Renton and M.A. Elbestawi, “High speed servo control of multi-axis machine tools”, International Journal of Machine Tools and Manufacture, Volume 40, Issue 4, March 2000, Pages 539-559

57. Shang-Liang Chen and Tsung-Hsien Hsieh, “Repetitive control design and implementation for linear motor machine tool”, International Journal of Machine Tools and Manufacture, Volume 47, Issues 12-13, October 2007, p1807-1816.

58. Mu-Tian Yan and Yau-Jung Shiu, “Theory and application of a combined feedback-feedforward control and disturbance observer in linear motor drive wire-EDM machines”, International Journal of Machine Tools and Manufacture, October 2007

59. K. K. Tan, S. N. Huang, H. F. Dou, T. H. Lee, S. J. Chin and S. Y. Lim, “Adaptive robust motion control for precise trajectory tracking applications”, ISA Transactions, Vol. 40, Issue 1, January 2001, Pages 57-71

60. P. Van Den Braembussche, J. Swevers, H. Van Brussel and P. Vanherck, “Accurate tracking control of linear synchronous motor machine tool axes”, Mechatronics, Vol. 6, Issue 5, August 1996, p 507-521

61. T. C. Tsao, "Optimal Feed-Forward Digital Tracking Controller Design," ASME Journal of Dynamic Systems, Measurement, and Control, 116, 583-592, 1994.

62. T.C. Tsao and M. Tomizuka, “Adaptive Zero Phase Error Tracking Algorithm for Digital Control"," ASME Journal of Dynamic Systems, Measurement, and Control, 109, 349-354, Dec. 1987.

63. J.Z.Xia and C.H. Menq, “Precision tracking control of nonminimum-phase systems with zero phase error”, International Journal of Control, Vol. 61, Issue 4, 1995, p791-807.

64. G. Pritschow and W. Philipp, “Research on the efficiency of feedforward controllers in direct drives,”, Ann. CIRP 41(1), 1992, p411-415.

65. H. Sung and S. Hara, “Properties of sensitivity and complementary sensitivity functions in single-input single-output digital control system”. International Journal of Control, 48(6), 1988, p2429-2439.

66. Linear Motor Application Catalog, www.Airex.com

67. Brushless AC motor commutation, Sinusoidal commutation with a PC based motion controller. Application Note.

68. Dal Y. Ohm and Jae H. Park, “About commutation and current control methods for brushless motors”, 29th Annual IMCSD Symposium, San Jose, July 26-29, 1999.

69.Http://www.danahermotion.com/education/learn_about_mc/servohandbook/drive/motorcontrol/commutation.php

70. Refaat, S. and Nahavandi, S., “Control loop for finding initial translator position of linear synchronous motor”, Int. Journal of Robotics & Automation, v 19, n 2, 2004, p 59-65.

71. Ion Boldea and S.A. Nasar, Linear motion Electromagnetic devices, Talylor & Francis, 2001.

72. Basak, Permanent magnet DC linear motors, Oxford University Press, 1996

73. G. F. Franklin and J. D. Powell, Feedback Control of Dynamic Systems, Addison-Wesley Publishing Company, Inc., 1995, 3rd edition.

74. Graham C. Goodwin, Stefan F. Graebe, and Mario E. Salgado, Control System Design, Prentice Hall, 2000.

75. John G. Proakis and Dimitris G. Manolakis, Digitial Signal Processing, Prentice Hall, 1996, 3rd edition.

76. Kobayashi, A., Machining of plastics, 1981, Robert E. Krieger Publishing Company.

77. Liu, X, DeVor, R.E, Kapoor, S.G. and Ehmann, K.F. The mechanics of machining at the microscale: assessment of the current state of the science. Journal of manufacturing science and engineering, Vol.126, Nov. 2004, p666-678.

78. Merchant, M.E., "Mechanics of the metal process: I Orthogonal cutting and A type 2 chip", Journal of applied physics, Vol.16, May 1945, p267-275.

79. Merchant, M.E., Mechanics of the metal process: II Plasticity conditions of orthogonal cutting. Journal of applied physics, Vol.16, June 1945, p318-324.

80. M. Weck, R. Hartel, K.Modemann and L.f. Werkzeugmascheinen, "Performance assessment in ultraprecision machining", Annals of the CIRP, Vol 37, 1, 1988, p499-502.

81. Y. Furukawa and N.Moronuki, "Effect of material properties on ultra precise cutting processes", Annals of the CIRP, Vol.37, 1988

82. B.L. Lawson, N. Kota and O.B. Ozdoganlar, "Effects of crystallographic anisotropy on orthogonal micromachining of single-crystal aluminum", Journal of manufacturing science and eignineering, Vol.130, June 2008, 031116-1-11.

83. J. Schaefer, C. Arcona, T.A.Dow, G.M. Moorefield, K. Falter and R.L. Rhorer, "Diamond tool point force measurement in a production environment", Proceeding of American Society for Precision Engineering, 1996, p412-415.

84. J.H.Dautzenberg and J.A.G.Kals, "Surface roughness caused by metal forming", Annals of the CIRP, vol. 34, 1, 1985, p477-479.

85. S. Takasu, M. Masuda, T. Nishiguchi, “Influence of study vibration with small amplitude upon surface roughness in diamond machining”, Annals of the CIRP, Vol.34, 1, 1995, p463-467.

86. C.F.Cheung and W.B.Lee, “A theoretical and experimental investigation of surface roughness formation in ultra-precision diamond turning”, International journal of machine tools & manufacture, 40 (2000), 979-1002.

87. C.F.Cheung and W.B.Lee, “Characterisation of nanosurface generation in single-point diamond turning”, Int. journal of machine tools & manufacture, 40 (2001), 851-875.

88. H. Hocheng and M.L.Hseih, “Signal analysis of surface roughness in diamond turning of len molds”, International journal of machine tools & manufacture, 44 (2004), 1607-1618.

89. T. Sata, M. Li, S. Takata, H. HIroka, C.Q. Li, X.Z.Xing and X.G. Xiao, “Analysis of surface roughness generation in turning operation and its applications”, Annals of the CIRP, Vol.34,1985

90. E.Brinksmeier and O.Riemer, “Measurement of optical surfaces generated by diamond turning”, International journal of machine tools & manufacture, 38(5-6), 1998, 699-705.

91. Alex Sohn, Lucas Lamonds and Ken Garrard, “Modeling of vibration in single-point diamond turning”, Proceeding of ASPE conference, 2007.

92. X.D. Lu and D.L. Trumper, “Spindle rotary position estimation for fast tool servo trajectory generation”, International journal of machine tools & manufacture, 47, (2007), 1362-1367.

93. K.P. Garrard and A. Sohn. Off-axis biconic mirror fabrication. Precision Engineering Center Annual Report, XX, 263-286, (2003).

94. Kirk Rogers and Jeff Roblee, “Freeform Machining with Precitech Servo Tool Options”, Precitech turtorials.

95. Marten F. Byl, Stephen J. Ludwick and David L. Trumper, “A loop shaping perspective for tuning controllers with adaptive feedforward cancellation”, Precision Engineering, Vol. 29 (1), January 2005, p27-40.

96. W. Messner and M. Bodson, “Design of adaptive feedforward algorithms using internal model principle”, International journal of adaptive control and signal processing, Vol.9(2), 1995, p199-212.

97. A.H. Sacks, M. Bodson and W. Messner, “Advanced methods for repeatable runout compensation”, IEEE Trans. on Magnetics, Vol.31(2), 1995, p1031-1036.

98. M. Bodson, A. Sacks and P. Khosla , “Harmonic generation in adaptive feedforward cancellation schemes”, Proceedings of the 31st IEEE Conference on Decision and Control, Vol.2, Dec. 1992, p1261 – 1266.

99. S. Weerasooriya, J.L. Zhang and T.S. Low, “Efficient implementation of adaptive feedforward runout cancellation in a disk drive”, IEEE Trans. on Magnetics, Vol,32(5), 1996, p3920 -3922.

100. Y. Zhou, M. Steinbuch and G. Leenknegt, “A cost-effective scheme to improve radial tracking performance for higher-speed optical disk drives”, Journal of Vibration and Control”, Vol.10, 2004, p795-810.

101. Y.S. Lu and S.M. Lin, “Disturbance-observer-based adaptive feedforward cancellation of torque ripple in harmonic drive systems”, Electrical Engineering, (2007) 90:95-106.

102. C. Kempf, W. Messner, M. Tomizuka and R. Horowitz, “A comparison of four discrete-time repetitive control algorithms”. IEEE Control Systems Magazine 12 (6), 1993, p 48–

103. S. Zhao and K.K. Tan, “Adaptive feedforward compensation of force ripples in linear motors”, Control Engineering Practice, Vol.13 (9), September 2005, p1081-1092.

104. B.A. Francis, W.M. Wonham, “The internal model principle of control theory”, Automatica, Vol. 12 (5), September 1976, p457-465.

105. M. Tomizuka and C. Kempf. “Design of discrete time repetitive controllers with applications to mechanical systems”, Proceedings of the 11th IFAC World Congress, 3:243–248, 1987.

106. C. R. Knospe, S. J. Fedigan, R. W. Hope and R. D. Williams, “A multitasking DSP implementation of adaptive magnetic bearing control”. Trans. on Control Systems Technology, Vol 5, No 2, 1997, p230–238.

107. C. R. Burrows and M. N. Sahinkaya, “Vibration control of multi-mode rotor-bearing systems”. Proc. of the Royal Society of London. Series A, Math.l and Phy. Sciences. Vol. 386, No, 1790. 1983. p77-94

108. S. R. Hall and N. M. Wereley, “Linear control issues in the higher harmonic control of helicopter vibrations”. Proc. of 45th Annu. Forum Amer. Helicopter Soc. Boston, USA. pp. 955–971. 1989.

109. L. A. Sievers and A. H. von Flotow, “Linear control design for active vibration isolation of narrow band disturbances”. Proc. of 27th Decision and Control Conf. Vol 2, IEEE, 1988, p1032–1037.

110. K. Ohnshi, M. Shibata and T. Murakami, “Motion control for advanced mechatronics”, IEEE/ASME Trans. on Mechatronics, Vol. 1, NO 1, March 1996, p56-67.

111. Lin Guo, “Reducing the manufacturing costs associated with hard disk drives-a new disturbance rejection control scheme”, IEEE/ASME Trans. On Mechatronics, Vol. 2 Issue 2, June 1997, p77-85.

112. D. Wu, Xiankui Wang, Tong Zhao and Weilong Lv, “Application of active disturbance rejection to tracking control of a fast tool servo system”, Proceedings of 2005 IEEE Conference on Control Applications, 28-31 Aug. 2005, p547 – 552.

113. K.K. Tan, T.H. Lee, H.F. Dou, S.J. Chin and S. Zhao, “Precision motion control with disturbance observer for pulsewidth-modulated-driven permanent-magnet linear motors”, IEEE Trans. on Magnetics, Vol.39, NO.3, May, 2003, p1813-1818.

114. K.K. Tan and Shao Zhao, “Precision motion control with a high gain disturbance compensator for linear motors”, ISA Trans., Volume 43, Issue 3, July 2004, p399-412

115. Dailin Zhang, Youping Chen, Wu Ai and Zude Zhou, “Precision motion control of permanent magnet linear motors”, The International Journal of Advanced Manufacturing Technology, Vol.35, NO. 3-4 / December, 2007.

116. T. Mita, M. Hirata, K. Murata, H. Zhang, “H_∞ control versus disturbance-observer-based control”, IEEE Trans. on Industrial Electronics, Vol.45(3), Jun 1998, p488-495.

117. S. Komada, M. Ishida and K. Ohnishi, “Disturbance observer-based motion control of direct drive motors”, IEEE Trans. on Energy Conversion, 6 (3), SEP 1991, p553-559.

118. J.N. Teoh, C. Du, G. Guo and L. Xie, “Rejecting high frequency disturbances with disturbance observer and phase stabilized control”, Mechatronics 18, 2008, p53-60.

119. Chun-Chih Wang and Masayoshi Tomizuka, "Design of Robustly Stable Disturbance Observers Based on Closed Loop Consideration Using H/sub infinity / Optimization and Its Applications to Motion Control Systems," Proceedings of the 2004 American Control Conference, Vol.4, pp.3764-3769, Boston, MA, June 2004.

120. K.K. Tan, S.Y.Lim, H. Tong, H. Dou, “High-precision control of linear actuators incorporating acceleration sensing”, Robotics and Computer Integrated Manufacturing 16 (2000), p295-305.

121. M.T. White and M. Tomizuka, “Increased disturbance rejection in magnetic disk drives by acceleration feedforward control and parameter adaptation”, Control Engineering Practice, v 5, n 6, June 1997, p 741-51

122. Soo Jeon and Masayoshi Tomizuka, "Benefits of Acceleration Measurement in Velocity Estimation and Motion Control," Control Engineering Practice,V15, no3, p325-332, 2007.

123. S. Douglas, “A Machining System for Turning Nonaxisymmetric Surfaces”, PhD Dissertation, University of Tennessee, 1983.

124. B.M. Lane, M. Shi, T.A. Dow, R. Scattergood, “Diamond tool wear when machining Al6061 and 1215 steel”, Wear, under review.

APPENDEX

Appendix A – FLORA Control System Electrical Schematics

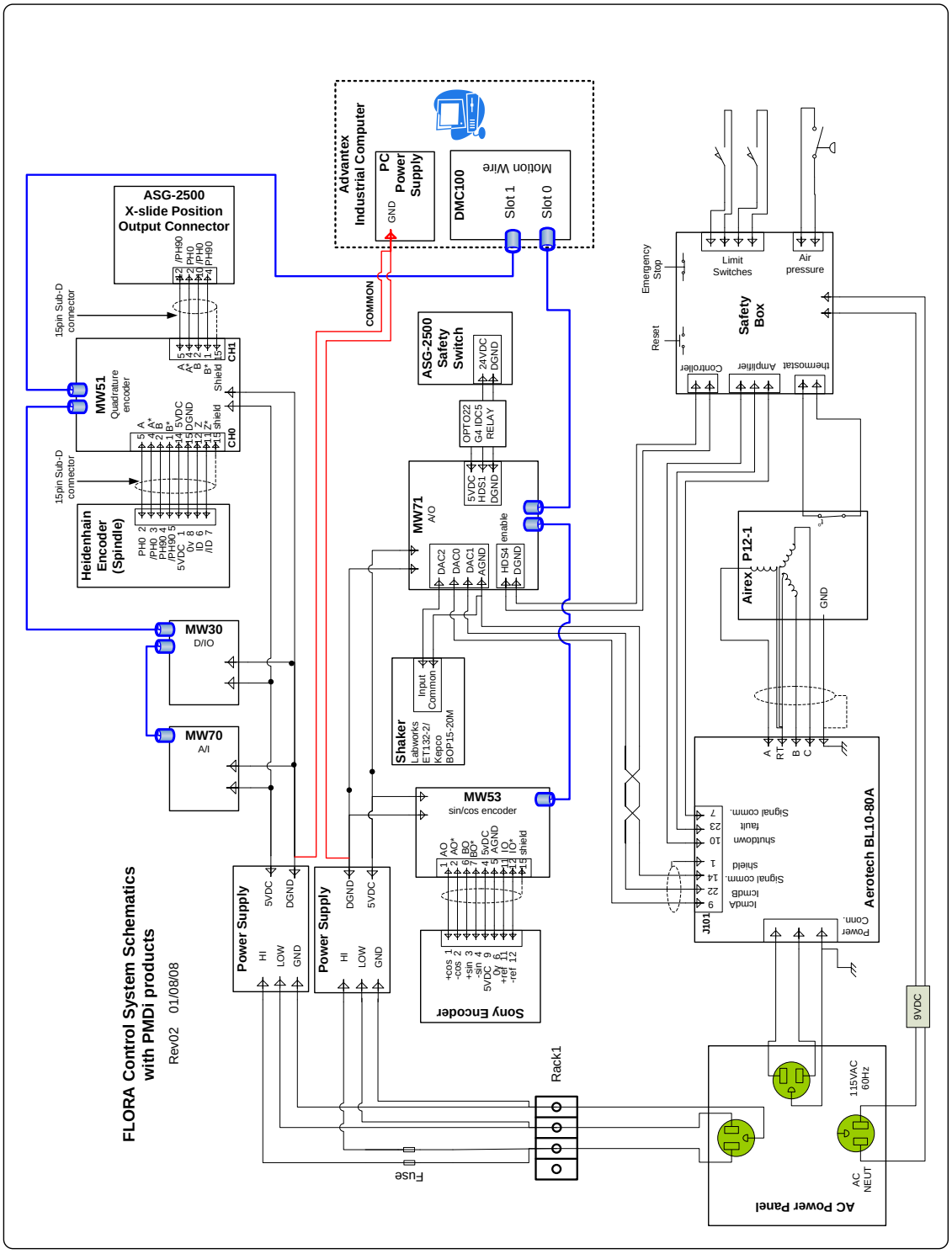

Appendix B – Concept of Cooling Process for Motor Coil

The concept of pressurized air cooling for the linear motor was developed by Jacob Galloway on a setup as shown in Figure B-1. The prototype emulates the thermal process of the linear motor, the motor "forcer" and "magnet track" are made of aluminum material. The experiment involved three major components: the motor model, the thyristor (dimmer switch), and the cartridge heater. Pressurized air is forced through the fitting on the front of "magnet track", the cartridge heater acted as the heat generated by the motor. The heater wires can be seen exiting the front of the motor portion of the model, while the thermocouple wire is seen on top.

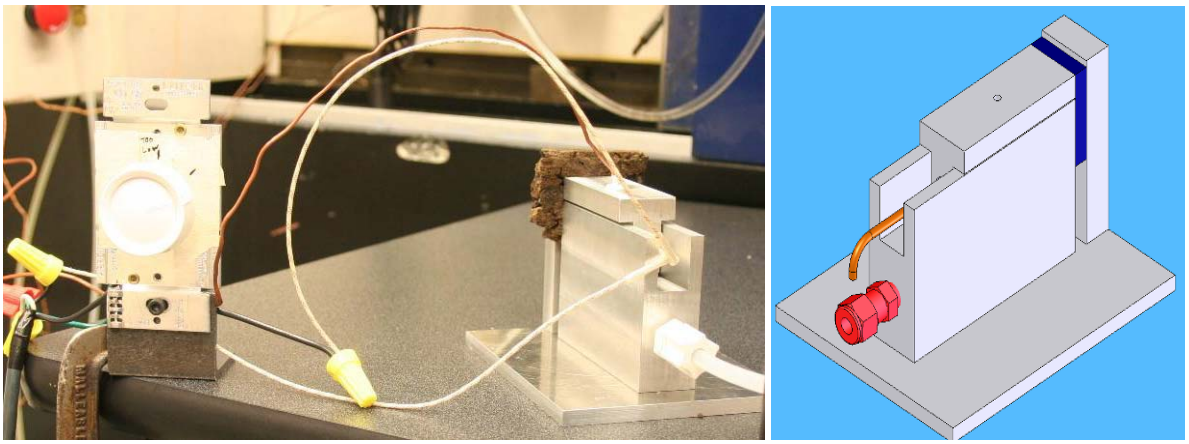

(a) A photograph of setup (b) 3D Model

Figure B-1 Experimental Setup

The basic idea is to put orifices on the base of "magnet track", so there is forced air convection in the gap between "forcer" and "magnet track". Equation (B.1) and (B.2) give a simplified modeling for this thermal system without and with the forced convection in the motor air gap. The coefficient of the forced air convection depends on the supplied air pressure and the size of orifice. Table B.1 shows the experimental results with single orifice of ∅0.5 mm under different heat input and air pressure level. The final motor temperature is

measured at equilibrium condition with a handheld thermometer. The forced air film coefficient is derived from the measured temperature. The measured temperature increases as heat input increases, and decreases as supply pressure increases. At 17.0 W, a supply pressure of 80 psi was able to keep the motor 22 °C cooler than a pressure of 40 psi. This figure also shows the film coefficients (*h*). At the same pressures, these values did not change as the heat generation changed. This shows that the data is consistent.

$$mC\dot{T}_{motor} = Q + \left(h_{free} A_{free} + \frac{kA_{cond}}{L} \right) \left(T_{amb} - T_{motor} \right) \tag{B.1}$$

$$mC\dot{T}_{motor} = Q + \left(h_{forced} A_{forced} + h_{free} A_{free} + \frac{kA_{cond}}{L} \right) \left(T_{amb} - T_{motor} \right) \tag{B.2}$$

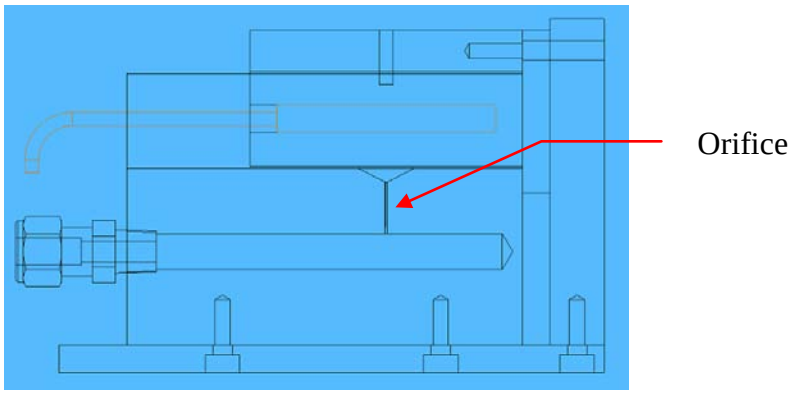

Figure B-2 The orifice on the base of "magnet track"

Table B.1 Final temperature readings from handheld device and film coefficients

Heat Generation (W)	Supply Pressure (psi)	Final Motor Temp(°C)	h (W/m2*K)
31.4	80	139	60.0
17.0	80	85	60.0
	60	93	53.2
	40	107	44.6
10.5	80	60.6	59.2
	60	64.6	53.8

Appendix C – Open Loop Operations

C.1 Sinusoidal commutation

Commutation is a process of channeling current in motor windings to produce actuation force. Brushless motors require "electronic commutation," a process where the drive determines which winding should carry current so the commanded force can be produced with the minimal current. The determination of the current relies heavily on the relative position between the motor coil and permanent magnet, as a result, the commutation, particularly, the sinusoidal commutation requires high resolution position feedback sensor.

Sinusoidal commutation is a type of electrical commutation that provides the smoothest force as a motor moves. The three windings are fed with three signals that vary sinusoidally with position. For example, with a commanding current *I*, a three-winding motor have three individual phase currents as follows:

$$\begin{cases} I_A = I * \mathbf{sin(}PhasePosition\mathbf{)} \\ I_B = I * \mathbf{sin(}PhasePosition + 120^\circ\mathbf{)} \\ I_C = I * \mathbf{sin(}PhasePosition + 240^\circ\mathbf{)} \end{cases} \quad \text{(C.1)}$$

Note that, in this dissertation work, a software based sinusoidal motor commutation in dual-phase command configuration is taken. The dual-phase inputs (i.e. Phase A and B) are sinusoidal and are 120º out of phase from each other; the third phase (i.e. Phase C) is internally generated by the amplifier. To obtain the phase position in the Equation (C.1), two critical parameters need to be measured.

Distance of a commutation cycle The travel distance of the piston in one commutation cycle of the linear motor is measured by applying voltages at phase position values ranging from 0º to 360º at a small constant current command (i.e. 0.5). The measured value for one cycle is 30.5 mm or about half the range of motion of the motor.

Zero phase detent position Zero phase detent position is the location where an electro-magnetic field of a permanent magnet and the motor coil are aligned. By applying zero

Phase Position command (0 to Phase A and 120º to Phase B) and small constant current command (i.e. 0.5 amp), the piston settles at a fixed position with respect to the encoder index point. This position measurement provides an offset value to obtain the relative piston displacement $x(t)$ with respect to the zero phase detent position. Motor phase position $\varphi(t)$ is obtained at any time instant for commutation purpose as shown by

$$\varphi(t) = \frac{x(t)}{30.5} * 2\pi \tag{C.2}$$

Figure C-1 shows the change of the motor actuation force around the detent position governed by Equation (C.2) where K_f is the motor force constant in WYE connection, I is the amplitude of applied current command, K_f =12.6 N/amp and I = 0.5 amp

$$F_{OL1} = -K_f \cdot I \cdot \sin(\varphi(t)) \tag{C.3}$$

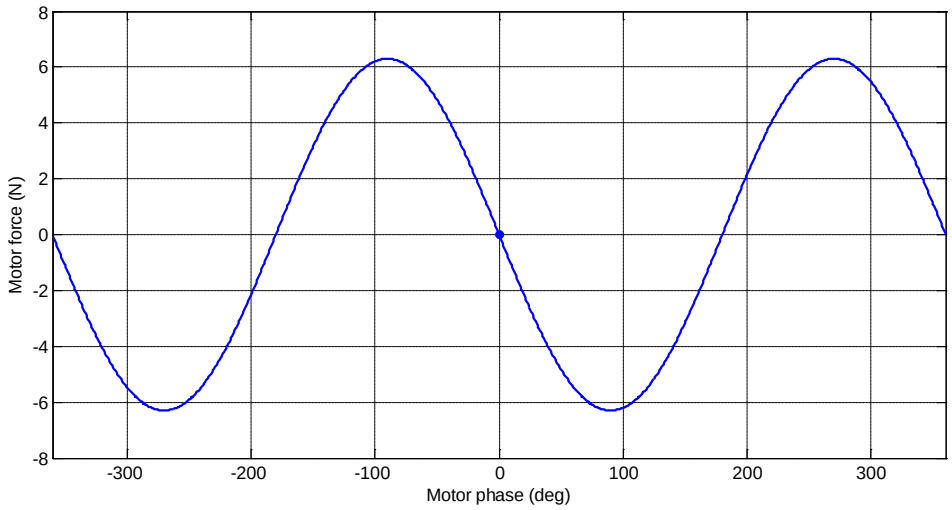

Figure C-1 Variation of motor actuation force in non-commutated operation

It can be seen from Figure C-1 that, by offsetting the commutation angle is offset by an additional 90º so that the magnetic vector of the permanent magnet remains 90º phase ahead of the magnetic vector of the coil. As a result, the motor force output is maximized during the commutated operation.

$$\begin{cases} I_A = I * \mathbf{sin(} PhasePosition + 90^\circ \mathbf{)} \\ I_B = I * \mathbf{sin(} PhasePosition + 120^\circ + 90^\circ \mathbf{)} \\ I_C = I * \mathbf{sin(} PhasePosition + 240^\circ + 90^\circ \mathbf{)} \end{cases} \quad \text{(C.4)}$$

C.2 Commutated Open Loop Operation

Excitation command procedure Since the piston has nothing but inertia to hold it in position, the excitation command for the open loop tests must be carefully selected to keep the piston from hitting the end of travel. The following procedures were developed.

- Use a cosine current command to avoid drift of the driven mass. The applied force and acceleration is a negative cosine wave and position response is a sine wave.
- Switch the cosine current command to new frequency at its peak value; that is, when the piston is stationary. This creates a smooth transition between different frequencies.
- Start the test sequence at low frequency so that the current commanding sequence increases from zero for smooth operation.
- Select command amplitudes *I* and frequencies ω based on the Equation (C.3) to make the position response amplitude *A* remain at the same level.

$$A = \frac{K_f I}{m\omega^2} \quad \text{(C.3)}$$

- Command amplitudes *I* and frequencies ω are limited by the continuous peak current requirement of the motor, 2.6 amp; the speed limit of 20 mm/sec due to the frequency limit of the Heidenhain encoder interpolator and retained for the test with Sony encoder. For noise reasons, the command amplitude *I* should be larger than 0.001 amp.

Figure C-2 shows the selection of test points (in dots) in three test groups. Corresponding current command amplitude will be calculated from Equation (C.3) to obtain 0.02mm position response amplitude for Group 1, 0.001mm for Group 2, and 0.0001mm for Group 3. The arrows in the Figure C-2 indicate the frequency increasing sequence in the execution. Figure C-3(a) shows the increasing current command to keep 0.02mm position response amplitude for test Group 1. Figure C-2 (b&c) are expanded views of the command and the

response. The 8 Hz excitation signal starts at 59.90845 second and the time duration for each frequency is 2 seconds.

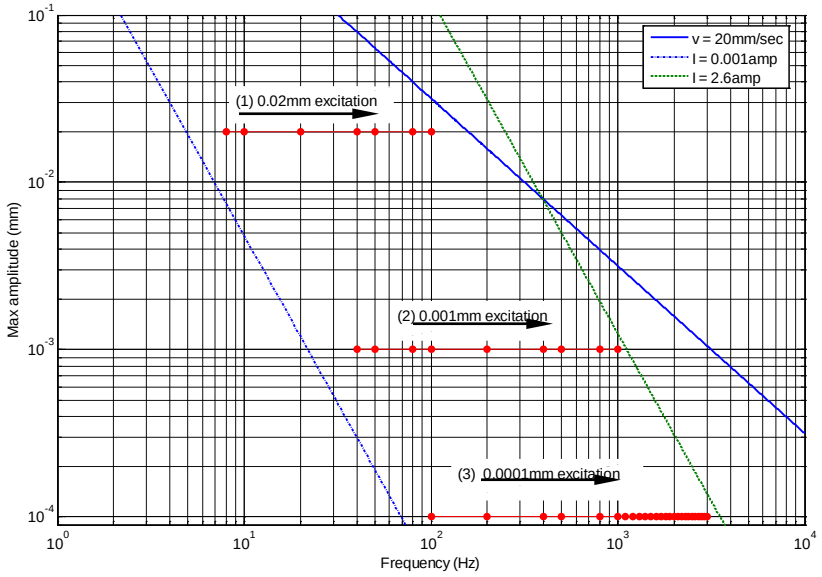

Figure C-2. Open loop frequency response test points selection

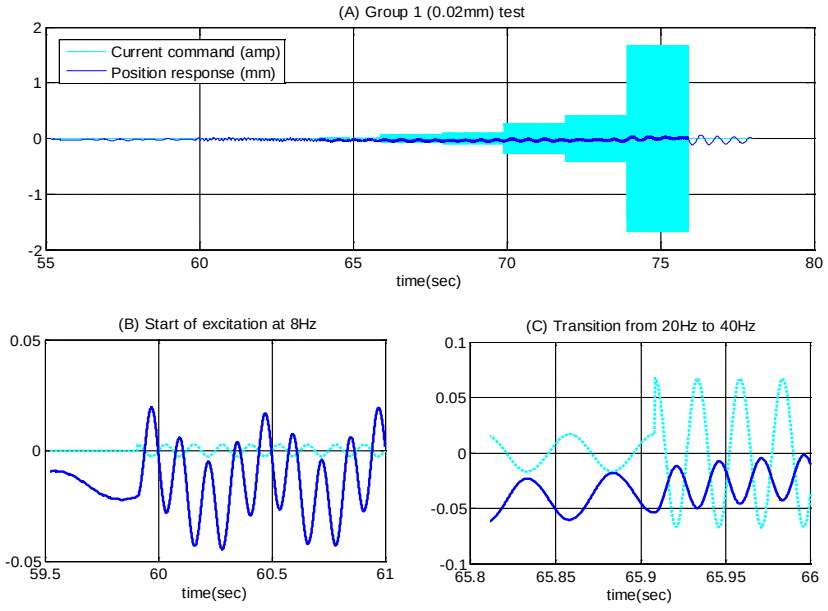

Figure C-3 Open loop responses to sinusoidal excitation with increasing frequency and amplitude

Test method Additional measures are taken to achieve smooth position response during the test:

- The applied current command is set as zero before and after the excitation command sequence.
- The motor is operated in commutated mode even before the excitation signal is activated.
- The driven mass is loosely held in place by a rubber band.

Data processing The application of systematic techniques to process the raw data is critical to generating valid open loop frequency response plots. The following process was developed:

- Apply a high pass filter to remove the low frequency position oscillation, for example, the 2 Hz natural frequency introduced by the rubber band used to hold the piston near center.
- Locate the time instant when the excitation command at a frequency is applied, take the response position data from that time instant. There is totally 40000 data points for each frequency level (2 seconds in 20 KHz sampling rate).
- Apply FFT of the 40000 data points to obtain magnitude and phase information at each excitation frequency level.
- Compare response with equivalent position commands: 0.02 mm position response amplitude for test Group 1, 0.001 mm for Group 2, and 0.0001 mm for Group 3, 180^{o} phase for all three groups. Take average values at the overlapping test points, the magnitude (in ratio) and phase frequency response to obtain as shown in Figure C-3 for the Heidenhain encoder.

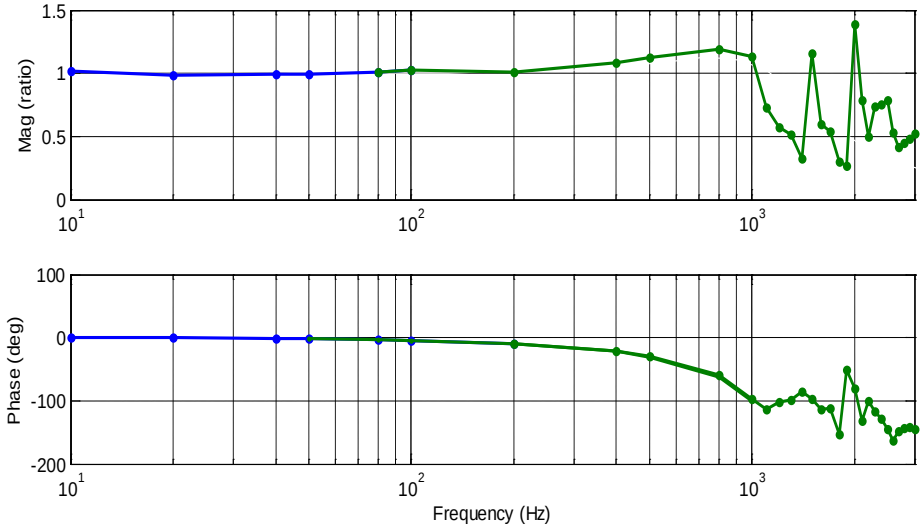

Figure C-4 Commutated open loop system frequency responses

Appendix D – Matlab SIMULINK Model of Servo Control

A control system with PID and acceleration feedforward controller

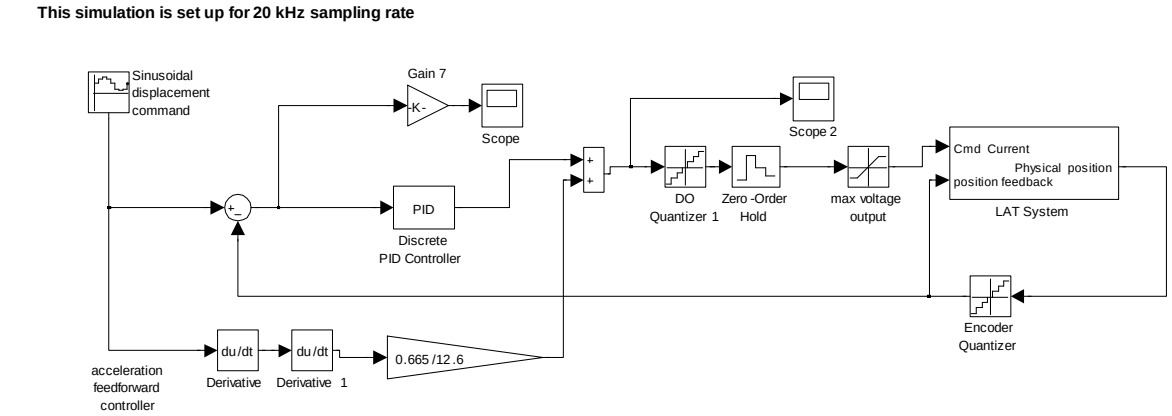

Open loop dynamics of FLORA

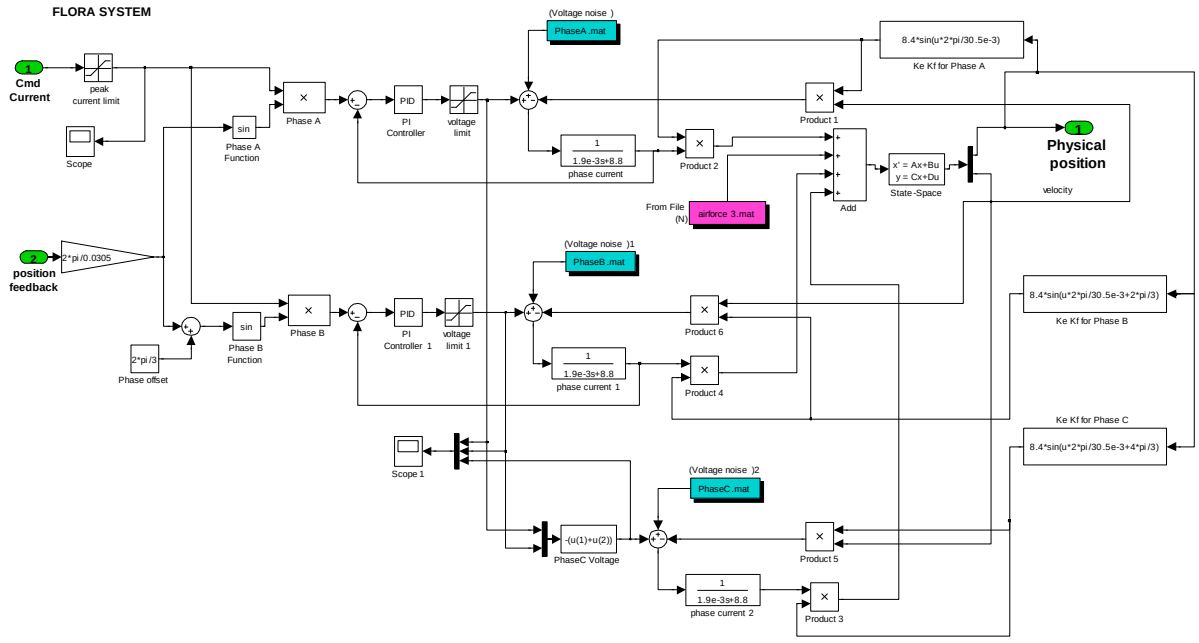

Appendix E – Machining of Biconic Mirror with Fiducial Feature

Rough Machining

Use conventional machining process to cut a blank out of 6061-T651 Aluminum as shown in Figure E-1. The thickness of the blank is large to avoid any distortion due to vacuum chuck attachment.

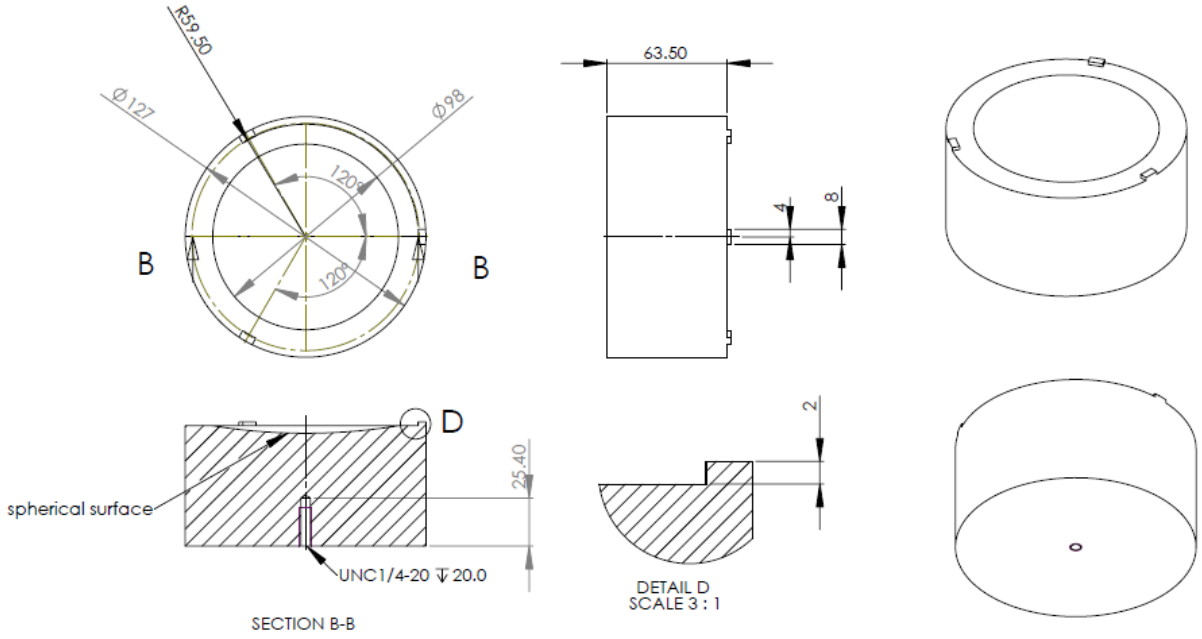

Figure E-1 Optical blank used for the mirror and fiducial fabrication.

Preparation Machining of RS Surfaces

Use a diamond tool with regular clearance angle and tool radius of 1 mm to cut three surfaces with following specifications

(1) Cut the flat between the radial position 57 mm and 49 mm

(2) Cut the spherical concave surface with a radius of 304.881 mm, the depth of spherical apex shall be 3.943 mm below the reference flat surface.

(3) Remove the material on the fiducial features till its top flat surface is 1.9 mm above the reference flat surface.

Detailed steps of Final Machining

Use the customized tool with 27° clearance angle. In the following steps, The command is (x,z) location in mm for machining the surface and return for the subsequent pass:

(1) Install the part with the θ=0° at the center of the selected fiducial feature.
(2) Set FLORA position at neutral value = 17.100 mm by active control
(3) Machine the flat reference surface (500 rpm spindle speed)
(4) Touch off on flat surface and remove 10 μm of material
(5) Shift the ASG-2500 DTM relative z position by -3.943+0.010 mm (*setz d -3.933*). This will set the desired position of the bottom of the sphere but the tool slightly above the surface. This sphere has already been machined so the relative position of the flat and bottom of sphere should be correct.
(6) Move the ASG to the relative (x,z) position to (0,5)
(7) Machine the sphere (500 rpm spindle speed)
(8) Close FLORA control and restart with the sphere program in which the FLORA position depends on the radial position.
(9) Run ASG machining motion cycle as (0,5)→(50,5)→(50,0)→(0,0)→(0,5), remove 10 μm of material to put the base of the sphere in the correct relationship with the flat (3.943). Depth of cut shall be 8 μm and feed rate 30 μm/rev for rough pass, depth of cut shall be 2 μm and feed rate 20 μm/rev for finish pass.
(10) Take off the part and measure the spherical surface, shows the spherical error of 225 nm.
(11) Put the part back to the chuck, Shift the ASG relative z position by 0.329 mm (*setz d 0.329*).
(12) Machine the M4 surface (500 rpm spindle speed)

(13) Close FLORA control, and reprogram and launch the FLORA control for the M4 biconic surface

(14) Run ASG machining motion cycle as (0,5)→(50,5)→(50,0)→(0,0)→(0,5), remove 0.545 mm of material. Depth of cut shall be 21 µm and feed rate 50 µm/rev for rough pass, depth of cut shall be 2 µm and feed rate 20 µm/rev for finish pass.

(15) The distance of the rotational center of M4 surface to the flat surface is 4.139 mm

(16) Shift the ASG relative z position by 1.9+3.943+0.216 mm (*setz d 6.059*).

(17) Move the ASG to the relative (x,z) position to (64, 5)

(18) Machine the fiducial surfaces (21 rpm spindle speed))

(19) Close FLORA control, and reprogram and launch the FLORA control for the fiducial surface

(20) Run ASG machining motion cycle as (59,5)→(64,5)→(64,0)→(59,0)→(59,5), remove 1.2 mm of material. Depth of cut shall be 20 µm and feed rate 50 µm/rev for rough pass, depth of cut shall be 2 µm and feed rate 20 µm/rev for finish pass.

Detailed specifications for customized tooling by Chardon Tool

New, vacuum brazed, single-crystal natural diamond tipped Carbide insert, 60º included angle on diamond, 0.9977 mm tip radius, minimum 40º of sweep, 0.09 waviness, 28º primary conical clearance, neutral top rake, 600X edge quality, insert style DCGW 21.5

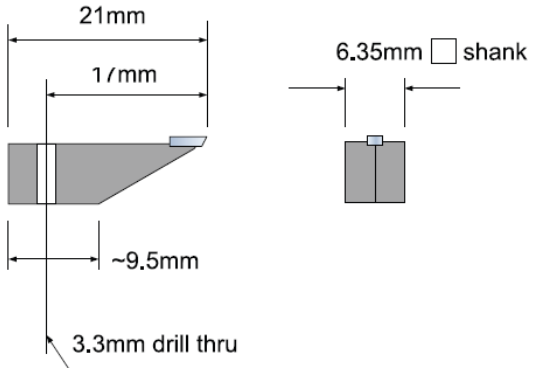

Figure E-2 Drawing of a customized tool insert

Appendix F – Code Listing for DSP and PC Program

Real time program listing in VisualDSP++ environment

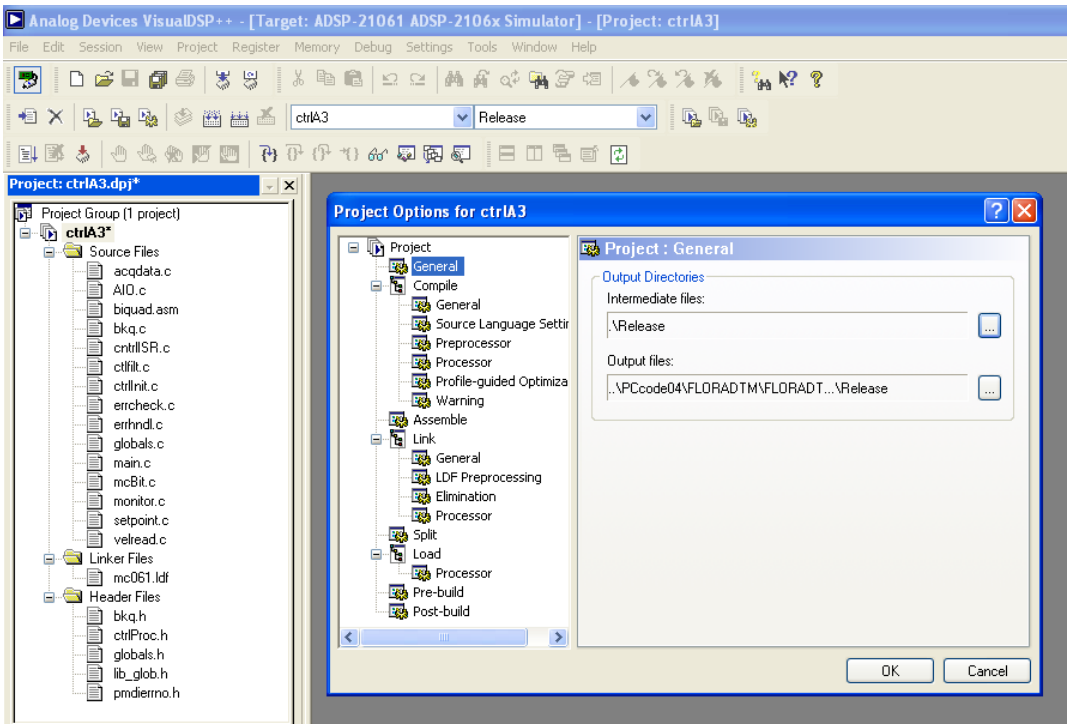

PC program listing in Visual C# environment

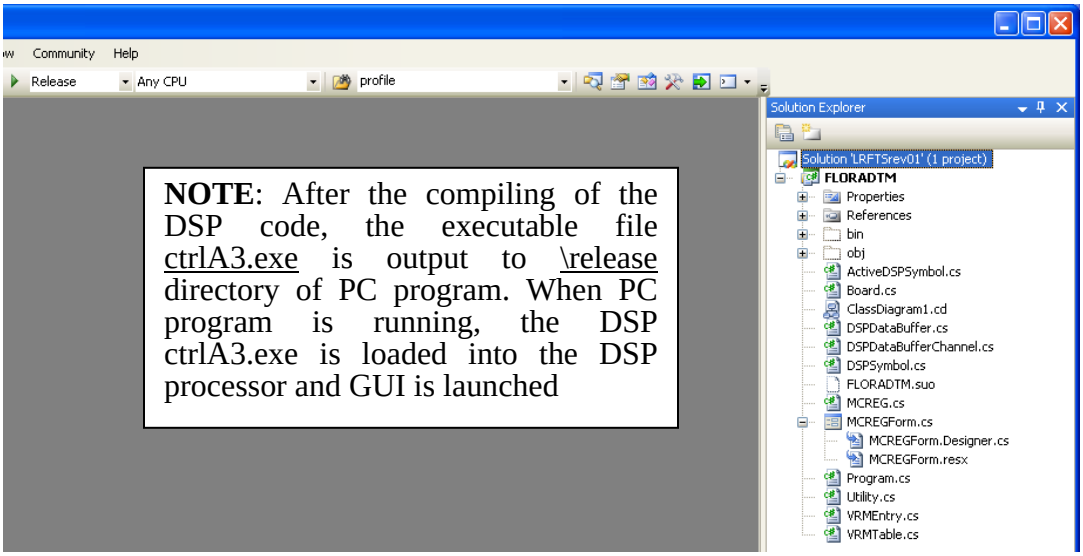

NOTE: After the compiling of the DSP code, the executable file ctrlA3.exe is output to \release directory of PC program. When PC program is running, the DSP ctrlA3.exe is loaded into the DSP processor and GUI is launched

Figure F.1 shows the overall flow diagram of embedded DSP code. The flow diagram was created with the help from Steve Furst.

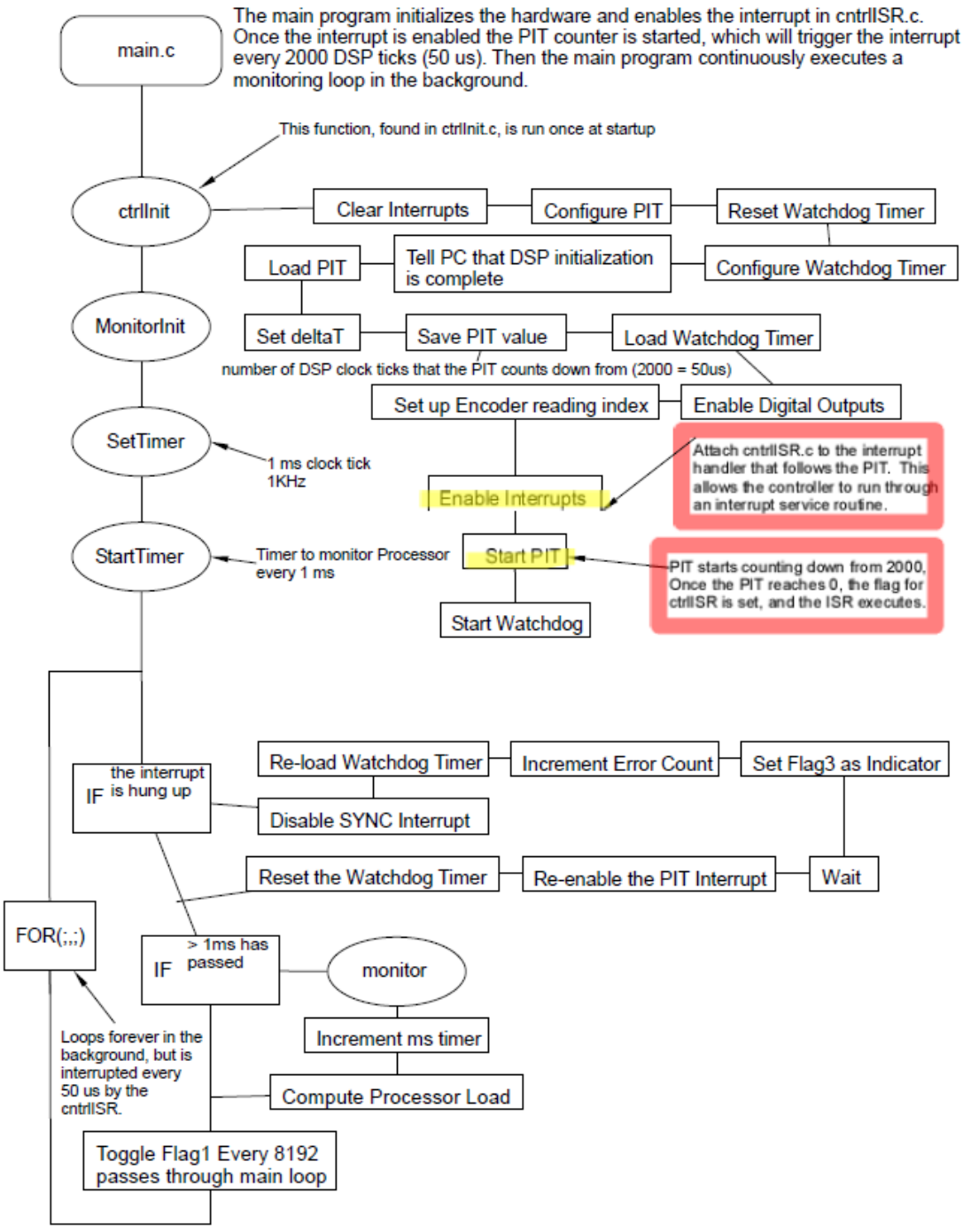

Figure F-3 Flow diagram for real time DSP code

Figure F.2 shows a detailed flow diagram for the control tasks executed on each sampling cycle. The flow diagram was created with the help from Steve Furst.

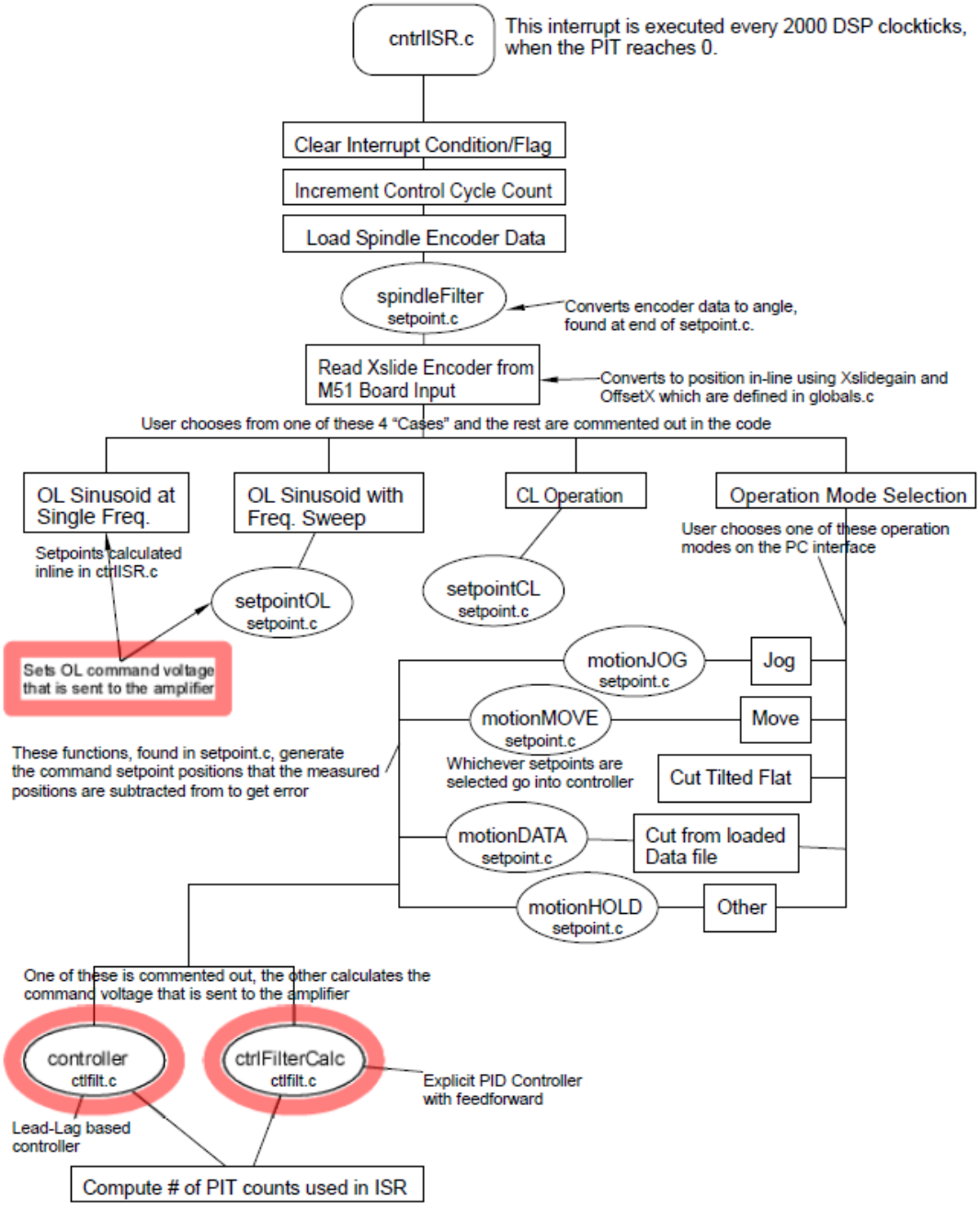

Figure F-2 Flow diagram for real time motion control task on each sampling cycle

F.1 DSP Code for Spindle Angular Position Generation

```
// This function is included in the <setpoint.c>
void spindleFilter()
{
       // number of samples to be averaged to obtain speed frequency double
      spindlenum = 1000.0;
       double omega = M_2PI*spindlerpm;

       double SpindleEnc = 0;
       double SpindleEncVar =0;
       double angle;

       // PART ONE: correct the rotor runout:
       grglSpindleEnc[0]=grglSpindleEnc[0]-5.264105*
                     cos(grglSpindleEnc[0]*grgfSpindleGain + 1.4029574 );

      // PART TWO: processing of spindle position
       // fix spindle encoder roll over issue
       if (gulCntrlCycleCnt == 1)
       {  //Capture reading when the program starts
             grglSpindleEncOld[0] = grglSpindleEnc[0];
       }
       SpindleEncVar = grglSpindleEnc[0] - grglSpindleEncOld[0];
       if ( SpindleEncVar >100.0)
       { SpindleEncVar += -20000.0 ; }
       if ( SpindleEncVar <-100.0)
       { SpindleEncVar += 20000.0 ; }

       ////////////////////////////////////////////////////////////
       // following lines to fix spindle encoder feedback glitches.
       // 20000 is the spindle encoder counts per rev
       if (gulCntrlCycleCnt > spindlenum)
       {   // remove the oldest speed from the accumulator
             SpindleSpeedAccum -= SpindleSpeed[SpindlePointer];
       }
       SpindleSpeed[SpindlePointer] = SpindleEncVar;
       SpindleSpeedAccum += SpindleSpeed[SpindlePointer];

       spindlerpm = SpindleSpeedAccum / spindlenum;

       SpindlePointer++;
       if (SpindlePointer == spindlenum) {
           SpindlePointer = 0;
       }
      SpindleEnc = (grglSpindleEnc[0]+0);   // shift 90deg for high spot

      // spindle filtering solution
       if (gulCntrlCycleCnt <= spindlenum )
       {  //Capture reading when the program starts
           grgfSpindleAng = (double)(SpindleEnc);
       }
       else
       {
           spindleaccum += SpindleEncVar - spindlerpm;
           grgfSpindleAng += spindlerpm ;

           if (spindleaccum >0) {
```

```
            grgfSpindleAng += 0.01;
            spindleaccum += -0.01;
        } else if (spindleaccum <0) {
            grgfSpindleAng += -0.01;
            spindleaccum += 0.01;
        }
    }  // end of filter

    if (grgfSpindleAng >= 20000)
    { grgfSpindleAng -= 20000; }
    else if  (grgfSpindleAng <= -20000)
    { grgfSpindleAng += 20000; }
    gfSpindleTHETA=grgfSpindleGain*grgfSpindleAng+grgfSpindleOffset-
                                                    gfOffsetTHETA;
    grglSpindleEncOld[0] = grglSpindleEnc[0];
    //   END OF PART TWO:

}
```

F.2 Implementation of Bilinear Interpolation in Polar Coordinates

The data structure of interpolation table

The data file for the interpolation table is structured as a single column array for the simplicity of loading from the PC hard drive into the DSP memory space.

Data array = [[N_R R_{step} $R_{\min}$ $R_{\min}$ N_θ N_{step} $\theta_{\min}$ $\theta_{\max}$] → continued in a row

[$R_{\min}$ … R_i … $R_{\max}$] [$\theta_{\min}$ … θ_j … $\theta_{\max}$] → continued in a row

[$ZC_{\min,\min}$ … $ZC_{i,\min}$ … $ZC_{\max,\min}$] → continued in a row

[$ZC_{\min,j}$ … $ZC_{i,j}$ … $ZC_{\max,j}$] → continued in a row

[$ZC_{\min,\max}$ $ZC_{i,\max}$ $ZC_{\max,\max}$]]’

The variables in data array are defined in the Table F.1, the 2D grid typically covers an area a little larger than the aperture of surface to be machined to avoid edge discontinuities.

Table F.1 A 2D grid of data points defining the surface geometry

	Angular position(N_θ data points in the step size of N_{step})				
Radial position (N_R data points in the step size of R_{step})	$\theta_{\min}$	…	θ_j	…	$\theta_{\max}$
$R_{\min}$	$ZC_{\min,\min}$		$ZC_{\min,j}$		$ZC_{\min,\max}$
…	…		…		…
R_i	$ZC_{i,\min}$	…	$ZC_{i,j}$	…	$ZC_{i,\max}$
…	…		…		…
$R_{\max}$	$ZC_{\max,\min}$	…	$ZC_{\max,j}$	…	$ZC_{\max,\max}$

The DSP code for bilinear interpolation

```
// This function is included in the <setpoint.c>
void  interSURFACE( double t, double r )
{
       int ti;
       int ri;
       double vt;
       double ur;
       double zI;
       double aI;
       int InT = (int)(grgfSurfaceData[0]);
       int InR = (int)(grgfSurfaceData[4]);
       double Idelta_T  = grgfSurfaceData[1];
       double Idelta_R  = grgfSurfaceData[5];
       double Imin_T = grgfSurfaceData[2];
       double Imax_T = grgfSurfaceData[3];
       double Imin_R = grgfSurfaceData[6];
       double Imax_R = grgfSurfaceData[7];

        if ( t < Imin_T ) { ti = 0;     t = Imin_T; }
   else if ( t > Imax_T ) { ti = InT-2; t = Imax_T; }
   else ti = ( int ) ( ( t - Imin_T ) / Idelta_T + 1.0 ) - 1;
        if ( r < Imin_R ) { ri = 0;     r = Imin_R; }
   else if ( r > Imax_R ) { ri = InR-2; r = Imax_R; }
   else ri = ( int ) ( ( r - Imin_R ) / Idelta_R + 1.0 ) - 1;

   vt = ( t - grgfSurfaceData[4+4+ti] ) / Idelta_T;
   ur = ( r - grgfSurfaceData[4+4+InT+ri] ) / Idelta_R;

grgfComProfile=(1.0-ur)*(1.0-vt)*grgfSurfaceData[8+InR+InT+(ri)+(ti)*InR]
         +    ur*(1.0-vt)*grgfSurfaceData[4+4+InR+InT+(ri+1)+(ti)   *InR]
         +    ur*vt*grgfSurfaceData[4+4+InR+InT+(ri+1)+((ti+1)*InR)]
```

```
         + (1.0-ur)*vt*grgfSurfaceData[4+4+InR+InT+(ri)+((ti+1)*InR)];

grgfSetptAcc[0]=(1.0-ur)*(1.0-vt)*grgfSurfaceData[8+InR+InT+InR*InT+ri+ti*InR]
     + ur*(1.0-vt)*grgfSurfaceData[4+4+InR+InT+InR*InT+(ri+1)+(ti)*InR]
     + ur*vt*grgfSurfaceData[4+4+InR+InT+InR*InT+(ri+1)+((ti+1)*InR)]
     +(1.0-ur)*vt*grgfSurfaceData[4+4+InR+InT+InR*InT+(ri)+((ti+1)*InR)];
}
```

PC code for data loading

```
// This function is included in the <MCREGForm.cs>
private void buttonDatafile_Click(object sender, EventArgs e)
{
   if ((listBoxMode.SelectedIndex == 4) &&
               (CheckBoxAmpEnable.Checked == false) &&
               (CheckBoxTestEnable.Checked == false))
      {
        string filename = textBoxDatafile.Text;
        int i = 0;
        try
        {
         using (StreamReader sr = File.OpenText(filename))
          {
           String input;
           this.buttonDatafile.ForeColor = System.Drawing.Color.Black;
           while ((input = sr.ReadLine()) != null)
           {
            grgfSurfaceData.write(ConvertStringDouble(input), i);
            i++;
            }
           sr.Close();
           }
         }
         catch (Exception error)
         {
           MessageBox.Show(error.Message);
          }

     //=following code is only for testing purpose to check if the data
     // is properly loaded from the harddrive to the memory space.
     TextWriter sw = new StreamWriter("trycopy.txt");
     for (int j = 0; j < (int)(grgfSurfaceData.readDouble()); j++)
     {
        sw.WriteLine(grgfSurfaceData.readDouble(j));
      }
               sw.Close();
    }
  }
```

The DSP code for motion trajectory generation by interpolation over data array

```
// This function is included in the <setpoint.c>
void motionDATA()
{
       int TestEnableStatus;//depends on the one variables:(gulEnableTest )
       double CutStartPos = 17.1;
       double omega = M_2PI*spindlerpm;
       double cosSpindleTHETA;
       double angle;
       double angleNEW;
       double angleMOD;
       double xslideNEW;
       double grgfComProfileNew;
       double amplitude;
       double wave;

       //for max amount change in the motion position command double
      steplimit = 12.8e-3;

       // number of data points for the spindle angle
      int InT = (int)(grgfSurfaceData[0]);
       double Imax_R = grgfSurfaceData[7];

      // parameters for residual error compensation
       double p1 =   1.18240747569419e-011;
       double p2 = -9.34830681210258e-010;
       double p3 = -1.23108145294418e-008;
       double p4 =    2.22999111732242e-006;
       double p5 = -4.29306135011253e-005;
       double p6 =   0.00014106790826081;

       double x1;
       double x2;
       double x3;
       double x4;
       double x5;
       double x6;
       double toolwaviness;

      // ============================================================
       // PART ONE:
       // ============================================================
       xslide = grgfXslidePos;
       if (xslide > 64.5)  xslide = 64.5;
       if (xslide < 0.0)   xslide = 0.0;
       x1=xslide;
       x2=x1*x1;
       x3=x2*x1;
       x4=x3*x1;
       x5=x4*x1;
       x6=x5*x1;

   // ============================================================
   // PART TWO:
   // ============================================================
   angle =  gfSpindleTHETA;

   // ============================================================
   // PART THREE:
   // ============================================================
```

```
   TestEnableStatus = 1;
   if ( (gulEnableTest & 0x1) ==0 ) {
             TestEnableStatus = 0;
   }

   // if the the test status (enabled or disabled) has been changed
   //(1) re-set the timer for test profile
   //(2) reset the position error, to make sure the position error sum
   //     will not transfer to the next  test
   if (TestEnableStatus != TestEnableStatusOld) {
          gulTestCycleCnt =0;
          TestEnableStatusOld = TestEnableStatus;
          bumpflag = 0;
    }

    // at the start of test, capture the position
    // so the relative position command can be generated.
    if (gulTestCycleCnt ==0) {
        gfStartPos = grgfActualPos[0];
        grgfComProfile = 0.0;
    }
    // To avoid any closed-loop controller actions before the closed-loop
    //  function is turned on, the <gfStartPos> shall be updated at every
    // sampling with current position measurement, so that the position
    // error remains zeros.
    if ((gulEnableTest==0)&&(TestEnableStatus == TestEnableStatusOld)) {
        gfStartPos = grgfActualPos[0];
        grgfComProfile = 0.0;
    }

    // If first entering Jog mode, capture current position as the start
       if (gulOperationModeOld != 4) {
        gfStartPos = grgfActualPos[0];
        grgfComProfile = 0.0;
       }

    // (1) if the starting position is not at set start position,
    //        move to the position at 0.5mm/sec speed
    // (2) grgfComProfile) shall remain at zero so that
    //        it would not accumulate at non-test phase
    if ( (gulEnableTest ==1) && (gfStartPos != CutStartPos) )
    {
          if ( fabs(CutStartPos-grgfActualPos[0]) > 0.0002 )
          {
              grgfComProfile+=5.0e-5*signof(CutStartPos,grgfActualPos[0]);
               grgfSetptAcc[0] = 0;
          }
          else
          {
              gfStartPos = CutStartPos;
              // reset the pause cycle when first reach the start position
             PauseCycle = 0;
              grgfComProfile = 0.0;
               grgfSetptAcc[0] = 0;
          }
    }


if (PauseCycle < 20010) { PauseCycle ++; }
```

```
if((gulEnableTest==1)&&(gfStartPos==CutStartPos)&&(InT>=2)&&(PauseCycle>20000) )
  {
       grgfComProfile=0.0;
       grgfSetptAcc[0]=0.0;

       //generate tool motion command when xslide
       // is within 5 mm of the profile edge
        if ( (xslide - (Imax_R+5.0)) < 0.001 )
        {
/*
      ///// ////////////////
      // Profile for biconics
      ///////////////////////
      // NRS surface
      interSURFACE (angle, xslide);
       grgfComProfile=grgfComProfile+(303.919-
                      (sqrt((double)(92345.06001889-xslide*xslide))));
      toolwaviness  = p1*x5 + p2*x4 + p3*x3 + p4*x2 + p5*x1 + p6;
      grgfComProfile = grgfComProfile - toolwaviness ;
*/


       // ///////////////////////
       //  Three sin wave profile for fiducial features
       // ////////////////////////
       angleMOD = angle;
       if (angle >= 2.0943951023932) { angleMOD = angle-2.0943951023932; }
       if (angle >=4.18879020478639) { angleMOD = angle-4.18879020478639;}
       if (angleMOD>1.0471975511966){angleMOD=angleMOD-2.0943951023932;   }
      interSURFACE (angleMOD, xslide);

       amplitude =0.0;
       amplitude = 0.6 - (61.5 - xslide)*(61.5 - xslide)/100.0;
       if (amplitude <0) { amplitude = 0.0;}
       wave = angleMOD*xslide;
       // To make sure the command starts from zero value
       if (  (angleMOD>=0.523598775598299)&&
                       (angleMOD<0.610865238198015) ) {bumpflag =1;}

       if ( (wave>=-12.0) && (wave<=12.0) && (bumpflag ==1) )
       {
        grgfComProfile=grgfComProfile+amplitude*(1+cos(M_2PI*wave/8.0));
        // acceleration calculated for 0.35Hz spindle speed
        grgfSetptAcc[0]=-amplitude*2.98315341291632*xslide*xslide*
                                    cos ( M_2PI * wave / 8.0 );
        }


     }    //    end   if ( (xslide - (Imax_R+5.0)) < 0.001 )


      angleOLD = angle;
      xslideOLD = xslide;

    }   // end of profile generation


    grgfSetptPos[0] =  grgfComProfile + gfStartPos;

    // maximum current drive level sets the limit the maximum acceleration
```

```
    // maximum command profile change sets the limit the max velocity
    //maximum command position change needed for 2mm20Hz motion is 12.56um
    if ( fabs(grgfSetptPos[0] - grgfSetptPosOld[0]) > steplimit )
    {
      grgfSetptPos[0]=grgfSetptPosOld[0]+steplimit*signof(grgfSetptPos[0],
                      grgfSetptPosOld[0]);
    }

    grgfSetptPosOld[0] = grgfSetptPos[0];
    gulTestCycleCnt++;


}
```

F.3 DSP Code for Controller Implementation with AFC

```
void controller() {

       int i, j, mode, iMask;
       double rgfTmp[MAX_AXES];
       double posErr, absPosErr, dband;


       // Compute the position error.
       posErr = grgfSetptPos[0] - grgfActualPos[0];

       // Check if the magnitude of the position error is less than
       // the controller deadband.
       dband = 0.6*fabs(grgfEncGain[0]);
       absPosErr = fabs(posErr);
       // limit the magnitude of position error fed into controller
       if (fabs(posErr) > 0.050 ) {  posErr = 0.050*fabs(posErr)/posErr; }
       if ( (gulEnableTest & 0x1) ==0 ) { posErr = 0.0; }

       // update the current position error
       if(absPosErr < dband) { grgfError[0] = 0.0; }
       else{  grgfError[0] = posErr;     }

       if ( (gulEnableTest & 0x1) ==0 ) {      posErr = 0.0;}


       // AFC
       // Compute model inverses. Indexing: 0 and 1 real and imag.
       // Compute w = 2*pi*f, and w^2 to calculate model inverse
       // Multiplication 2*exp(-jwt)*e(t)=2*(cos(wt)*e(t) - j*sin(w)*e(t)).
      // Index 0: 2*cos(wt)*e(t), Index 1: -2*sin(w)*e(t)
       corr_meas[0] = cosine_for_cc*posErr; // Real part = cos * err
       corr_meas[1] = -sine_for_cc*posErr; // Imaginary = -sin * err

       corr_meas[2] = cosine_for_cc2*posErr; // Real part = cos * err
       corr_meas[3] = -sine_for_cc2*posErr; // Imaginary = -sin * err

       corr_meas[4] = cosine_for_cc3*posErr; // Real part = cos * err
       corr_meas[5] = -sine_for_cc3*posErr; // Imaginary = -sin * err
```

```
        // System model inverse here (P/(1+K*P))^-1  (jw) for PID
        model_inverse[0] = 119.215225680892;
        model_inverse[1] = -318.585567566834;
        model_inverse[2] = 116.864605705282;
        model_inverse[3] = -129.215532966031;
        model_inverse[4] =  112.959242856831 ;
        model_inverse[5] = - 52.8735617164067;

        // AFC: U(k+1) = U(k) + A(w) * X(k). 0: real, 1: imag
        U_new[0] = leak*U_old[0] + cc_gain*(model_inverse[0]*corr_meas[0] –
                                model_inverse[1]*corr_meas[1]);
        U_new[1] = leak*U_old[1] + cc_gain*(model_inverse[1]*corr_meas[0] +
                                model_inverse[0]*corr_meas[1]);
        U_new[2] = leak*U_old[2] + cc_gain*(model_inverse[2]*corr_meas[2] –
                                model_inverse[3]*corr_meas[3]);
        U_new[3] = leak*U_old[3] + cc_gain*(model_inverse[3]*corr_meas[2] +
                                model_inverse[2]*corr_meas[3]);
        U_new[4] = leak*U_old[4] + cc_gain*(model_inverse[4]*corr_meas[4] –
                                model_inverse[5]*corr_meas[5]);
        U_new[5] = leak*U_old[5] + cc_gain*(model_inverse[5]*corr_meas[4] +
                                model_inverse[4]*corr_meas[5]);

        // Save new values for next period
        U_old[0] = U_new[0];
        U_old[1] = U_new[1];
        U_old[2] = U_new[2];
        U_old[3] = U_new[3];
        U_old[4] = U_new[4];
        U_old[5] = U_new[5];
        // Realise time signals according force commands U(k)
        // Multiplication exp(jwt)*U(t) = (cos(wt)*U(t) - j*sin(w)*U(t)).
       //  Index 0: real. Index 1: imag.
        grgfCCDrive=2.0*(U_new[0]*cosine_for_cc  - U_new[1]*sine_for_cc);
        grgfCCDrive=grgfCCDrive+2.0*(U_new[2]*cosine_for_cc2-U_new[3]*sine_for_cc2);
        grgfCCDrive=grgfCCDrive+2.0*(U_new[4]*cosine_for_cc3-U_new[5]*sine_for_cc3);

        // Saturation
        if (grgfCCDrive < -0.05) {
            grgfCCDrive = -0.05;
               leak = leak - 0.001; }
        if (grgfCCDrive > 0.05) {
            grgfCCDrive = 0.05;
               leak = leak - 0.001; }

//     grgfAInput=grgfCCDrive;


// lag 100Hz, lead 1KHz (alpha=15), crossover 1KHz for lag -double lead compensator
//double LL2B[4]={20407.3448617034,-57410.8436483769,53821.89115747,
                                                        -16814.560718652 };
//   double LL2A[4]={ 2, -3.18478433036103, 1.36024856904466, -0.175464238683629 };
// lag 20Hz, lead 100Hz (alpha=6), crossover 100Hz for lag -double lead compensator
//double LL2B[4]={233.250161209448,-692.344624912307,685.013881774837,
                                                        -225.919180812271 };
//double LL2A[4]={2,-5.70373352355122,5.41843877523586,-1.71470525168464};

// PID controller
double LL2B[3]={ 3312.764,         -6502.636,                    3192};
double LL2A[3]={ 1,                 -1,                      0};
```

```
      // shift the position error to the right in the structure
            grgfError[4]=grgfError[3];
            grgfError[3]=grgfError[2];
            grgfError[2]=grgfError[1];
            grgfError[1]=grgfError[0];

      // update the current position error
            if(absPosErr < dband) {
                  grgfError[0] = 0.0;
            } else{
                  grgfError[0] = posErr;
            }

     // for lag-double lead compensator
     // shall remove FF control value, not part of difference equation.
     // grgfDrive[0]=grgfDrive[0]-feedforward;

     rgfTmp[0] = LL2B[0] * grgfError[0];
     for(i=1; i<sizeof(LL2B); i++) {
         rgfTmp[0] += LL2B[i] * grgfError[i]-LL2A[i] * grgfPOSDrive[i-1];
     }
     rgfTmp[0] = rgfTmp[0] / LL2A[0];

      // Clip the drive.
      for(i=0; i<1; i++) {
            if(fabs(rgfTmp[i]) > grgfCtrlSaturation[i]) {
                  rgfTmp[i] = (SIGNF(rgfTmp[i]))*grgfCtrlSaturation[i];
            }
      }

      grgfPOSDrive[4] = grgfPOSDrive[3];   // 1~4 for all past drive level
      grgfPOSDrive[3] = grgfPOSDrive[2];
      grgfPOSDrive[2] = grgfPOSDrive[1];
      grgfPOSDrive[1] = grgfPOSDrive[0];
      grgfPOSDrive[0] = rgfTmp[0];         // the current drive level

    //acceleration feedforward controller=======
    feedforward=grgfCtrlKa[0]*grgfSetptAcc[0];

    // Copy temp value to drive. Save old values
      for(i=0; i<1; i++) {
            grgfDrive[i] = grgfPOSDrive[i];
//          grgfDrive[i] = grgfPOSDrive[i] + feedforward + grgfCCDrive;
//          grgfDrive[i] = grgfPOSDrive[i] + feedforward;
//          grgfOldError[i] = grgfError[i];
//          grgfVOldError[i] = grgfVError[i];
      }

}
```

F.4 DSP Code for Controller Implementation with DOB

```
void controller3(int nAxes) {
```

```
       int i, j, mode, iMask;
       float rgfTmp[MAX_AXES];
       float posErr, absPosErr, dband;


            // Implementation two: DOB
// to filter the position feedback to obtain actual force for DOB: MS^2/Kf
double numDOB1[3]={84444.4444444445,-168888.888888889, 84444.4444444445};
double denDOB1[3] = {       1,         2,         1};
//tofilter F(s)=>DOB2=tf([(2*pi*200)^2],[1 2*0.7*2*pi*200 (2*pi*200)^2]);
Double numDOB2[3]={0.000944487536776733,0.00188897507355347, 0.000944487536776733};
double denDOB2[3] = {1, -1.91204292815954, 0.915820878306645};

double DOB1 = 0.0;
double DOB2 = 0.0;

       for(i=0; i<1; i++) {
              // Compute the position error.
              posErr = grgfSetptPos[i] - (grgfActualPos[i]);

              // limit the magnitude of position error fed into controller
              if (fabs(posErr) > 0.015 ) {
                  posErr = 0.015*fabs(posErr)/posErr;
              }

              if ( (gulEnableTest & 0x1) ==0 ) {      posErr = 0.0;   }

              // Check if the magnitude of the position error is less than
              // the controller deadband.
              dband = 0.6*fabs(grgfEncGain[i]);
              absPosErr = fabs(posErr);

       // update the current position error
              if(absPosErr < dband) {grgfError[0] = 0.0;
              } else{
                     grgfError[0] = posErr;
              }


       }

       // ====================================
       // Cascade control loop implementation
       //====================================

       // First loop around position

       // Compute the position error derivative.
       for(i=0; i<nAxes; i++) {
              grgfErrorDeriv[i] = (grgfError[i] - grgfOldError[i])*gfCtrlFreq;
       }

       // Compute the position error integral.
       for(i=0; i<nAxes; i++) {
              grgfErrorSum[i] += 0.5*(grgfError[i]+grgfOldError[i])*gfCtrlDeltaT;
       }

       // Clip the error integral to avoid integral windup.
       for(i=0; i<nAxes; i++) {
```

```
            if(grgfCtrlKi[i] == 0.0) {
                  grgfErrorSum[i] = 0.0;
            } else {
      if((fabs(grgfErrorSum[i]))*grgfCtrlKi[i]>grgfCtrlPWindup[i]) {
                        grgfErrorSum[i] = SIGNF(grgfErrorSum[i])*
                              grgfCtrlPWindup[i] / grgfCtrlKi[i];
                  }
            }
      }

      // Compute the drive. (store ongoing values in rgfTmp)
      for(i=0; i<nAxes; i++) {
            rgfTmp[i] = grgfCtrlKp[i]*grgfError[i];
            rgfTmp[i] += grgfCtrlKd[i]*grgfErrorDeriv[i];
            rgfTmp[i] += grgfCtrlKi[i]*grgfErrorSum[i];
            rgfTmp[i] += grgfCtrlKv[i]*grgfSetptVel[i];
      }

    // for DOB implementation plan TWO

      positionCOM[2]= positionCOM[1];
      positionCOM[1]= positionCOM[0];
      positionCOM[0]= -grgfError[0];
      // positionCOM[0]= grgfActualPos[0];
     DOB1  = numDOB1[0] * positionCOM[0];
     DOB1 += numDOB1[1] * positionCOM[1] - denDOB1[1] * driveDOB1[0];
     DOB1 += numDOB1[2] * positionCOM[2] - denDOB1[2] * driveDOB1[1];
     DOB1 = DOB1 / denDOB1[0];
       driveDOB1[2] = driveDOB1[1];
       driveDOB1[1] = driveDOB1[0];
       driveDOB1[0] = DOB1;         // the current drive level

      grgfPOSDrive[2] = grgfPOSDrive[1];
      grgfPOSDrive[1] = grgfPOSDrive[0];
      // the current drive level
     grgfPOSDrive[0] = (grgfDrive[0]-grgfDisturbOld)-DOB1;
      DOB2 =  numDOB2[0] * grgfPOSDrive[0];
     DOB2 += numDOB2[1] * grgfPOSDrive[1] - denDOB2[1] * driveDOB2[0];
     DOB2 += numDOB2[2] * grgfPOSDrive[2] - denDOB2[2] * driveDOB2[1];
     DOB2 = DOB2 / denDOB2[0];
       driveDOB2[2] = driveDOB2[1];
       driveDOB2[1] = driveDOB2[0];
       driveDOB2[0] = DOB2;         // the current drive level

       grgfAInput = DOB2;



/*
      // Second loop around velocity

      // Subtract feedback velocity, call this Velocity error
      for(i=0; i<nAxes; i++) {
            grgfVError[i]=rgfTmp[i]-(grgfCtrlKvf[i]*grgfActualVelFilt[i]);
      }

      // Integrate the velocity error.
      for(i=0; i<nAxes; i++) {
      grgfVErrorSum[i]+=0.5*(grgfVError[i]+grgfVOldError[i])*gfCtrlDeltaT;
      }
```

```
	// Clip the velocity error integral
	for(i=0; i<nAxes; i++) {
		if(grgfCtrlKiv[i] == 0.0) {
			grgfVErrorSum[i] = 0.0;
		} else {
			if((fabs(grgfVErrorSum[i]))*grgfCtrlKiv[i]>grgfCtrlVWindup[i])
{
				grgfVErrorSum[i] = SIGNF(grgfVErrorSum[i])*
					grgfCtrlVWindup[i] / grgfCtrlKiv[i];
			}
		}
	}

	// Compute drive
	for(i=0; i<nAxes; i++) {
		rgfTmp[i] = grgfCtrlKpv[i]*grgfVError[i];
		rgfTmp[i] += grgfCtrlKiv[i]*grgfVErrorSum[i];
		rgfTmp[i] += grgfCtrlKa[i]*grgfSetptAcc[i];
		rgfTmp[i] += grgfCtrlBias[i];
	}

	// Output drive biquad filter
	for(i=0; i<nAxes; i++) {
		for(j=0; j<gsOutFilt[i].nBiquads; j++) {
			rgfTmp[i] = biquad(rgfTmp[i],gsOutFilt[i].bParams[j]);
		}
	}

*/


	// Clip the drive.
	for(i=0; i<1; i++) {
		if(fabs(rgfTmp[i]) > grgfCtrlSaturation[i]) {
			rgfTmp[i] = (SIGNF(rgfTmp[i]))*grgfCtrlSaturation[i];
		}
	}

if (fabs(grgfAInput) > 0.2) {
    grgfAInput = SIGNF(grgfAInput)*0.2;
}
	// Copy temp value to drive. Save old values
	grgfDrive[2] = grgfDrive[1];
	grgfDrive[1] = grgfDrive[0];
	for(i=0; i<1; i++) {
//	grgfDrive[i] = rgfTmp[i]+grgfAInput; // for  DOB implementation only
		grgfDrive[i] = rgfTmp[i] + grgfDisturb +grgfAInput;
		grgfOldError[i] = grgfError[i];
		grgfVOldError[i] = grgfVError[i];
	}

    grgfDisturbOld = grgfDisturb;  // disturbance force

		if(fabs(grgfDrive[0]) > grgfCtrlSaturation[0]) {
	grgfDrive[0]=(SIGNF(grgfDrive[0]))*grgfCtrlSaturation[0];
		}

}
```

Appendix G – Matlab Code Listing Surface Data Generation

G.1 Generation of Machining Data for Biconic Surface

Generate biconic surface profile

```
%% m4polar2.m

% M4 rectangular aperture definition
x_halfwidth   =  30;              % 94 mm in x direction
y_halfwidth   =  30;              % 76 mm in y direction
x_decenter    =  -2.01;           % center of aperture in x
y_decenter    = 227.41;           % center of aperture in y
x_rotation    =  35.3;            % tilt of workpiece reference flat

% constants defining the M4 biconic shape
% [x_curvature y_curvature x_conic_constant y_conic_constant]
K = [1/377.3939, 1/406.8829, 0.0778, 0.1265];

% tool radius for cutting tool radius
%toolR = 0.9977;

% nominal polar grid size and spacing
maxR       = 49;                  % radial size of polar mesh
minR       =  0;
r_spacing  =  1;                  % 1 mm     spacing
th_spacing =  1;                  % 1 degree spacing

plotflag = 0;

%% Form data mesh for on axis machining
%
% A polar mesh is created (ie, spider web pattern) in the xy plane centered at
% origin.  The (R,theta) mesh is converted to Cartesian coordinates, translated
% along the y axis by the aperture decenter value and rotated about the x axis.
% The mesh is not translated in the x direction.

% half-meridians must match at center
Nt = ceil(180/th_spacing)*2 - (rem(180,th_spacing)~=0) + 1;

% polar grid must be larger than aperture radius
% wR = hypot(x_halfwidth,y_halfwidth);
wR = sqrt(x_halfwidth^2+y_halfwidth^2);
if maxR < wR
   error('radial grid is smaller than aperture');
end

% adjust spacing to get integral steps from max radius to center
Nr = ceil((maxR-minR)/r_spacing) + 1;
r_spacing = maxR/Nr;

% form radial and azimuthal vectors
r  = linspace(maxR,  0,Nr);
th = linspace(   0,360,Nt) * pi/180;
```

```
% check azimuthal angles, half meridian pattern should form full meridians
% ie, angles from 0 to 180 should match angles from 180 to 360
if abs(max((th-fliplr(2*pi-th)))) > 1e-10
   error('meridians do not match on opposite sides of polar grid');
end

% create circular polar mesh, spider web pattern
[rad,theta] = meshgrid(r,th);
rad   = rad';
theta = theta';

% convert polar mesh to Cartesian coordinates
[xx,yy] = pol2cart(theta,rad);
xx(abs(xx)<1e-10)=0;               % force small values to zero
yy(abs(yy)<1e-10)=0;

% rotate grid about the x axis
H = h_rotX(x_rotation*pi/180);
B = [xx(:) yy(:) zeros(numel(xx),1) ones(numel(xx),1)] * H;
[xr,yr,zr] = dealcol(B);

% translate to aperture location (y direction only)
xrt = xr;
yrt = yr + y_decenter;

%% biconic surface data for on axis aperture

% find z values on biconic surface for rotated and translated polar grid
[zrt,C,Nx,Ny,Nz] = biconicZ(reshape(xrt,size(xx)),reshape(yrt,size(yy)),K);

zrt(abs(zrt)<1e-10) = 0;           % force small values to zero
zz = zrt - reshape(zr,size(zrt));  % offset z to "finish" rotation

% find z value at x=y=0, offset surface data so that z=0 at x=y=0
z0 = griddata(xx,yy,zz,0,0);
zz = zz - z0;

% plot the surface
% find minimum z value, add to plot title
[zo,iz] = min(zz(:));
[j,k]   = ind2sub(size(zz),iz);

if(plotflag ==1)
h1 = figure;
polarplot3d(zz,'plottype','surfn','radialrange',[maxR 0],'meshscale',4);
view([-60 46]);

title(sprintf(['m4 biconic surface\n'...
               'min z =%.3f at (x,y)=(%.3f,%.3f)'],zo,xx(j,k),yy(j,k)));
sfprops();
end
%% best fit sphere

% least squares sphere
[center,radius,residuals] = spherefit([xx(:) yy(:) zz(:)],true);

% plot residual surface
if (plotflag ==1)
h2 = figure;
polarplot3d(reshape(residuals,size(xx)),'radialrange',[maxR 0],'meshscale',4);
```

```
view([-68 70]);
title(sprintf(['radial residual before tool compensation\n'...
               'center=(0,0,%.3f), radius=%.3f'],center(3),radius));
sfprops();
end

%% tool radius compensation

% distance vectors across part (full meridian)
Rp = repmat(linspace(maxR,-maxR,2*Nr-1)',1,Nt);

% build full meridian sag table for radius comp function
qi  = floor(Nt/2);                % midpoint
qz1 = zz(:,1:qi);                 % 0   to (180 - one azimuthal increment)
qz2 = zz(:,qi+1:end-1);           % 180 to (360 - one azimuthal increment)
qz3 = flipud(qz2(1:end-1,:));     % qz1 from smallest radius to largest
qz4 = flipud(qz1(1:end-1,:));     % qz4 form smallest radius to largest

QZ = [qz1 qz2; qz3 qz4];          % form full meridian data table
QZ(:,end+1) = QZ(:,1);            % 0 and 360 must be the same

% 2d radius comp along each full meridian
[rrc,zzc] = radius_comp(Rp,QZ,-toolR);

% verify radius comp (euclidean distances should all be equal to toolR)
dist = hypot(rrc-Rp,zzc-QZ);
if max(abs(dist(:)-toolR)) > 1e-7, error('radius comp failure'); end

% interpolate to original evenly spaced radial grid locations
Zp = zeros(size(zzc));
for k=1:Nt
   Zp(:,k) = interp1(rrc(:,k),zzc(:,k),Rp(:,k),'pchip','extrap');
end

% delete redundant data
Rp(Nr+1:end,:) = [];
Zp(Nr+1:end,:) = [];

% add compensated surface to plot
if (plotflag ==1)
axes(get(h1,'currentaxes'));
hold on;
polarplot3d(Zp,'radialrange',[maxR 0],'axislocation','off','meshscale',4);
view([-60 46]);
sfprops();
end
%% best fit sphere to compensated surface

% least squares sphere
[xxc,yyc] = pol2cart(theta,Rp);
[cc,Rc,resid] = spherefit([xxc(:) yyc(:) Zp(:)],true);

% plot residual surface
if (plotflag ==1)
h3 = figure;
polarplot3d(reshape(resid,size(xxc)),'radialrange',[maxR 0],'meshscale',4);
title(sprintf(['radial residual after tool compensation\n'...
               'center=(0,0,%.3f), radius=%.3f'],cc(3),Rc));
view([-68 70]);
sfprops();
```

```
end

%% plot all meridians in 2d
if (plotflag==1)
h4 = figure;
subplot(2,1,1);
hold on;
plot(Rp,zz);                        % uncompensated data
plot(Rp,Zp);                        %   compensated data
grid on;
title(sprintf(['all meridians\n'...
               'max fts excursion = %.4f mm'],max(range(Zp'))));
xlabel('radius (mm)');
ylabel('z sag (mm)');

subplot(2,1,2);
plot(180/pi*theta',Zp');
grid on;
title('all radii');
xlabel('angle (\circ)');
ylabel('z sag (mm)');
sfprops();
end
Generate data file in polar grid
% % biconic3.m
% Calculate the acceleration commmand from the complete position profile
% with 0.05 degree grid, but output accleration at 1 degree grid
% generate profile only for NRS part.

[M,N]=size(Zp);
for i = 1:M
    for j=1:N
        Zs(i,j) = cc(3)-sqrt(Rc^2-xxc(i,j)^2-yyc(i,j)^2);
        Znrs(i,j)=Zp(i,j)-Zs(i,j);
    end
end

position=Znrs;

spindle=8.4;      % Hz: rotational speed
th_spacing =1;  % degree
th_final =1;    % degree
deltaT=th_spacing/360/spindle;    % the time interval bewtween two data points
acc=zeros(M,360/th_final+1);
pos=zeros(M,360/th_final+1);
[MM,NN]=size(acc);
maxR=49;

% must have the order of number from small to big values.
for i=1:25
    temp= position(i,:); position(i,:)=position(50+1-i,:); position(50+1-i,:)=temp;
end

for i = 1:M
    acc(i,1)=(position(i,2)-2*position(i,1)+position(i,N-1))/deltaT^2;
    acc(i,NN)=acc(i,1);
    pos(i,1)=position(i,1);
    pos(i,NN)=pos(i,1);
    jj=2;
    for j=2:(N-1)
```

```
        if (rem(j,20) ==1)
            acc(i,jj)=(position(i,j+1)-2*position(i,j)+ ...
                                        position(i,j-1))/deltaT^2;
            pos(i,jj)=position(i,j);
            jj=jj+1;
        end
    end
end

mintheta=0.0; maxtheta=360.0;  steptheta=th_final;
minx=0.0;    maxx=maxR;       stepx=1;
angle = (mintheta:steptheta:maxtheta)*2*pi/360;
xslide = minx:stepx:maxx;
final=[];
final = [length(angle); steptheta*pi/180; mintheta*2*pi/360; maxtheta*2*pi/360];
final =[final; length(xslide); stepx; minx; maxx];
final =[final; angle'];
final = [final; xslide'];

for j=1:length(angle)
    final=[final; pos(:,j)];
end

for j=1:length(angle)
   final=[final; acc(:,j)];
end

         fid = fopen('biconics4.txt','wt');
        fprintf(fid,'%20.16f\n',final);
        fclose(fid);
```

G.2 Generation of Machining Data for Fiducial Surface

```
%% Plot 1  bumps for tool radius compensation.
A0 = 0.6;
A1 = 1/50/2;   % curvature at vertex of parabola, ie peak of cosine wave
L0 = 8;
scale = 1;
R0 = 61.5;

% tool radius
toolR = 0.9977;

maxR       = 64.5;                  % radial size of polar mesh
minR       =  58.5;
minTH = -5.0;
maxTH = 5.0;
r_spacing  =  0.1;                  % 1 mm     spacing
th_spacing =  0.05;                  % 1 degree spacing

%% Form data mesh for on axis machining
% A polar mesh is created (ie, spider web pattern) in the xy plane
% centered at origin.  The (R,theta) mesh is converted to Cartesian
% coordinates, translated along the y axis by the aperture decenter value
% and rotated about the x axis. The mesh is not translated in x direction.
```

```
% adjust spacing to get integral steps from max radius to center
Nr = ceil((maxR-minR)/r_spacing) + 1;
% form radial and azimuthal vectors
r  = linspace(minR,maxR, Nr);

% half-meridians must match at center
Nt = ceil((maxTH-minTH)/th_spacing) + 1;
th = linspace(   -5,5,Nt) * pi/180;

% create circular polar mesh, spider web pattern
[rad,theta] = meshgrid(r,th);
rad   = rad';
theta = theta';

% convert polar mesh to Cartesian coordinates
[xx,yy] = pol2cart(theta,rad);
xx(abs(xx)<1e-10)=0;               % force small values to zero
yy(abs(yy)<1e-10)=0;

%% Calcualate the surface profile
z = zeros(size(xx));
for k=1:Nr
    for j=1:Nt
        A = A0 - A1*(R0-rad(k,j)).^2;
        wave=theta(k,j)*rad(k,j);
        z(k,j)=0.6;
        if ( ( wave<=4 )&&(wave>=-4) )
            z(k,j)=A*cos(2*pi*wave/L0)+A +0.6;
        end
    end

end

figure; h1=plot3k({xx yy z.*scale});
set(gca,'dataaspectratio',[1 1 0.5]);

% polarplot3d(z,'plottype','surfn','radialrange',[maxR minR],'meshscale',4);
% view([-60 46]);
% sfprops();
%% tool radius compensation

% distance vectors across part (full meridian)
Rp = rad;
QZ=z;

% 2d radius comp along each full meridian
[rrc,zzc] = radius_comp(Rp,QZ,toolR);

% verify radius comp (euclidean distances should all be equal to toolR)
dist = hypot(rrc-Rp,zzc-QZ);
if max(abs(dist(:)-toolR)) > 1e-7, error('radius comp failure'); end

% interpolate to original evenly spaced radial grid locations
Zp = zeros(size(zzc));
for k=1:Nt
   Zp(:,k) = interp1(rrc(:,k),zzc(:,k),Rp(:,k),'pchip','extrap');
end

% delete redundant data
```

```
Rp(Nr+1:end,:) = [];
Zp(Nr+1:end,:) = [];

% add compensated surface to plot
axes(get(h1,'currentaxes'));
hold on;
 plot3k({xx yy Zp});

 % tool radius compensation value.
 pos=Zp-toolR-z;
 figure
 plot3k({xx yy pos});

% form the data array
 mintheta=-5.0; maxtheta=5.0;  steptheta=th_spacing;
minx=minR;    maxx=maxR;       stepx=r_spacing;
angle = (mintheta:steptheta:maxtheta)*2*pi/360;
xslide = minx:stepx:maxx;
final=[];
final = [length(angle); steptheta*pi/180; mintheta*2*pi/360; maxtheta*2*pi/360];
final =[final; length(xslide); stepx; minx; maxx];
final =[final; angle'];
final = [final; xslide'];

for j=1:length(angle)
    final=[final; pos(:,j)];
end

acc=zeros(size(pos));
for j=1:length(angle)
    final=[final; acc(:,j)];
end
         fid = fopen('bump.txt','wt');
         fprintf(fid,'%20.16f\n',final);
         fclose(fid);
```